2

“Integrated modelling concepts for bank filtration processes: coupled ground water transport and biogeochemical reactions”

“model” group: Institute for Ecohydrology and Inland Fisheries

Responsible project leader: Prof. Dr. Gunnar Nützmann

Content

List of Figures

List of Tables

2. Integrated modelling concepts for bank filtration processes: coupled ground water transport and biogeochemical reactions

2.1. Investigations at Lake Tegel Bank filtration site

2.1.1. Objectives

The main objective of this part of the NASRI project was the modelling of hydraulic and hydrogeochemical processes during bank filtration at the Lake Tegel test site. Based on hydrogeological, geo- and hydrochemical investigations (see the chapter above) numerical models are used in order to understand the time-dependent and spatial distributed flow and transport regimes in the vicinity of well galleries taking into account the natural conditions and anthropogenic influences, e. g. pumping regimes. These models should be sufficiently correct to allow an integration and interpretation of the measured data including a predictive analysis. On the other hand, they should be simple enough to really be used in order to optimise the operational scheme.

The focus of this study is divided into two parts: (a) modelling of spatially and temporally changing three-dimensional flow structures to identify flow paths and water budgets for transport modelling; (b) development of a conceptual reactive transport model for the Lake Tegel test site in order to identify and verify observed time series of water chemistry and quality depending on transient water flow paths and velocities. Because the infiltration behaviour of the Lake Tegel sediments has shown effects, which can not be explained by the common used description of groundwater flow mechanisms only, some possible physical effects were considered, e. g. the dependence of viscosity and/or leakance on water temperature. Then, integrated flow and reactive transport modelling allows to evaluate the relation between transient groundwater movement and hydrogeochemical processes.

Beside others, the main objective of the project phase was to get a detailed and complex hydraulic model of the test site and based on that, development of a conceptual understanding of the hydro- and geochemical reactions at the Lake Tegel field-test site.

The key questions dealt with were:

What are the flow paths and travel time distributions dependent on continuously changing pumping regimes and bank sediment properties?

What is the proportion of bank-filtrate and landside groundwater in the production wells?

What are the dynamic hydrochemical conditions at the test site, in particular with regard to redox conditions?
Which chemical reaction network can be identified?
The combination of these questions is important because only with the knowledge of the spatialdistribution and dynamics of the processes studied,understanding of the predominant hydraulic mechanisms is possible. Furthermore, it is important to understand and to quantify the behaviour of specific substances studied by all working groups, relating these to field conditions present at the transect at Lake Tegel.

2.1.2. Methods

2.1.2.1. Computational Methods

MODFLOW is a well-known finite difference groundwater flow model. It was developed by the US Geological Survey (USGS) in 1988 (McDonald et. al 1988) as a modular and extensible simulation tool for modeling groundwater. Since 1988 it has been developed continuously, for this study MODFLOW 2000 (Harbaugh et al. 2000) is applied. MT3DMS (Zheng et al. 1998) is based on the MODFLOW suite and is used for conservative tracer and heat transport calculations. Water budgets are calculated with PMWBLF (Harbaugh 1990). PHT3D (see below) also uses the MODFLOW-MT3DMS suite.
PEST (Doherty 2004) is a program for nonlinear parameter estimation. PEST was coupled to MODFLOW which results in more precise calibrations with less effort.
The subprogram to calculate steady-state water balance from MODFLOW was extended to transient water balance. Several tools, either as subprogram/macro or as executable had been developed in order to handle the huge amount of data. The MODFLOW code had been extended to include temporal variable parameters in the reservoir package.
PHREEQC (Parkhurst & Appelo, 1999) is a widespread, well documented geochemical software package originating from the software package PHREEQE (Parkhurst et al., 1980) which consideres aqueous chemical equilibrium and batch reactions as mineral precipitation/dissolution, ion exchange, 1D transport, and kinetics.
During the last years reactive transport packages with interfaces to PHREEQC (Parkhurst & Appelo, 1999) were developed, e. g. PHAST (Parkhurst & al., 2004) which uses HST3D (Kipp, 1997) as flow/transport code, and PHT3D (Prommer, 2002) which uses MT3DMS (Zheng & Wang, 1999) as transport code and is embodied to the latest versions of the GUI Processing Modflow Pro (Chiang 2003).
The actual limitation of this software actually are Isothermal conditions during simulation, and only one reaction framework for the whole model domain.

PHT3D is chosen to model reactive transport, as it is based on the widespread Modflow suite and widespread PHREEQC and the reaction setup is highly adaptable to specific problems.

2.1.2.2. Measurement of infiltration

In order to obtain leakance values for infiltration, a simple in situ method is applied. Amounts of infiltrated water are measured directly under natural field conditions. A cylinder is used which is open at the bottom and closed at the top, leaving a small hole at a flange where a hose can be put up (Figure 1).

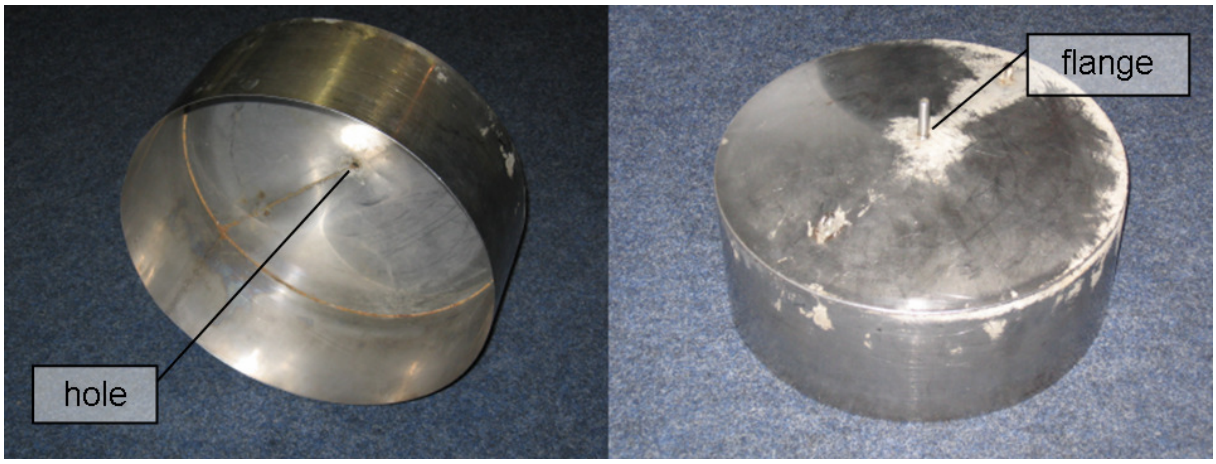

Figure 1 Barrel used for direct infiltration measurements. The open bottom is pushed into the ground, a hose with the reservoir bag is plugged to the flange at the top.

The bottom of the cylinder is inserted a few cm into the lake bed, to the flange on the top a hose is put up (Figure 2). At the end of the hose is a water filled plastic bag acts as reservoir. The difference in volume of the reservoir bag within a defined time is equal to the amount of infiltrated water. As inside the barrel the pressure is the same as outside the water infiltrates under natural field conditions.

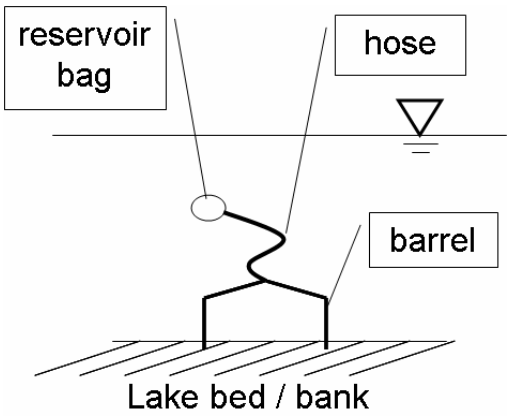

Figure 2 Vertical cross section through an infiltration barrel during infiltration measurement

2.1.2.3. Previous information

Previous Modelling

Models of different model concept, purpose and scale have been set up which include the transect at well 13. Although the model concepts are not adequate for answering the questions of this study, some benefit could be obtained.

(a) A steady state model by Eichhorn (2000) was set up to quantify the bank filtrate ratio, flow paths and travel times at the transect. The model is calibrated to data from June 1999, its extent is shown in Figure 3. The benefit from the model is an estimation of the kf values of the bed of Lake Tegel. Travel time information is neither detailed enough as the model is steady state nor applicable as the study is carried out for the hydraulic situation in 1999. As in this study turned out that the boundary conditions in the north, south and West are not correct and therefore the calculated flow paths are not valid.

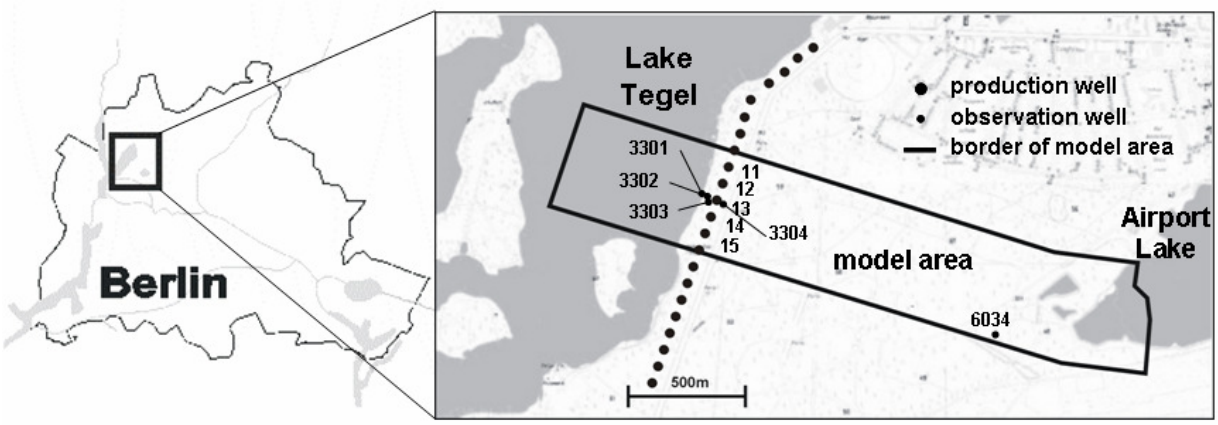

Figure 3 Model area of the steady state hydraulic Model by Eichhorn (2000)

(b) WASY (2004) set up a steady state as well as a transient catchment model on behalf of BWB (see Figure 4) to evaluate the impact of different pumping scenarios on the water resources and to give recommendations for future water management. A special issue herein is the behaviour of contaminated sites. The benefit for this study is the specification of the water divides between well field West and the adjacent well fields as the no flow boundary between well field West and well field East. This model also approves the postulation of the existence of old bank filtrate at the bottom of the main aquifer Massmann (personal communication). According to WASY (2004) this water infiltrated at the eastern bank of Scharfenberg (Figure 6) and at the Western bank of Lake Tegel at the height of well field North.

The model is calibrated steady state to selected data of 2002, and run transient for 2002 as well. This period is much shorter than the sampling period of the NASRI project (May 2002 - September 2004) and not sufficient to detect long term effects. The temporal and spatial discretisation is too coarse to give a detailed description of the transect, besides the model is too bulky/extensive and hardly manageable for this purpose. The reactive transport potentials of FEFLOW (Diersch 2002) are not as sophisticated as MODFLOW-PHT3D (Prommer 2002).

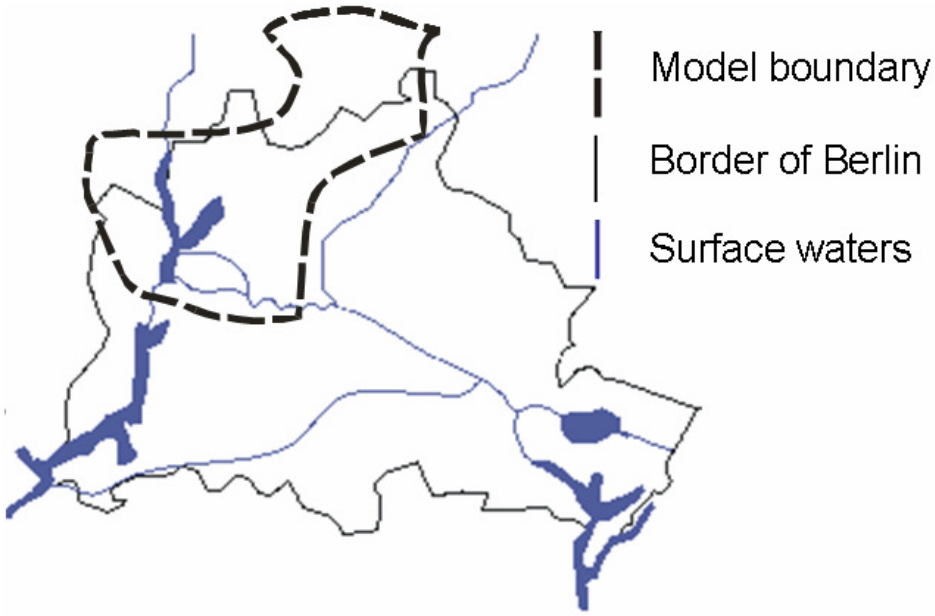

Figure 4 Model area of the model catchment (dashed line) for WW Tegel and Spandau set up by WASY GmbH 2004

(c) Rümmler (2003) and Wiese et al (2004) set up a transient two-dimensional model to assess the effects of oscillating pumping regimes on bank filtrate with approximated field conditions (see Figure 5). With this model the leakance factor could be roughly estimated. Though representing a hypothetical well field operation mode, the pumping rates are within real range and it could be detected that the boundary conditions as shown in Figure 5are not correct, that the model area has to be enlarged towards north, West and south. It is developed to the model presented in this Report.

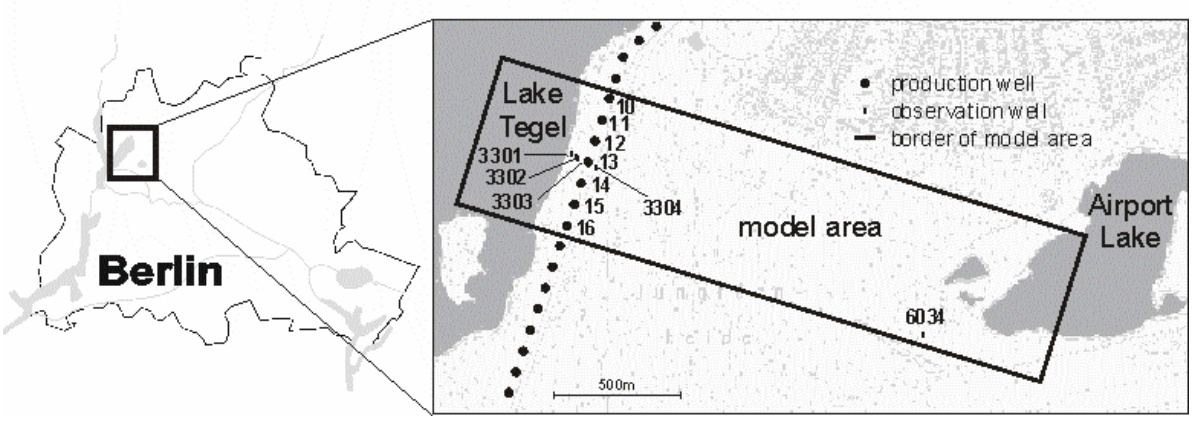

Figure 5 Model area of Rümmler (2003) and Wiese et. al. (2004)

Hydrogeology

Lake Tegel and the aquifers in the region are sandy formations formed during quarternary Saale ice-age. Lake Tegel (Figure 7) has maximum depth of 17m, with the deeper regions already being filled up with thick sediments and mud, decreasing and vanishing towards the shore (Brühl et al. 1986, Pachur et al. 1977). The two upper aquifers are important for the well field West, sealed to the bottom by thick Pleistocene mud and silt layers. (Pachur et. al. 1977) The main aquifer, where the wells are screened, is about 30 m thick and predominantly covered by glacial till of about 4 m thickness. The upper aquifer is about 10 m thick, half of which is saturated. The aquifers consist of glaciofluviatile fine to coarse sands resulting in a range of k_f values between 10^{-4} to $5*10^{-4}$m/s (Fugro 2000). At the transect the analysis of sieve curves resulted in mean k_f values of $2.9*10^{-4}$ m/s for the aquifer (Fritz, personal communication). A vertical cross section of the transect was set up by the group Hydrogeo. A tertiary fine sand aquifer with 70 m thickness lies below, although separated by 20 to 30 m thick glaciofluvial silt and clay, piezometric heads and present modelling suggest that connections to the second aquifer exist.

The airport lake (Figure 7) has a depth of 40 m and thus penetrates both upper aquifers. For further information see HSM Tegel (Hydrogeologic Structural Model), Fugro 2000.

The bathimetry of Lake Tegel is available, the origin of the data is not known.

Sieve analyses of the lake bottom in front of the transect (Sievers 2001) result in k_f values of $5.4*10^{-6}$ m/s for the upper 12 cm.

2.1.3. Modelling

Two ways have been chosen in order to increase our knowledge of the test sites by means of modelling. Hydraulics was modelled separately to geochemistry but unexpected hydraulic results were obtained and thus questions remaining unresolved made it impossible to merge

the two aspects in a way which makes sense. Nevertheless, interesting results have been worked out which probably are useful for understanding and operation of test site Tegel and bank filtration in general.

2.1.3.1. Hydraulic and transport modelling

Model input time series

It was intended to include all factors of possible relevance and asses their hydraulic impact. Data were collected from NASRI, BWB and the Berlin authority for urban development and environmental protection (SENSUT) and the "Institut für Geologische Wissenschaften Fachbereich Geochemie, Hydrogeologie, Mineralogie, FU Berlin". Most of the available data were incorporated in the model:

Water levels

-from 17 observation wells and extraction wells 12 to 14 as for Lake Tegel with intervals from monthly to hourly were provided by the group Hydrogeo

-from 13 observation wells with monthly intervals in the catchment were provided by BWB

-from Lake Tegel, Airport lake and 1 observation well in the catchment with daily intervals (Jan. 1998 – May 2005) was provided by SENSUT.

Physico-chemical parameters of the transect

-Water temperature data with monthly intervals (May 2002 – Aug. 2004) for observation wells, extraction wells and Lake Tegel was provided by the group Hydrogeo. Partially hourly intervals are available

-SENSUT provided the temperature of Lake Tegel for the time before the NASRI project.

Tracer data

-Tracer Data as chloride and boron was provided by the group Hydrogeo for observation wells, extraction wells and Lake Tegel with monthly intervals (May 2002 – Aug. 2004) and by SENSUT for Lake Tegel (Jan. 1998 – May 2005)

-Monthly data (May 2002 – Apr. 2004) of the stable Isotopes 18O and 2H are provided by the group Hydrogeo.

Well data

-Daily operational hours (1999-2005), well switching times (hourly) (1999-2004), pumpage test data (2 to 4 times per year 1998-2005) were provided for well field West, monthly sums of extracted water from each well field and amounts of artificial recharge of waterworks Tegel (1993-2005) was provided by BWB.

Precipitation

Daily data of precipitation for waterworks Tegel was provided by BWB (1998-2005).

Investigation area and corresponding model set up

The area of main interest is the transect at well 13 at the well field West (Figure 7) However during the evolution of modelling, the area that has to be regarded is much larger for three reasons:

i) During the NASRI Project it turned out that part of the water of Well 13 is of an age of at least 10 to 15 years and infiltrated on the other side of Lake Tegel.

ii) The ratios of extracted water, between the well fields and within well field West between the wells, may vary considerably. In order to minimise boundary effects, the model area has to be much larger than the transect.

iii) During some periods groundwater levels at the transect are lower than the elevation where most of the infiltration from Lake Tegel occurs. This means that changes in pumping rates are not be mitigated any more by changes in infiltration and thus drawdown affects much larger regions and the catchment grows larger. The location of the well fields pertaining to waterworks Tegel is shown in .

The model area now includes large parts of Lake Tegel with the islands Reiswerder, Scharfenberg, Lindwerder, the entire well field West, up to the Airport lake (see Figure 6).

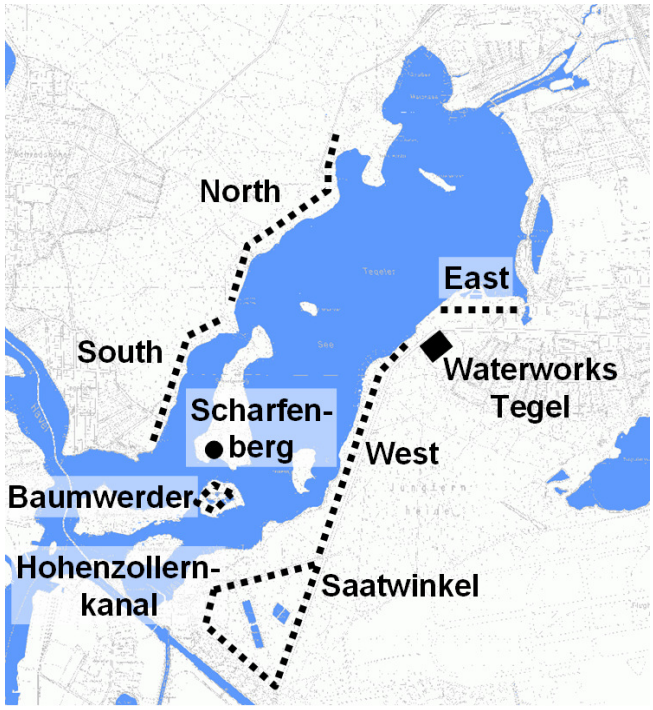

Figure 6: Location of the well fields pertaining to the waterworks Tegel. The dotted lines represent vertical abstraction wells, the black dot represents the horizontal well at Scharfenberg.

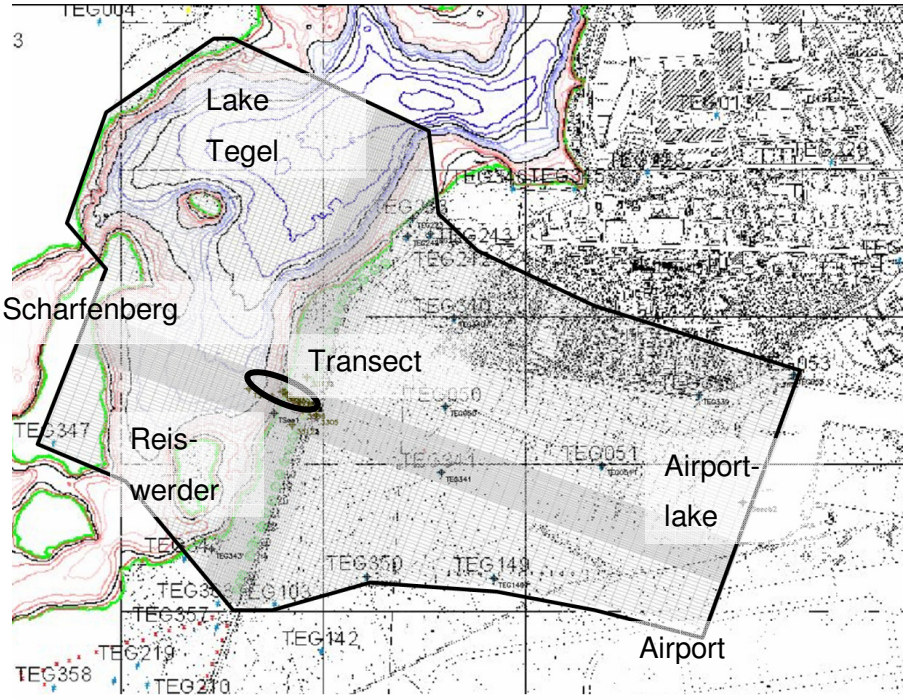

Figure 7: Extent of the hydraulic model, model cells are represented by grey lines the border by a thick black line, the bathymetry of Lake Tegel is represented by Isolines with a colour ramp from red to blue in with black 5 m intervals. Wells of the well field West are dots in green colour.

No Flow Boundaries

In the north a no flow boundary is applicable, as the ratio ob abstracted water between the adjacent well field East and well field West (Figure 6) maintains almost constant. However, modelling also showed that the not flow boundary north of well field West has to be shifted to the north, as well field West extracts water from the extended regions of shallow water next to the waterworks Tegel (Figure 8).

The lower face of the model generally is a no flow boundary, with exception of a region where contact to the underlying aquifer exists.

Specified Head boundaries

Starting from the western boundary at the location of the Airport lake and continuing clockwise the choice of boundary conditions is based of the following situation:

Western boundary: Piezometers in the model area filtered in different aquifers show that at the airport lake upper and lower aquifer have the same head, as groundwater flows mainly horizontally. So to both aquifers the same boundary condition is assigned. As this region still is under influence of the well field the boundary has to be transient. At the southern model boundary the ratio of extraction amounts between the well field West and adjacent Saatwinkel vary by factor 3, so highly variable flow directions and water levels occur, which is

respected with time variant specified head boundaries. Unfortunately it is not possible to move it farer from the well field to have at least one control piezometer in between because from the airport (Figure 8, bottom right) not data is available. On Scharfenberg a piezometer exists at the horizontal well. To avoid setting a time invariant watershed the level of the hydraulic heads is introduced as function of time. The western boundary represents the well field North. It is set to a constant head of 29 m asl. This simplification appears to be correct, as Lake Tegel sediments reach deeply into the aquifer and recharge from Lake Tegel above the boundary is considered. At Scharfenberg the situation is similar, besides modelling shows the head of the boundaries are rather insensitive parameters.

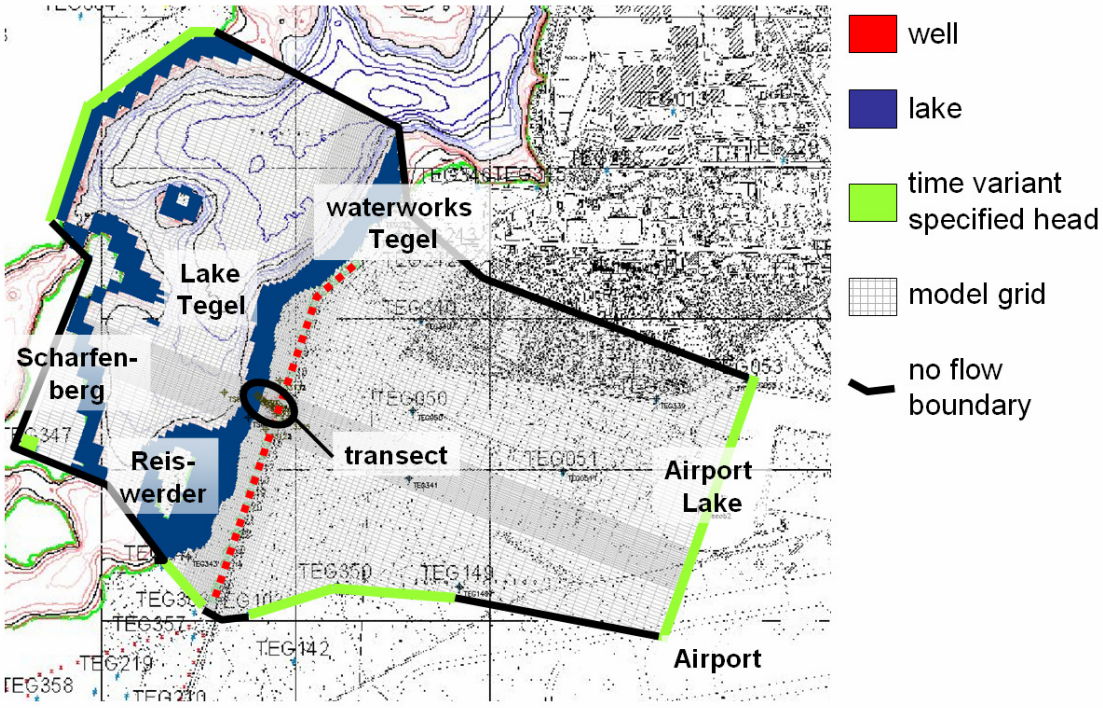

Figure 8 Top view of the boundary conditions of the model area, wells of the well field West are marked red, Lake Tegel introduced as 2nd/3rd type boundary is marked blue, time variant specified head boundaries use a pale green. Please note that boundaries are not assigned to every layer (see Fig. 9). All borders with no value assigned are "no flow" boundaries. Tiny grey lines represent the model grid.

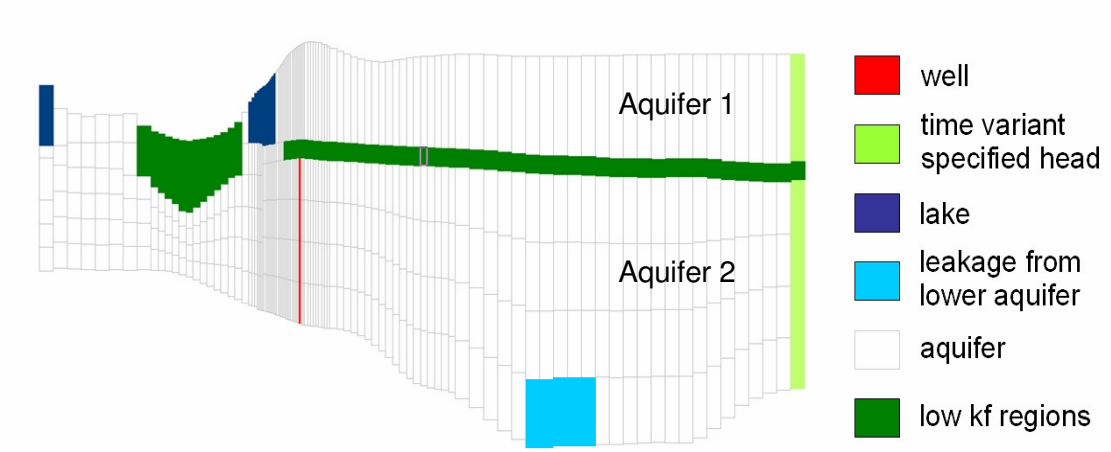

Figure 9 Cross section of the model at well 13, wells are marked with red color, Lake Tegel as 2nd/3rd type with dark blue, leakage from the underlying aquifer by 3rd type as light blue, the eastern bourndary with pale green. All white fields belong to the aquifer, dark green represents rather impermeable material as the mud and sediments of Lake Tegel and the glacial till, respectively. All borders with no value assigned are "no flow" boundaries. Tiny grey lines represent the model grid.

Wells

Using daily well operation time and pumpage, pumping rates are calculated. Amounts are checked using the sums from the water meters and hours of well operation, both registered at the well capacity measurements which take place between 2 and 4 times a year. Wells are only filtered in the second aquifer (exemplary see Figure 9). Different pumping rates for each wells 10 to 16 are split up to the model layers according to the filter depth as, vertical flow might affect the conditions at the transect. For the other wells, due to the distance to the transect, the Dupuit assumption is used the pumping rates are split according to the layer thickness.

Bottom water

Piezometric heads from the 3rd aquifer (below the model, see Figure 9) show hydraulic contact to the second aquifer, especially pronounced West of the airport lake. Geological profiles and drilling profiles show a glacial trough in this area. Flow direction is from the third to the second aquifer. Though the extent and place of the recharge area can not be located exactly, the amount of intruding water is calibrated.

Lake Tegel

Characteristics of infiltration of lake water to the aquifer are widely unknown. The parametrisation of the boundary condition presented here is result of model calibration. Sievers (2001) showed that sulfate is reduced within the upper cm of mud. As sulfate concentrations are almost the same in Lake Tegel and the adjacend groundwater, it is a strong indication that mud inhibits infiltration of lake water. Thus infiltration is assigned only to

the shallow regions (>25 m above sea level, surface water level is approximately 31.3 m above sea level, as the bathymetry is known). As further simplification regions with the same elevation are assumed to have the same leakance factors. The temporal behaviour of the leakance factor as well as the distribution of the leakance factor by water depth are estimated by inverse modelling using the software PEST. As the temporal behaviour is estimated as well as the distribution of the leakance by depth, different parameter combinations result in an almost equally good model fit. The Figure 10 and Figure 11 show exemplarily such a parameterisation.

In comparison to a k_f value the leakage has the advantage to include the unknown thickness of the clogging layer, so two unknown parameters which have to be estimated are lumped thus only one parameter has to be estimated. The leakance is related to the k_f value according to equation 1:

$$L\ [1/s] = k_f\ [m/s] / m\ [m] \qquad (1)$$

where L is the leakance, k_f the hydraulic conductivity and m the thickness of the clogging layer.

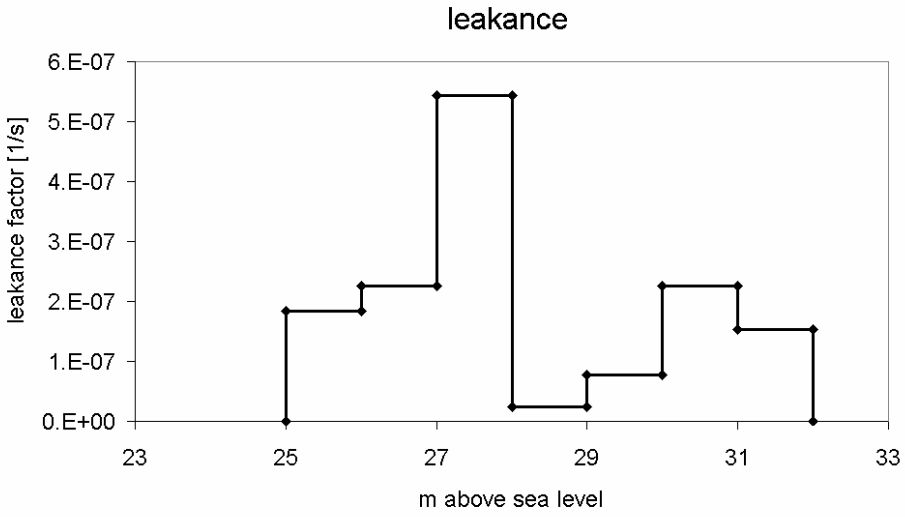

Figure 10 Distribution of the leakance according to the elevation of the bed of Lake Tegel.

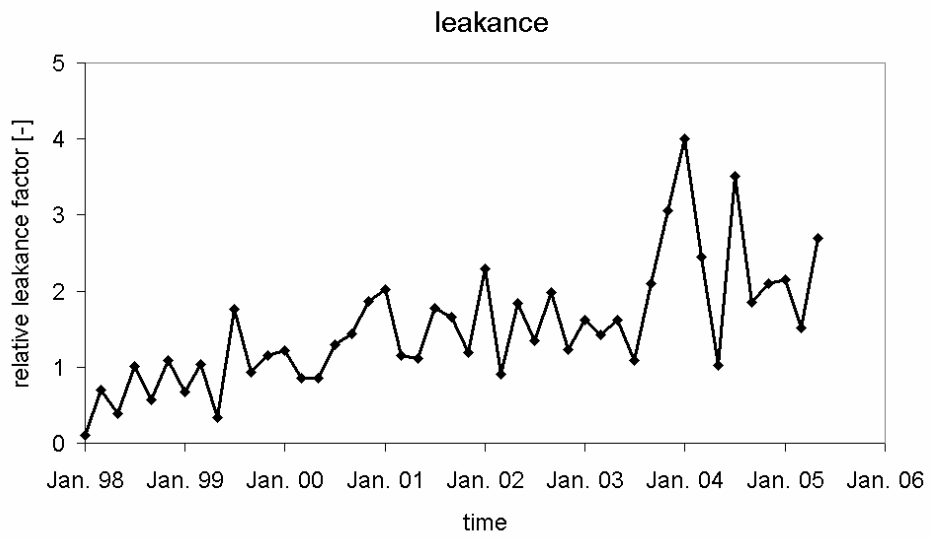

Figure 11 Relative leakance factor. The leakance values in Fig. 8 are multiplied with the relative leakance factor at each stress period.

Aquifer parameters

According to sieve analysis carried out at the transect (Fritz 2002), drilling profiles in the modelarea, and parameter estimation a homogeneous k_f value of $3.5*10^{-4}$ $m*s^{-1}$ is applied to the aquifers in the entire model. The present information does not support a reliable spatial distribution of the k_f value. Specific yield is set to 0.2 (20%), obtained by calibration of the velocity of propagation of drawdown events induced by the well field West. These values correspond with the specific yield measured near the artificial groundwater recharge site near Lake Tegel (Greskowiak 2005). The specific storage coefficient is set to $5*10^{-5}$.

Discretisation

Spatially the model is discretised in 174 rows, 117 columns and 6 layers. The rows are either 15 or 5 m wide, the columns have a width between 5 and 50 m. The layer thickness depends on the thickness of geologic formations and land surface elevation (see Figure 8, Figure 9).

The interval between 1. Jan. 1998 and 30. Apr. 2005 is modelled, including the entire duration of the NASRI project. Temporally the discretisation varies between the different stages of model evolution. The temporal discretisation is one week, with a 3 month steady state period at the beginning of the simulation period, in total 370 stress periods.

Results of infiltration measurements

Three measurement campaigns to measure the amount of water infiltrating to the aquifer were carried out near sampling well 3311 directly at the transect at the bank of Lake Tegel. The leakance factor is calculated according to equation 2:

$$l = (v * dl) / (h_w + dl) \quad (2)$$

where l is the leakance factor [s^{-1}], v is the infiltration velocity [m/s], dl is the thickness of the inner colmation [m] and h_w is the water depth [m]. It is assumed that the inner colmation has a water content of nealy 100% of the porespace. The thickness of the inner colmation is estimated to be 1 m (Sievers, personal commucation). The ground water level does not affect the infiltration as below the infiltration area it is lower than the lake bed resulting in atmospheric pressure.

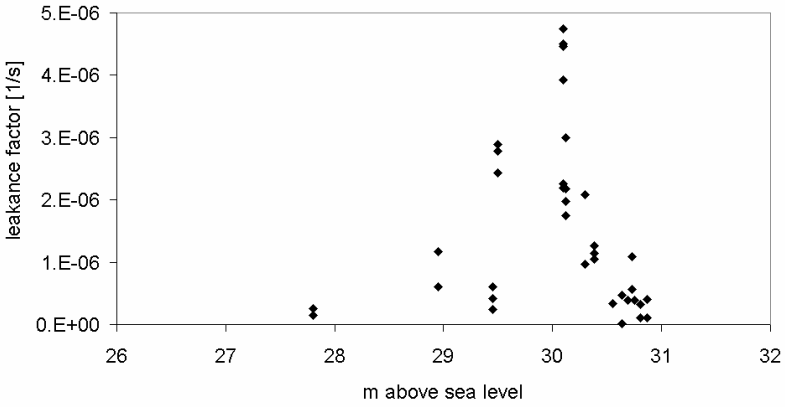

Figure 12 Leakance factor calculated according to measured infiltration rates. The depth of the lake bed is assumed to be 1 m.

The spatial variability of the leakance factor is very high. For the water depth of about 1 m, corresponding to 30.3 m above sea level, the range of infiltration is from 10^{-6} to $4.8*10^{-6}$ (Figure 12).

Results of flow and transport modelling

Temporal variant leakance

The leakance factor shows to vary by time. The reason for this behaviour could not be determined, but several observations suggest it increases with the pumping rate. The trend of temporally increasing leakance factor is the same for different depth distributions of the leakance factor, though some characteristics are different (Figure 13, Figure 15). Two scenarios are presented here.

In Figure 14and Figure 15 the temporal leakance factor and the leakance distribution by elevation of the lake bed are calibrated simultaneously, however the calibrated depth

dependent leakance (Figure 14) seems to have too high values for the deeper water (25 to 28 m above sea level) compared with the shallow water (29 to 32 m above sea level).

The depth distribution of infiltration is set as fixed (Figure 16), according to the present assumptions about infiltration characteristics. The temporal leakance factor is calibrated (Figure 13).

As only scarce measurements of the infiltration characteristic exists (compare section 3.1.3) none of these scenarios may be preferred. But the existence a temporal variable leakance factor is confirmed.

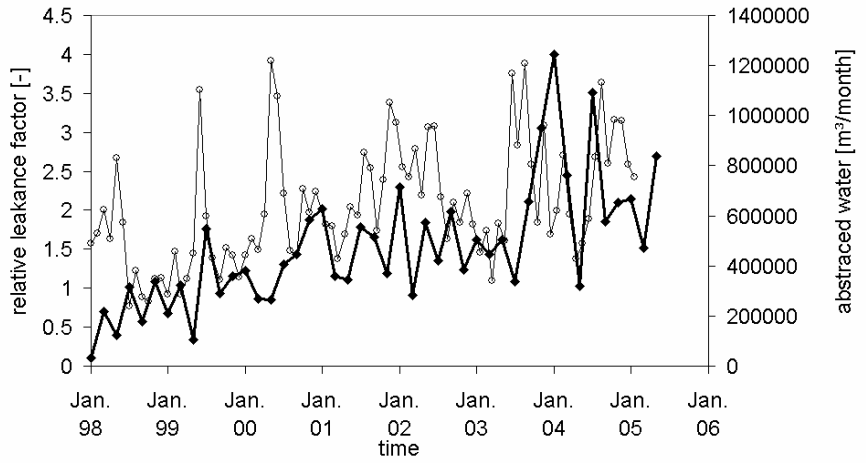

Figure 13 Calibrated relative leakance factor of the lake sediments of Lake Tegel (thick line, diamonds, left y-axis) in comparison with the monthly abstracted water from the well field West (thin line, circles, right y-axis), calibrated simultaneously with the depth dependent leakance distribution shown in Fig. 14.

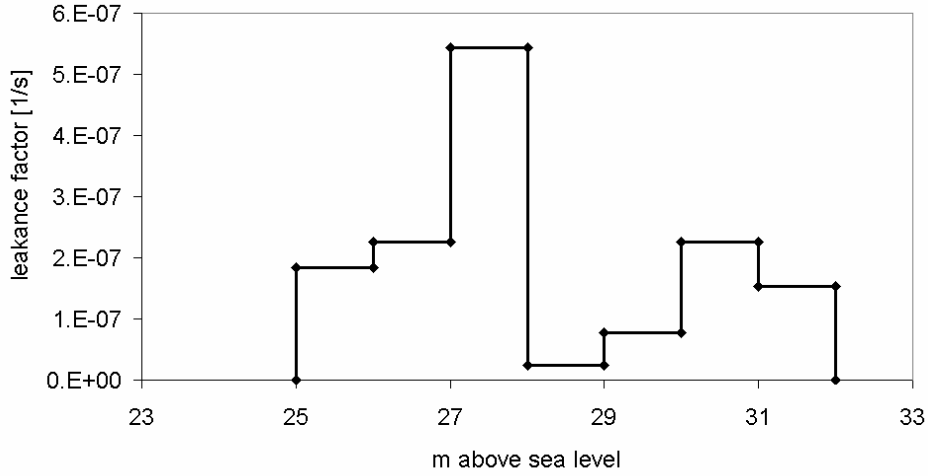

Figure 14 Calibrated distribution of the leakance factor by depth, corresponding with Fig. 13

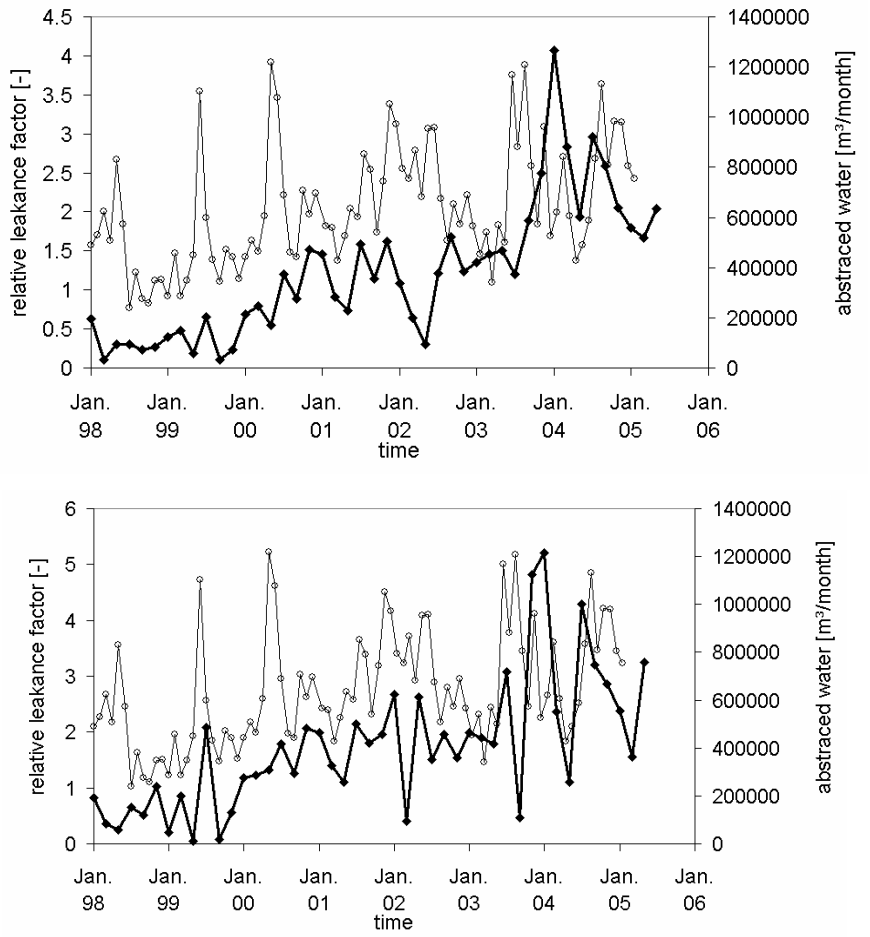

Figure 15 Calibrated relative leakance factor of the lake sediments of Lake Tegel (thick line, diamonds, left y-axis) in comparison with the monthly abstracted water from the well field West (thin line, circles, right y-axis), calibrated using the depth dependent leakance distribution of Fig. 16

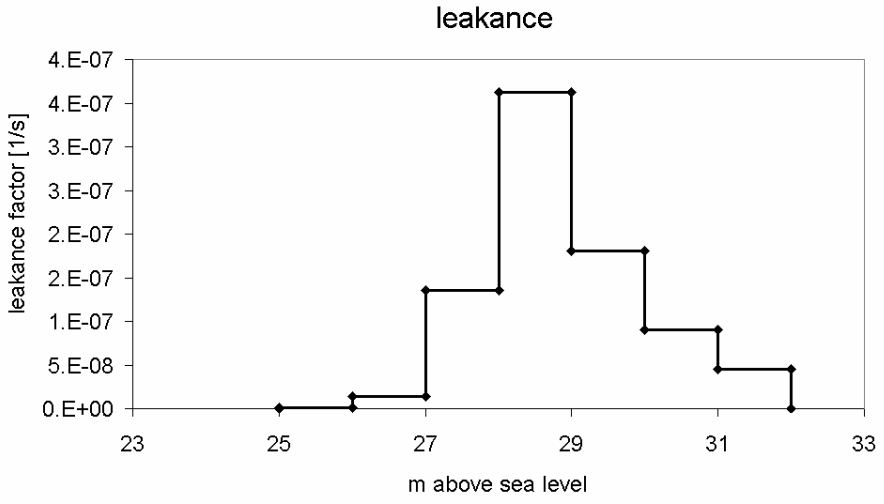

Figure 16 Hypothetical distribution of the leakance factor by depth, corresponding with Fig. 15

Comparing the relative leakance factors of Figure 15, the factor of the lower picture has higher variations than can be seen in the upper. This is a hint, the upper scenario to be closer to the real conditions than the lower. Taking also into account calibration sets the highest leakance factor to 27 to 28 m, which corresponds to a water depth of about 5 m, it seems to be likely that leakance factors tend to be highest in water depth of 4 to 6 m.

Three types of bank filtrate

The bank filtrate extracted by well 13 has 3 different origins: The top of the well gets water which infiltrated directly in front of the transect. The middle region of the well extracts water which infiltrated north of Reiswerder, the bottom extracts water which infiltrated at the shore of Scharfenberg (Figure 17). The flowfield is expressed in this way, as infiltration in the shallow regions of Lake Tegel around Reiswerder is significant.

This flowfield explains boron and chloride concentration measurements. Observation well 3301 shows a different water composition than the rest of the transect (NASRI 2005). At the beginning of the study period, namely in summer 2002, the latter can be seen as the concentrations of eg. chloride (Figure 18) and boron (Figure 19) being significantly higher than concentrations in Lake Tegel. Assuming a travel time of a few months, these concentrations cannot be explained. However, assuming a travel time of at least 15 month, the concentrations match the lake concentrations. Temporal variations of physico-chemical parameters in observation well TEG374, situated 2 m above the lower bound of the aquifer, can be assigned to water of about 20 month years age infiltrated north of Reiswerder, mixing with water showing concentrations of anthropogenic substances higher than surface water concentrations during the last 15 years, which can be assigned to water which infiltrated at the western shore of Scharfenberg. The travel time can not be determined as the model period covers only 4 years, but extrapolation of a three month duration stationary flow field are with 15 years in the same order of magnitude.

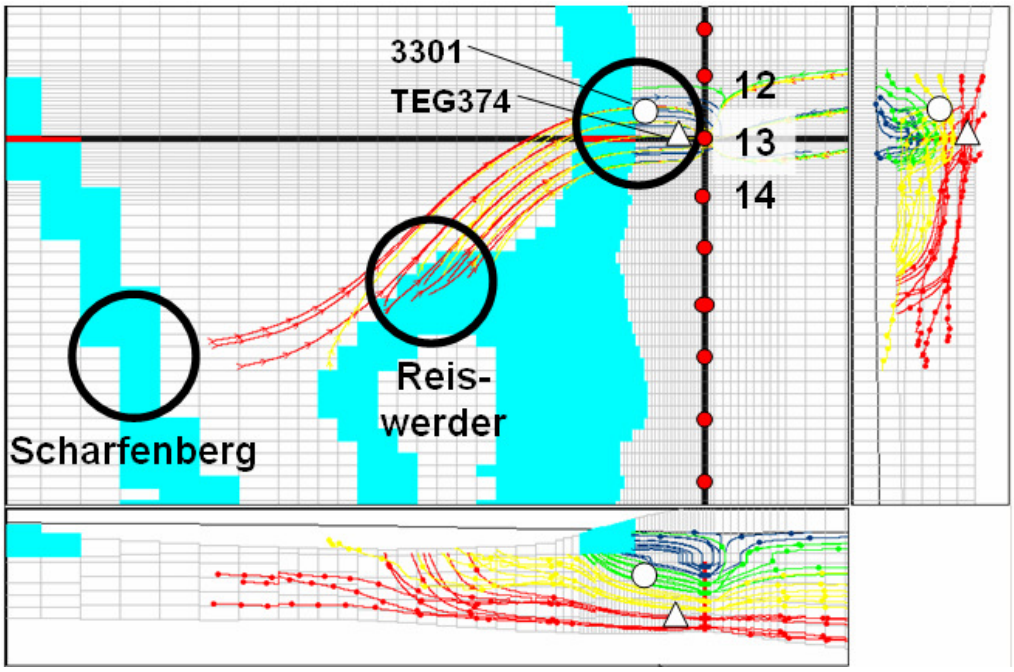

Figure 17 Backward flow lines from well 13, view from top (big image), and two cross sections along the black cross on the top view (right and bottom image). Total simulation length is 10 years, tick labels mark an interval of 1 year. The lower and right cross sections are projections along the axes of the black lines. The stationary flow field between January and March 2001 is extrapolated to the duration of 10 years. A colour ramp from blue to red is used to mark particles arriving in different depths of well 13, big black circles indicate their infiltration area. Small red circles indicate wells, the white circle indicates observation well 3301, the white triangle observation well TEG374. The grey areas indicate areas of leakage from Lake Tegel into the groundwater. The top view is a zoom of Fig. 8, well 13 lies within the transect.

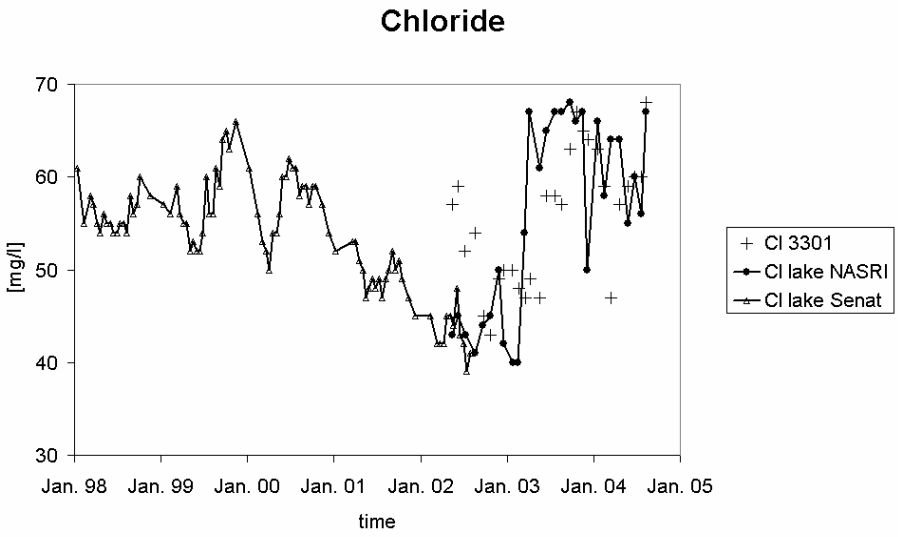

Figure 18: Concentration of chloride measured in Lake Tegel by Senat Berlin and NASRI and observation well 3301 measured by Nasri. During 2002 chloride values measured by the Senat are 5 mg/l. Without respecting this discrepance, the travel time to 330.

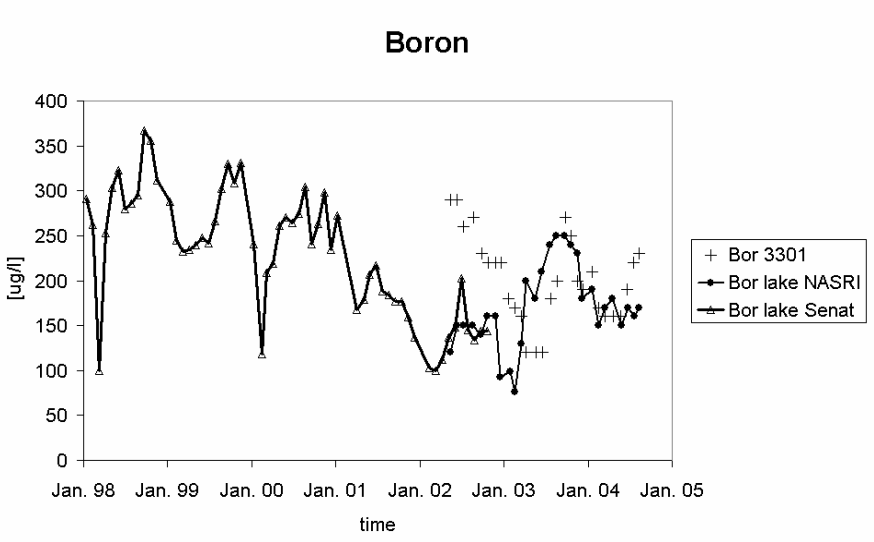

Figure 19 Concentration of boron measured in Lake Tegel by Senat Berlin and NASRI and observation well 3301 measured by Nasri. It can be seen that concentrations in summer 2002 in 3301 match boron concentrations of Lake Tegel at least 2 years ago. However, as boron may be retarded in the subsurface, travel times can not be assessed from this graphic.

Age dating

Age dating of water extracted from 3301 in spring 2003 showed an age of 20 month (NASRI 2004). This coincided quite well with the modelled travel times of 15 month and is higher than the minimum age boundary of 15 months obtained by chloride data. The model reveals that the age of 20 month is the real age of the water and not an artefact of old and young waters mixing.

Anthropogenic chemical substances

Anthropogenic chemical substances (as ADOPH, MTBE) are detected in observation well TEG374 in high concentrations (NASRI 2004). It was postulated that these substances infiltrated into the subsurface many years ago, when surface water concentrations are much higher than nowadays. As the model starts in 1998, modelling of this infiltration is not directly possible, but extrapolation of the hydraulic conditions to the past result in travel times of 12 to 15 years, which is about the minimum flow time possible, to show the concentrations observed in TEG374.

Glacial till extent

Using a precursor of the model described in section 2.3.1 the extent of the glacial till acting as aquitard can be estimated much more reliable by evaluating the drawdown by pumping experiments rather than conservative geological interpretation of pointwise borehole profiles.

The first image of the first line in Figure 20 shows such an estimation of the glacial tills extent. The advantage is a pumping experiment provides areal information of hydraulic properties and reacts to very tiny confining layers which may be overseen during drilling. However it has to be taken into account the shape of the sill shown in all figures is a best estimation for the real shape, which always remains unknown.
Analysis of grain size distributions of 3301, 3302 and suggest horizontal k_f values of 1.8 to 3.4 10^{-4}m/s. Statistically the distribution is not significant, but variability of hydraulic conductivity in vertical direction in contrast to the relatively constant horizontal average conductivity suggests the influence on the hydraulic properties by k_f value variability of the aquifer is less important than of the marl.
A calibration sequence with a constant k_f value of $5*10^{-4}$ m/s is shown in Figure 20. The first line shows a till as it was estimated by geologic profiles (Fritz 2002). Data is taken from a pumping test carried out from 13th till 26th June 1999. (Fritz 2002) During this test different wells or combinations of wells were run during 1 day, each combination followed by 1 day without pumping.

The first line of Figure 20 shows that observation well 3301 (screened below the elevation of the aquitard) reacts rather confined, with a sudden drop of piezometric head as the wells start pumping. The simulation with the till not covering 3301 does not reproduce this behaviour. In the second line of figure 20, where 3301 is assumed to be under a confining layer, this behaviour is reproduced much better. Observation well 14 was, however, screened above the elevation of the aquitard. This can be achieved by assuming the tills extend also around well 14. This calibration (line 3 in Fig. 20) already significantly improves the modelled behaviour of observation well 3312. However, the window in the till directly around well 14 is maintained according to its geological profile and the reaction of 3312 still is much too strong. When the window is closed the reaction improves.
So it has to be assumed that the confining layer at well 14 is so tiny that it could not be recognized during drilling. The same has to be assumed for observation well 3301, whose geological profile does only show a tiny till layer of about 10 cm. This suggest that the fluviatile filling around Lake Tegel according to Voigt et. al. 2000, is missing at the transect or has an extend which is very small.

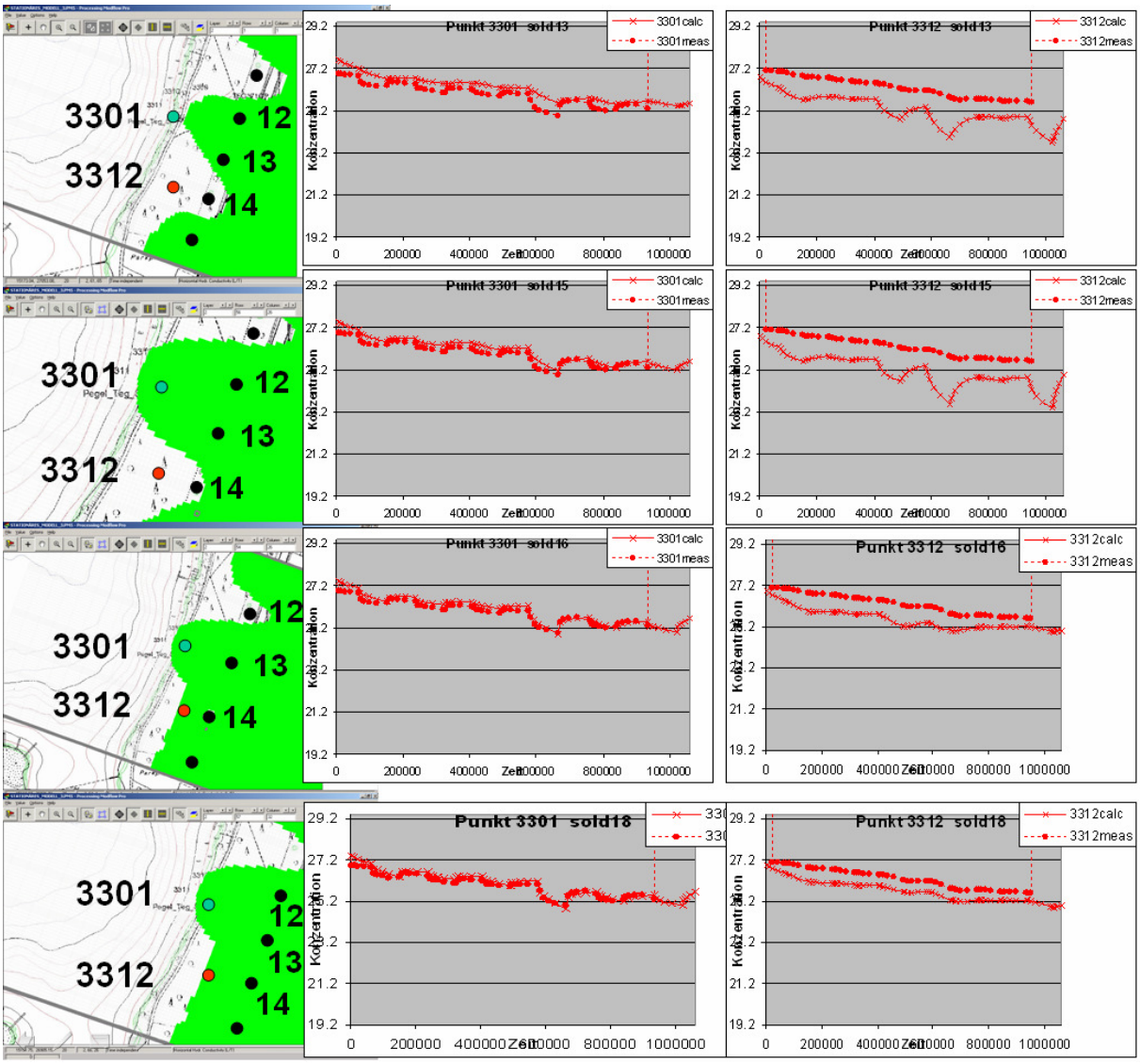

Figure 20 Variation of the extend of the till (left column) and response of observation wells 3301 (middle column, deep aquifer) and 3312 (right column, shallow aquifer). The graphs show the simulated (crossed line) and measured (dotted line) piezometric head over the time using observations and pumping rates from 13th to 26th June 1999. The numbers 12 to 14 denote abstraction well 12 to 14 of well field West.

Water balance

The origin of the water extracted by the well field West as average between Jan. 1998 and May 2005 may be seen from Table 1. Total bank filtration ratio is 70%, split up to 54% of relatively young (>3 years) and 16% of old (~15 years). Interesting is the relatively high portion of bottom water from the 3rd aquifer of 11%, as this has not been detected in previous works.

Table 1 Cumulative water balance for the whole model period, identical with the added up waterbalance from figure 21. The water quantity of Scharfenberg and Western bank of Lake Tegel is calculated as the difference of the well field West to the terms of line 2 to 5.

	m^3	% of well field west
abstraction well field West	64751134	100
leakance eastern bank Lake Tegel	35127411	54
eastern boundaries	10404901	16
bottom water	7293932	11
recharge	2574587	4
Scharfenberg and western bank	9350303	14

The transient water balance is presented in Figure 21. The high temporal variation of the pumping rate of well field West shows up mitigated in the flow of the boundary conditions as the storage capacity has a mitigating effect. Nevertheless, the variations in leakance from Lake Tegel e.g. in winter 2004 are considerably and the reason is not obvious (compare section 3.1.4.1).

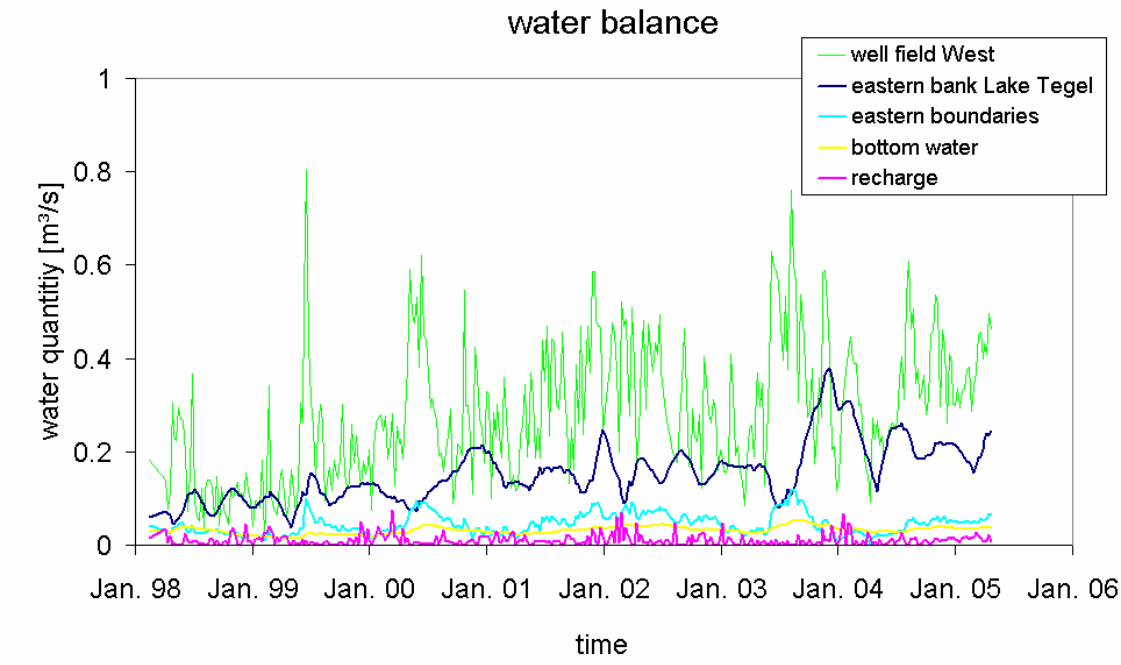

Figure 21 Transient water balance for the model area.

Bottom water

Piezometric heads of Piezometers west of the airport lake show that water from the 3rd aquifer, underlying the main aquifer intrudes into the modelarea (Figure 22, Figure 23). The difference between the existence or non-existence of bottom water results in piezometric head differenced of 20-30 cm. This is remarkable, especially considering the small distance to the boundary condition of 300 m and the well documented piezometric head of the boundary by observation well TEG053 which is located in a distance of 330 m from TEG339.

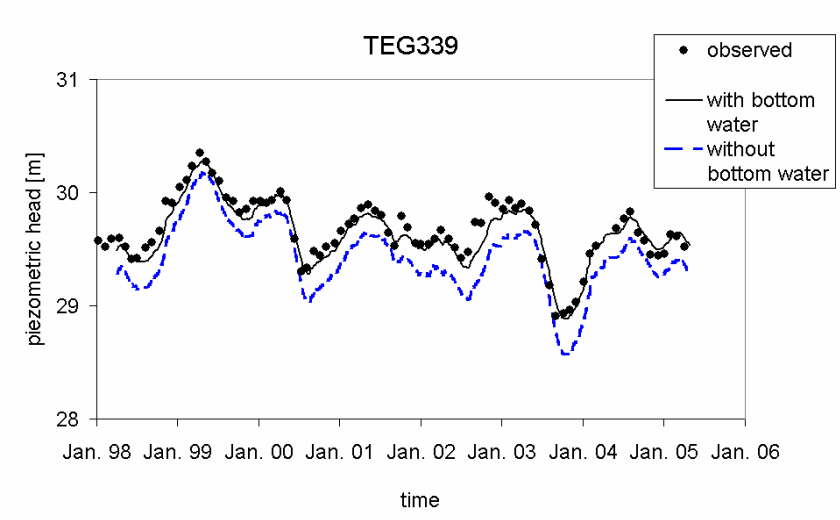

Figure 22 Piezometric head of observation well TEG339: black circles represent the observed piezometric heads, the tiny black continuous line show the model results with bottom leakage incluced, the blue dashed line shows the model results without bottom leakage.

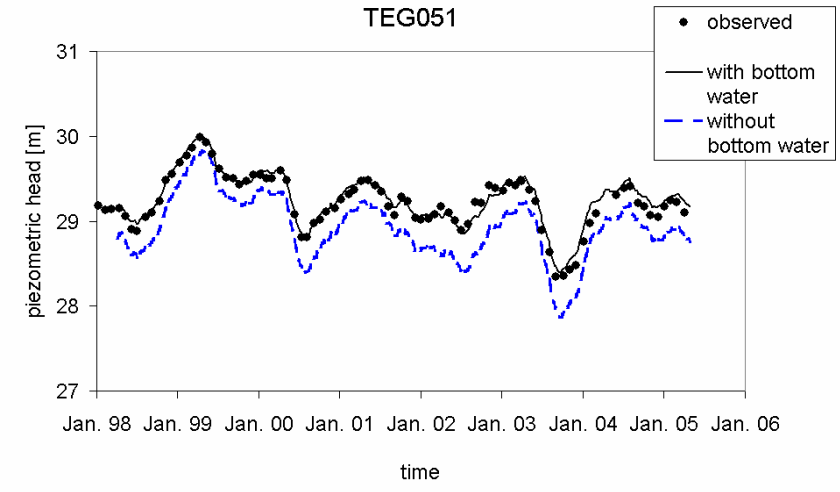

Figure 23 Piezometric head of observation well TEG051: black circles represent the observed piezometric heads, the tiny black continuous line show the model results with bottom leakage incluced, the blue dashed line shows the model results without bottom leakage.

As addtional example the heads of TEG051 (Figure 23) are shown. This coincides with piezometric heads of the 3rd aquifer reacting parallel to piezometric heads of the main aquifer (Figure 24). A large glacial trough exists in the region of the observation wells cited above (Fugro 2000) disturbing the aquitard between the 2nd and the 3rd aquifer. With the present model a hydraulic contact could be detected.

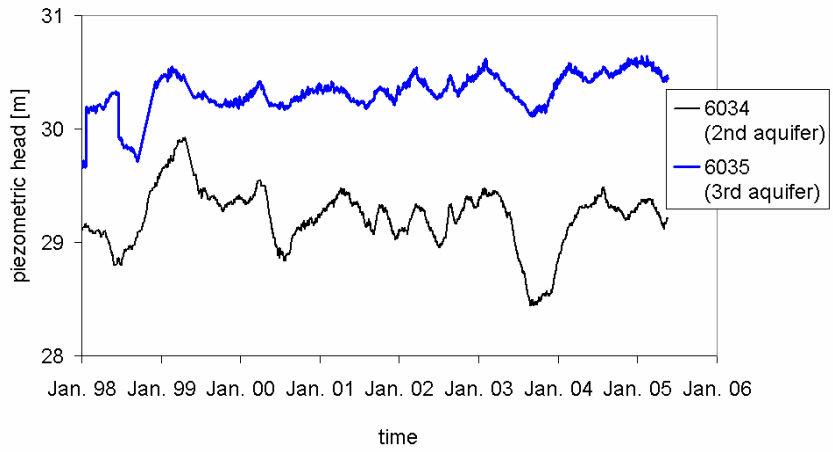

Figure 24 Piezometric heads of the observation wells 6034 and 6035. The two wells are built at the same location.

Open questions

The reasons for the temporal variant leakance could not be identified. Although the leakance factor appears to be proportional to the pumping rate on the scale of some years, and sometimes also on the scale of a few month (Spring 99, summer 2000 to spring 2002, Figure 13, Figure 15) in Summer-Autumn 2003 the leakance reacts delayed, in winter-spring 1998 and spring 2000 the leakance does not react at all to the increased pumping rate. Different mechanisms, which may be the reason for such a conductance, were introduced eg. k_f of the bank being linear or nonlinear dependent on the pressure gradient, including inertia of the bank in reacting to changes, however without satisfying result. It was taken into account that the pumping rates may vary considerably with the water level in the wells, but this hypothesis could not explain the present conductance. Changes of the boundary conditions within a reasonable range did not considerably affect the temporal conductance of the bank.

The maximum leakance factor calculated from measured infiltration rates is located in a water depth of about 1.4 m (section 2.3.1.3). Simulations however suggest in 4-6 m depth

the the leakance factor has its maximum. As local heterogeneity is high, the model results seem to be more reliable.

Leakance factors calculated for the bank on the scale of the whole model area are about one order of magnitude lower than values obtained by measurements (section 3.2, Sievers 2001). The discrepance may be explained by the fact that sampling always disturbs the sediments, which causes observed values that are too high. Spatial variability may also be an explanation, as all measurements have been carried out in front of the transect.

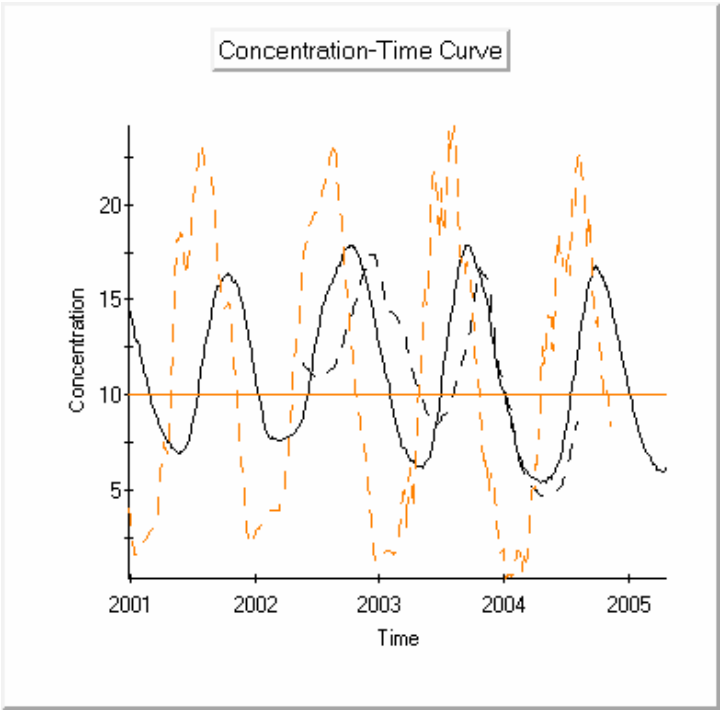

Figure 25: Water temperature of Lake Tegel (orange dashed line) observed water temperature in observation well 3301 (black dashed line) and modelled water temperature in observation well 3301 (plain black line)

Water temperature measured in 3301 during the regular sampling could not be modelled. The minimum temperature in 2002 is 11°C (Figure 25). Temperatures modelled are always considerably lower than the mean annual temperature of 10 °C. This behaviour probably occurs due to water infiltrating in front of Reiswerder, which affects observation well 3301. Transport simulation of ^{18}O however could reproduce the measured concentrations.

2.1.3.2. Geochemical modelling

Three steps have to be carried out in order to set up a geochemical model. A simplified or generic flow and transport model was set up, the chemical analyses are verified, and a reaction module is set up, calibrated and verified to the measured data.

Setup of the generic flow and transport model

In order to assess the biogeochemical and hydrochemical development and characteristics along the riverbank filtration test site and as preparation to expand the calibrated/verified flow and transport model ‘test site Tegel’ as reactive transport model, a generic/conceptual flow model was set up which considers:

i) The idealised geological stratification of the Tegel Test site

ii) The Lake Tegel as 3rd kind flow boundary

iii) Three wells from well field West with strongly unsteady pumping regime as typical for the test site ‘Lake Tegel’

The model area was specified as a rectangle 1000 m in length, 100 m in width, and 50 m in vertical thickness. The horizontal and vertical model geometries and discretisation are shown by Figure 26 and Figure 27.

Figure 26: horizontal model geometry

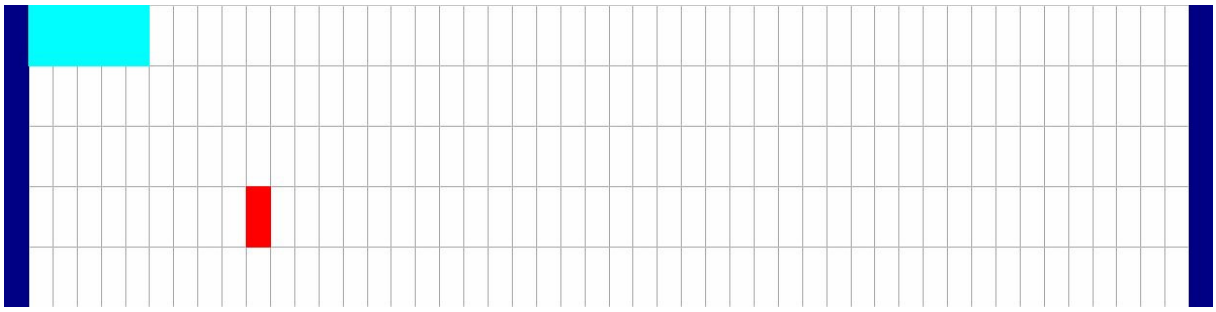

Figure 27 model vertical cross section

The 3D-model is spatially discretised by 50 columns, 5 rows, and 5 layers. As Figure 27 shows, the well field is assigned to a depth of 20 m below the model surface as derived from the screen positions of the production wells at the Tegel test site. The model top was assigned at 35 m above sea level, the model bottom at –15.0 m above sea level, according to a geological profile (Fugro 2000).

The hydrogeological model applied to the generic model is based on the information available from the investigations at the Tegel test site (NASRI 2003) and a hydrogeological structural model (Fugro 2000) which show an about 50 m thick aquifer partially intersected by an aquitard (glacial till) of up to 5 m thickness, see Figure 26. Near the Lake Tegel bank, no aquitard was detected during drilling, so all model layers in this part are homogeneous.
As shown by Figure 28, the aquitard was placed to third model layer (from the model top) by an adequate k_f value parameterization. A k_f value of 43.2 m d^{-1} (or $5*10^{-4}$ m s^{-1}) was assigned to the aquifer, whereas to the aquitard a k_f value of $8.6*10^{-3}$ m d^{-1} (or $1*10^{-7}$ m s^{-1}) was assigned. As a first approach, isotropic conditions were assumed. Additionally, a storage coefficient of $1*10^{-5}$ (as required for transient simulations) and an effective porosity of 0.25 were specified to the whole generic model.

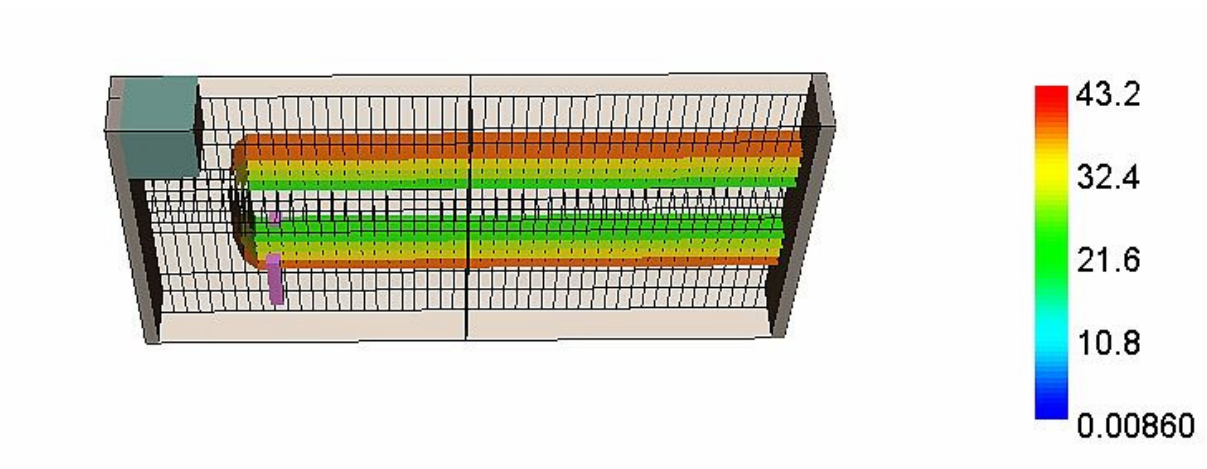

Figure 28 Aquitard within the generic model (bar column shows k_f values in [m d^{-1}])

Reflecting the local conditions at the Tegel test site, an initial hydraulic head of 28.0 m above sea level was specified for all model layers. Below the lake (left) the constant head boundary was set to a hydraulic head of 28.0 m. To the right model constant head boundary (landside) a hydraulic head of 28.5 m above sea level was assigned.

Because at the Tegel test site the screens of the production wells are below the base of the aquitard, the well nodes were placed within the fourth model layer (counted from the model top).

Flow field of the generic flow model

The flow model was run transient over 1095 days. In a first period (up to a simulation time of 365 days), no pumping was assigned to the wells in order to achieve a reliable initial flow solution. After 365 days, the wells were switched on applying an oscillating pumping regime. The central well (900 m^3 d^{-1}) is operated in alternation with the border wells (each 450 m^3 d^{-1}) in periods of 10 days (Figure 29).

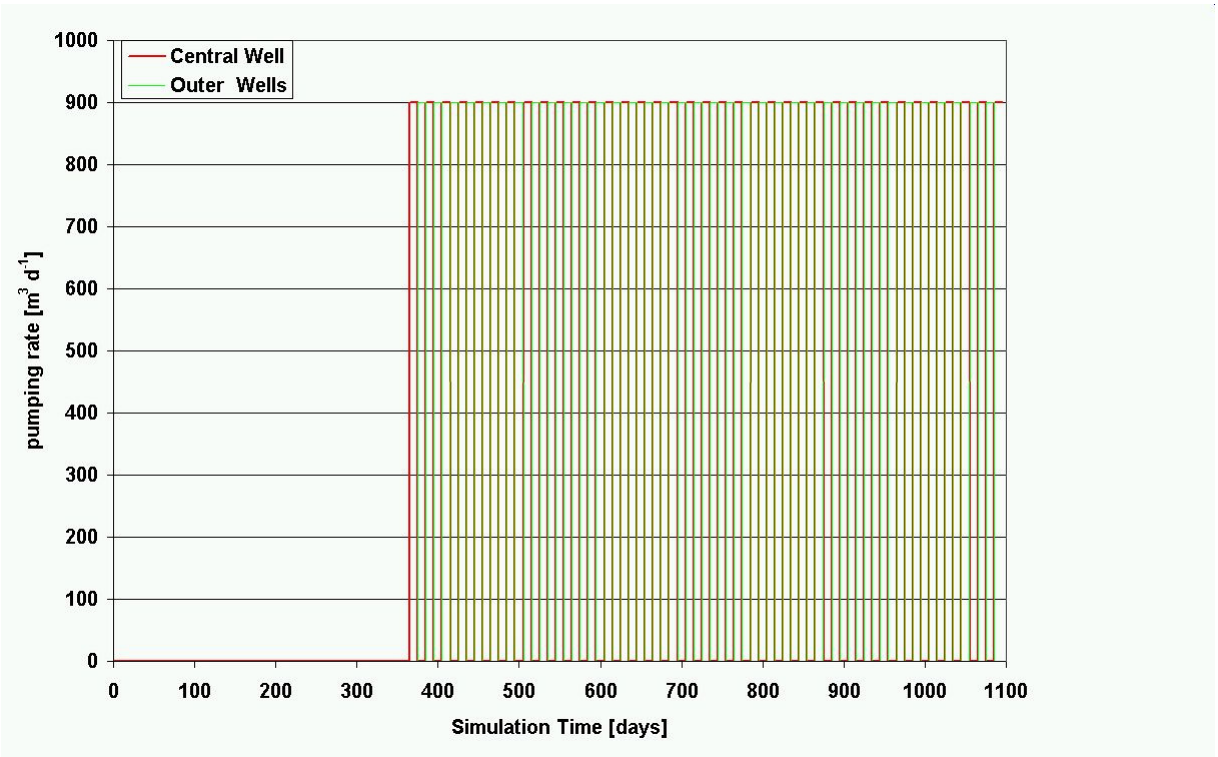

Figure 29 Pumping schedule assigned to the wells during simulation time

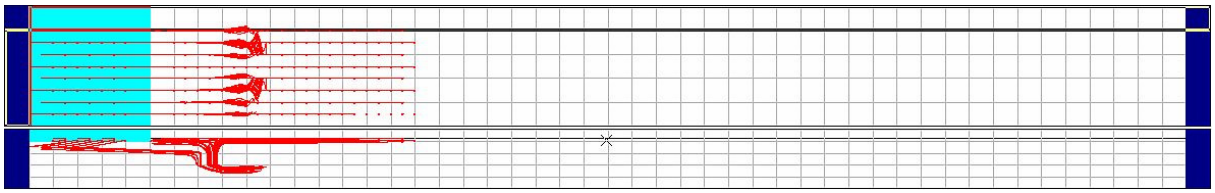

Figure 30 Transient flow paths in the generic model area (upper section base view, lower section vertical cross section along y axis). Light blue represents 3rd type boundary Lake Tegel, dark blue constant head boundaries. Red lines are flowpaths.

As a result of the applied pumping regime the flow paths calculated using transient simulation are shown by Figure 23. Due to the applied pumping regime the calculated flow paths (which are saved at every time step) are smeared as they approach the actually active (and actually switched off) wells. The flow paths were started as well from the river as from the land side to get an overview about the transient flow field between the river and the well field as well as the impact of the aquitard on the flow field. Vertically, the flow paths started at the land side are expected to flow around the aquitard in order to reach the production wells screened below the aquitard. If the aquitard is modelled using a greater leakage, a significant vertical flow (though retarded) through the aquitard especially above the filter screens is possible. The flow paths started at the river side are also influenced by the extent of the aquitard resulting also in a downwards deviation near the aquifer border followed by a tracking below the aquitard toward the wells.

Reflecting the highly transient flow regime, piezometric head distributions only can be given for the 2 regime situations applied here. By Figure 31 and Figure 32 the calculated vertical piezometer head distributions are shown for two situations

i) Outer wells are pumping

ii) Only the central well is pumping

For both situations, the drawdown cone around the well gallery is expected to occur within the deeper parts of the aquifer also due to the modelled geology, especially the extension of the aquitard, which generates a strong vertical piezometer head gradient. Below the aquitard, flow is horizontal toward the active production wells. By both flow path analysis and piezometer head distribution the most probable pattern of hydrodynamic transport (as basic for the reactive transport) can be evaluated.

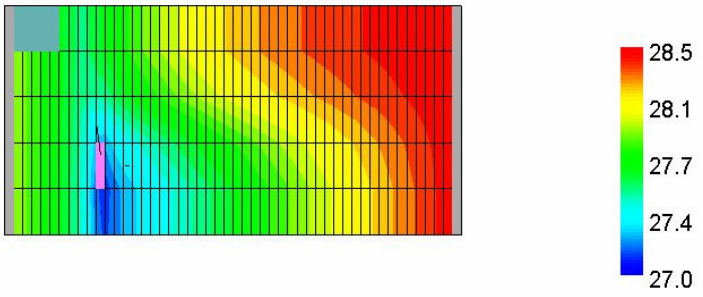

Figure 31 Hydraulic heads after 379 days (outer wells active as indicated by the magenta bar)

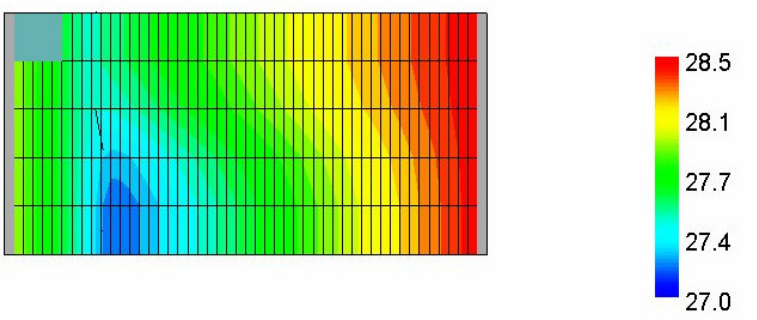

Figure 32 Hydraulic heads after 469 days (central well active)

Evaluation of hydrochemical analyses

A verification of groundwater sample analyses as good as possible is a prerequisite for an adequate reactive transport simulation at the riverbank filtration test site. In order to estimate correct initial and boundary hydrochemical conditions all available chemical analyses of sufficient quality (ion charge balance error) were subjected to a verification using PHREEQC (Parkhurst & Appelo 1999).

As data basis, 293 groundwater and 25 surface water analyses sampled at the Tegel transsect are available from January 2002 to September 2004. 4 groundwater analyses were not complete (due to a lack of temperature, pH, E_H, O_2, or relevant cation/anion data). Only analyses with less than 5% ion balance error were processed. The ion balance error was calculated for each analysis dataset based the main cation and anion concentrations (in meq l^{-1}) provided as input for PHREEQC calculation using equation 3.

$$Ion - Balance - error = \frac{\sum cations + \sum anions}{\sum \text{cations} - \sum anions} \cdot 100 \qquad (3)$$

Applying this criterion, 9 groundwater analyses had to be discarded. Finally 280 groundwater analyses were provided to be processed by PHREEQC. All 25 surface water analyses taken from Lake Tegel fulfilled the required quality criteria and were processed.

Conceptually, the analysed hydrochemistry is regarded as a result of solution equilibration with an adequate mineral assemblage within the aquifer matrix. The selection of typical equilibrium mineral-assemblages relies to the core matrix analyses (NASRI, 2003). Relevant mineral phases to be considered in this context are Calcite ($CaCO_3$), Pyrolusite (MnO_2), Ferrihydrite ($Fe(OH)_{3\ (amorphous)}$), Rhodochrosite ($MnCO_3$), and Siderite ($FeCO_3$). Using MATLAB, an automated processing of the large amount of chemical analyses data by PHREEQC was performed.

An uncertainty exists for the verification of the chemical analyses arises from the scarcely known matrix composition (one drilling core analysed). Especially the content of trace minerals such as Calcite, Fe- and Mn oxides/hydroxides and carbonates affect the equilibrium.

The parameters analysed and used for verification using PHREEQC are listed in Table 2.

Table 2 Analysed chemical parameters (NASRI DATABASE, 2004) and chemical parameters used for verification by PHREEQC. Grey fields denote parameters used for PHREEQC processing.

Analytical Parameter	Unit	Analytical Parameter	Unit
Temperature	°C	El. Conductivity	µS/cm
pH	-	DOC	mg/l
O_2	mg/l	TOC	mg/l
E_H	mvolt	UV 254	1/m
Fe (total)	mg/l	AOX	µg/l
Mn	mg/l	AOCl	µg/l
Acid Capacity pH 4.3	meq/l	AOBr	µg/l
Base Capacity pH 8.2	meq/l	AOI	µg/l
CO_2	mg/l	B	µg/l
HCO_3	mg/l	EDTA	µg/l
Ca	mg/l	NTA	µg/l
Mg	mg/l	AMDOPH	µg/l
Na	mg/l	AMPH	µg/l
K	mg/l	DMAPH	µg/l
NH_4-N	mg/l	Carbazepin	µg/l
NO_3-N	mg/l	Phenazon	µg/l
Cl^-	mg/l	Propyphen	µg/l
SO_4	mg/l	MTBE	µg/l

Parameters affected by PHREEQC equilibration are all components involved in precipitation/dissolution reactions or redox reactions, available from the PREEQC database such as: pH, E_H (pe), Ca, TIC (predominantly HCO_3^-), Fe, Mn, O_2, NO_3-N and NH_4^+-N.

Other parameters (such as Na, K, Mg, Cl) are assumed to be involved only in aqueous chemical equilibria and are therefore expected to be unchanged during PHREEQC calculations. Due to the observed redox conditions, SO_4 is also expected to be practically not involved. Temperature is included as a important parameter for equilibrium constants and therefore chemical speciation.

The parameters CO_2 and HCO_3^- were summed up to the PHREEQC input parameter tetravalent inorganic carbon (C(4)). Because PHREEQC requires pe values instead of E_H as data input, E_H was therefore converted to pe using equation 4

$$pe = -\lg(e^-) = \frac{F}{2.303 \cdot R \cdot T} \cdot E_H \qquad (4)$$

with

F = FARADAY constant 96484 [C/mol or J/(Volt * mol)]

R = 8.315 [J/(°K * mol)]

T in [°K]

E_H in [Volt] (Appelo & Postma, 1996)

The assumed initial mineral concentrations to get equilibrated are given by Table 3, and are in the order of magnitude as detected by the core analysis (NASRI, 2003).

Table 3 Assigned initial Mineral concentrations

Mineral	Initial concentration		
	mol l^{-1}aq [1)]	weight %	mg element/kg dry soil
Calcite	5.9×10^{-2}	0.1	-
Ferrihydrite or Siderite	1.132×10^{-1}	-	1170
Pyrolusite or Rhodochrosite	3.8×10^{-3}	-	29

[1)] used for PHREEQC calculations

An adequate choice of the mineral phase assemblage is decisive to verify the sampled analysis data set.

Analyses typical for an iron reducing environment could adequately be verified on the basis of a phase assemblage Calcite+Ferrihydrite+Rhodochrosite+Siderite+Pyrolusite. For all analytical datasets showing a pe value less than 3.0, deduced from redox potential measurements, an equilibrium phase assemblage without Pyrolusite was assigned.

The initial mineral concentrations in the surface water samples were set to zero. This way, the minerals potentially (if oversaturated) can be equilibrated. The range of redox conditions was found from oxic conditions in the surface water and in the shallow groundwater samples to anoxic conditions (until iron oxide reduction stage) in the deeper groundwater samples (NASRI, 2003).

Figure 33 to Figure 39 give an overview of the verification of the analytical data by PHREEQC.

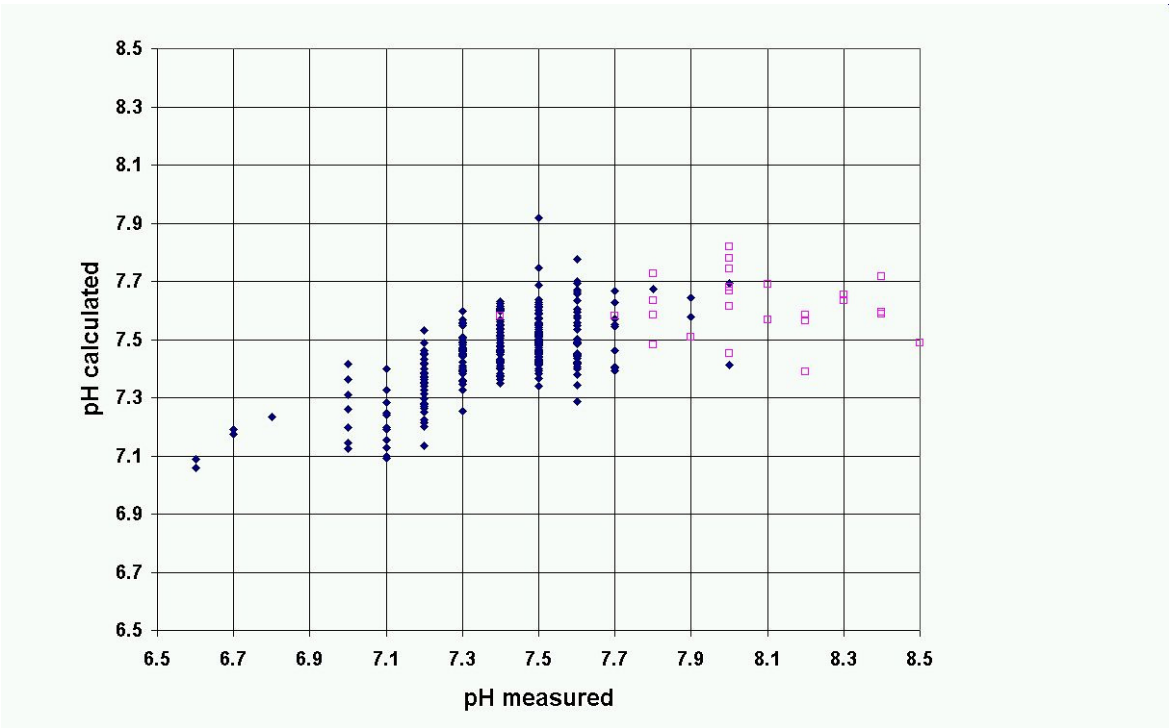

Figure 33 Scatter diagram of all measured and calculated pH values of groundwater samples (blue ♦) and surface water samples (pink □) from the Tegel test site

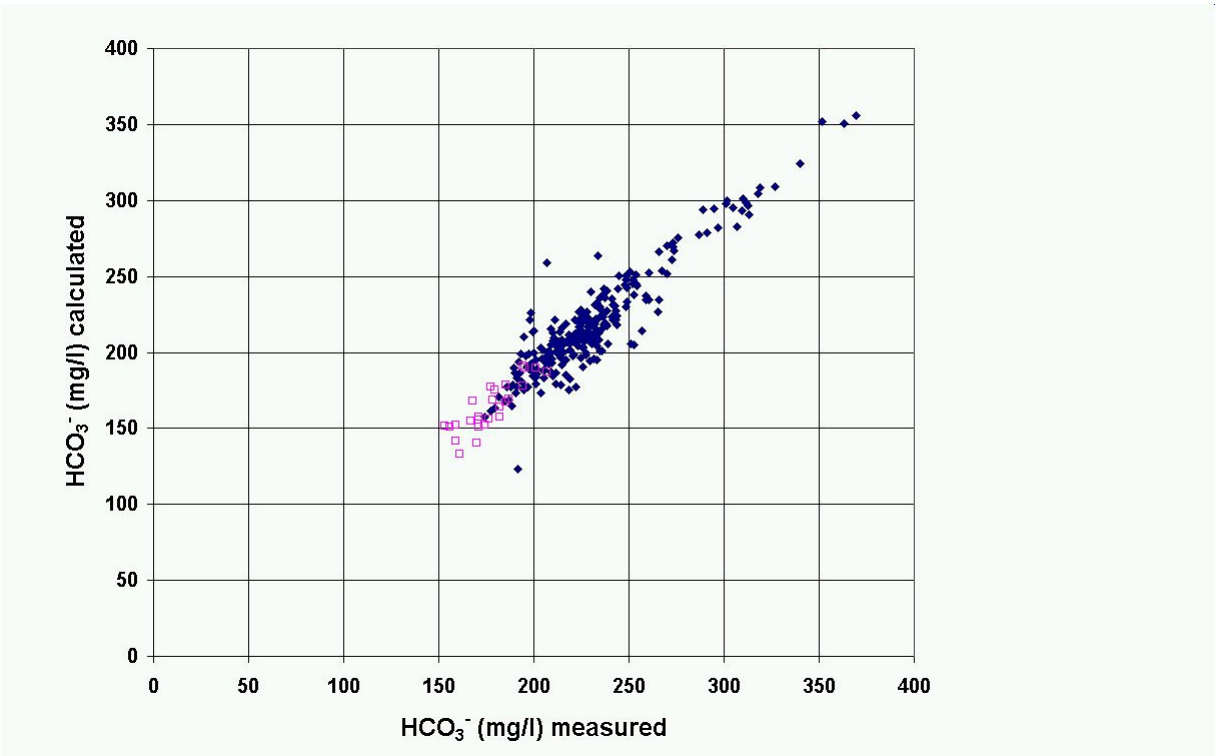

Figure 34 Scatter Diagram of all measured and calculated HCO3- concentrations of groundwater samples (blue ♦) and surface water samples (pink □) from the Tegel test site

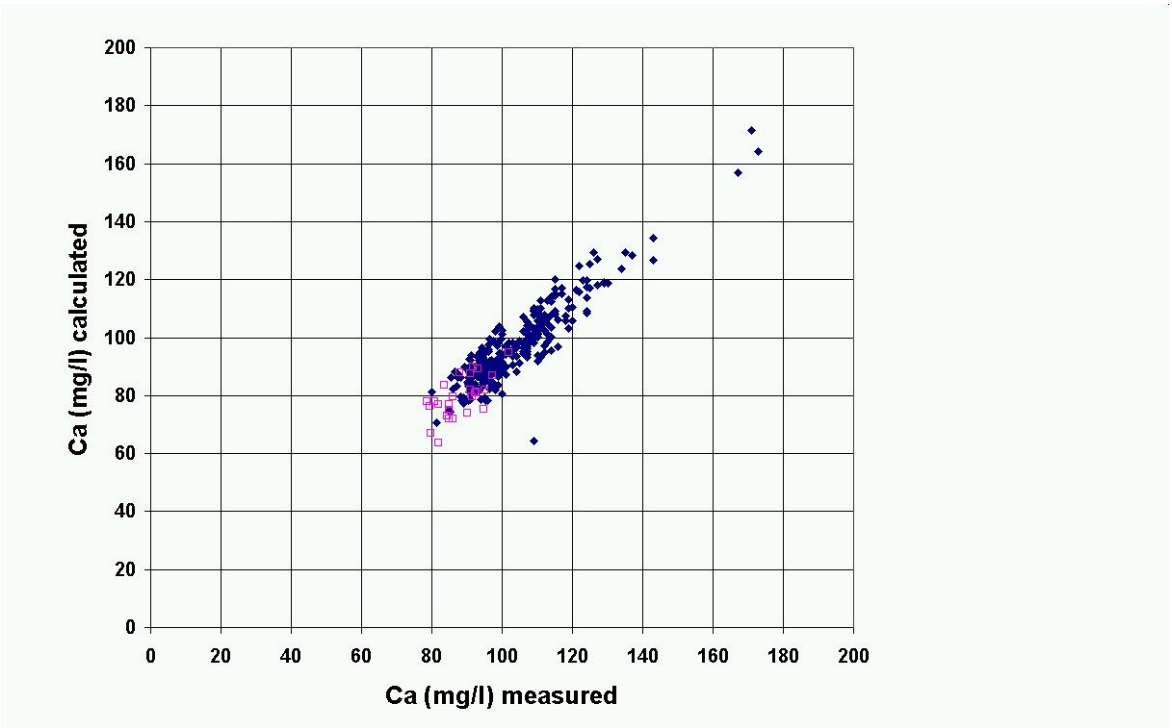

Figure 35 Scatter Diagram of all measured and calculated Ca concentrations of groundwater samples (blue ♦) and surface water samples (pink □) from the Tegel test site

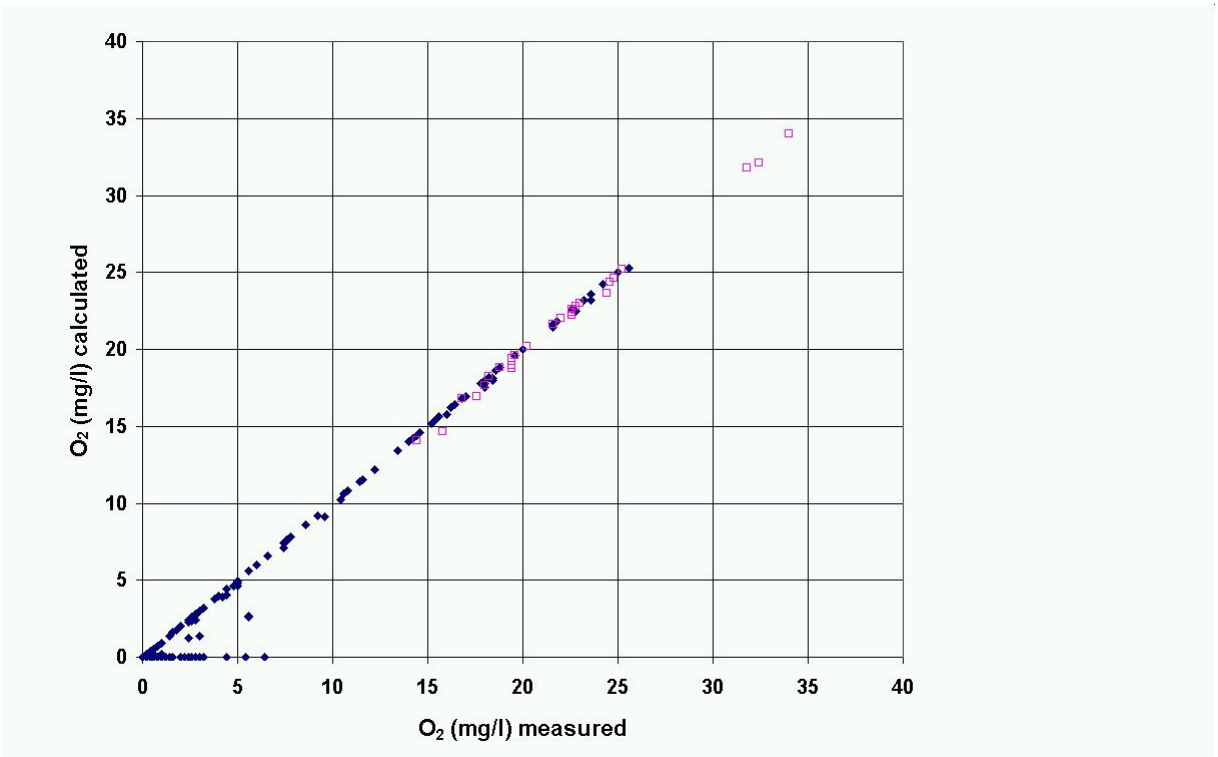

Figure 36 Scatter Diagram of all measured and calculated O2 concentrations of groundwater samples (blue ♦) and surface water samples (pink □) from the Tegel test site

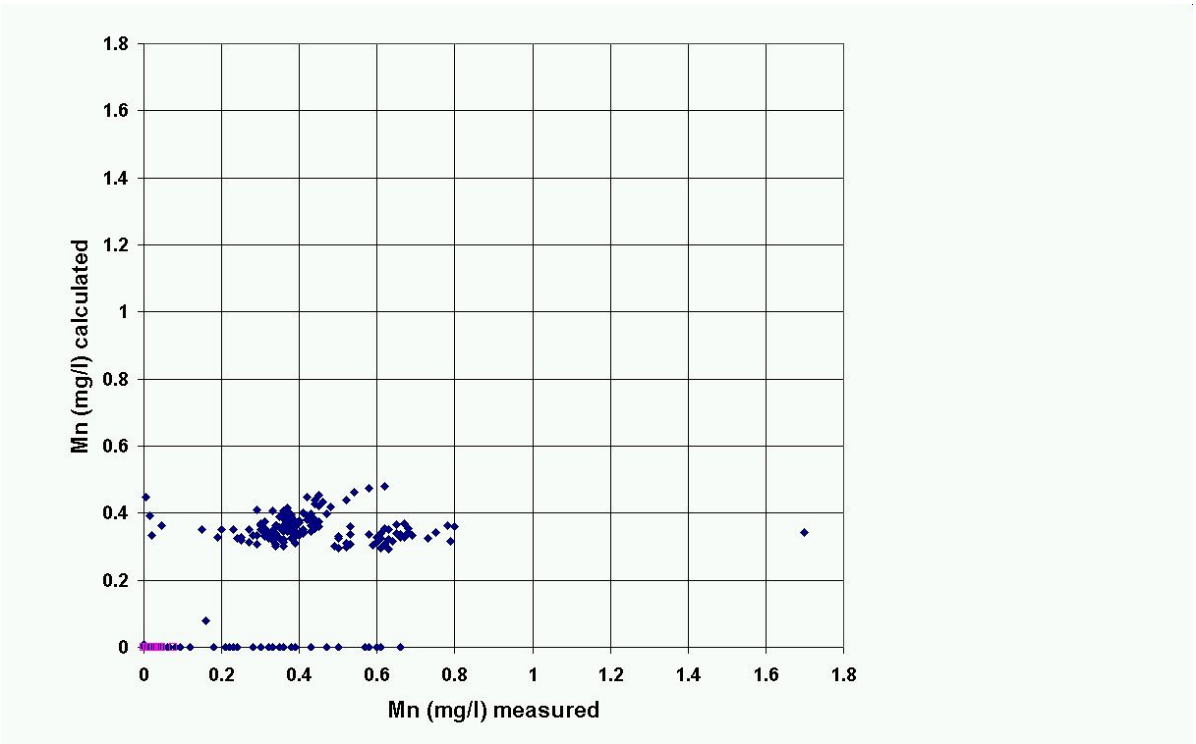

Figure 37: Scatter Diagram of all measured and calculated Mn concentrations of groundwater samples (blue ♦) and surface water samples (pink □) from the Tegel test site

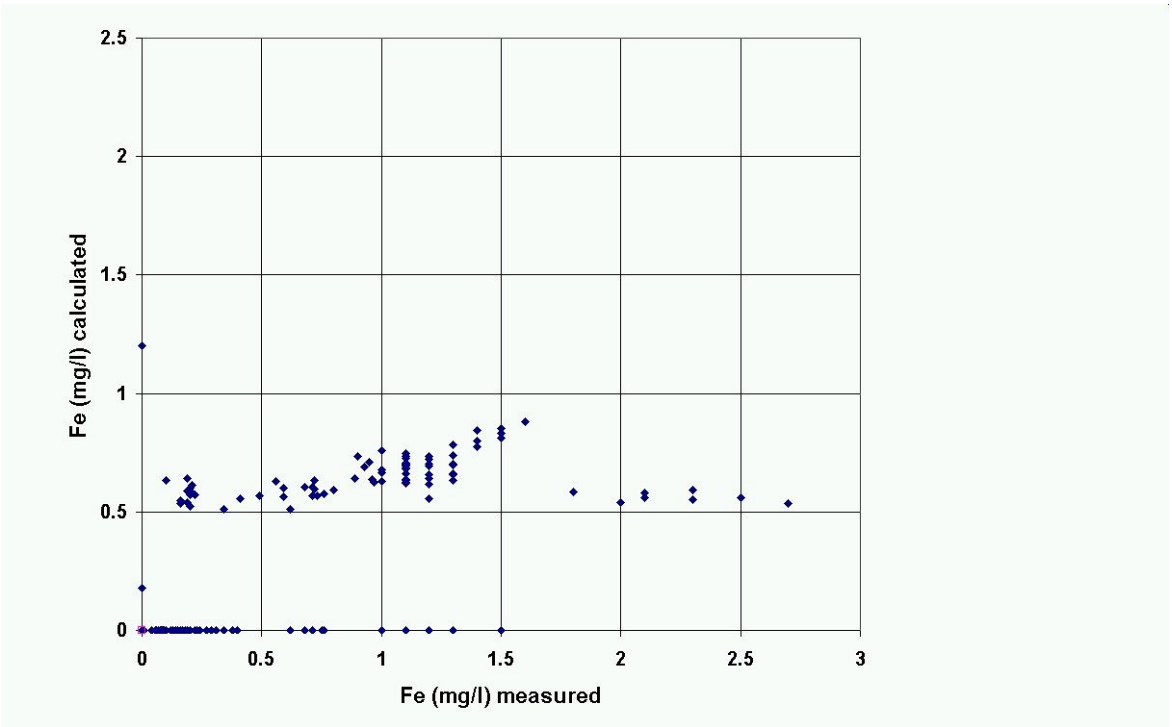

Figure 38Scatter Diagram of all measured and calculated Fe concentrations of groundwater samples (blue ♦) and surface water samples (pink □) from the Tegel test site

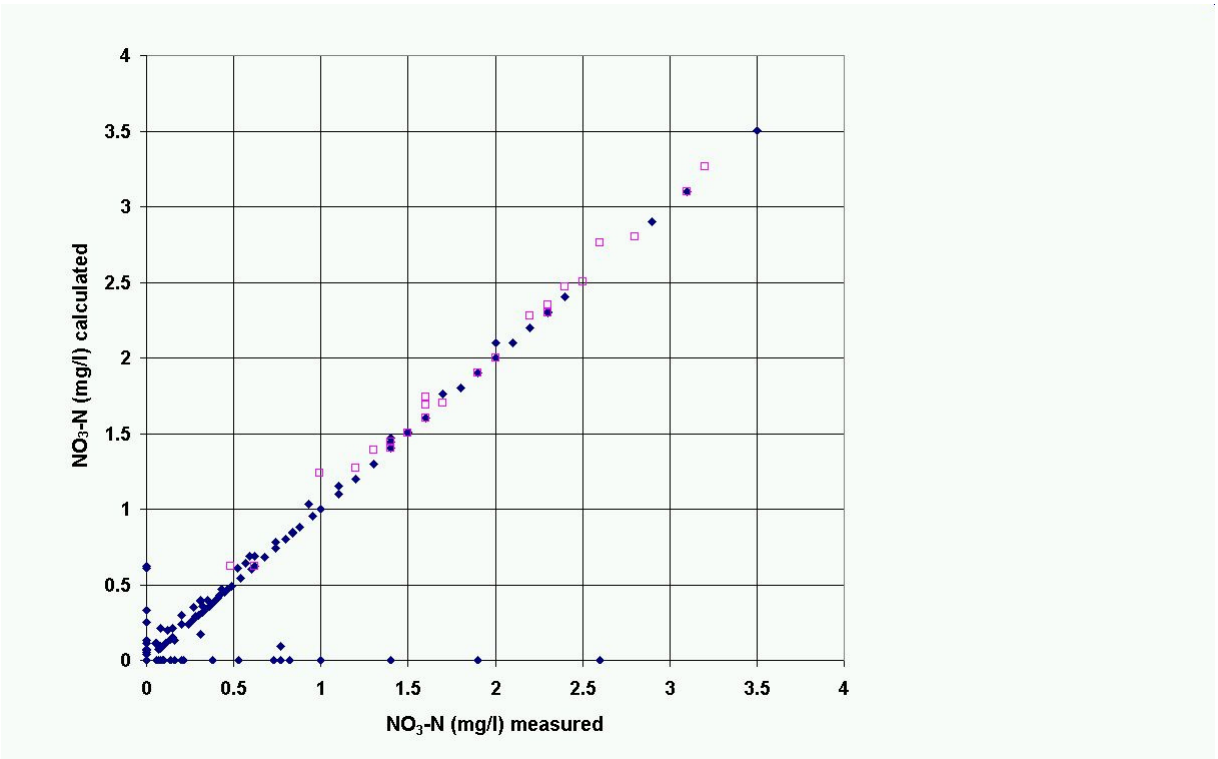

Figure 39Scatter Diagram of measured and calculated NO3-N concentrations of groundwater samples (blue ♦) and surface water samples (pink □) from the Tegel test site

Figure 33 to Figure 39 show that the processed chemical analyses are in a good agreement for HCO_3^- (Figure 34), Ca (Figure 35) and as long as oxic conditions prevail, for O_2 (Figure 36) and NO_3-N (Figure 39), only in partial agreement for pH (Figure 33), Mn (Figure 37) and Fe (Figure 38) reflecting charge balance assumption for pH, and specified mineral equilibria for Fe and Mn. NH_4-N was not found to be stable after PHREEQC processing (and therefore not verified) because inorganic Nitrogen was assumed to be in redox equilibrium. At oxic conditions NO_3^- is the only stable N-species, so that analysed NH_4^+ is added to the analysed NO_3^- concentration.

The discrepancies between calculated and measured pH values (Figure 33) may result from the fact that the pH calculation within PHREEQC is performed based on the charge balance (as performed during the reactive transport simulation using PHT3D, see Prommer 2002). In other cases (such as surface water analyses) the cursory assumption of calcite and other mineral equilibrium, which has applied to all processed analyses, may not be valid.

Due to the fact, that in most cases calcite saturation occurs, the measured Ca and HCO_3-concentrations are for most cases satisfactorily verified (Figure 34 and Figure 35). As long as

conditions are oxic, measured O_2 and NO_3-N concentrations could also be well verified. The calculated Fe and Mn concentrations reflect in general the applied mineral equilibria resulting in nearly constant values depending on the actual redox conditions. For anoxic conditions, Mn and Fe concentrations can be reproduced only at the same magnitude order as analysed, if rhodochrosite and/or siderite is stable during PHREEQC processing. Following this approach, Mn and Fe concentrations measured in oxic environment are not verified by PHREEQC processing, which assumes equilibration with Iron and Manganese oxides under these conditions and which results in calculated Fe and Mn concentrations near zero.

As expected the measured redox potentials (not shown) in most cases were not confirmed by the calculation except for analyses reflecting an anoxic iron reducing environment. Reasons may be a possible surface passivation of the electrode in oxic environments, or the fact that no redox equilibrium was reached (Lindberg & Runnels, 1984). For the reactive transport modelling, nevertheless an (equilibrated) pe value is required and had to be calculated in spite of the difficulties described above.

Reactive Transport: Conceptual chemical reaction framework

The conceptual chemical reaction framework set up for verification of the groundwater and surface water analyses (see section 2.2.2.1.) at the Tegel test site is applied and extended to the reactive transport modelling presented here.
As given by the PHT3D intrinsic systematics the following has to be specified: aqueous components controlled by chemical equilibrium or by kinetics, minerals and solids controlled by chemical equilibrium or by kinetics, and as a special case, the pH and the pe as immobile components resulting from charge balancing and from the operation valence electron balancing. All components considered by reactive transport modelling are given by

Table 4.

Table 4 Summary of components considered in the reactive transport modeling (indicated by a cross)

Component	Aqueous controlled by chemical equilibrium	Aqueous kinetically controlled	Immobile controlled by chemical equilibrium	Immobile kinetically controlled
pH			x	
pe			x	
C(4)	x			
C(-4)	x			
Ca	x			
Mg	x			
Na	x			
K	x			
Cl	x			
Fe(2)	x			
Fe(3)	x			
Mn(2)	x			
Mn(3)	x			
S(6)	x			
S(-2)	x			
N(3)	x			
N(5)	x			
N(0)	x			
N(-3)	x			
O(0)	x			
DOC		x		
Particulate OC				x
Calcite			x	
Pyrolusite			x	
Ferrihydrite			x	
FeS (ppt)			x	
Rhodochrosite			x	
Siderite			x	

All aqueous components controlled by chemical equilibrium or by kinetics are subjected to hydrodynamic transport. pH and pe are treated formally as immobile, but they are calculated using the chemical equilibria of all species, charge balance (derived from mobile species) and operational valence electron balances (using mobile and immobile species). DOC is

treated as a mobile component controlled by biogeochemical degradation kinetics (MONOD approach) using terminal electron acceptors here available as O_2, NO_3^-, Pyrolusite (MnO_2), Ferrihydrite ($Fe(OH)_{3(amorphous)}$) and SO_4^{2-}. Particulate OC (organic carbon) is considered as a kinetically controlled immobile component releasing DOC.
The minerals Calcite ($CaCO_3$), Pyrolusite (MnO_2), Ferrihydrite ($Fe(OH)_{3\ (amorphous)}$), FeS (ppt), Rhodochrosite ($MnCO_3$), and Siderite ($FeCO_3$) are immobile components subjected to chemical equilibrium.

The kinetics of DOC degradation are formulated using a MONOD approach. Here, with DOC, the reactive fraction of DOC (differing from refractory DOC fractions) is denoted. The overall DOC decay rate R_{DOC} is formulated as the sum of individual decay rates with a given terminal electron acceptor:

$$R_{DOC} = R_{O_2} + R_{NO_3^-} + R_{MnO_2} + R_{Fe(OH)_3} + R_{SO_4^{2-}} \tag{5}$$

$$R_{O_2} = \frac{\partial c_{DOC,O_2}}{\partial t} = -k_{O_2} \cdot c_{DOC} \cdot \frac{c_{O_2}}{k_{m,O_2} + c_{O_2}} \tag{6}$$

$$R_{NO_3^-} = \frac{\partial c_{DOC,NO_3^-}}{\partial t} = -k_{NO_3^-} \cdot c_{DOC} \cdot \frac{c_{NO_3^-}}{k_{m,NO_3^-} + c_{NO_3^-}} \cdot \frac{I_{O_2}}{I_{O_2} + c_{O_2}} \tag{7}$$

$$R_{MnO_2} = \frac{\partial c_{DOC,MnO_2}}{\partial t} = -k_{MnO_2} \cdot c_{DOC} \cdot \frac{c_{MnO_2}}{k_{m,MnO_2} + c_{MnO_2}} \cdot \frac{I_{O_2}}{I_{O_2} + c_{O_2}} \cdot \frac{I_{NO_3^-}}{I_{NO_3^-} + c_{NO_3^-}} \tag{8}$$

$$R_{Fe(OH)_3} = \frac{\partial c_{DOC,Fe(OH)_3}}{\partial t} = -k_{Fe(OH)_3} \cdot c_{DOC} \cdot \frac{c_{Fe(OH)_3}}{k_{m,Fe(OH)_3} + c_{Fe(OH)_3}} \cdot \frac{I_{O_2}}{I_{O_2} + c_{O_2}} \cdot \frac{I_{NO_3^-}}{I_{NO_3^-} + c_{NO_3^-}} \cdot \frac{I_{MnO_2}}{I_{MnO_2} + c_{MnO_2}} \tag{9}$$

$$R_{SO_4^{2-}} = \frac{\partial c_{DOC,SO_4^{2-}}}{\partial t} = -k_{SO_4^{2-}} \cdot c_{DOC} \cdot \frac{c_{SO_4^{2-}}}{k_{m,SO_4^{2-}} + c_{SO_4^{2-}}} \cdot \frac{I_{O_2}}{I_{O_2} + c_{O_2}} \cdot \frac{I_{NO_3^-}}{I_{NO_3^-} + c_{NO_3^-}} \cdot \frac{I_{MnO_2}}{I_{MnO_2} + c_{MnO_2}} \cdot \cdot \frac{I_{Fe(OH)_3}}{I_{Fe(OH)_3} + c_{Fe(OH)_3}} \tag{10}$$

with k_i as rate constants, $K_{m,i}$ as MONOD constants, and I_i as inhibitor constants for the terminal electron acceptor i.

The solution kinetics of particulate OC is formulated as

$$R_{OC} = \frac{\partial c_{OC}}{\partial t} = -k_{sol} \cdot c_{OC} \cdot (c_{DOC,sat} - c_{DOC}) \tag{11}$$

using k_{sol} as solubility rate constant, $c_{DOC,sat}$ as OC solubility, and the DOC concentration. Depending on the relation of the DOC concentration to the particulate OC solubility, particulate OC dissolution or precipitation is possible. This term was introduced because

along the Tegel test site DOC concentrations were found independent from the terminal electron acceptor consumption.
Basics about coupling of biogeochemical reactions to inorganic hydrogeochemistry are available from Brun & Engesgaard (2002) and Barry et al. (2002).

To perform reactive transport simulations using PHT3D, initial and boundary concentrations must be assigned to each modeled component. From the evaluation of the NASRI chemical database (NASRI Database, 2004), an oxic redox environment for the shallow sample points, and an anoxic redox environment for the deeper sample points can be deduced. As typical analyses for the oxic redox environment a dataset from well 3305 and for the anoxic redox environment a dataset from well 3304 (NASRI Database 2004) were chosen and assigned to the model. As representative analysis for the surface water hydrochemistry related to the river package, a surface water analysis dataset from the NASRI Database (2004) was chosen and assigned as boundary concentrations.

The effective chemical composition of the groundwater recharge was deduced from precipitation water analyses as outlined by Merkel & Planer-Friedrich (2002). Conceptually, the initial precipitation water chemistry is concentrated by subtracting the evaporation and the surface run-off from the precipitation.

The initial and boundary hydrochemistry assigned to the reactive transport model is available from

Table 5.

The parameter set ‘oxic milieu’ (

Table 5) was assigned to the entire 1st model layer and to the 2nd model layer except for the lake. The remaining model part was specified with the parameter set ‘anoxic milieu’ (

Table 5). The specified head boundaries (left and right model boundaries) were specified in the same way as the initial conditions of the neighbouring blocks (the left boundary as oxic only in the 1rst model layer, the right boundary as oxic in model layer 1 and 2 from the top).

Table 5: initial and boundary hydrochemistry assigned to the reactive model (units mol l^{-1} for dissolved components except pH and pe, and mol l(bulk)$^{-1}$ for solids)

Component	Oxic milieu	Anoxic milieu	Surface water	Groundwater Recharge
DOC	$1*10^{-7}$	$1*10^{-4}$	$5*10^{-4}$	$1*10^{-20}$
C(4)	$5.668*10^{-3}$	$3.296*10^{-3}$	$1.082*10^{-5}$	$1.082*10^{-5}$
C(-4)	$1*10^{-20}$	$1*10^{-20}$	$1*10^{-20}$	$1*10^{-20}$
Ca	$4.174*10^{-3}$	$2.938*10^{-3}$	$2.122*10^{-3}$	$2.233*10^{-5}$
Cl	$1.242*10^{-3}$	$1.609*10^{-3}$	$1.863*10^{-3}$	$8.295*10^{-5}$
Fe(2)	$3.02*10^{-17}$	$1.320*10^{-5}$	$1*10^{-20}$	$1*10^{-20}$
Fe(3)	$4.437*10^{-8}$	$3.311*10^{-8}$	$1*10^{-20}$	$1*10^{-20}$
Mg	$7.741*10^{-4}$	$3.169*10^{-4}$	$4.527*10^{-4}$	$2.233*10^{-5}$
Mn(2)	$9.99*10^{-15}$	$7.882*10^{-6}$	$1*10^{-20}$	$1*10^{-20}$
Mn(3)	$1*10^{-20}$	$1*10^{-20}$	$1*10^{-20}$	$1*10^{-20}$
N(3)	$1.79*10^{-17}$	$1*10^{-20}$	$1*10^{-20}$	$1*10^{-20}$
N(5)	$1.258*10^{-4}$	$1*10^{-20}$	$1.357*10^{-4}$	$1.934*10^{-4}$
N(0)	$1*10^{-20}$	$1.572*10^{-5}$	$1*10^{-20}$	$1*10^{-20}$
N(-3)	$1*10^{-20}$	$1*10^{-20}$	$1*10^{-20}$	$1*10^{-20}$
Na	$1.302*10^{-3}$	$1.428*10^{-3}$	$2.333*10^{-3}$	$6.189*10^{-5}$
K	$5.146*10^{-5}$	$4.018*10^{-5}$	$3.327*10^{-4}$	$6.366*10^{-5}$
O(0)	$1.134*10^{-3}$	$1*10^{-20}$	$1.376*10^{-3}$	$5.012*10^{-4}$
S(-2)	$1*10^{-20}$	$1*10^{-20}$	$1*10^{-20}$	$1*10^{-20}$
S(6)	$2.636*10^{-3}$	$1.729*10^{-3}$	$1.437*10^{-3}$	$5.462*10^{-5}$
pH	6.918	7.212	8.549	4.056
pe	13.791	1.458	5.715	16.566
Calcite	$1.478*10^{-2}$	$1.479*10^{-2}$	0	0
Ferrihydrite	$2.83*10^{-2}$	$2.83*10^{-2}$	0	0
Pyrolusite	$9.5*10^{-4}$	0	0	0
Rhodochrosite	0	$9.5*10^{-4}$	0	0
Siderite	0	$8.32*10^{-6}$	0	0
FeS (ppt)	0	0	0	0
Particular OC	$1*10^{-5}$	$2*10^{-2}$	0	0

The applied kinetic parameters are summarised in

Table 6 for Monod parameters and in Table 7 for the dissolution of particulate OC.

Table 6 Assigned Monod kinetics parameters

Parameter	Dimension	Value
k_{O2}	d^{-1}	$1*10^{-7}$
k_{NO3}	d^{-1}	$1*10^{-8}$
k_{MnO2}	d^{-1}	$1*10^{-8}$
$k_{Fe(OH)3}$	d^{-1}	$5*10^{-10}$
k_{SO4}	d^{-1}	$1*10^{-9}$
$K_{m,O2}$	mol l^{-1}	$1*10^{-4}$
$K_{m,NO3}$	mol l^{-1}	$1*10^{-5}$
$K_{m,MnO2}$	mol l^{-1}	$1*10^{-5}$
$K_{m,Fe(OH)3}$	mol l^{-1}	$1*10^{-4}$
$K_{m,SO4}$	mol l^{-1}	$1*10^{-4}$
I_{O2}	mol l^{-1}	$1*10^{-5}$
I_{NO3}	mol l^{-1}	$1*10^{-5}$
I_{MnO2}	mol l^{-1}	$1*10^{-5}$
$I_{Fe(OH)3}$	mol l^{-1}	$1*10^{-5}$

Table 7 Assigned particulate OC dissolution parameters

Parameter	Dimension	Value
k_{sol}	d^{-1}	$5*10^{-4}$
$C_{DOC,sat}$	mol l^{-1}	$1*10^{-8}$

All values depicted in

Table 6 and Table 7 are first approaches. The MONOD decay constants are specified as not exceeding the minimum value given by Hunter et al. (1998) for the decay of DOC ($3*10^{-5}$ $year^{-1}$). A first indication for the order of magnitude for the solubility of particulate OC ($C_{DOC,sol}$) is given by the sampled DOC values along the Tegel test site (4-7 mg DOC l^{-1}).

Model runs showed that beside the local availability of particulate OC, the ratio between MONOD decay constants of DOC and the dissolution constant of particulate OC is mainly decisive for the spatial distribution of redox zoning. The supply of DOC is controlled by the solution rate constant for particulate OC (k_{sol}) and the local concentration of particulate OC in the aquifer matrix. The hydrochemical feature along the Tegel transect test site as deduced from the results of the sampling campaign (NASRI DATABASE (2004), especially the spatial distribution of the redox zones) is verified on principle by the conceptual reactive transport model. From the simulation results the great impact of the local flow field and of the geologic pattern, such as variations in the leakance of the river bed or the local aquitard distribution, on the local hydrochemical groundwater composition is illustrated. Further, simulation results will be strongly influenced by the interplay of hydrodynamic transport, biodegradation kinetics, the extent of supply of reactive DOC by dissolution of particulate OC, and the spatial distribution of particulate OC within the aquifer system. As in most cases, compared to groundwater analyses informations about the aquifer matrix composition are scarce. In the NASRI project, only one drilling core was analysed (NASRI 2003). From all theses perceptions it follows that only a general verification of hydrochemistry has to be aimed in the light of the uncertainties discussed above.

Results of reactive transport model simulation

The reactive transport simulation was performed using a time step of 1 day over a total simulation time of 1095 days. The reactive transport simulation results are demonstrated as vertical cross sections showing the initial and final component concentration distributions by Figure 40- Figure 53. The range of calculated concentrations are shown using the colour bars positioned on the right side of the plots

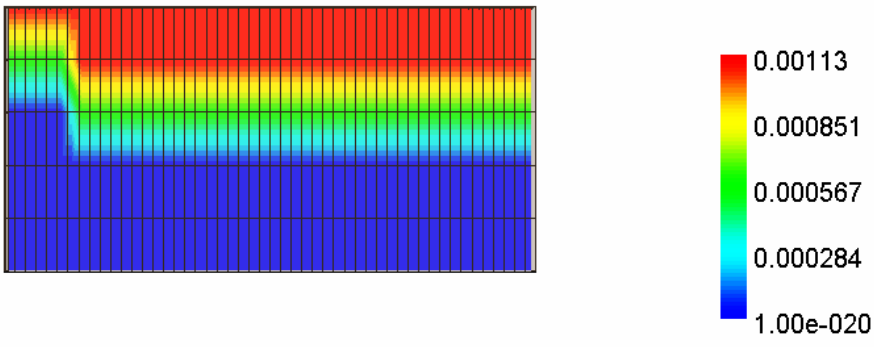

Figure 40 Initial O(0) concentrations (mol l^{-1})

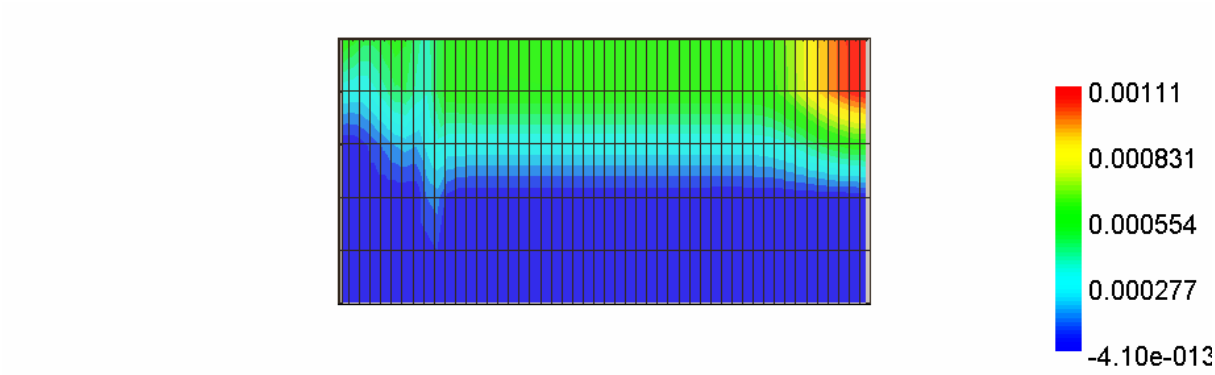

Figure 41 Calculated O(0) concentrations (mol l^{-1}) at the end of the simulation (after 1095 d)

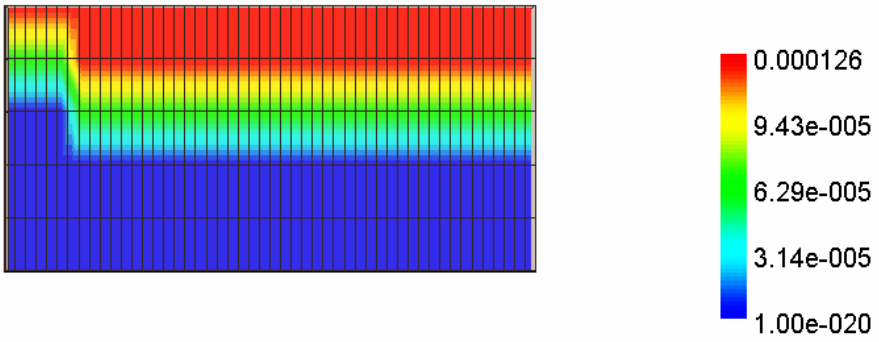

Figure 42: Initial NO_3-N concentrations (mol l^{-1})

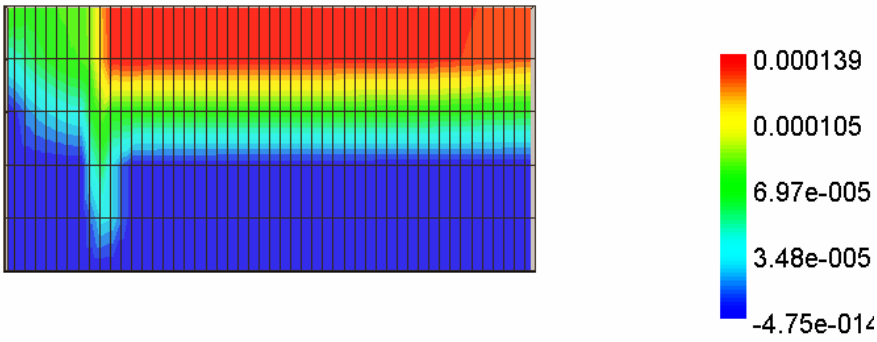

Figure 43 Calculated NO_3-N concentrations (mol l^{-1}) at the end of the simulation (after 1095 d)

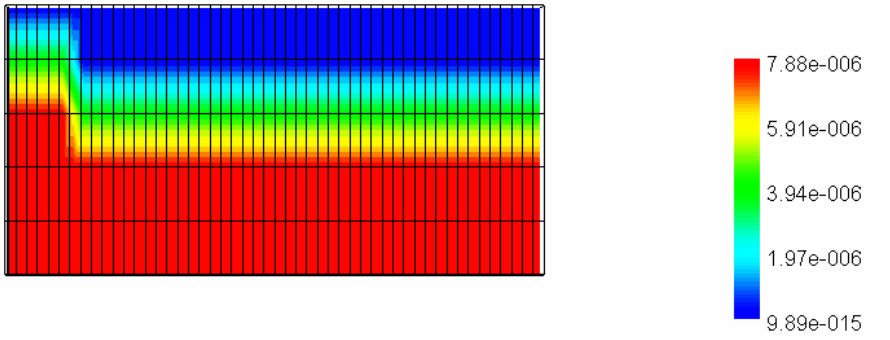

Figure 44 Initial Mn concentrations (mol l^{-1})

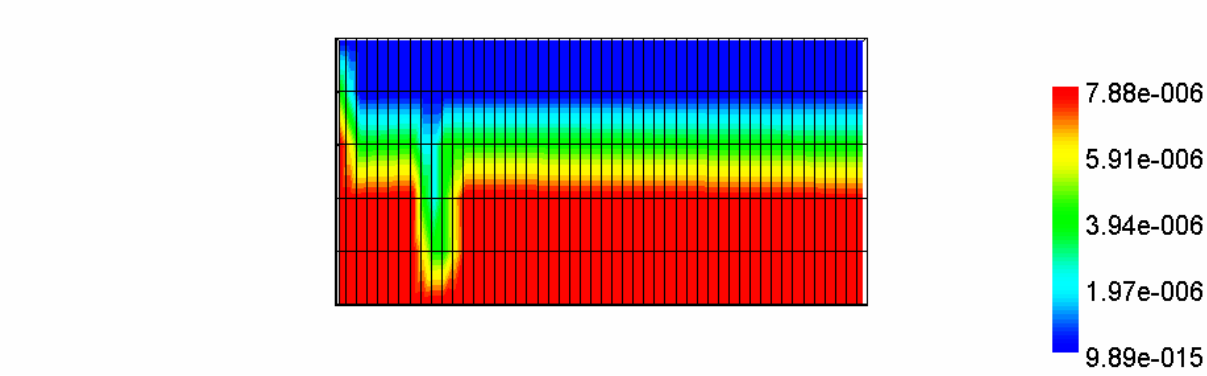

Figure 45 Calculated Mn concentrations (mol l^{-1}) at the end of the simulation (after 1095 d)

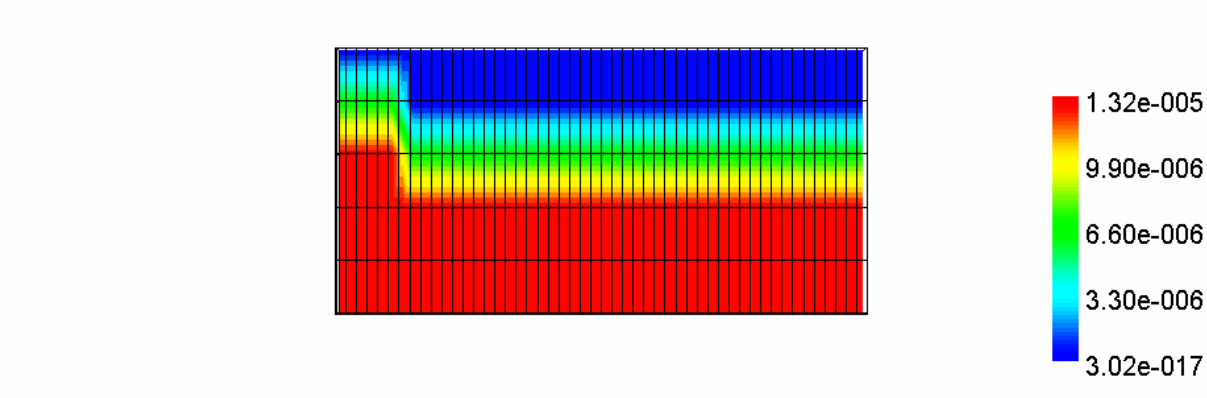

Figure 46 Initial Fe concentrations (mol l^{-1})

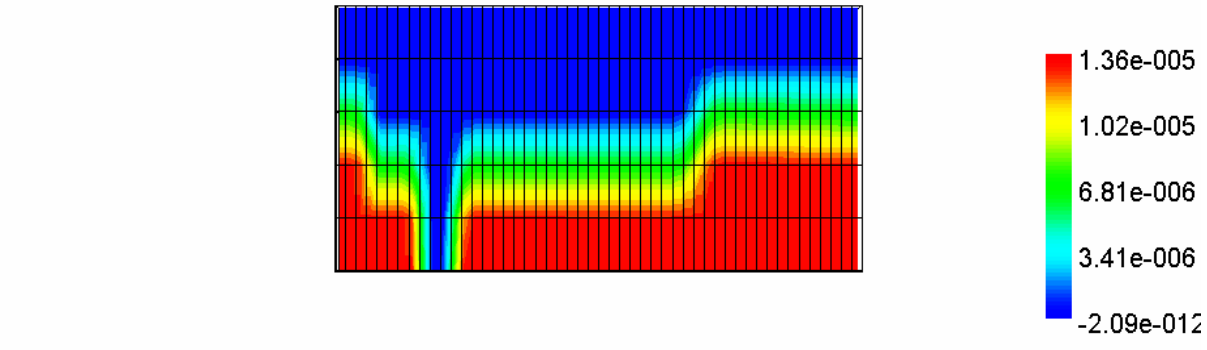

Figure 47 Calculated Fe concentrations (mol l^{-1}) at the end of the simulation (after 1095 d)

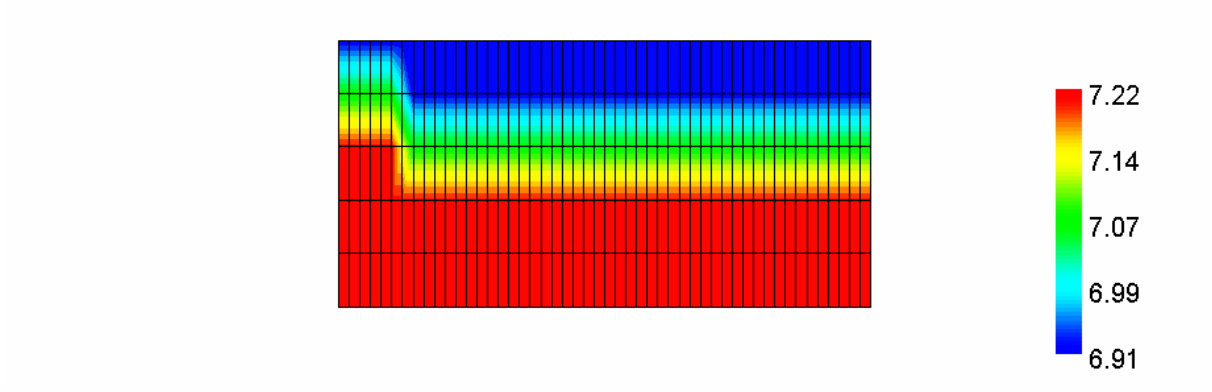

Figure 48 Initial pH values

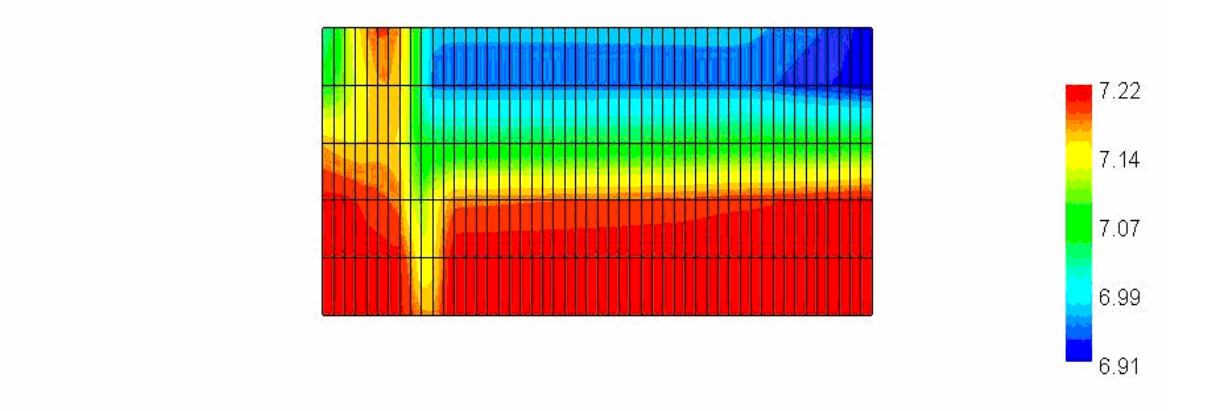

Figure 49 Calculated pH values at the end of the simulation (after 1095 d)

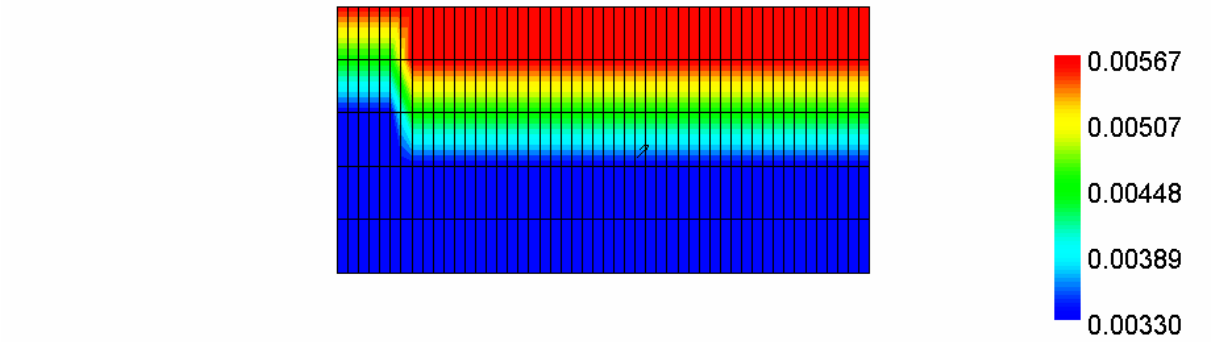

Figure 50 Initial HCO_3^- concentrations (mol l^{-1})

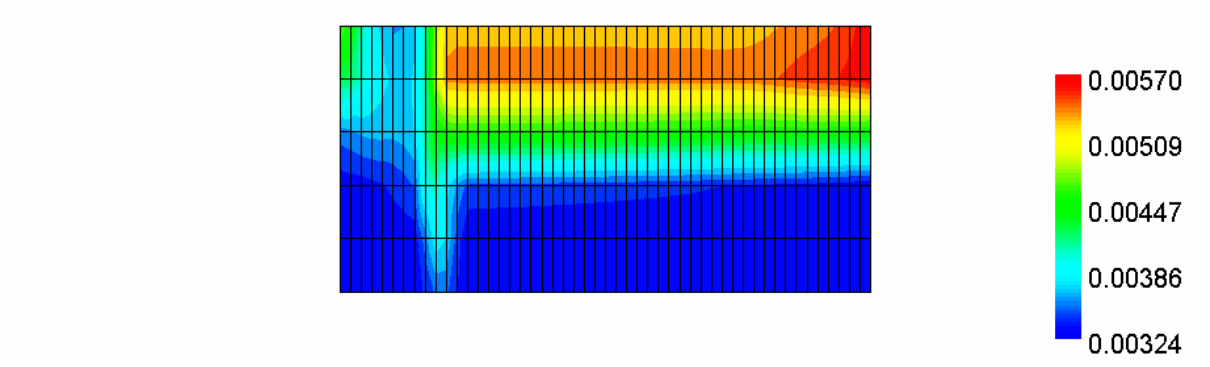

Figure 51 Calculated HCO_3^- concentrations (mol l^{-1}) at the end of the simulation (after 1095 d)

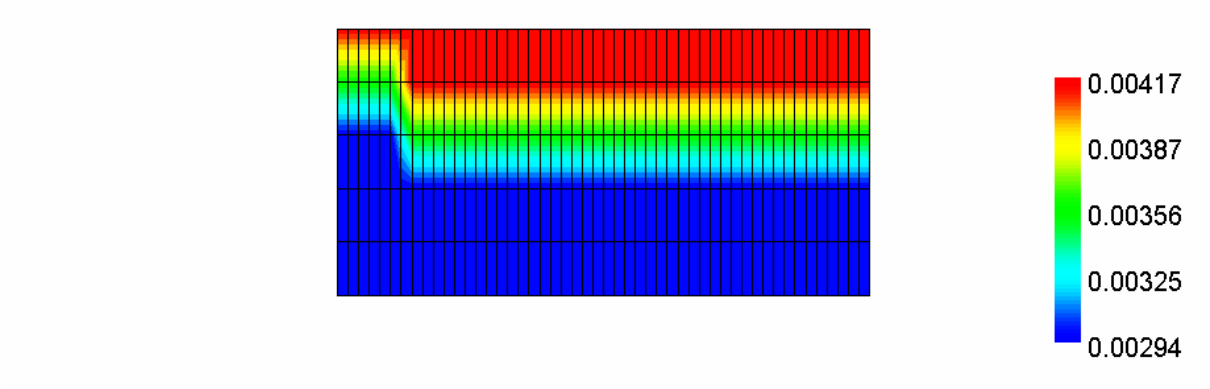

Figure 52: Initial Ca concentrations (mol l^{-1})

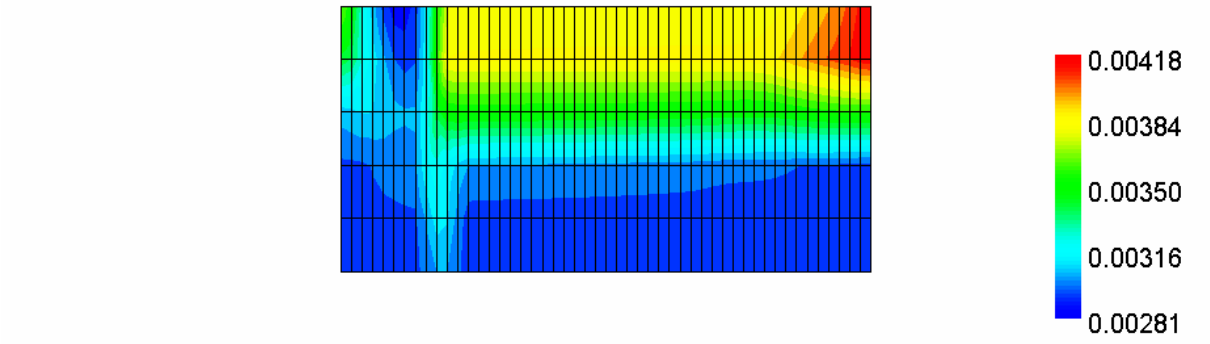

Figure 53 Calculated Ca concentrations (mol l^{-1}) at the end of the simulation (after 1095 d)

The hydrochemical feature along the Tegel transect test site as deduced from the results of the sampling campaign (NASRI DATABASE (2004), especially the spatial distribution of the redox zones) is verified on principle by the conceptual reactive transport model. From the simulation results the great impact of the local flow field and of the geologic pattern, such as variations in the leakance of the river bed or the local aquitard distribution, on the local

hydrochemical groundwater composition is illustrated. Further, simulation results will be strongly influenced by the interplay of hydrodynamic transport, biodegradation kinetics, the extent of supply of reactive DOC by dissolution of particulate OC, and the spatial distribution of particulate OC within the aquifer system. As in most cases, compared to groundwater analyses information about the aquifer matrix composition is scarce. In the NASRI project, only one drilling core was analysed (NASRI 2003). From all theses perceptions it follows that only a general verification of hydrochemistry has to be aimed in the light of the uncertainties discussed above.

2.1.4. Major Conclusions and Summary

Hydraulic modelling revealed that the leakance factor of the bank is time variant. The reason for this behaviour could not been identified, however it seems to increase with increasing pumping rates of the well field West. This effect stabilizes bank filtration and should be considered for further studies.

Leakance factors show a high spatial variance, factor 4 within a distance of 1.4 m is measured. Merging this with increased leakance by increased pumping rates, infiltration occurs as fingering, with the regions of high infiltration rather stabilizing than being clogged by increased suspended matter in the infiltration water.

The maximum leakance factor calculated from measured infiltration rates takes place in a water depth of about 1.4 m (Section 3.1.3). Simulations however suggest in 4-6 m depth the the leakance factor has its maximum. As local heterogeneity is high, the model results seem to be more reliable.

Water at the transect is demonstrated to be stratified in three fractions of bank filtrate. The existence of the medium aged fraction is detected by the hydraulic model. As the medium aged fraction is more similar to the young than to the old fraction it was considered to be part of the young fraction, thus travel times for the sum of bankfiltrate at well 13 would been underestimated. This may be an explanation why many substances show up in the observation wells just below the glacial till but are not detectable in the abstraction well 13.

A point of vulnerability

It was demonstrated, that using a generic hydrogeological model approximated to results of hyrogeological investigations (NASRI, 2003) the redox zoning observed along the Lake Tegel riverbank filtration test site can be verified by reactive modelling. The applied reactive transport modelling software PHT3D (Prommer, 2002) has been proven as a suitable modelling tool, which can also deal complicated hydrochemical conditions.

As a first attempt, the reactive model is based on a simplified pattern of hydrogeological pattern considering the observed hydrogeological situation and a highly transient idealised pumping regime of the well field as performed in principle by the well field pumping management. The reactive transport model set up on the generic flow model is based on schematized concentration parameters such as surface water chemistry, oxic groundwater chemistry within the shallow groundwater and anoxic groundwater chemistry for the deeper groundwater, but the applied conceptual reactive network was shown to be adequate to verify by principle the observed redox zonation along the Lake Tegel test side described by (NASRI, 2003). Both infiltration from Lake Tegel and groundwater flow from Land side were recognized to be important factors of redox zoning formation. As a main factor influencing the reactive transport modelling results the interaction of DOC biodegradation kinetics and supply of DOC by dissolution of particulate organic carbon was recognized. Furthermore, it results that a correct flow modelling also in detail is a precondition to verify the observed redox zoning. Other factors, such as seasonal temperature oscillations affecting the shape of redox zoning (see contribution of J. Greskowiak on the artificial recharge pond) were not considered. In assessing the results of reactive modelling, the scarce data basis about the mineralogical aquifer composition has to be taken into account.

2.1.5. References

Appelo, C. A. J., & Postma, d. (1996): Geochemistry, Groundwater and Pollution. Balkema, Rotterdam.

Barry, D. A., Prommer, H., Miller, C. T., Engesgaard, P., Brun, A., & Zheng, c. (2002): Modelling the fate of Oxidable Organic Contaminants in Groundwater. Adv. Water Resour., 25., 945-983.

Beulker, C., Gunkel, G., Hoffmann, A., Kosmol, J., (2005) Fluorrescence Markers of POM transport and Biogenic Metabolism in litoral sediments, Limnology and Oceanography Methods, submitted Dec. 2005

Bouwer, H. (2002). Artificial Recharge of Groundwater: Hydrogeology and Engineering. Hydrogeology Journal, 10(1), 121-142.

Bouwer, H; Rice, R. C.; (1989) Effect of Water Depth in Groundwater Reacharge Basins on Infiltration, Journal of Irrigation and Drainage Engineering, Vol. 115, No. 4, p. 556-567

Brühl, H.; Sommer-von Jarmersted, C; (1986) Ergebnisbericht: Baugrunduntersuchung auf der Kabeltrasse im Tegeler See (Wasserwerk Tegel – Trafostation Tegelort); Institut für Angewandte Geologie der Freien Universität Berlin, unpublished work

Brun, a., Engesgaard, p. (2002): Modelling Transport And Biogeochemical Processes In Pollution Plumes: Literature Review and Model Development. J. Hydrol., 256., 211-227.

Chiang, W.-H., (2003) Processing Modflow Pro,V 7.0, Users guide,

Diersch, H. J.-D., (2002), Grundwassersimulationssystem FEFLOW. User-/Reference-Manual. WASY GmbH Berlin, 2002

Doherty, John, (2004) PEST – Model independent Parameter estimation, User Manual 5th Edition, Watermark Numerical Computing

Eichhorn, S.; (2000); Numerische Strömungsmodellierung der Uferfiltration am Tegeler See, Diplomarbeit; Institut für Geologie, Geophysik und Geoinformatik FU Berlin

Fritz, B. (2002) Untersuchungen zur Uferfiltration unter verschiedenen wasserwirtschaftlichen, hydrogeologischen und hydraulischen Bedingungen, Dissertation, Fachbereich für Geowissenschaften, FU Berlin.

FUGRO (2000) Hydrogeologischen Stukturmodell für das Wasserwerk, FUGRO GmbH, im Auftrag BWB, Juni 2000, unpublished work

Greskwiak, J., Prommer, H., Massmann, G., Johnston, C. D., Nützmann, G., Pekdeger, A. (2005); The impact of variably saturated conditions on hydrogeochemical changes during artificial recharge of groundwater, Applied Geochemistry vol. 20, 1409-1426

Harbaugh, AW (1990), A computer program for calculating subregional water budgets using results from the U.S. Geological Survey modular three-dimensional ground-water flow model: U.S. Geological Survey Open-File Report 90-392, 46 p.

Harbaugh AW, Banta ER, Hill MC and McDonald MG (2000), MODFLOW-2000, The U.S. eological Survey modular ground-water model User guide to Modularization concepts and the ground-water flow process, U. S. Geological Survey, Open-file Report 00-92.Hunter, k. S., Wang, y. & van Cappellen, p.(1998): Kinetic modelling of Microbially-Driven Redox Chemistry of Subsurface Environments: Coupling Transport, Microbial Metabolism and Geochemistry. J. Hydrol. 209, 53-80.

Kipp, K. L. (1997): Guide to the revised heat and solute transport SIMULATAOT: HST3D, version 2. U.S. Geological Survey, Water Resources Investigation Report 97-4157, Denver, Co., U.S.A.

Lin, Chunye; Greenwald, Dan; Banin, Amos (2003) Temperature Dependence of Infiltration Rate During Large Scale Water Recharge into Soils, Soil Sci. Soc. Am. J. 67 p. 487–493

lindberg, r. b. & runnels, d. d. (1984): Ground water redox reactions: An analysis of equilibrium state applied to Eh measurements and geochemical modeling. Science 225, 925-927.

McDonald MG and Harbaugh AW (1988), MODFLOW, A modular threedimensional finite difference ground-water flow model, U. S. Geological Survey, Open-file Report 83-875, Chapter A1

Merkel, B. J. & Planer-Friedrich, B. (2002): Grundwasserchemie, praxisorientierter Leitfaden zur numerischen Modellierung von Beschaffenheit, Kontamination und Sanierung aquatischer Systeme. Springer, Berlin, Heidelberg.

NASRI (2003): Natural and Artificial Systems for Recharge and Infiltration, 1st Report. Kompetenzzentrum Wasser, Berlin.

NASRI database (2004): Natural and Artificial Systems for Recharge and Infiltration, Chemical Analyses Database (Time interval 2002-2004). Kompetenzzentrum Wasser, Berlin. unpublished work

Pachur, Hans-Joachim and Haberland, Wolfram (1977). Untersuchungen zur Morphologischen Entwicklung des Tegeler Sees (Berlin). Die Erde 108[4], 320-341

parkhurst, d. l., thorstenson, d. c., & plummer, l. n. (1980): PHREEQE – a computer program for geochemical calculations. U.S. Geological Survey Water-Resources Investigation Report 80-96, Denver, Co., U. S. A., pp 195.

Parkhurst, D. L., & Appelo, C. A. J. (1999): User's Guide to PHREEQC (Version 2) – a computer program for speciation, batch-reaction, one-dimensional transport, and inverse geochemical calculations. U.S. Geological Survey Water-Resources Investigation Report 99-4259, Denver, Co., U. S. A., pp 312.

Parkhurst, D. L., Kipp, K. L., Engesgaard, P. & Charlton, S.R. (2004): PHAST – a computer program for simulating groundwater-flow, solute transport, and multicomponent geochemical reactions. U.S. Geological Survey Techniques and Methods 6–A8, 154 p.

Prommer, H. (2002): A reactive multicomponent transport model for saturated porous media. Draft of user's manual version 1.0, contaminated land assessment and remediation research centre, the university of Edinburgh (available from http://www.pht3d.org)

Ripl, W., Heller, S., and Linnenweber, C. (1987) Limnologische Untersuchungen an den Sedimenten des Tegeler Sees. Eigenverlag Fachgebiet Limnologie, Technische Universität Berlin.

Rümmler, J. (2003) 2-Dimensional-horizontal-ebene Simulation der Grundwasserströmungsverhältnisse unter Uferfiltrationsbedingungen, Diplomarbeit; Mathematisch-Naturwissenschaftliche Fakultät 2, Geographisches Institut, Humboldt-Universität zu Berlin

Sievers, J., (2001), Geochemische und hydraulische Untersuchungen an Mudde- und Sandkernen aus dem Tegeler See. unveröffentlichte Diplomarbeit, Institut für Geowissenschaften, FU Berlin.

Stuyfzand, P.,. Juhàsz-Holterman, M., de Lange, W. (2004), Riverbank filtration in the Netherlands: well fields, clogging and geochemical reactions, NATO Advanced Research Workshop: Clogging in Riverbank Filtration Bratislava, 7-10 Sept. 2004.

Terzaghi, Karl; Peck, Ralph B., (1948) Soil Mechanics in Engineering Practice, John Wiley & Sons, Inc., New York

Voigt, I., Eichberg, M., (2000) Hydrogeologische Übersichtsprofile Nr.1- Nr.10, erstellt von der Fugro im Auftrag der BWB, 2002.

WASY (2004) Hydrogeologisches Fachgutachten zur Auswirkung grundlegender Änderungen des Betriebs zur Grundwasseranreicherung Wasserwerk Tegel, Unpublished Work, WASY Gesellschaft für wasserwirtschaftliche Planung und Systemforschung mbH, Berlin. unpublished work

Wiese, B., Holzbecher, E., Rümmler, J, and Nützmann, G. (2004) Effects of Oscillating Pumping Regimes of Bank-Filtration Galleries. Proc. International Conference on Finite-Element Models, FEM-MODFLOW, Modflow and more 2004, Carlovy Vary, Czech Republic, 411-414.

Zheng, C., & Wang, P. P. (1998): MTD3MS, A modular three-dimensional transport model. Technical Report, US Army Corps of Engineers Watewrways Experiment Station, Vicksburg, Miss., U.S.A.

2.2. Investigations at the Lake Tegel Artificial Recharge Site

2.2.1 Objectives

This part of the NASRI project focussed on the hydraulic and hydraulic processes and their interaction occurring during artifical recharge of groundwater at the field site GWA Tegel. The research conducted for this part of the NASRI project was aimed to meet the following objectives:

(1) Understanding the impact of transient saturated and unsaturated conditions directly below the artificial recharge pond at GWA Tegel on the dynamics of hydrogeochemical changes during infiltration, and verifying the findings by multicomponent reactive transport modelling

(2) Providing a process-based modelling framework to interpret the seasonal degradation behaviour of the pharmaceutical residue phenazone within the aquifer surrounding the artificial recharge pond at GWA Tegel

In order to meet these objectives, the research was carried out by three separate studies in close collaboration with the NASRI group Hydrogeology. For clarity, the studies are described by three chapters, each of them containing a methods and results (and discussion) section. The final chapter summarizes the conclusions of all three studies and gives prospects for future research.

2.2.2 Hydraulic and hydrogeochemical changes below the pond

2.2.2.1 Materials and Methods

From July 2003 until December 2003, sampling of (i) the pond water, (ii) groundwater from an observation well (screened at 6-8 m below the pond), and (iii) water extracted from four ceramic suctions cups at 50 cm, 100 cm, 150 cm and 200 cm below the artificial recharge pond was carried out on a weekly base. Water content and pressure heads were continuously recorded at two different depths, i.e., 50 cm and 150 cm below the pond. The locations of all these probes are shown schematically in Figure 54. Alkalinity and pH were measured in the field immediately after sampling. Alkalinity was determined by Gran Titration. All samples were analyzed for major ions and dissolved organic carbon (DOC) using standard methods. Data from samples with a charge balance error of more than 5 % were discarded. Dissolved oxygen (DO) concentrations were measured by optical sensor-type oxygen probes (Hecht and Kölling 2001) placed next to the suction cups. All of the

installations, including the groundwater monitoring well, are positioned approximately 4 m from the edge of the pond.

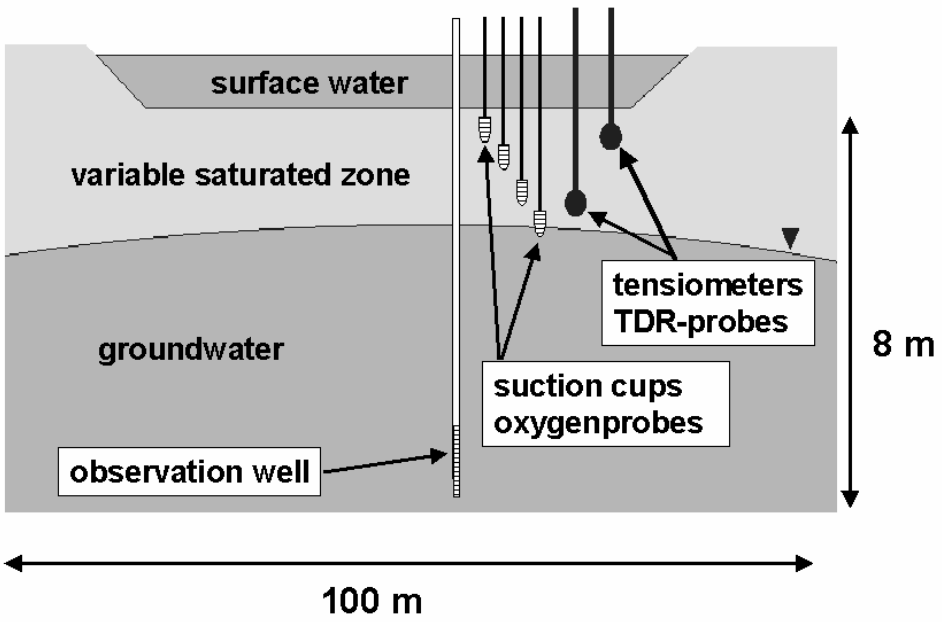

Figure 54 Schematic cross-section of study area and locations of sample collection and measurement devices.

2.2.2.2 Results and discussion

Hydraulic conditions

Measured time-series of water contents (Figure 57) and pressure heads (data not shown) below the pond indicated that the transient hydraulic conditions of each operational cycle could be classified hydraulically into four different major stages. Stage 1 marked the transition from unsaturated to saturated conditions beneath the pond (Figure 57), which occurred soon after the removal of the clogging layer once infiltration was restarted. The saturated conditions prevailed for approximately 50 days (Stage 2) until the of the groundwater table dropped abruptly within a few days. The decline of the water table forced air from the pond margins to the centre beneath the recharge pond and water contents fell from about 40-45 % to 30-35 % (Figure 57). The unsaturated conditions prevailed for 40 days (Stage 3). During the last period of the operational cycle (Stage 4) the pond was empty and the redevelopment of the pond took place. Hence, no recharge occurred. A schematic diagram of the relevant hydraulic stages is given in Figure 56.

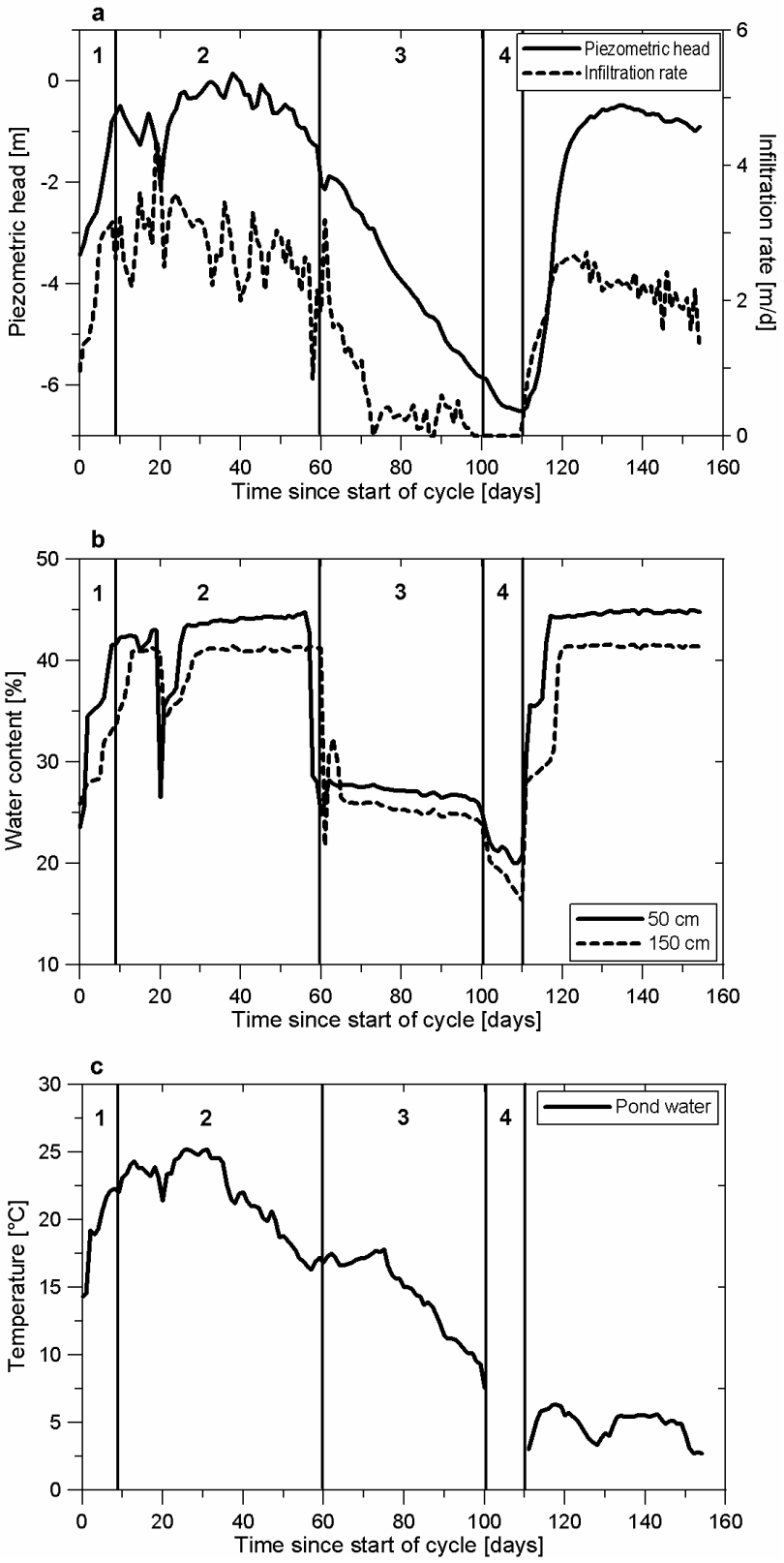

Figure 55: Piezometric head at a depth of 8 m below the pond and infiltration rate. The data for the infiltration rate has been provided by the BWB; b. Water contents at depths of 50 cm and 150 cm below the pond; c. Temperature of the pond water. The numbers 1-4 refer to the Stages 1-4 of the operational cycle. Note that the pond was dry during Stage 4.

Dynamics and Distribution of redox environments

During Stage 1, oxygen concentrations declined from about 5 mg/l to zero at all observed depths (Figure 57), i.e., oxygen was consumed within the first 50 cm below the pond. During the entire Stage 2, DO concentrations remained zero at all observed depths. About 20 to 30 days after the beginning of Stage 2, nitrate concentrations at various depths started to drop below the concentrations found in the surface water (Figure 58). At 50 cm and 100 cm depth nitrate was totally depleted within a few days, whereas the concentrations in the groundwater decreased more slowly (Figure 58). In contrast, at 150 cm and 200 cm depth, nitrate was not fully consumed.

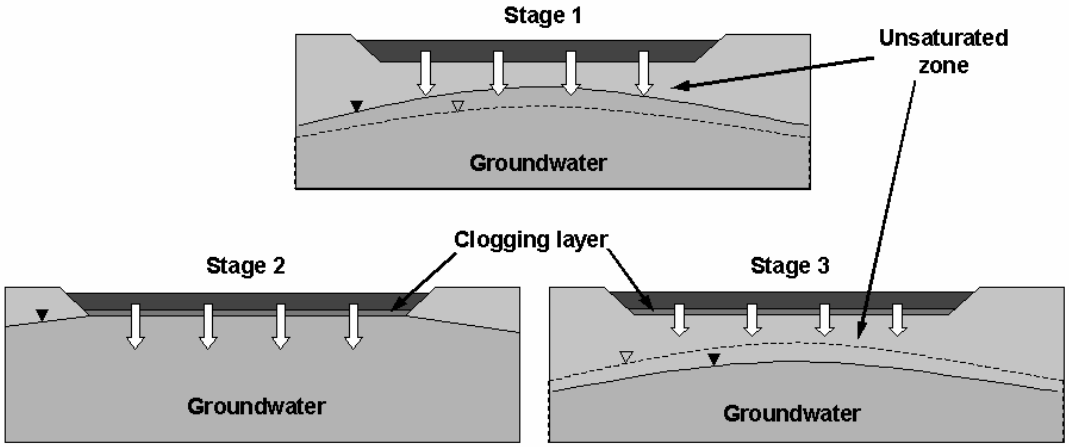

Figure 56 Schematic cross-sectional diagram of the pond for the Stages 1, 2 and 3.

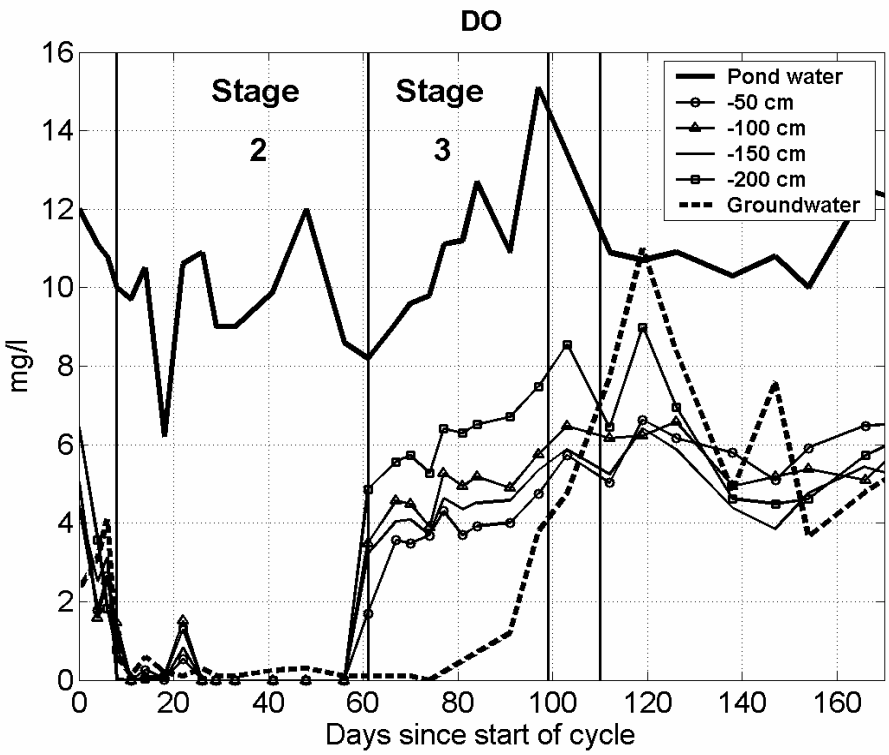

Figure 57 Oxygen concentrations in the pond and groundwater and at depths of 50 cm, 100 cm, 150 cm and 200 cm beneath the pond.

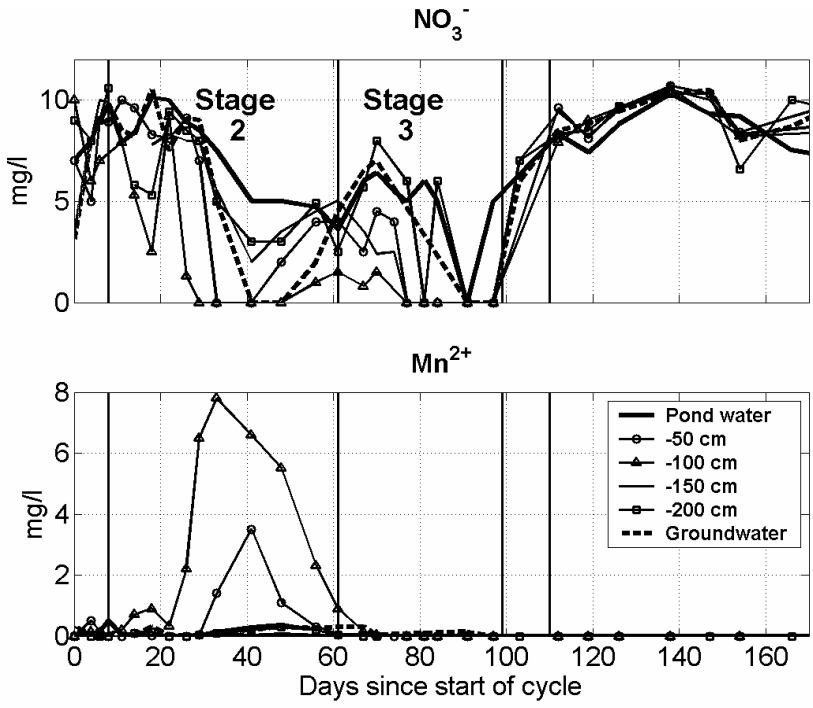

Figure 58 Nitrate (as NO_3^-) and manganese (Mn^{2+}) in the pond and groundwater and at depths of 50 cm, 100 cm, 150 cm and 200 cm beneath the pond.

At locations where nitrate was depleted, the redox-environment shifted to manganese reducing conditions, as indicated by an increase of manganese (Mn^{2+}) concentrations (up to

8 mg/l, see Figure 58). At a depth of 100 cm below the pond, where Mn^{2+} concentrations were highest, iron (Fe^{2+}) concentrations increased to 0.3 mg/l (Figure 59), indicating that iron reduction took place during Stage 2. The heightened Mn^{2+} concentrations at these depths lasted for approximately 10 days before they started to decline again. The decline was most likely the result of a decrease in water temperature (Figure 55), associated with a decrease of microbial activity and coincided with a simultaneous rise of nitrate concentrations beneath the pond (Figure 58). During Stage 1 and Stage 2, sulphate concentrations were generally around 140 mg/l and did not show any significant variations with depth (Figure 59). Although not directly observed, sulphate reduction is assumed to have occurred at non-detectable levels during Stage 2, as it is known to take place in parallel or even before iron reduction, dependent on the local geochemical setting (Postma and Jakobsen 1996).

During the rapid change from water saturated (Stage 2) to water unsaturated conditions (Stage 3), oxygen concentrations increased up to 5 mg/l (Figure 2.4). Although aerobic respiration seems to be the dominant redox reaction during Stage 3, nitrate concentrations at 3 suction cups were still somewhat lower than in the surface water (Figure 58). These patchily distributed zones of more reducing conditions (also observed in Stage 2) are considered to result from (i) the formation of anaerobic microsites caused by particulate organic carbon contained in the sediment and (ii) non-uniform flow caused by the physical heterogeneity of the sediment, i.e., hydraulic conductivity. Concomitant with the appearance of atmospheric oxygen (during the transition from Stage 2 to Stage 3) extremely high sulphate concentrations of up to 370 mg/l were observed in the water extracted from three suction cups. However, in the following 20 days they declined rapidly and returned to background concentrations (Figure 59). The observed peaks of sulphate concentrations are most likely caused by the rapid oxidation of iron sulphide minerals that had formed previously (during Stage 2) as a result of sulphate reduction. However, rapid oxidation of sulphide minerals due to water table fluctuations has been observed for other, comparable hydrogeochemical systems (e.g., Sinke et al. 1998). Concomitant with the peaks of sulphate concentration, very high concentrations of calcium were observed at the same locations below the pond (Figure 59). As sulphide oxidation produces protons, the heightened calcium concentrations apparently resulted from pH buffering by the dissolution of calcite.

During the next recharge cycle, i.e., approximately after day 100, DO concentrations did not decrease when the sediment below the pond became saturated again, as is was the case in the previous cycle. This is thought to result from lower microbial activity due to lower temperatures during winter. During the entire winter period, the redox status remained aerobic, independently from the hydraulic situation below the pond.

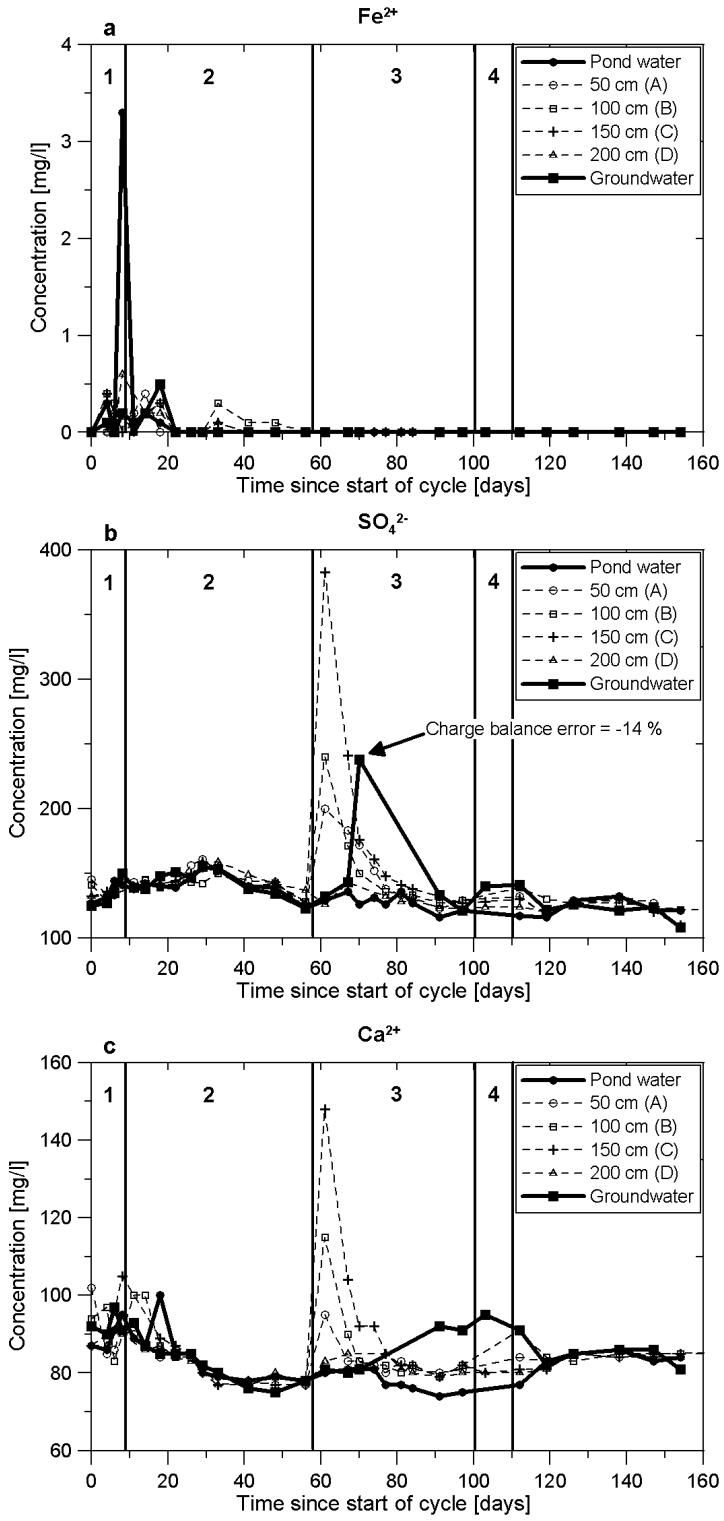

Figure 59 Concentrations of a. dissolved iron (Fe^{2+}), b. sulphate (SO_4^{2-}) and c. calcium (Ca^{2+}) in the pond water, groundwater (depth 8 m) and at depths of 50 cm, 100 cm, 150 cm, 200 cm below the pond. The numbers 1-4 refer to the Stages 1-4 of the operational cycle.

Carbon system

The effect of organic carbon degradation on the carbonate system below the pond was observed during the entire sampling period and can be seen most clearly when the hydrochemical compositions of the surface water and the groundwater are compared.

During Stage 2, dissolved oxygen and nitrate contained in the infiltration water are fully consumed due to organic carbon degradation as expressed by the reactions 2.1 and 2.2 (Table 2.1). For simplification purposes, organic carbon is represented by CH_2O. According to reaction 2.1, the full depletion of 10 mg/l dissolved oxygen (surface water concentration) accounts for a degradation of about 3.7 mg/l organic carbon. When the system moved to nitrate reducing conditions, the consumption of 10 mg/l dissolved oxygen plus 5 mg/l nitrate according to reactions 2.1 and 2.2 requires about 4.9 mg/l organic carbon. This is more than twice the amount of DOC assumed to be mineralised during transport to the monitoring well (Figure 60). From this, it is evident that there must have been an additional carbon source besides DOC causing the observed consumption of oxidation capacity. Since the total organic carbon (TOC) concentration generally does not exceed the DOC concentration in the surface water of the pond (unpublished data of BWB), the additional carbon source must have been POC within the sediments below the pond. The DIC concentrations of the groundwater were about 4 - 5 mg/l higher than in the surface water (Figure 60) and matched the mineralised organic carbon concentration of 3.7 - 4.9 mg/l that is calculated from the observed TEA consumption. This implies that calcite dissolution due to carbonic acid production (as a result of organic carbon degradation) did not significantly contribute to the DIC production during Stage 2.

Atmospheric oxygen had a profound impact on the organic carbon degradation during the entire Stage 3. The heightened concentrations of calcium and DIC in the groundwater compared to the surface water during Stage 3 (Figure 59and Figure 60) indicates that calcite dissolution took place as a result of aerobic organic carbon degradation described by reaction 2.3 (Table 8). At the end of Stage 3, the difference between the DIC concentrations (mainly as bicarbonate) of the groundwater and surface water (13 mg/l = 1.1 mmol/l, Figure 60) was twice as high as the difference between the calcium concentrations (20 mg/l = 0.5 mmol/l, Figure 59). This concentration ratio is as expected from reaction 2.3 and indicates that calcite dissolution was taking place and was caused by the degradation of organic carbon. As a result of calcite dissolution, the pH of the groundwater remained stable during this stage (Figure 60). During Stage 3, the DOC concentrations of the groundwater did not differ significantly from the surface water concentrations (Figure 60), suggesting that sedimentary POC was degraded in preference to DOC.

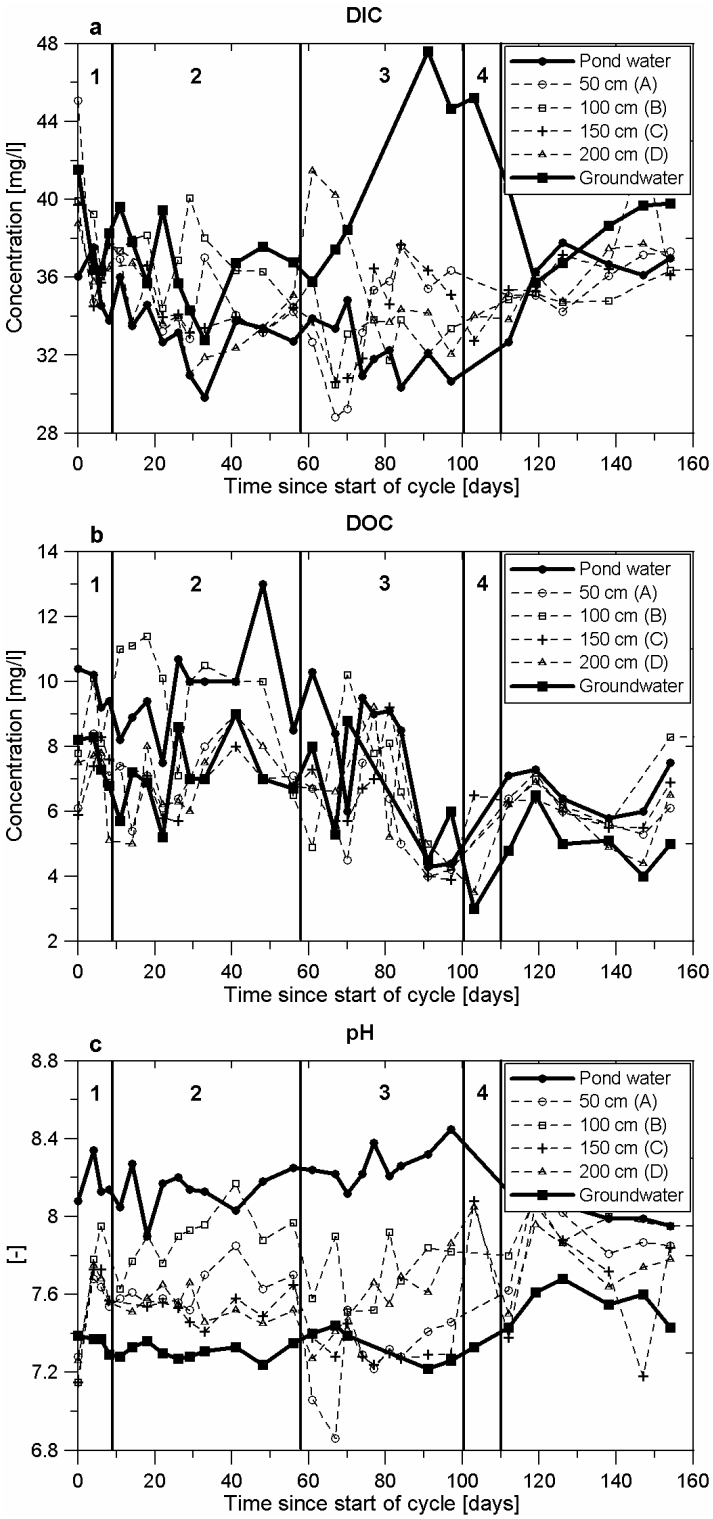

Figure 60 Concentrations of a. **dissolved inorganic carbon (DIC),** b. **dissolved organic carbon (DOC) and** c. **pH in the pond water, groundwater (depth 8 m) and at depths of 50 cm, 100 cm, 150 cm, 200 cm below the pond. The numbers 1-4 refer to the Stages 1-4 of the operational cycle.**

This is possible, as labile (highly degradable) POC is expected to be available for decomposition, which is assumed to originate from seasonal blooms of algae within the pond and transport into the first meters of the profile.

Table 8 Summery of the relevant geochemical reactions occurring below the pond.

$CH_2O + O_2 \rightarrow H^+ + HCO_3^-$	(2.1)
$5CH_2O + 4NO_3^- \rightarrow H^+ + 5HCO_3^- + 2N_2 + 2H_2O$	(2.2)
$CH_2O + CaCO_3 + O_2 \rightarrow Ca^{2+} + 2HCO_3^-$	(2.3)

2.2.3 Reactive transport modelling of the unsaturated zone

It was shown in the previous chapter, that during summer the lateral intrusion of air from the pond margin due to transient unsaturated hydraulic conditions seem to have a considerable impact on the hydrogeochemistry of the seepage water. During this study, a two-dimensional multi-component reactive transport model was developed in order to (i) verify this hypothesis and (ii) find out how far gaseous oxygen migrates from the margins towards the centre below the pond during the unsaturated conditions (Stage 3), since there were no observations available clarifying this. The model included advective and dispersive transport of the relevant major ions in the water phase and O_2 and CO_2 in the gas phase. Thereby, heterogeneous reactions were considered between immobile (e.g., minerals, sediment bound organic matter), water and gas phase. Kinetic reactions were only included when the local equilibrium assumption (LEA) appeared to be violated. All other reactions (e.g., aqueous speciation, dissolution/degassing of gaseous O_2 and CO_2) were assumed to occur instantaneously.

2.2.3.1 Conceptual gas transport model

The transient pore velocity field of air within the unsaturated zone below the pond was approximated as radial symmetric, assuming that the pond was a circle. When assuming (i) air to behave incompressible and (ii) a slip boundary for air flow at the groundwater table and at the lower end of the clogging layer, an analytical solution based on the so-called squeezing flow model (James, 2002; Lee and Ladd, 2002) can be used to simulate the pore velocity field $v_{a,r}$ of air in r-direction below the pond. The following relationships hold:

$$v_{a,r}(r,u) = -\frac{1}{2}\frac{v_V}{u}r + \frac{1}{2}\frac{v_V}{u}\frac{R^2}{r} - \frac{R}{r}v_H \quad \text{, for } R > 0 \text{ and } r \geq R \qquad (3.1)$$

$$v_{a,r}(r,u) = -\frac{1}{2}\frac{v_V}{u}r \quad \text{, for R=0} \tag{3.2}$$

The parameters are explained in Figure 61. Thereby, Eqn. 3.1 was developed in order to account for the lateral propagation of the air-front in the early stage of the unsaturated conditions (Figure 61). When the air-front reaches the centre of the pond, the horizontal pore velocity of air can be described by Eqn. 3.2, which is the original squeezing flow model (James, 2002; Lee and Ladd, 2002).

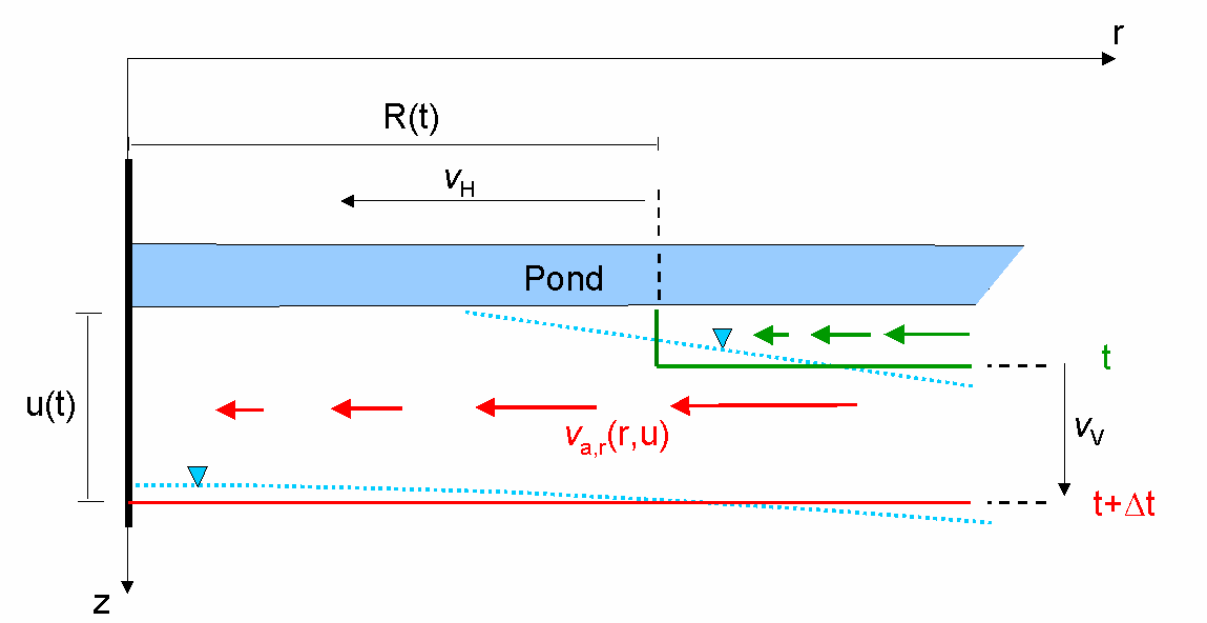

Figure 61 Conceptual radial symmetric model of the air flow in r-direction below the pond. The z-axis represents the symmetry axis at the center of the pond. The blue dotted lines are the groundwater tables at time t and t+Δt, respectively. The red line and green are the corresponding conceptual groundwater tables. Thereby, u is the distance from the pond's bottom to the conceptual groundwater table, v_v is the falling velocity of the groundwater table during the unsaturated stage, v_H is the propagation velocity and R the position of the air-front in the early stage of the unsaturated conditions.

The pore velocity of air in vertical direction can be approximated by:

$$v_{a,z}(z,u) = \frac{z}{u}v_v \quad \text{, for } 0 \le z \le u \tag{3.3}$$

Clearly, this model is a drastic simplification of the real physical system, since in reality the air flow depends on the water saturation changes during the transient unsaturated

conditions, which were not explicitly modelled in here. Such a system can only be fully described by complete multi-phase flow models (e.g., Gray and Hassanizadeh, 1998). However, the simplification made here is justifiable, since (i) the aim of this study is the simulation of the principal pattern of air intrusion and its impact on the hydrochemistry of the seepage water and (ii) only few fully coupled two-phase flow and multi-component reactive transport models exist, which might be able to simulate such a hydrogeochemical system, e.g., UTCHEM (Pope et al., 1999) or RETRASO (Saaltink et al., 2004) and are too complex that they could have applied to the here described field site within the predefined time schedule of the project.

2.2.3.2 Conceptual solute transport model

The transport of the solutes in the water phase through the variably saturated zone to TEG366 is assumed to be purely vertical within the entire pond area. Thus, the pore velocity of water v_w is depends on the recharge rate (Darcy velocity) and the water content of the sediment.

2.2.3.3 Conceptual reaction model

Redox reactions

The breakdown of organic matter leads to the sequential consumption of terminal electron acceptors (TEA's), such as oxygen, nitrate, manganese- and iron(hydr)oxides, sulfate and carbonate. At the study site, biodegradation of organic matter was only observed under aerobic, denitrifying and manganese reducing conditions:

Aerobic respiration:

$$CH_2O(NH_3)_{0.15} + 1.3O_2 \rightarrow HCO_3^- + 0.15NO_3^- + 1.15H^+ + 0.15H_2O \quad (3.4)$$

Denitrification:

$$CH_2O(NH_3)_{0.15} + 0.89NO_3^- \rightarrow HCO_3^- + 0.52N_2 + 0.11H^+ + 0.67H_2O \quad (3.5)$$

Manganese reduction:

$$2[CH_2O(NH_3)_{0.15}] + 4.45\ MnO_2(s) + 6.9H^+ \rightarrow 2HCO_3^- + 0.15N_2 + 4.45Mn^{2+} + 4.9H_2O \quad (3.6)$$

In the above equations $CH_2O(NH_3)_{0.15}$ represents a simplified version of the generalised organic matter composition $(CH_2O)_{106}(NH_3)_{16}(H_3PO_4)$.

Biodegradation was thought to be kinetically controlled and described by standard Monod-type rate expressions. Thus, the following rate expression for the degradation of organic matter was considered:

$$r_{OM} = f_T \left[r_{ox} \left(\frac{C_{ox}}{K_{ox} + C_{ox}} \right) + r_{nitr} \left(\frac{C_{nitr}}{K_{nitr} + C_{nitr}} \right) \left(\frac{K_{ox\_inh}}{K_{ox\_inh} + C_{ox}} \right) + r_{mn} \right] \tag{3.7}$$

where r_{OM} is the overall degradation rate of organic matter, r_{ox},, r_{nitr} and r_{mn} are the maximum rate constants under aerobic, denitrifying and manganese reducting conditions, respectivly. C_{ox} and C_{nitr} are the concentrations of DO and nitrate, respectively. K_{ox} are K_{nitr} are halfsaturations concentrations and K_{ox_inh} is an inhibition constant. Monod-terms for organic matter and MnO_2(s) (pyrolusite) were not included, assuming that the concentration of organic matter and pyrolusite were not rate limiting throughout the simulation time. Moreover, f_T describes the dependence of the organic matter mineralisation rate on the temperature T (°C) as propsed by Jenkinson (1990):

$$f_T = \frac{47.9}{1 + \exp\left[\frac{109}{T + 18.3} \right]} \tag{3.8}$$

Mineral reactions

During subsurface flow, biodegradation reactions, such as Eqn. (3.4)-(3.6) can affect the hydrogeochemical environment considerably and may induce further reactions, for instance dissolution/precipitation of minerals. Based on sediment analyses, calcite ($CaCO_3$) and rhodochrosite ($MnCO_3$) were assumed to dissolve or precipitate during the simulation. Whereas rhodochrosite was set in equilibrium with the aqueous solution, dissolution/precipitation of calcite was assumed to be kinetically controlled based on the formulations found by Plummer et al. (1978).

2.2.3.4 Numerical model

Both the conceptual gas and solute transport model were implemented into the numerical two-dimensional multi-component reactive transport model PHUNSAT2D, which was newly developed within this study. PHUNSAT2D couples the two-dimensional transport simulator ASM (Chiang et al., 1998) and the geochemical model PHREEQC-2 (Parkhurst and Appelo,

1999) through a sequential split operator technique. The coupling procedure is adopted from PHT3D (Prommer et al., 2003), a multi-component reactive transport model for saturated porous media. For the simulation of the equilibrium reactions, including aqueous speciation, the original PHREEQC-2 standard database was used. Kinetic reactions that were not part of the standard database, were added as BASIC-routines (Parkhurst and Appelo, 1999).
The redox reactions (3.4) – (3.6) are linked to Eqn. 3.7 by applying the so-called partial equilibrium (or two step) approach (PEA). It relies on the assumption that (i) the electron donating step (i.e., oxidation of organic carbon) is the rate-limiting step that controls the reaction kinetics and (ii) that the electron accepting step (i.e., consumption of TEAs) can therefore be simulated as instantaneous reactions (e.g., Postma and Jakobsen, 1996). This means, the TEAs are automatically consumed in the order of their thermodynamic favourability.

2.2.3.5 Model domain, initial and boundary conditions, and simulation time

The horizontal extent of the model domain was 52.5 m from the centre of the pond to the pond margin, assuming the pond's shape was approximately circular. Vertically the model domain ranged from the bottom of the pond (31 m.a.s.l) to the lower end of the filter screen of TEG366 (23 m.a.s.l).
The (transient) boundary conditions of the gas transport were as follows: The top of the model domain and the approximate location of the groundwater table were set as no-flux-boundaries (2nd type). Below the groundwater table, gas transport was not calculated. Throughout the simulation of the unsaturated Stage 3, the lower boundary (groundwater table) changed its location, as it was measured in the field (see previous chapter). The propagation velocity v_H and the position of the air-front R in the early stage of the unsaturated conditions, was derived from a modelling exercise, in which the variably saturated flow of water below the pond and the adjacent aquifer was simulated with HYDRUS2D (Šimůnek et al., 1999). The right boundary (pond center) was set as flux-boundary (3rd type). The left boundary (pond margin) was set as constant concentration boundary (1st type) for the O_2 and CO_2 concentration, i.e., partial pressure of the soil air. Their values were set as typical for soil air, i.e., pO_2 = 0.1 atm and pCO_2 = 0.01 atm. For the solute transport in the water phase, the left and the right boundary were set as no-flux-boundary. The top of the model domain was set as constant concentration boundary for the considered aqueous components. Their concentration values were taken from the pond water composition described in the previous chapter. The lower boundary of the model domain was set as flux-boundary.
Fresh and highly degradable organic matter (OM_{high}), which was assumed to originate from seasonally occurring algae blooms (see previous Chapter), was placed within the first 20 cm below the simulated recharge pond representing the clogging zone. A second, less

degradable fraction of organic matter (OM_{low}) was placed in the remaining model domain. In contrast to OM_{high}, OM_{low} did not contain organic nitrogen.
The simulation time was from day 40 since the start of the recharge cycle (middle of Stage 2, see previous chapter) to the end of Stage 3 (see previous Chapter). The model accounted for the seasonal temperature variations of the pond water during the simulation time.

2.2.3.6 Calibration

During model calibration of the model, the kinetic rate parameters of Eqn. 3.7 were adjusted such that the simulation satisfactorily reproduced the concentrations of the relevant components observed at TEG366.

2.2.3.7 Results and Discussion

After model calibration, the observed concentration pattern of essentially all relevant components was adequately described by the final simulation (Figure 62). The results in particular showed that calcium and total dissolved inorganic carbon (DIC) started to increase compared to the pond water concentration, as soon as unsaturated conditions (Stage 3) developed below the pond. This clearly demonstrates that the intrusion of gaseous oxygen enhanced the mineralisation of organic carbon and subsequently the dissolution of calcite, as it was hypothesised in the previous chapter. Moreover, the simulation agreed with the observed behaviour of dissolved oxygen (DO) and nitrate. The model revealed that during saturated conditions (Stage 2), DO was already completely consumed within the clogging zone. Nitrate, however, passed the clogging zone and depleted before reaching TEG366. As soon as gaseous oxygen penetrated underneath the pond at the beginning of Stage 3, nitrate reduction ceased (as a result of aerobic conditions) and organic nitrogen contained in the clogging zone was oxised to nitrate, leading to an increased nitrate concentration at TEG366 compared to the pond water. Although DO was completely consumed within the saturated part of the aquifer before reaching TEG366, nitrate did not so and thus could break through to the monitoring well. The breakthrough of nitrate ceases when the residence time became to long due to the decreasing recharge rate, leading to a full depletion of nitrate within the saturated part of the aquifer. Towards the end of Stage 3, the DO concentration at TEG366 didn't increase until the water saturated layer between groundwater table and filter screen (**Figure** 62 and Figure 63) became small enough for a breakthrough before DO was entirely consumed. Interestingly, nitrate didn't break through. The model revealed that nitrate was now also completely consumed within the clogging zone due to the longer residence time in this zone at the end of Stage 3.

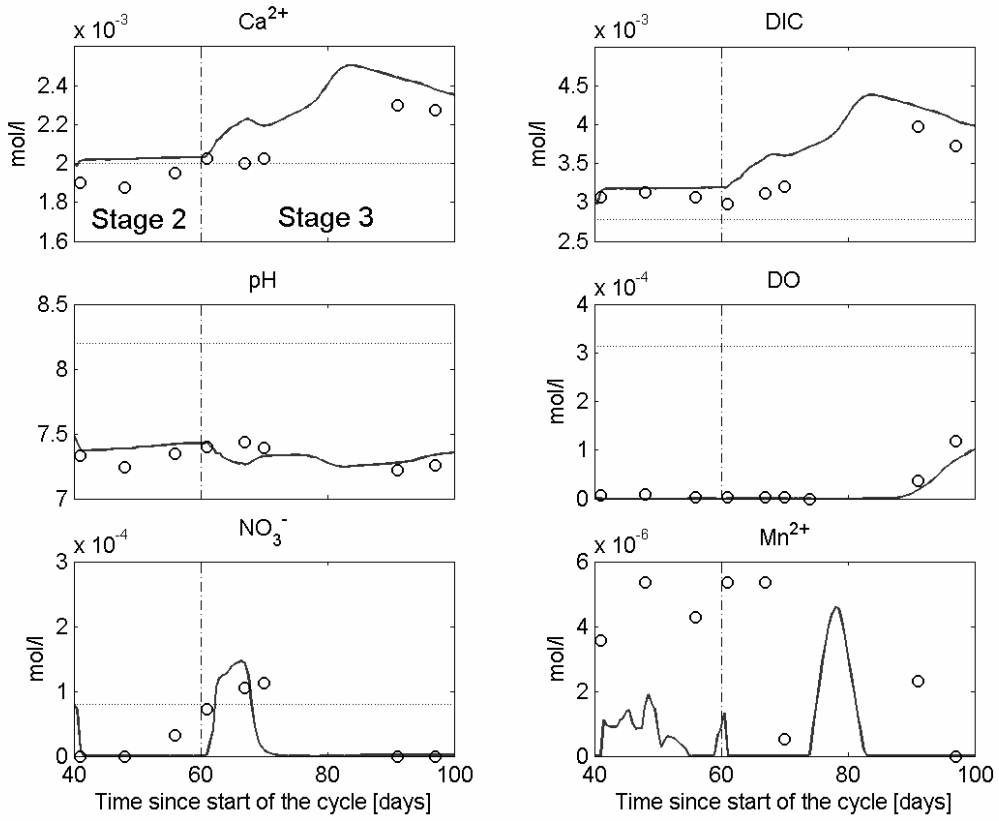

Figure 62 Simulated and observed pH and concentrations of calcium, total dissolved inorganic carbon (DIC), dissolved oxygen (DO), nitrate and dissolved manganese at TEG366. Horizontal lines represent average pond water concentrations.

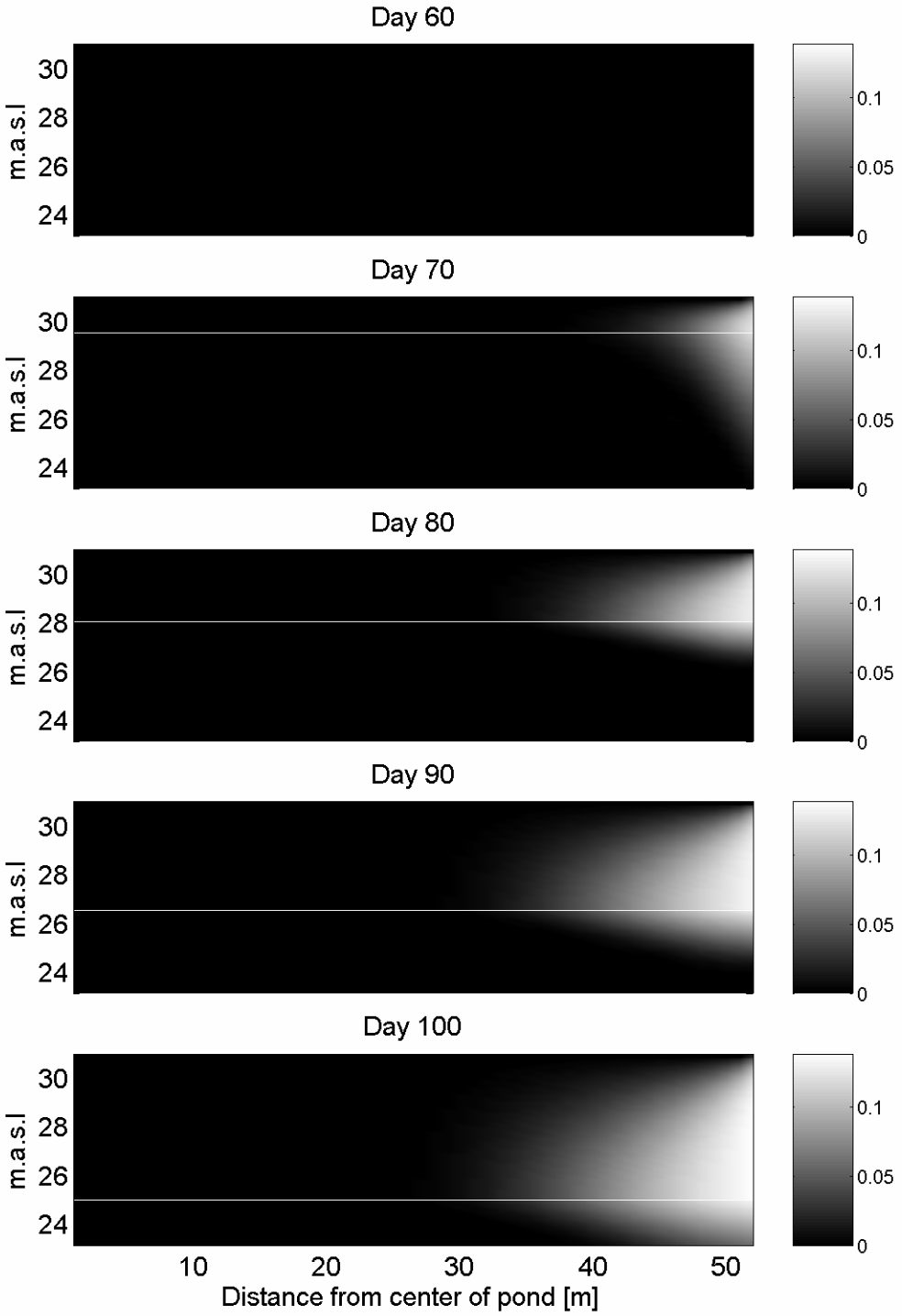

Figure 63 Simulated concentration of dissolved oxygen (DO) within the cross-sectional area below the pond for different times after the start of the cycle (Stage 3). White vertical line indicates approximate position of the groundwater table.

The simulated concentrations of dissolved manganese were in the same order of magnitude of the observed concentrations. However, the model could not reproduce the observed concentration pattern. The discrepancy appears acceptable, as the deviations between simulated and the relatively low measured manganese concentrations are unlikely to have a significant impact on the electron balance.

The cross-sectional view of the simulation showed that during the entire simulation period the gaseous oxygen front did not reach the centre area below pond (Figure 63). Aerobic conditions only developed within the first 20m from the pond margins. Thus, the enhanced mineralisation of organic carbon and dissolution of calcite very likely occur only below the fringe area of the pond rather than below the entire pond.

2.2.4 Modelling redox dynamics and the fate of phenazone

2.2.4.1 Observed Redox zonation and travel times

The redox status of the groundwater in the surrounding pond area is generally characterized by aerobic, denitrifying and manganese reducing conditions. Thereby, the position and the extent of these redox zones were found to be strongly dependent on the seasonal temperature changes of the recharge water (see Final NASRI Report 1 of NASRI group Hydrogeology). During summer, when the microbial activity is higher, dissolved oxygen (DO) and nitrate become depleted in the close vicinity of the pond and manganese reducing conditions were found to be dominating most parts of the studied aquifer section. During winter, however, manganese reducing conditions were only found in the deep monitoring well TEG369UP, which is located at the maximum distance from the pond. Average travel times of the recharged water from the pond to the monitoring wells were estimated from stable isotope data and from observed temperature variations (see Final NASRI Report 1 of NASRI group Hydrogeology). A clear breakthrough of the seasonal stable isotope signal was only available at TEG396UP (average travel time was about 50 days). This allowed the calculation of a (site-specific) retardation factor for temperature transport, i.e., R = 2.1 (see Final NASRI Report 1 of NASRI group Hydrogeology). A similar retardation factor has been found by Prommer and Stuyfzand (2005) for an artificial recharge site in the Netherlands. Note, that the travel times were highly variable in time, dependent on the recharge rate (Figure 64).

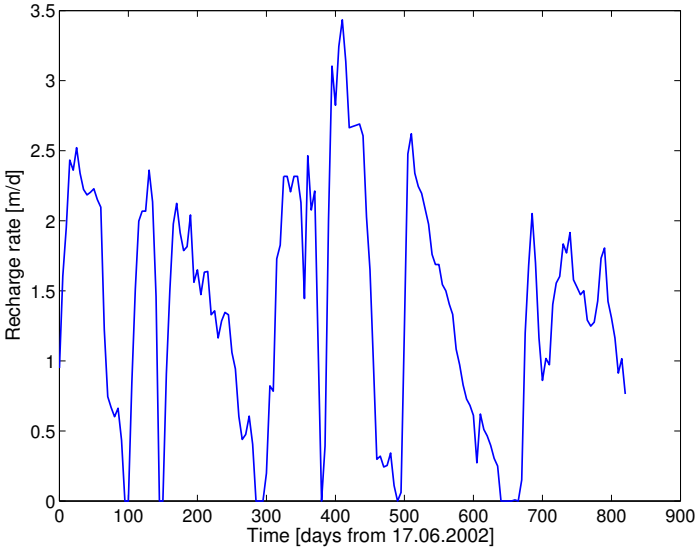

Figure 64 Time series of recharge rate (data was kindly provided by Berliner Wasser Betriebe).

2.2.4.2 Flow and non-reactive transport model

In a first step a flow and non-reactive transport model was set up for the aquifer surrounding pond 3. The simulations were performed for a radial symmetric vertical two-dimensional profile, assuming that (i) the ponds shape could be approximated as a circle and (ii) the recharged water spreads radially and homogeneously from the pond. The flow simulations were carried out with the USGS flow simulator MODFLOW (McDonald and Harbaugh, 1988). The transport simulator MT3DMS (Zheng and Wang, 1999) was used for the transport of temperature, which, under consideration of the site-specific retardation factor, served for the calibration of the non-reactive transport processes.

The horizontal extent of the model domain was 134 m, i.e., the distance from the centre of the pond to the two most distant monitoring wells TEG369OP/UP. In vertical direction the domain extended from the bottom of the pond, i.e., 31 m below sea level (m.b.s) to -10 m.b.s, where an aquitard of the Holstein interglacial forms the base of the aquifer (Voigt and Eichberg, 2000). A no-flow boundary was set at the symmetry axis (left) representing the center of the pond. The right boundary was set as constant head boundary with an average value of the hydraulic heads as measured at TEG369OP/UP. A time-variant flux boundary represented the recharge pond. An additional no-flow boundary approximated the time-averaged groundwater surface between the pond margin and downstream boundary, neglecting the temporarily unsaturated conditions below the pond. The model discretisation was 2 m in horizontal direction. In vertical direction it ranged from 0.5 m at the upper part to 4 m at the lower part of the model domain. The model aquifer was assumed to be isotropic and homogeneous. Furthermore, the model did not explicitly incorporate the glacial till layer,

because its abundance was found to be very patchy in this area (see Final NASRI Report 1 of NASRI group Hydrogeology).

The total simulation time was 825 days, discretised into 165 stress periods and starting from 17th June 2002. The time-variant fluxes and seasonal temperatures in the pond were defined for each stress period on the base of 5-day-averages that were calculated from daily recharge and temperature values, respectively.

2.2.4.3 Reaction network

The simulated reaction network was largely taken from Chapter 3. There were the following modifications: (1) the original temperature function was changed to a function propsed by O'Connell (1990) and Kirschbaum (1995, 2000):

$$f_T = \exp\left[\alpha + \beta T\left((1 - 0.5\frac{T}{T_{opt}})\right)\right] \tag{4.1}$$

where α and β are fitting parameters, and T_{opt} (°C) is the optimal temperature for the decomposition process. (2) Calcite was here simulated as to be in equilibrium with the aqueous solution.

2.2.4.4 Phenazone degradation

Phenazone is an analgesic PhAC contained in the painkillers Antipyrin® and SpaltN® (Zühlke, 2004). It has been previously detected in surface waters, groundwater and drinking water of Berlin (Reddersen et al., 2002, Zühlke, 2004). Laboratory experiments demonstrated that phenazone is degradable under oxic conditions (Sauber et al., 1977, Zühlke, 2004) by the aerobic bacteria *Phenylobakterium immobile* (Lingens et al, 1985). Sorption of phenazone to filter material, sludge or soil samples was found to be negligible (Reddersen et al, 2002; Zühlke, 2004).

In the model, it was assumed that the degradation rate of phenazone is dependent on the DO concentration, similar to other micropulltants such as pesticides (Vink and van der Zee, 1997, Tuxen et al. 2005). Further it was assumed that the degradation rate is temperature-dependent, as the degradation of phenazone is due to microbial metabolism. Those rate dependencies were incorporated, which leads to the following rate expression for phenazone degradation:

$$r_{phena} = f_T r_{phena\_\max}\left(\frac{C_{ox}}{K_{phena\_ox} + C_{ox}}\right) C_{phena} \quad (4.2)$$

where, r_{phena} is the degradation rate of phenazone, r_{phena_max} is the maximum degradation rate constant, K_{phena_ox} is the halfsaturation concentration and C_{phena} is the concentration of phenazone.

2.2.4.5 Numerical Model

The multi-component reactive transport model PHT3D was used to set up the conceptual reaction model and simulate the biogeochemical characteristics at the artificial recharge site. PHT3D couples the transport simulator MT3DMS and the geochemical reaction model PHREEQC-2 via sequential split operator technique. The simulation of equilibrium and kinetic reactions was carried out as in Chapter 2.3.

4.5.1 Simulated initial and recharge water composition and aquifer composition

The simulated recharge water comprised only of components that were relevant for this study rather than the complete set of components analysed. To account for the time variant surface water quality, their concentrations were adjusted for each stress period based on monthly measurements by the NASRI group Hydrogeology. The applied concentration ranges are listed in Table 9. Note that total dissolved organic carbon (DOC) was not included in the simulation, since the consumption of TEAs seemed to be mainly driven by the mineralisation of labile OM that was filtrated within the first 1-2 meters below the pond and which appeared to originate from seasonal algae blooms (see Chapter 2.2). Thus, high degradable OM_{high} was emplaced within the first 2 m below the simulated recharge pond. Furthermore, it was assumed that its concentration would never become rate limiting, as in reality there is a continuous input of organic matter from periodic algae blooms. Less degradable OM_{low} was emplaced in the remaining model domain. Thereby, OM_{high}/OM_{low} is the relative reactivity r_{reac}. The initial concentrations of the two types of SOM, as well as the initial concentrations of the simulated minerals can be found in Table 9. As the simulation starts in summer 2002, the initial groundwater composition represented a typical summer situation given in Table 9.

2.2.4.6 Calibration

The calibration of the reactive transport model occurred in two steps. In the first step, the flow and non-reactive transport model was calibrated in order to reproduce the observed groundwater temperature variations that were recorded daily at the monitoring wells TEG367, TEG368OP, TEG368UP, TEG369OP and TEG369UP. The monitoring wells TEG365 and TEG366 were not used for calibration, since the breakthrough of the seasonal

temperature signal at these locations was not distinguishable from the signal in the pond water due to too short travel times. For the locations of the monitoring wells see final NASRI Report 1 of NASRI group Hydrogeology. The so derived flow field and transport parameters served as the base for the reactive transport model and were not further modified during the reactive simulations. Thus, the calibration of the biogeochemical processes occurred separately in a second step. Therein, mainly rate parameters of the kinetic reactions were adjusted in order to reproduce the observed field data at the monitoring wells TEG365, TEG366, TEG368OP, TEG368UP, TEG369OP and TEG369UP. The sensitivity of the model behaviour against the rate parameters was recorded during the calibration process and evaluated further below. Note that the equilibrium reaction constants provided by the PHREEQC-2 standard database were not modified und thus not involved in the calibration process.

Table 9 Initial and range of recharge water composition, and initial concentrations of minerals and OM used for the model simulations.

Component	Unit	Initial concentration	Range of concentration in recharge water
DO	[mol L^{-1}]	0	$1.8 \times 10^{-4} – 6.7 \times 10^{-4}$
NO_3^-	[mol L^{-1}]	0	$2.6 \times 10^{-5} – 1.7 \times 10^{-4}$
Mn^{2+}	[mol L^{-1}]	6.56×10^{-06}	0
Ca^{2+}	[mol L^{-1}]	2.3×10^{-3}	$1.7 \times 10^{-3} – 2.5 \times 10^{-3}$
TIC	[mol L^{-1}]	3.5×10^{-3}	$2.4 \times 10^{-3} – 3.4 \times 10^{-3}$
pH	[-]	7.2	7.5 – 9.1
pE	[-]	9	11.6 – 13.2
Phenazone	[mol L^{-1}]	0	0.11 – 1.2
Pyrolusite	[mol L_{bulk}^{-1}]	3.0×10^{-3}	-
Calcite	[mol L_{bulk}^{-1}]	1.7	-
Rodochrosite	[mol L_{bulk}^{-1}]	0	-
OM_{high}	[mol L^{-1}]	1	-

OM_{low}	[mol L^{-1}]	1	-

2.2.4.7 Results and discussion

Non-reactive transport

The solute transport processes determined by the proposed flow and non-reactive transport model were solely dependent on the effective porosity n_e and the longitudinal and transversal dispersivities α_L and α_T, respectively. Thus, these parameters were adjusted during calibration of the non-reactive transport model. The simulation results of the calibrated non-reactive transport model agree very well with the observed data, especially with its dynamics (Figure 65). The good fit clearly supports the simplifying assumptions made for the conceptual flow and non-reactive transport model.

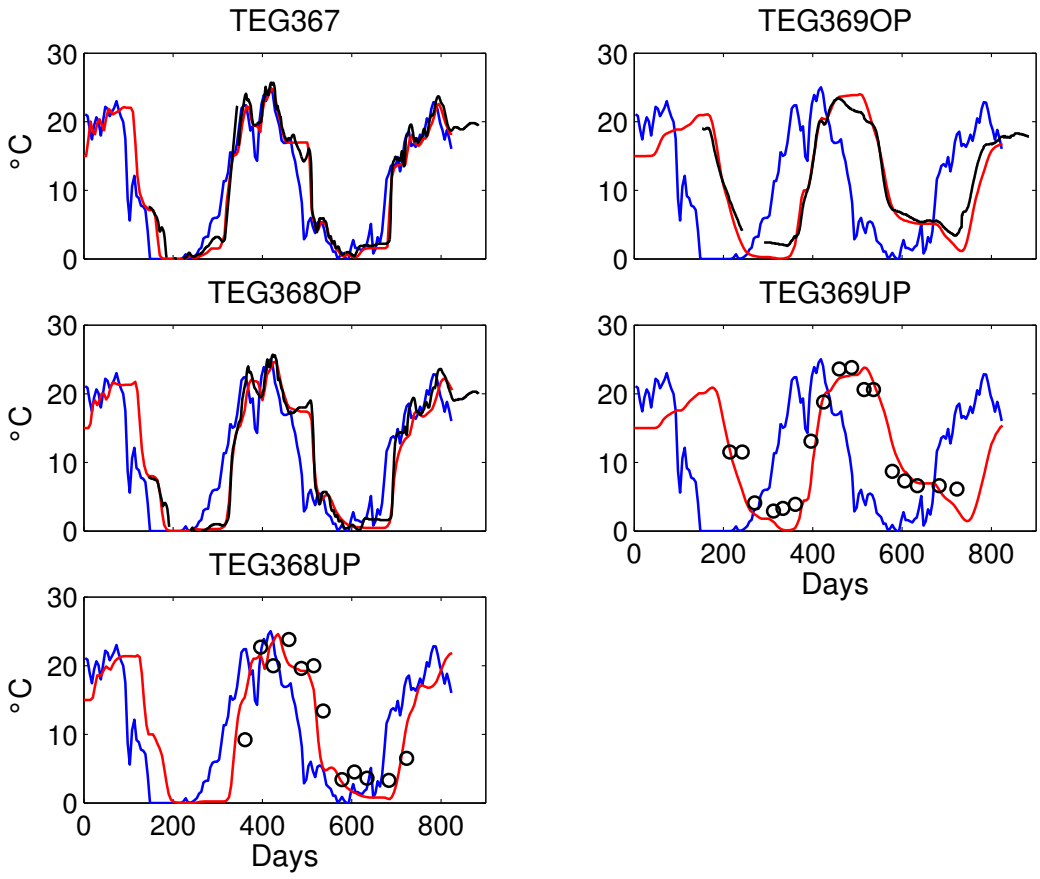

Figure 65 Calibration results of non-reactive transport model for the monitoring wells TEG367, TEG368OP/UP and TEG369OP/UP. Blue lines represent the temperature of the pond water. Black lines and black circles represent the observed temperature with data loggers and (monthly) manual measurements, respectively. Red lines indicate the simulated temperature.

Reactive transport

The final calibrated biogeochemical transport model is capable of reproducing almost all biogeochemical characteristics and their seasonal dynamics that were observed in the aquifer surrounding the recharge pond. The simulation results and the influence of the most relevant parameters are discussed below.

Redox system

The simulation results of nearly all components showed a very good agreement with the observed data at all monitoring wells when variably water temperatures were taken into account (Figure 66). Thereby, the fate of DO, nitrate, Mn^{2+} and phenazone was highly affected by the proposed biogeochemical reaction network, as the contrast to the corresponding non-reactive simulations show. During winter, almost no consumption of oxygen occurred and its breakthrough was observed at all monitoring wells except TEG369UP. As long as aerobic conditions prevailed and nitrate reduction has not started yet, nitrification of organic nitrogen is the dominant process causing the elevated nitrate concentrations at all monitoring wells compared to the pond water. These effects could be well reproduced by the simulation. In summer, DO concentrations became depleted before the reaching TEG365 and TEG366 and thus were zero further downstream. However, nitrate did not fully deplete and break through at all of the monitoring wells. These breakthroughs had a very dynamic behaviour, which resulted from the drastic variations in recharge rate and thus travel times. This means, breakthrough occurred when recharge rates were highest and vice versa. The observed behaviour of the nitrate breakthroughs during summer could also be successfully simulated.

Although the simulated Mn^{2+} concentrations in principle reproduced the seasonal pattern they still significantly deviate from the observed data. In the simulation, manganese reduction only started when nitrate was entirely depleted. This contradicted the observations, which rather showed a simultaneous occurrence of manganese and nitrate reduction. During the calibration procedure, a number of manganese (hydr)oxide minerals of different solubility other than pyrolusite were tested in order to reproduce this behaviour. However, none of them could account for the observed overlap of nitrate and manganese reduction. A

possibility to overcome this problem would be to adjust the solubility of pyrolusite within the PHREEQC-2 database, since in general the solubility of a mineral reflects its reactivity (Jakobsen and Postma, 1999). However, in order to satisfactorily simulate the observed overlap of nitrate and manganese reduction, a solubility change of about 4 orders of magnitude would have been necessary, which we think is not justifiable. For comparison, Jakobsen and Postma (1999) adjusted the reaction constant of $Fe(OH)_3(s)$ during model calibration only within one order of magnitude. However, as the crude simulation of the manganese reducing conditions did not affect the fate of phenazone on which this paper was focussed on, we decided to refrain from improve the simulation with respect to manganese reduction.

In order to evaluate the impact of temperature on the proposed biogeochemical reaction network, extra simulations considering different constant temperatures were carried out. They show that with constant temperatures of 5°C, 10°C and 15°C, the seasonal dynamics of the redox components, pH and phenazone cannot be reproduced at all (Figure 67). The dynamic behaviour of breakthroughs only results from the time variant recharge rates. In principle, the same breakthrough pattern is generated for higher temperatures. The only difference, however, is a shift of the redox zones towards the recharge pond due to the higher reaction rates.

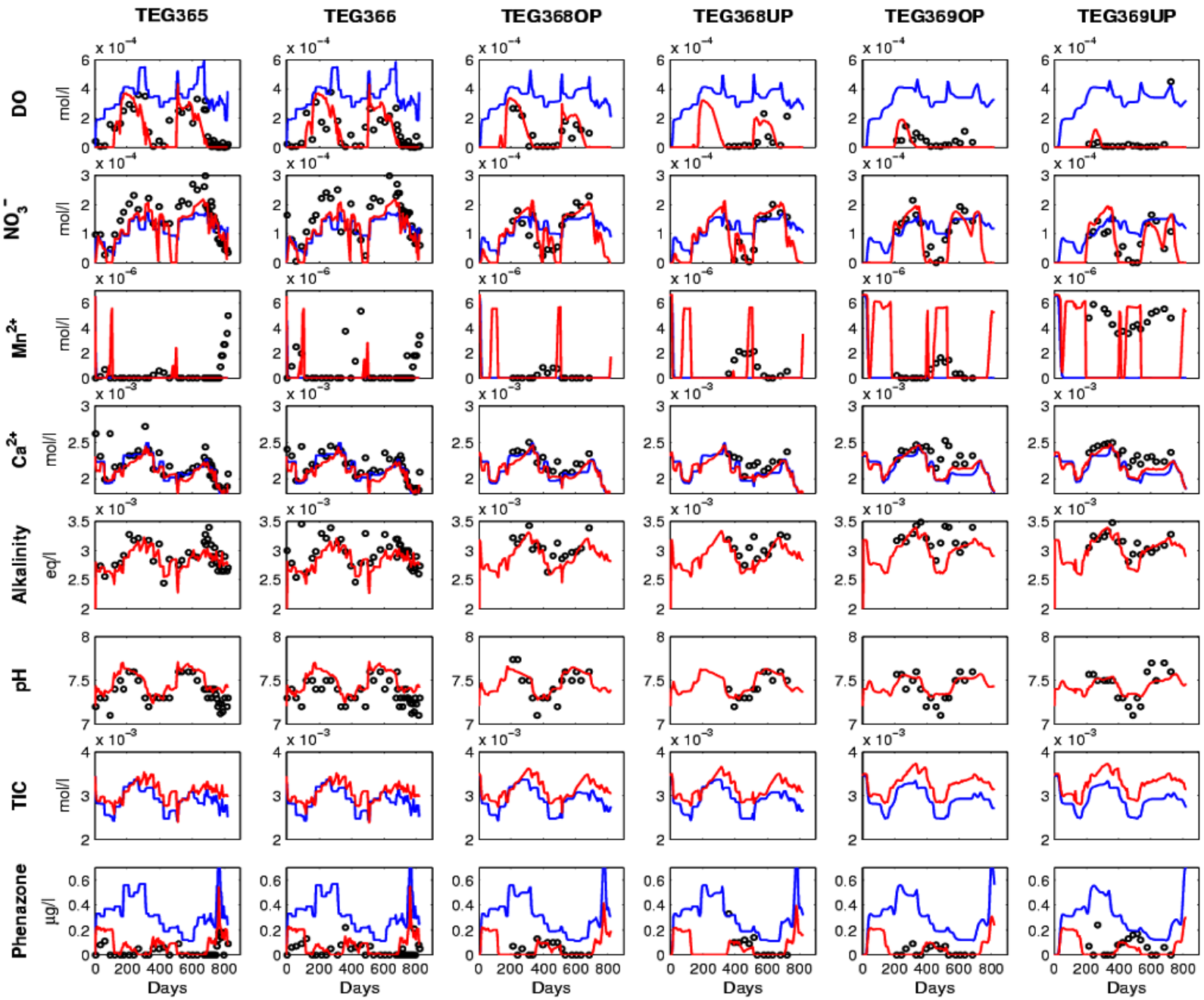

Figure 66 Simulation results for dissolved oxygen (DO), nitrate, Mn^{2+}, calcium, alkalinity, pH, TIC and phenazone at the monitoring wells TEG365, TEG366, TEG368OP/UP and TEG396OP/UP. Black circles represent the observed data and red lines represent the final calibrated reactive transport simulation. The blue lines represent the non-reactive simulation, in which all biogeochemical reactions were excluded.

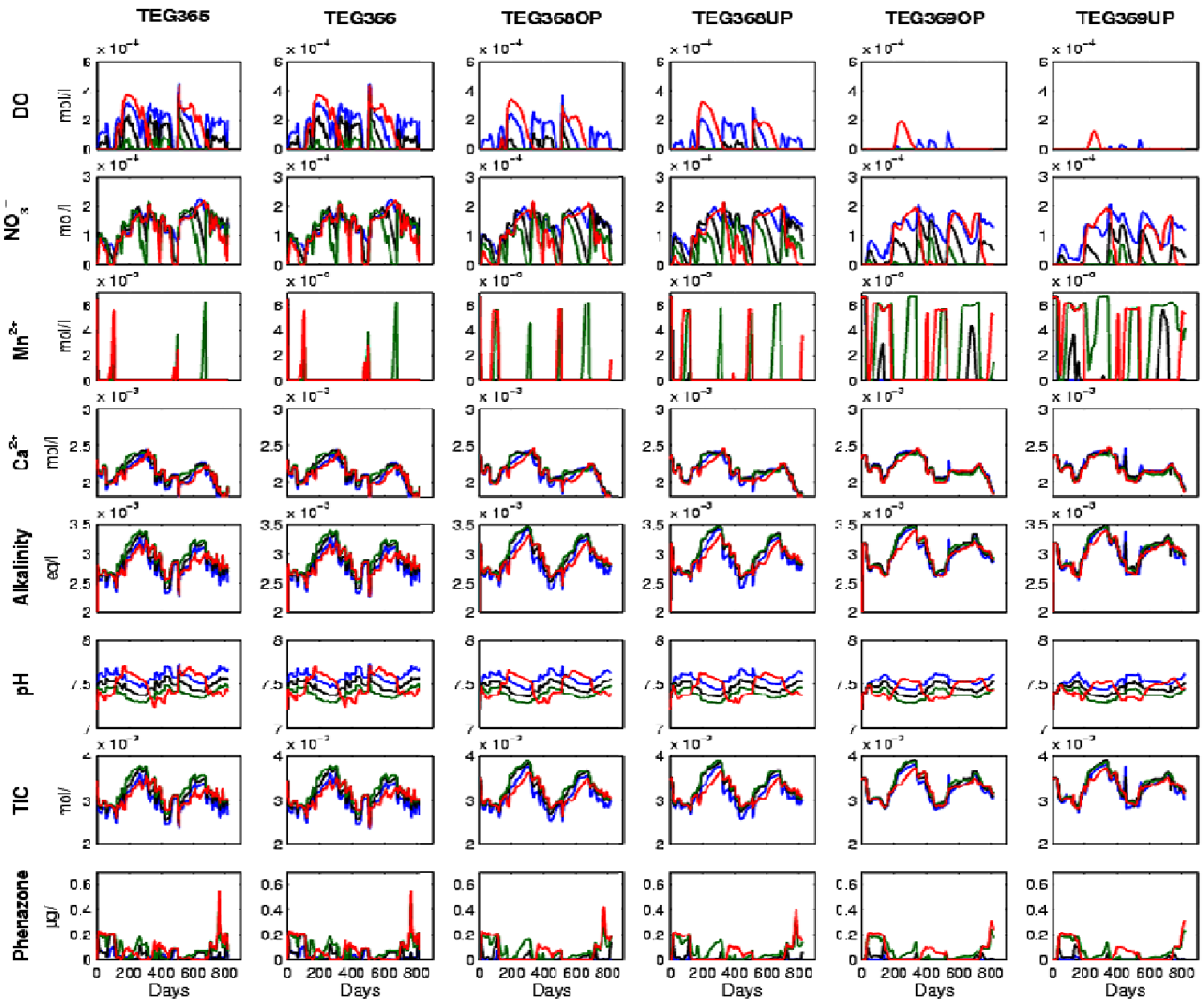

Figure 67 Temperature dependence of dissolved oxygen (DO), nitrate, Mn^{2+}, calcium, alkalinity, pH, TIC and phenazone at the monitoring wells TEG365, TEG366, TEG 368OP/UP and TEG396OP/UP. The blue, black and green lines represent simulations with constant temperatures of 5℃, 10℃ and 15℃, respectively. The red lines represent the final calibrated reactive transport simulation (variable temperature).

Carbonate system

The seasonal dynamics of calcium and carbonate concentrations are generally reflected by the pond water concentrations, as the non-reactive simulation shows (Figure 66). Moreover, the constant temperature simulations reveal that there is no significant dependence on temperature (Figure 4.4). In contrast, pH shows considerable temperature dependence (Figure 4.4). The lower pH at high temperatures is thought to be due to the fact that protons were less buffered, as the solubility of calcite is lower for higher temperatures.

Phenazone degradation

The simulated phenazone concentrations of the final calibrated model agreed very well with the observed concentrations at all monitoring wells (Figure 66). In contrast, the constant temperature simulations clearly failed to reproduce the good fit of the final model simulation (Figure 67). In general, it appears that higher temperatures lead to higher phenazone concentrations. If the degradation rate was dependent on temperature alone, the opposite behaviour would be expected, which suggests that phenazone degradation must also be affected by the redox status. In order to be able to evaluate the impact of the temperature and redox effect separately, the final calibrated model was modified and three different cases were considered.

In *Case 1* the degradation rate has been decoupled from temperature, i.e., the temperature function in Eqn. 4.2 has been set to unity. The simulation results for *Case 1* are shown in Figure 4.5. With the original value of r_{phena_max}, the simulation can satisfactorily account for the observed phenazone concentrations. With lower r_{phena_max}, the breakthrough concentrations increase and diverge from the observations. However, the observed breakthrough times are still well simulated.

In *Case 2*, the degradation rate of phenazone has been decoupled from the DO concentration, i.e., the Monod-term in Eqn. 4.2 has been set to unity. Even for a broad range of r_{phena_max}, the simulation cannot reproduce the observed phenazone concentrations at all (Figure 68). The simulation rather shows an inverted dynamics of phenazone concentrations in comparison to the observed. This is because in *Case 2*, the degradation rate of phenazone is solely dependent on temperature, which leads to higher breakthrough concentrations in winter and vice versa.

Case 3 was a combination of *Case 1* and *Case 2*. Therein, degradation rate of phenazone has been decoupled from both temperature and DO concentration and thus follows a first-order rate law. This means the breakthrough pattern of phenazone at the monitoring wells is solely dependent on r_{phena_max} and the recharge rate. Again, even for a broad range of r_{phena_max} it was not possible to reproduce the observed concentrations at the monitoring wells

(Figure 68). This analysis showed that the temperature dependency of the degradation rate is not necessary in order to describe the fate of phenazone within the aquifer. On the other hand, the observed breakthrough pattern of phenazone could not be reproduced, if the redox dependence of the degradation rate was neglected. Hence, the unsatisfying simulation of phenazone concentrations in the constant temperature simulations (Figure 67) solely results from the inadequate reproduction of redox conditions.

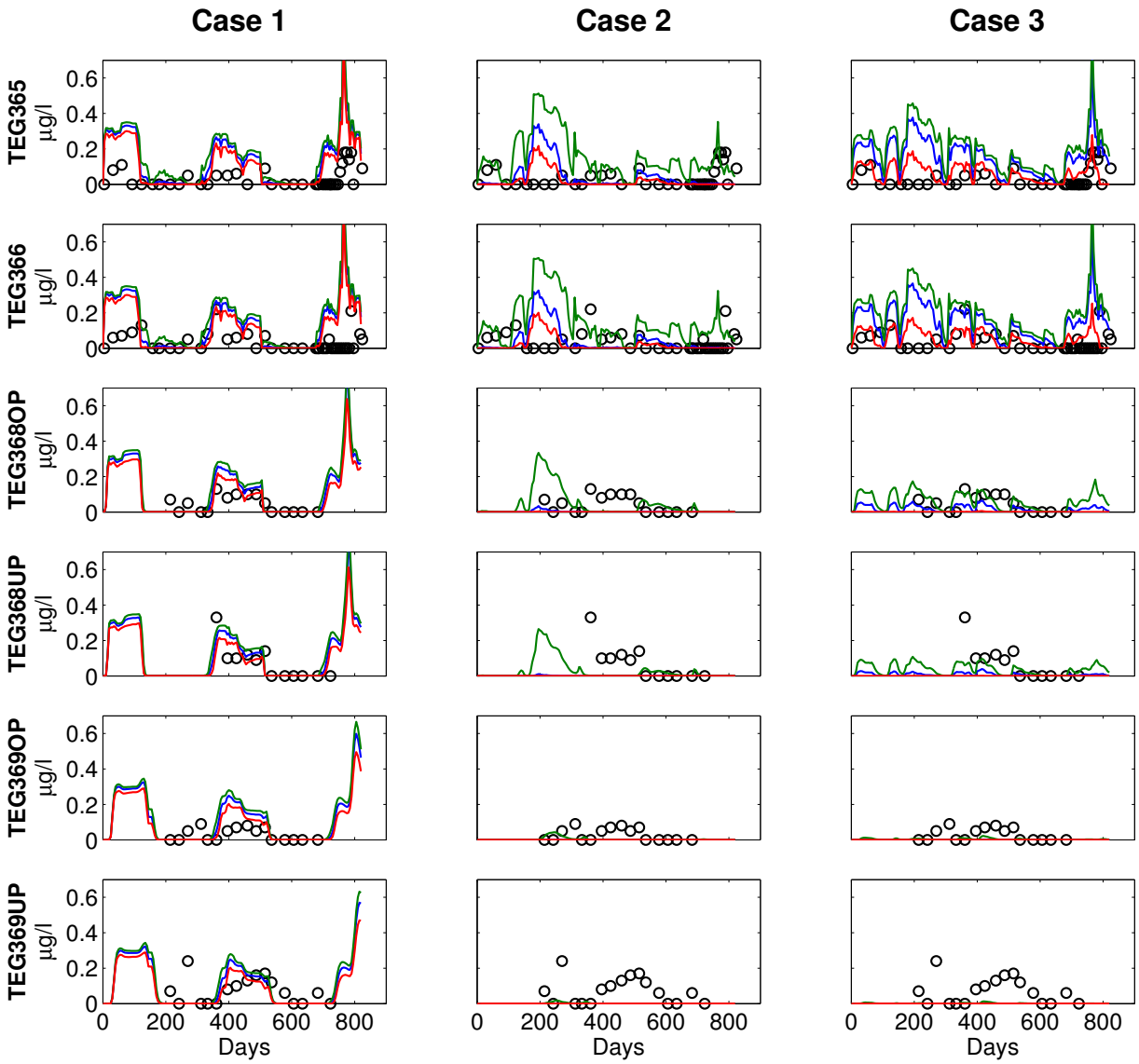

Figure 68: Simulated phenazone concentrations for temperature decoupled (Case 1), redox decoupled (Case 2) and first-order (Case 3) degradation rate. Case 1: red, blue and green lines represent a r_{phena_max} of 12.0 d^{-1}, 6.0 d^{-1} and 3.0 d^{-1}, respectively; Case 2: red, blue and green lines represent a r_{phena_max} of 3.0 d^{-1}, 1.5 d^{-1} and 0.25 d^{-1}, respectively; Case 3: red, blue and green lines represent a r_{phena_max} of 0.75 d^{-1}, 0.25 d^{-1} and 0.125 d^{-1}, respectively;

2.2.5 Conclusions and prospects

The artificial recharge pond in Berlin was investigated with the aims of (i) identifying the hydraulic regime and its impact on the dynamics of the hydrogeochemical environment immediately below the pond, and (ii) providing a quantitative process-based modelling framework for simulating the fate of the redox-sensitive PhAC phenazone within the surrounding aquifer of the pond.

Directly below the recharge pond, the hydrogeochemical environment is predominantly impacted by transient hydraulic conditions and seasonal temperature variations. Thereby, the entire hydraulic system is controlled by the formation of a clogging layer at the bottom of the pond resulting in alternating saturated/unsaturated conditions below the pond. During summer, when the infiltrated water is relatively warm (about 20-25°C), the spatial and temporal distribution of different redox conditions is strongly determined by the prevailing hydraulic conditions and their dynamics below the pond. When the sediment below the pond is fully water saturated in the earlier part of the operational recharge cycle, nitrate reducing and manganese reducing conditions are dominant. Iron and sulphate reducing conditions develop only in anaerobic micro-sites due to chemical and/or physical heterogeneity. When the hydraulic conditions change from water saturated to water unsaturated conditions, which is approximately in the middle of the recharge period, remarkable changes of the local hydrogeochemistry below the pond can be observed. They result from the temporal re-oxidation of previously formed iron-sulphides due to the lateral intrusion of atmospheric oxygen penetrating from the pond margins into the centre below the pond. During the following unsaturated period, the availability of atmospheric oxygen enhances the mineralisation of particulate organic carbon, which in turn promotes the dissolution of calcite. Reactive transport modelling of the area below the pond supported this hypothesis. However, modelling also revealed that the described processes seem not to occur in the center below the pond. Whereas in summer the dynamics and the character of the hydrochemical system are strongly affected by the hydraulic situation, hydrogeochemical changes are relatively independent from the hydraulic conditions in winter.

The modelling study at larger scale for this site showed that the hydrogeochemical processes, in particular the redox processes, are predominantly controlled by seasonal temperature changes rather than transient groundwater flow due to varying recharge rates. The influence of transient saturated/unsaturated conditions appeared not to be important for the behaviour of the hydrogeochemical system on that scale. It could be clearly demonstrated that solely the redox dependency of the degradation rate of phenazone controls the fate of phenazone in the subsurface of this artificial recharge site rather than variations in recharge rate and the temperature dependence of the phenazone's degradation rate.

With the successful simulation of the redox dynamics and the fate of phenazone at the Berlin site, one can expect that it is also possible to model the fate of other phenazone-type pharmaceuticals such as 1-acetyl-1-methyl-2-dimethyloxamoyl-2-phenylhydrazide (AMDOPH), 1-acetyl-1-methyl-2-phenylhydrazid (AMPH), Acetoaminoantipyrin (AAA), formylaminoantipyrin (FAA), 1,5-dimethyl-1,2-dehydro-3-pyrazolone (DP) and 4-(2-methylethyl)-1,5-dimethyl-1,2-dehydro-3-pyrazole (PDP) that were also detected at the artificial recharge site.

An appealing option for the site operator (BWB) might be the ability to simulate the quality of the water extracted by the surrounding production well field, because the extraction water quality is likely to be altered by operational changes of the pumping regime or recharge rates. The development of a three-dimensional reactive transport model for a larger model domain capturing the production well field is undoubtedly possible, since a calibrated site-specific reaction module for the aquifer now exists.

2.2.6 References

Chiang, W.-H., Kinzelbach, W., Rausch, R. (1998), Aquifer simulation model for Windows, Gebrüder Borntraeger, Berlin – Stuttgard, 137 p.

Gray, W.G. and Hassanizadeh, S.M. (1998), Macroscale continuum mechanics for multiphase porous-media flow including phases, interfaces, common lines and common points, Advances in Water Resources, 21(4), 261-281.

Hecht, H. and Kölling, M. (2001) A low-cost optode array measuring system based on 1mm plastic optical fibers – new technique for in situ detection and quantification of pyrite weathering processes. Sensors and Actuators B 81, 76-82.

Jakobsen, R., and D. Postma (1999), Redox zoning, rates of sulfate reduction and interactions with Fe-reduction and methanogenesis in a shallow sandy aquifer, Rømø, Denmark, Geochim. Cosmochim. Acta, 63(1), 137-151.

James, T. (2002), Numerical Solution of Advection-Diffusion Equations for Radial Flow, Master thesis, University of Oxford.

Jenkinson, D.S. (1990), The turnover of organic carbon and nitrogen in soil. Philosophical Transactions of the Royal Society of London. Series B, Biological Sciences; 329:p361-368.

Kirschbaum, M.U.F. (1995), The temperature dependence of soil organic matter decomposition, and the effect of global warming on soil organic storage, Soil Biol., Biochem., 27(6), 753-760.

Kirschbaum, M.U.F. (2000), Will changes in soil organic carbon act as a positive or negative feedback on global warming ?, Biogeochemistry, 48, 21-51.

Lee, J., and Ladd, A.J.C. (2002), A computer simulation study of multiphase squeezing flows, Physic of Fluids, 14(5), 1631-1641.

Lingens, F., Blecher, R., Blecher, H., Blobel, H., Eberspächer, J., Fröhner, C., Görisch, H., Görisch, H., Layh, G. (1985), Phenylobacterium immobile gen. nov., sp. Nov., a Gram-Negative Bacterium that degrades the Herbicide Chloridazon, Int. J. Syst. Bact., 35(1), 26-39.

McDonald, J. M., and A. W. Harbaugh, MODFLOW (1988), A Modular 3D Finite Difference Ground-Water Flow Mode, Open-file Report 83-875, U.S. Geological Survey.

O'Connel (1990), Microbial decomposition (respiration) of litter in eucalypt forests of south Western Australia: An empirical model based on laboratory incubations, Soil Biol. Biochem., 22(2), 153-160.

Parkhurst D. L., and C. A. J. Appelo, (1999), PHREEQC (Version 2) - A computer program for speciation, batch-reaction, one-dimensional transport, and inverse geochemical calculations, Water Resources Investigations Report 99-4259, U. S. Geological Survey.

Plummer, L.N., Wigley, T.M.L., Parkhurst, D.L. (1978), The kinetics of calcite dissolution in CO_2 water systems at 5° to 60° and 0.0 to 1.0 atm CO_2, Am. J. Sci. 278, 179-216.

Postma, D., and R. Jakobsen (1996), Redox zonation: equilibrium constraints on the Fe (III)/SO4-reduction interface, *Geochim. Cosmochim. Acta,* 60, 3169-3175.

Pope, G. A., Sepehrnoori, K., Sharma, M.M, McKinney D.C, Peitel, G.E., Jackson, R.E. (1999), The dimensional NAPL fate and transport model, Technical Report, U. S. Environmental Protection Agency, EPA/600/R-99/011, 361 p.

Prommer H., Barry, D.A., Zheng, G.B. (2003), MODFLOW/MT3DMS-based multi-component reactive transport modelling. Groundwater, 42(2), 247-257.

Prommer, H., and P. J. Stuyfzand (2005), Identification of temperature-dependent water quality changes during a deep well injection experiment in a pyritic aquifer, *Environ. Sci. and Technol*., 39(7), 2200-2209.

Reddersen, K., Heberer, T., Dünnbier, U. (2002), Identification and significance of phenazone drugs and their metabolites in ground- and drinking water, Chemosphere, 539-544.

Saaltink, M.W., Batlle, F., Ayora, C., Carrera, J., Olivella, S. (2004), RETRASO, a code for modeling reactive transport in saturated and unsaturated porous media, Geologica Acta, 2(3), 235-251.

Sauber, K., Müller, R., Keller, E., Eberspächer, J., Lingens, F. (1977), Degradation of Antipyrin by Pyrazon-Degrading Bacteria, Z. Naturforsch, 32c, 557-562 (in german).

Šimůnek, J., Šejna, M., van Genuchten, Th.-M. (1999), The HYDRUS2D Software package for simulating the two-dimensional movement of water, heat and multiple solutes in variably saturated media – Version 2.0, Tech. Rep., U.S. Salinity Laboratory, USDA, ARS, Riverside, CA..

Sinke, A.J.C., Dury, O., Zobrist, J. (1998). Effects of a fluctuating water table: column study on redox dynamics and fate of some organic pollutants. J. Cont. Hydrol. 33, 231-246.

Tuxen, N., Reizel, L.A., Albrechtsen, H-.J., Bjerg, P.L. (2005), Oxygen-enhanced Biogedradation of Phenoxy Acids in Groundwater at Contaminated Sites, Groundwater (in press).

Vink, J.P.M., Van der Zee, S.E.A.T.M. (1997), Pesticide biotransformation in surface waters: Multivariate analyses of environmental factors at field sites. Water Research, 31 (11), 2858-2868.

Zheng, C., and P. P. Wang (1999), MT3DMS: A modular three-dimensional multispecies model for simulation of advection, dispersion and chemical reactions of contaminants in groundwater systems, Documentation and User's Guide, Contract Report SERDP-99-1, U.S. Army Engineer Research and Development Center, Vicksburg, MS.

Voigt, I., and Eichberg, M., (2000), Hydrogeologisches Strukturmodell Wasserwerk Tegel, Fugro Consult GmbH.

Zühlke, S. (2004), Verhalten von Phenazonderivaten, Carbamazepin und estrogenen Steroiden während verschiedener Verfahren der Wasseraufbereitung, PhD Thesis, Technische Universität Berlin (in german).

2.3 Laboratory experiments: Modelling studies on Column experiments

2.3.1 Methods

2.3.1.1 Reactive transport model of the large column

There are many examples of soil column flushing simulation models involving bio-geochemical degradation reactions. Examples are given by Von Gunten & Zobrist (1996), Schäfer et al. (1998a, 1998b), and Amirbahman et al. (2003). These models require a large database including an adequate reaction framework and exact knowledge about soil matrix composition (see Heron et al., 1996), otherwise reaction models can be partially ambiguous (Appelo et al. 1998). Up scaling from micro-columns studies leads to field-site scale models studying riverbank filtration, or contamination of groundwater by reducing leachate plumes originating from landfills or oil spills (Lensing et al. 1994, Van Breukelen et al. 1998, Hunter et a. 1998, Prommer et al. 1999a, 1999b, Brun et al. 2002). Large-scale semi-technical soil columns are of intermediate scale between small laboratory columns and field sites.

In contrast to numerous small laboratory column experiment simulations and field-site scale models there are a few references for large soil column experiments simulating river bank filtration (Drewes & Jekel 1996, NASRI 2003). The experiments performed by Drewes & Jekel (1996) dealt with the elimination of organic trace compounds under different redox conditions by evaluating only mass balances. Simulations of non-reactive tracer transport through large uniform and layered soil columns (column length of about 6 m) are Reported by (Porro et al. 1993a, 1993b). Reactive transport simulation within a large column is available from Phanikumar et al. (2002) who studied microbial-mediated degradation of chlorinated hydrocarbons. The goal of all these studies was to verify the observed breakthrough of contaminants using an problem adequate reaction framework.

2.3.1.2 Semi-technical soil column experiment

The experimental set-up of the large soil column ensemble is shown in PART 6. It consisted of 6 soil columns 5 m in length connected in line. Sampling was possible on 21 sampling points (5 points along the first column, 10 points along the adjacent columns, one point at the inlet, 4 points between the columns and one point on the outlet). Initially the column soil matrix was loaded by interstitial residual air over its whole length, and it took a time interval of about 10 months until this interstitial air was nearly completely removed from the column sections apart from the inlet (Figure 69). The new experiment started in April 2003 and is still ongoing. A decrease of the DOC concentration resulting from oxygen consumption due to

biodegradation was noticeable only near the inlet, while DOC concentrations were found nearly constant and independent of oxygen concentrations in the column sections apart from the inlet. The inorganic hydrochemistry sampled on the sample points along the length of the individual columns reflected the time variable composition of the sampled flushing surface water. A mineralogical analysis of the soil column material was not available, but from core analysis from different waterworks test sites in Berlin, a calcite content of 0.1 weight % was Reported. Thus a calcite content in the soil column matrix seems probable (cf. NASRI 2003). Detailed results are presented by Horner et. al. (2004).

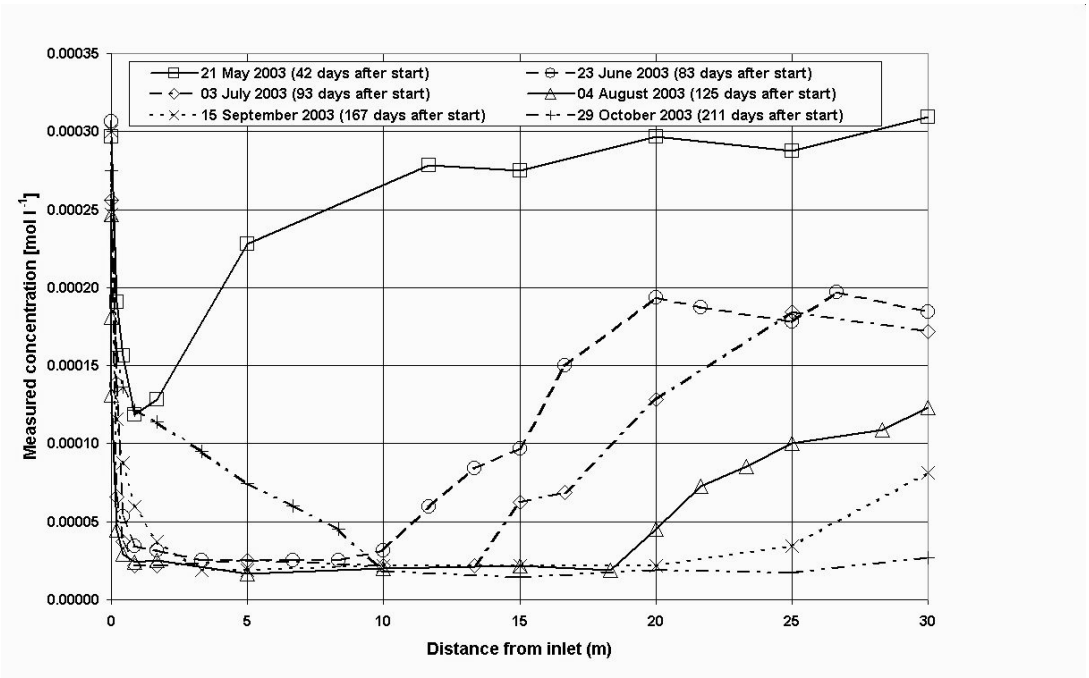

Figure 69 : Oxygen breakthrough during soil column flushing.

2.3.1.3 Basics of reactive transport

Brun & Engesgaard (2002) presented two approaches for modelling biodegradation: the singe step and the two step process model. The single step process models describe the biodegradation reaction as a geochemical reaction using a definite electron acceptor. Examples for single process models are presented by Kinzelbach et al. (1991), Lensing (1994), Schäfer et al. (1998a, 1998b), Abrams et al. (1998), and Abrams & Loague (2000). The two-step process models conceptualise the overall biogeochemical degradation as a fermentation process consuming available terminal electron acceptors depending on the actual redox state using a partial equilibrium approach for the redox half reactions. Only organic degradation is the rate-limiting process for two-step process models. Using the latter approach, a close coupling of biodegradation kinetics to inorganic hydrochemistry is

straightforward. Jakobsen & Postma (1999), Prommer et al. (1999a, 1999b) and Prommer (2002) used PHREEQE (Parkhurst et al. 1980) or PHREEQC (Parkhurst & Appelo 1999) as the geochemical equilibrator in the second (partial equilibrium) step. The reactive transport model presented here also follows this approach. The reactive multi-species transport is given by equation 1.

$$\frac{du_i}{dt} + v \cdot \nabla u_i - D \cdot \nabla(\nabla u_i) = ss_i \tag{1}$$

and for a solid species pi by equation 2

$$\left(\frac{\rho_b}{\theta}\right) \cdot \frac{dp_i}{dt} = ss_i \tag{2}$$

where v is the pore velocity (L/T), D is the hydrodynamic dispersion coefficient (L^2/T), ρ_b is the bulk density (M/L^3), and θ is the porosity. The source/sink term ss_i subsumes all external and internal sources and sinks, focussing on the chemical reactions (kinetics and/or chemical equilibrium). In general, the chemical reaction term is strongly non-linear. The aqueous total component concentration u_i results from the master species concentration c_i, and Nc concentration of complexed (or secondary) aqueous species and their stochiometric coefficients a_i derived from from the association reactions involving the master species (equation 3)

$$u_i = c_i + \sum_{j}^{N_c} (X_j \cdot a_j) \tag{3}$$

The complex concentrations Xj are calculated using the mass action relations derived from the master species concentrations and their equilibrium constants available from thermodynamic databases (Appelo & Postma 1996). The numerical solution of the reactive transport equation is made difficult by the different mathematical nature of the advective-dispersive subset (partial differential equation systems) and of the chemical reaction term (ordinary differential equation systems for kinetic terms and non linear algebraic equation systems for equilibrium reaction terms). Thus, an adequate strategy to solve the reactive transport equation results by coupling both subsets sequentially, e. g. by coupling MATLAB (The MathWorks 2003) as a powerful intrinsic solver for partial differential equation systems with PHREEQC. An external program such as PHREEQC can easily be called from the MATLAB environment so that a coupling of both transport and reaction subsets is simply performed (for details see Horner et al. 2004). Numerical errors inevitably result from the coupling procedure (operator splitting) due to the different time marching for the physical transport step and for the chemical speciation step (Herzer & Kinzelbach 1989, Engesgaard

& Kipp 1992, Walter et al. 1994, Barry et al. 2002). The numerical error introduced by the chemical perturbation can be minimized by internal iteration between the physical transport step and chemical speciation step during a time step, or by using small time steps if only one operator split per time step is performed. Based on the assumption of a local equilibrium for a given time step a constant mass balance including dissolved total concentration ui and solids pi (equation 4) will result

$$u_i^{before} + (\rho_b / \theta) \cdot p_i^{before} \equiv u_i^{after} + (\rho_b / \theta) \cdot p_i^{after} \quad (4)$$

where „before“ and „after“ denote the time before and after the reaction step. Computational load will increase dramatically by performing internal iterations. To limit the computational load, here the option of one operator split per time step was chosen.

2.3.2 Modelling

2.3.2.1 Conceptual model

From the previous developing of the column experiment difficulties result to provide reliable initial conditions over the whole column. As noted above, it is evident that the decrease in oxygen concentration in the column portions far from inlet does not correlate with the measured changes of DOC concentrations. There are two options to explain this observation

Continuous supply of DOC by dissolution of particular organic carbon over the whole column extent so that oxygen is consumed by biodegradation also in the inner portions of the column,

Or, if no particular organic carbon is available over the whole column extent, a continuous dissolution and flushing of oxygen from interstitial air implying a double-porosity approach in the inner column portions.

Close to the inlet, oxygen consumption can be attributed to preferential biodegradation as indicated by the decrease of both oxygen and DOC. In the inner part of the column, physical removal of oxygen bubbles was also chosen for model conceptualisation. The double porosity approach for oxygen was formulated as follows (equations 5a and 5b)

$$\frac{\partial M_{mobile}}{\partial t} = \theta_{mobile} \cdot R_{mobile} \cdot \frac{\partial C_{mobile}}{\partial t} = \alpha \cdot (C_{immobile} - C_{mobile}) \quad (5a)$$

$$\frac{\partial M_{immobile}}{\partial t} = \theta_{immobile} \cdot R_{immobile} \cdot \frac{\partial C_{immobile}}{\partial t} = \alpha \cdot (C_{mobile} - C_{immobile}) \quad (5b)$$

using the concentrations Cmobile and Cimmobile, the compartment porosities θmobile and θimmobile, the retardation coefficients Rmobile and Rimmobile, and the mobile-immobile exchange coefficient α, as outlined by (Parkhurst & Appelo 1999). As the first numerical test

runs showed, the biodegradation reaction front movement near the inlet was considerably slowed in relation to the apparent flow velocity determined from tracer experiments performed in the column (NASRI 2003) so that sorption had to be considered as an additional process. Sorption was conceptualised using the Freundlich approach

$$Q_{orgc} = k_f \cdot (C_{orc})^{nex} \quad (6)$$

with the concentration of sorbed organic carbon Q_{orgc}, the distribution coefficient k_f, and an empirical exponent n_{ex}.

Two differently reactive fractions of DOC as indicated by chromatographic analysis (NASRI, 2003) were considered using individual rate constants λ_1 and λ_2 (indicated using j in equation 7)

$$\frac{\partial C_{orgc,j}}{\partial t} = -\lambda_j \cdot C_{orgc,j} \quad (7)$$

of the biodegradation kinetics following a simple first-order approach. As a consequence of different rate constants, the refractory or less reactive DOC fraction can be expected to prevail far from the inlet.

Only scarce information was available about the matrix composition of the column aquifer. Because surface water from Lake Tegel (Berlin) used to flush the column is Reported to be saturated/over saturated with respect to calcite (cf. NASRI 2003), and aquifer material sampled below the groundwater surface along the Lake Tegel test site has calcite contents within a magnitude order of 0.1 weight % (NASRI 2003), the calcite equilibrium was included in the reaction framework. Iron and manganese oxides/hydroxides also are to be expected in trace amounts. They were included in reactive transport modelling as solids in order to be able to model also anaerobic redox conditions if all oxygen has been consumed during flushing.

2.3.2.2 Discretisation and parameterization

The soil column was modelled as a 1D finite-difference domain. In detail, the physical parameters of the model domain are listed in Table 10. The pore velocity was specified as confirmed by tracer tests (NASRI 2003). A simulation time of 587 d was set up for the model simulation (i.e. the time interval ranging from April 2003 to November 2004, for which measurements were available). The chemical species considered by the reactive transport model, and their initial and boundary conditions are listed in Table 11. As a first approximation, the initial and inflow concentrations were specified using the mean values

sampled along the column system and for the surface water (NASRI 2003). By assuming oxic conditions at the start of the simulation, nitrogen, ammonium, methane and sulphide concentration were set to zero, but included as species to provide possible redox half reactions if anaerobic or anoxic conditions are achieved during biodegradation. Initial and boundary concentration conditions were equilibrated using PHREEQC (Parkhurst & Appelo 1999). At each simulation time, the reactive transport model requires a local charge balance. Initial solution and inflow solution ion charge balances were achieved by modification of Cl^- or alternatively of Na^+ concentrations (cf. Table 11). Except for oxygen, the inflow was modelled as a fixed time-constant concentration boundary. For oxygen, time-variable inflow concentrations had to be specified that reflected the experimental implications about the real inflow conditions as good as possible in order to verify the observed breakthrough. As the most important solid buffering pore solution hydrochemistry calcite was included. During the simulation, solution charge balance was achieved by adapting the actual pH, in contrast to the speciation of the initial and influx concentrations.

Table 10 Discretisation and physical parameters used for the semi-technical soil column simulation.

Parameter	Unit	Value
Length of column	m	30.0
Spatial discretisation interval	m	0. 50
Time step length	d	0.25
Final solution time	d	211
Pore velocity	$m\ d^{-1}$	1.0
Dispersivity	m	0.1
Effective porosity	-	0.25
Bulk density	$kg\ dm^{-3}$	1.80

Table 11 Initial and boundary conditions: chemical parameters and concentrations (NASRI 2003)

Parameter	Unit	Initial	Boundary inflow
Temperature	°C	20	20
pH	-	7.56	7.89
pe	-	13.5	13.2
O_2 (mobile)	mol l^{-1}	$3.0x10^{-4}$	See Table 3
O_2(immobile)	mol l^{-1}	$3.0x10^{-4}$	0.0
Cl^-	mol l^{-1}	$1.0x10^{-3}$	$8.1x10^{-4}$
NO_3-N	mol l^{-1}	$2.0x10^{-4}$	$2.0x10^{-4}$
N_2-N	mol l^{-1}	$1.0x10^{-12}$	0.0
NH_4-N	mol l^{-1}	$1.0x10^{-12}$	0.0
Ca	mol l^{-1}	$1.36x10^{-3}$	$1.99x10^{-3}$
Na	mol l^{-1}	$4.67x10^{-3}$	$1.0x10^{-3}$
HCO_3^-	mol l^{-1}	$3.36x10^{-3}$	$9.92x10^{-4}$
C(-4) , as CH_4	mol l^{-1}	$1.0x10^{-12}$	0.0
DOC (reactive)	mol l^{-1}	$1.0x10^{-8}$	See Table 3
DOC (refractory)	mol l^{-1}	$1.0x10^{-8}$	See Table 3
OC particulary	mol l^{-1}	0.0	0.0
SO_4^{2-}	mol l^{-1}	$1.5x10^{-3}$	$1.5x10^{-3}$
HS^-	mol l^{-1}	0.0	0.0
Calcite	mol l^{-1}	$9.6x10^{-3}$	0.0

Table 12 Specified time variable boundary conditions: chemical parameters and concentrations

Parameter	Unit	Time interval (d)	Boundary inflow
O_2 (mobile)	mol l^{-1}	0-50	$2.0x10^{-4}$
		50.25-146	$1.0x10^{-4}$
		146.25-220	$2.0x10^{-4}$
		220.25-350	$1.5x10^{-4}$
		350.25-400	$5.0x10^{-5}$
		400.25-587	$3.2x10^{-5}$
DOC (reactive)	mol l^{-1}	0-50	$2.0x10^{-4}$
		50.25-146	$2.0x10^{-4}$
		146.25-220	$2.0x10^{-4}$
		220.25-350	$2.0x10^{-5}$
		350.25-400	$2.0x10^{-5}$
		400.25-587	$2.0x10^{-5}$
DOC (refractory)	mol l^{-1}	0-50	$3.0x10^{-4}$
		50.25-146	$3.0x10^{-4}$
		146.25-220	$3.0x10^{-4}$
		220.25-350	$3.3x10^{-4}$
		350.25-400	$3.3x10^{-4}$
		400.25-587	$3.9x10^{-4}$

Table 13 most adequate combination of kinetic, sorptive and exchange parameters used to simulate the column experiment.

Parameter	Unit	Value
Retardation coefficient mobile O_2	-	1.0
Retardation coefficient immobile O_2	-	4.2
Exchange coefficient mobil-immobil	-	0.1
Porosity mobile (θ_{mobile})	-	0.3
Porosity immobile ($\theta_{immobile}$)	-	0.1
Sorption coefficient (k_f)	-	4.8
FREUNDLICH exponent (n_{ex})	-	0.99
Decay rate constant λ_1	d^{-1}	1.5×10^{-3}
Decay rate constant λ_2	d^{-1}	1.0×10^{-10}
Decay rate constant λ_3	d^{-1}	1.5×10^{-3}

2.3.3 Results and discussion

In summary, sensitive parameters influencing model calibration are the kinetic and sorption parameters of the organic carbon fractions and the double porosity exchange parameters for oxygen. Optimization as included as tools within the MATLAB software package was not performed because of the implications of the externally accessed PHREEQC module. By multiple simulation runs the combination of kinetic, sorption and exchange parameters were extrapolated. Table 12 gives the most adequate parameter combination resulting from these multiple runs to verify the sampled breakthrough. The simulation results are shown as breakthrough curves in Figure 70 – Figure 74 providing the simulation results for oxygen in relation to the sampled oxygen breakthrough. They generally illustrate that using the conceptual model set up a quite good match of measured and modelled oxygen breakthrough can be achieved. Figure 74 depicts the flushing stage when oxic conditions were forced to change to anoxic conditions. Here the simulation reacts faster (dropping the oxygen concentration to zero) than available from the measurement.

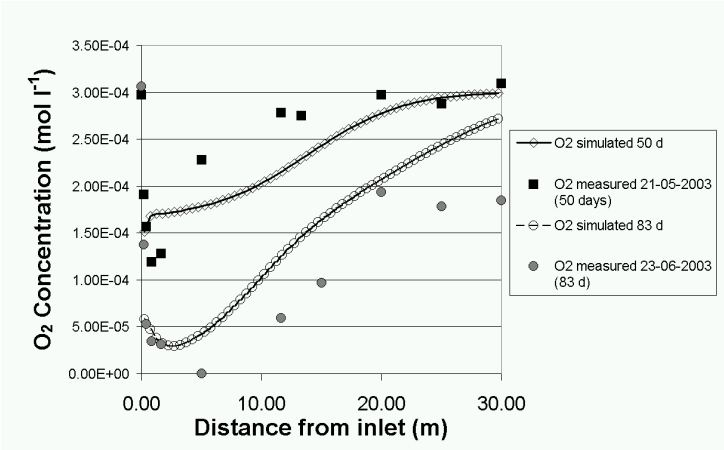

Figure 70 Measured and simulated Oxygen breakthrough during soil column flushing (1)

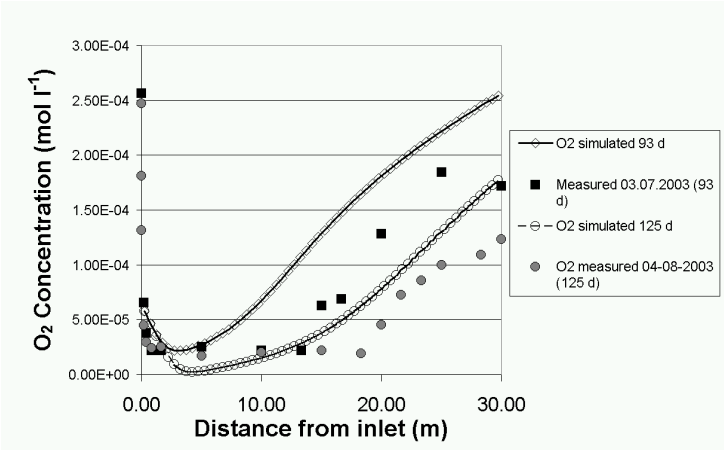

Figure 71 Measured and simulated Oxygen breakthrough during soil column flushing (2)

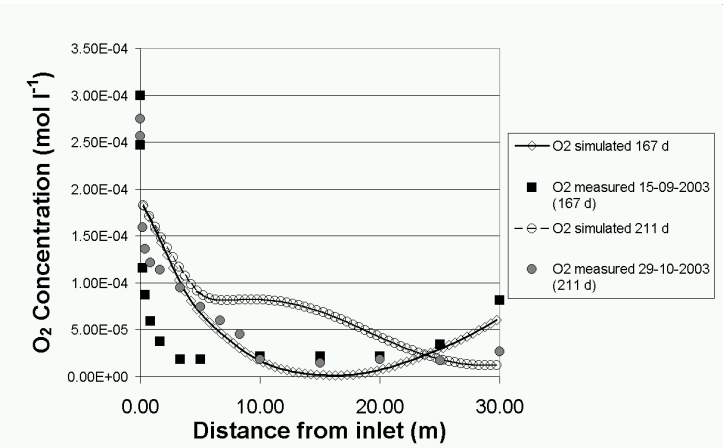

Figure 72 Measured and simulated Oxygen breakthrough during soil column flushing (3)

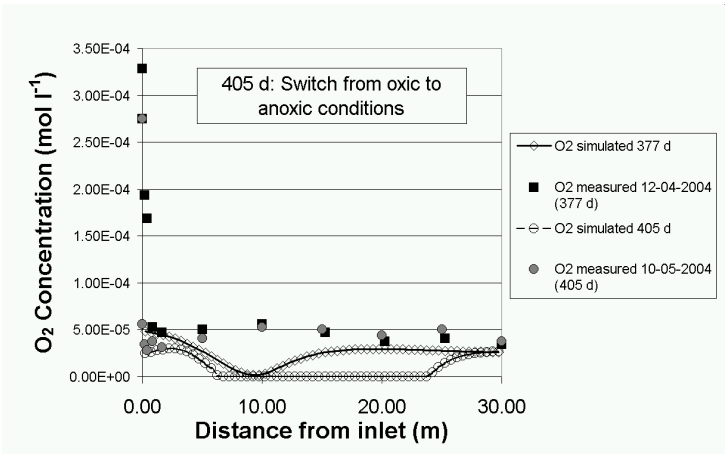

Figure 73 Measured and simulated Oxygen breakthrough during soil column flushing (4)

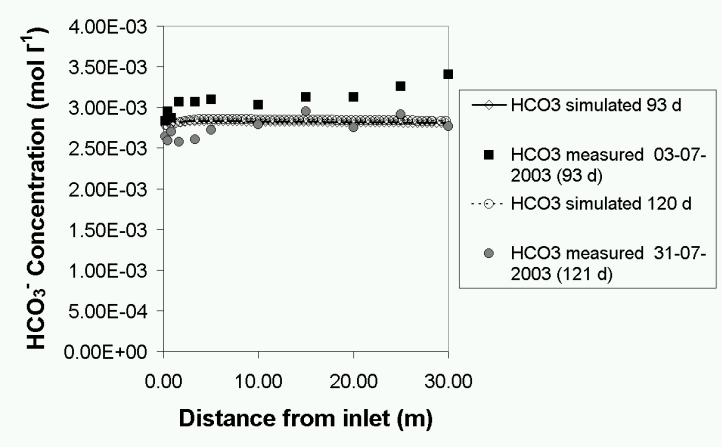

Figure 74 Measured and simulated Oxygen breakthrough during soil column flushing (5)

The verification of the pore water hydrochemistry - here shown in terms of HCO_3^- ,pH and Ca (Figs. Figure 75 -Figure 80) - confirms that mainly the calcite equilibrium is critical for the sampled pore water hydrochemical composition as conceptualised by the reaction framework set up. Differences between simulation results and measurements may reflect variable hydrochemical composition of the applied surface water as available from the NASRI Database and uncertainty about the initial pore water chemistry. Other minerals able to act as electron acceptors such as Pyrolusite (MnO_2) and Ferrihydrite ($Fe(OH)_{3,\ amorphous}$), are confirmed to not by model simulation the be consumed by biodegradation. By measurement, only low Mn concentrations of $1x10^{-7}$ to $3x10^{-6}$ mol l^{-1} were found in the pore solution under anoxic conditions (NASRI Database) indicating some activation of Pyrolusite as terminal electron acceptor during biodegradation.

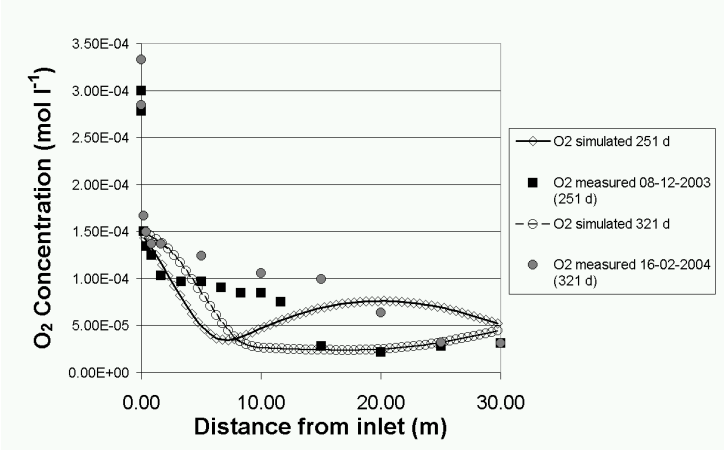

Figure 75 Measured and simulated HCO_3^- breakthrough during soil column flushing (1)

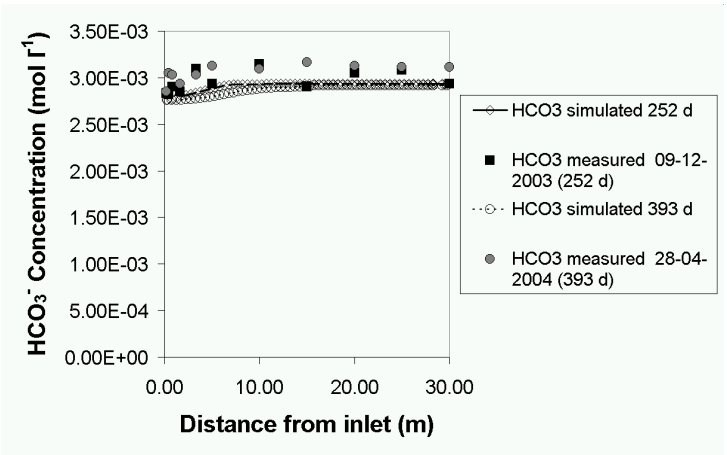

Figure 76 Measured and simulated HCO_3^- breakthrough during soil column flushing (2)

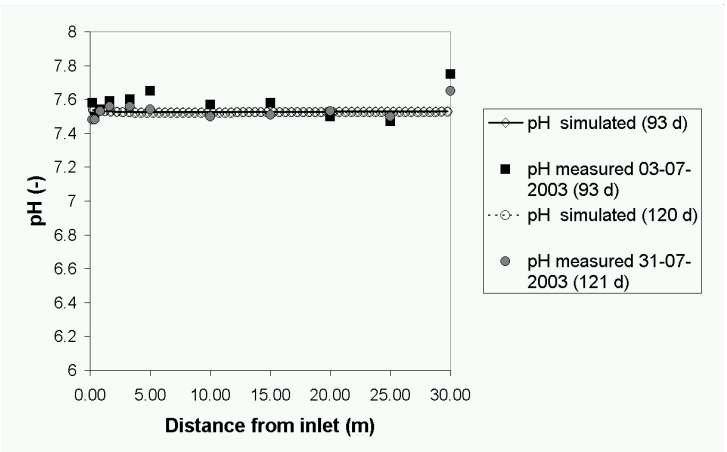

Figure 77 Measured and simulated pH breakthrough during soil column flushing (1)

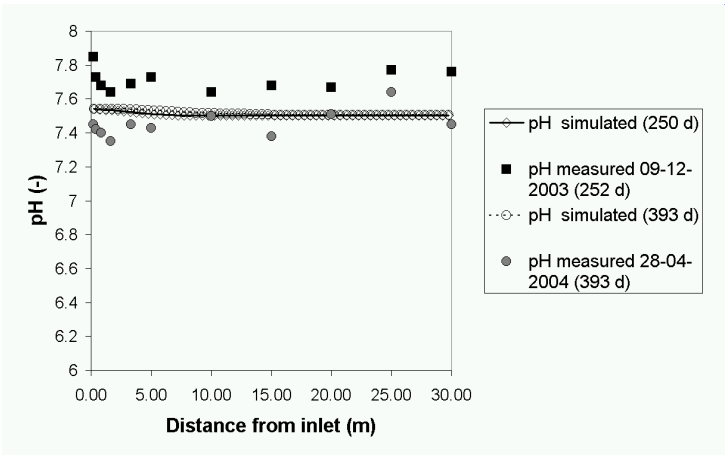

Figure 78 Measured and simulated pH breakthrough during soil column flushing (2)

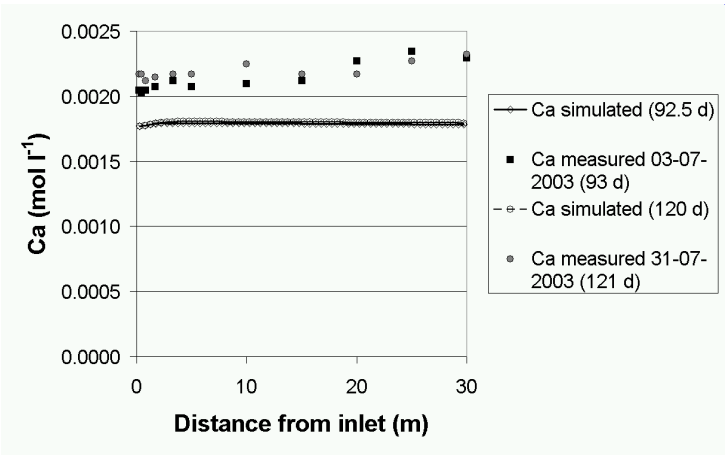

Figure 79 Measured and simulated Ca breakthrough during soil column flushing (1)

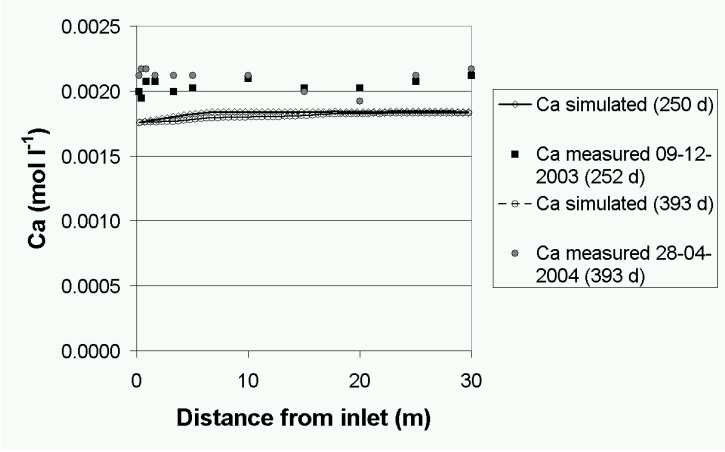

Figure 80 Measured and simulated Ca breakthrough during soil column flushing (2)

2.3.4 Major conclusions and summary

Based on a conceptual model, which includes biodegradation and sorption of differently reactive organic carbon species, a double porosity approach for residual oxygen and hydrogeochemical speciation, a large soil column flushing experiment was simulated by reactive transport modelling. The conceptual model accounts for a biodegradation kinetics approach for DOC and a chemical equilibrium approach to model the geochemical response on biodegradation. The applied numerical reactive transport model combines a MATLAB tool (to solve the advection-dispersion PDE, the double porosity exchange term for oxygen and the sorption term for DOC) and a PHREEQC module as solver for chemical equilibrium and biodegradation kinetics and has proven to verify the observed breakthrough of oxygen, DOC and inorganic hydrochemistry. In summary, the assessment of the simulation results must reflect the data uncertainties among the soil matrix composition (trace minerals and biomass resulting from older experiments), variable inflow hydrochemistry (due to technical implications and to seasonal variable composition of the infiltrated surface water), and the fate of the column before starting the actual flushing experiment. The simulation results are applicable to the issue of riverbank filtration waterworks test sites in Berlin characterized by a particular unsteady pumping regime.

2.3.5 References

AMIRBAHMAN, A., SCHÖNENBERGER, R., FURRER, G. & ZOBRIST, J. (2003): Experimental study and steady-state simulation of biogeochemical processes inlaboratory columns with aquifer material. J. Contam. Hydrol., 64., 123-125.

APPELO, C. A. J., V., POSTMA, D. (1996): Geochemistry, groundwater and pollution. Balkema, Rotterdam.

APPELO, C. A.J., VERWEIJ, E., SCHÄFER, H. (1998): A hydrogeochemical transport model for an oxidation experiment with pyrite/calcite/exchangers/organic matter containing sand. Appl. Geochemistry, 13., 257-268.

BARRY, D. A., PROMMER, H., MILLER, C. T., ENGESGAARD, P., BRUN, A., & ZHENG, C. (2002): Modelling the fate of oxidable organic contaminants in groundwater. Adv. Water Resour., 25., 945-983.

VAN BREUKELEN, B. M., APPELO, C. A. J., OOLSTHOORN, T. N. (1998): Hydrogeochemical modelling of 24 years of Rhine water infiltration in the dunes of the Amsterdam water supply. J. Hydrol., 209., 281-296.

BRUN, A., ENGESGAARD, P. (2002): Modelling transport and biogeochemical processes in pollution plumes: literature review and model development. J. Hydrol., 256., 211-227.

BRUN, A., ENGESGAARD, P., & ROSBJERG D. (2002): Modelling transport and biogeochemical processesin pollution plumes: Vejen lanfill, Denmark. J. Hydrol., 256., 228-247.

DREWES, J. E., & JEKEL, M. (1996): Simulation of groundwater recharge with advanced treated wastewater. Wat. Sci. Tech., 33 (10-11), 409-418.

VON GUNTEN, U., & ZOBRIST, J. (1996): Biogeochemical changes in groundwater-infiltrating systems: column studies. Geochim. Cosmochim. Acta, 57., 3895-3906.

HERON, G., CHRISTENSEN, T. H., & TJELL J. C. (1996): Oxidation capacitiy of aquifer sediments. Environ. Sci. Technol., 29., 187-192.

HERZER, H., & KINZELBACH, W. (1989): Coupling of transport and chemical processes in numerical transport models. Geoderma, 44., 115-127.

HOLZBECHER, E., MASSMANN, G., HORNER, CHR., PEKDEGER, A. (2001): Redox processes in the Oderbruch Aquifer. In: GEHRELS, H., PETERS, N. E., HOEHN, E., JENSEN, K., LEIBUNDGUT, C., WEBB, B., & ZAADNOORDLIJK, W. J. (eds.): Impact of Human activity on Groundwater Dynamics), (Sixth Scientific Assembly of the IAHS, Maastricht, the Netherlands, July 2001) , IAHS Publication 269, IAHS Press, Wallington, UK, 229-238.

HOLZBECHER, E., HORNER, CHR. (2003): A reactive transport model for redox components – verification of transport and test of field data. In: SCHULTZ, H. D., & HADELER, A. (eds.): GeoProc 2002 Geochemical Processes in Soil and Groundwater, Wiley–VCH Verlag GmbH Co. KgaA, Weinheim, Germany, 414-433.

HORNER,CHR., HOLZBECHER, E. &NÜTZMANN, G. (2004) : A Coupled Transport and Reaction Model for long Column Experiments simulating Bank Filtration. Hydrological Processes (in print).

HUNTER, K. S., WANG, Y., VAN CAPPELLEN, P. (1998): Kinetic modelling of microbially-driven redox chemistry of subsurface environments: coupling transport, microbial metabolism and geochemistry. J. Hydrol., 209, 53-80.

JAKOBSEN, R., & POSTMA, D. (1999): Redox zoning, rates of sulfate reduction and interaction with Fe-reduction and methanogenesis within a shallow sandy aquifer. Geochim. Cosmochim. Acta, 63, 137-151.

KINZELBACH, W., SCHÄFER, W., & HERZER, J. (2004): Numerical modelling of natural and enhanced denitrification in aquifers. Water Resour. Res. 27 (6)., 1123-1135.

LENSING, H. J., VOGT, M., & HERRLING, B. (1994): Modelling of of biological mediated redox processes in the subsurface. J. Hydrol., 159, 125-43.

MASSMANN, G (2001): Infiltration of river water into the groundwater – investigation and modeling of hydraulic and geochemical processes during bank filtration in the Oderbruch, Germany. Dissertation zur Erlangung des Doktorgrades des Fachbereichs Geowissenschaften der Freien Universität Berlin. Dissertation.de, Verlag im Internet., Berlin.

NASRI, (2003): Natural and Artificial Systems for Recharge and Infiltration, 1st NASRI Report. Kompetenzzentrum Wasser, Berlin.

PHANIKUMAR, M. S., HYNDMAN, D. D., WIGGERT, D. C., DYBAS, M. J., WIGG, M. W., & CRIDDLE, C. S. (2002):): Simulation of microbial transport and carbon tetrachloride biodegradation in intermittently-fed aquifer columns. Water Resour. Res., 38 (4)., 1-13.

PARKHURST, D. L., THORSTENSON, D. C., & PLUMMER, L. N. (1980): PHREEQE – a computer program for geochemical calculations. U.S. Geological Survey Water-Resources Investigation Report 80-96, Denver, Co., U. S. A., pp 195.

PARKHURST, D. L., & APPELO, C. A. J. (1999): User's Guide to PHREEQC (Version 2) – a computer program for speciation, batch-reaction, one-dimensional transport, and inverse geochemical calculations. U.S. Geological Survey Water-Resources Investigation Report 99-4259, Denver, Co., U. S. A., pp 312.

PORRO, I., WIERENGA, P. J., HILLS, R. G. (1993a): Solute transport through large uniform and and layered soil columns. Water Resour. Res., 29 (4), 1321-1330.

PORRO, I., WIERENGA, P. J. (1993b): Solute transport through large unsaturated soil column. Groundwater., 31 (2), 193-200.

PROMMER, H., BARRY, D. A. & DAVIS, G. B. (199a): A one-dimensional reactive multi-component transport model for biodegradation petroleum hydrocarbons in groundwater. Environ. Model. Softw., 14, 213-233.

PROMMER, H., DAVIS, G. B. & BARRY, D. A. (199b): Geochemical changes during biodegradation of petroleum hydrocarbons: field investigations and biogeochemical modelling. Org. Geochem., 30, 423-435.

PROMMER, H. (2002): A reactive multicomponent transport model for saturated porous media. Draft of user's manual version 1.0, contaminated land assessment and remediation research centre, the university of Edinburgh (available from http://www.pht3d.org)

SCHÄFER, D., SCHÄFER, W., & KINZELBACH W. (1998a): Simulation of reactive processes to biodegradation in aquifers, 1 structure of the three-dimensional reactive transport model . J. Contam. Hydrol., 31., 167-186.

SCHÄFER, D., SCHÄFER, W., & KINZELBACH W. (1998b): Simulation of reactive processes to biodegradation in aquifers, 2. model application to a column study on organic carbon degradation. J. Contam. Hydrol., 31., 187-209.

THE MATHWORKS (2003): MATLAB, The language of technical computing (Version 6). The MathWorks Inc. 3 Aple Hill drive, Natick, MA 01760-2098, U.S.A.

WALTER, A. L., FRIND, E. O., BLOWES, D. W., PTACEK, C. J., & MOLSON, J. W. (1994): Modelling of multicomponent reactive transport in groundwater 1. model development and evaluation. Water Resour. Res., 30 (11), 3137-3148.

2.4 Modelling of enclosure experiments: microcystin and bacteriophages

2.4.1 Methods: Inversion Modules VisualCXTFIT and MATLAB®

For inverse modelling two different software tools, VisualCXTFIT and MATLAB®, are applied corresponding to the inversion of different parameters in two steps. Modelling is based on the general transport equation, a partial differential equation for the unknown fluid phase concentration *c*:

$$\theta R \frac{\partial c}{\partial t} = \nabla \mathbf{D} \nabla c - \mathbf{v} \nabla c - \theta R \lambda c \qquad (1)$$

with the parameters: porosity θ, retardation R, dispersion tensor **D**, Darcy-velocity **v** and degradation rate λ. For column or enclosure experiments it is common to make the assumption that flow can be treated as one-dimensional. Then the transport equation can be formulated in a simpler form:

$$R \frac{\partial c}{\partial t} = \frac{\partial}{\partial x} \alpha_L u \frac{\partial c}{\partial x} - u \frac{\partial c}{\partial x} - \lambda R c \qquad (2)$$

with longitudinal dispersivity α_L and interstitial 'real' flow velocity u. Altogether there are four parameters: α_L, u, R and λ. Instead of u one may use the porosity $\theta = v/u$ as parameter, because the Darcy-velocity v is given implicitly by the applied flow rate. In the literature one often finds the combination $\mu = \lambda R$ used in estimation runs, for example in CXTFIT (1995). The first two of the four parameters are species independent, the latter two are usually species dependent. The first two parameters can be best obtained from tracer experiments, because for tracers the 1D transport equation reduces to:

$$\frac{\partial c}{\partial t} = \frac{\partial}{\partial x} \alpha_L u \frac{\partial c}{\partial x} - u \frac{\partial c}{\partial x} \qquad (3)$$

Within the project the inversion procedure was divided into two steps. In the first step species-independent parameters are determined from the tracer experiments, followed by the second step for the remaining parameters for each specie separately:

Determination of velocity u and dispersivity α_L from tracer experiments

Determination of retardation R and degradation rate λ from experiments with non-tracers

Step (1) was performed using VisualCXTFIT, which is a graphical user interface (GUI) for the CXTFIT code for parameter estimation. CXTFIT was developed at the U.S. Salinity Laboratories (Toride *et al*., 1995) and is based on analytical solutions of the 1D transport equation. Analytical solutions have the advantage that direct solutions of the differential equation have no problems with discretization errors, as they appear in numerical solutions. On the other hand analytical solutions exist only for specific conditions and can not be given for general boundary and initial conditions. However for the given experimental set-up in the enclosures as well as in the columns it was possible to use CXTFIT.
The VisualCXTFIT user interface for CXTFIT was developed within the NASRI project. An EXCEL-Add-in is produced, which allows the input and manipulation of measured data, as well as the specification of the inversion parameters and options. Moreover a graphical representation of the results is produced in the EXCEL sheet. Detailed descriptions as well as application examples are given by Nützmann *et al*. (2005).
Step (2) was performed using a newly developed tool for parameter inversion, written as m-file module in MATLAB® (2002). The module has been used for inversions of transport processes only, but could be used for other applications as well. The MATLAB® module works also for the inversion of temperature time series. For such an application the module is described in detail by Holzbecher (2005).

Within the MATLAB® module direct simulations of the transport equation are performed. The direct solution is obtained by using the 'pdepe'-solver, which is part of core MATLAB®. The direct solver is called within an inversion procedure, which is based on the MATLAB® optimization module. There various options, concerning the search algorithm and the numerical parameters can be specified.

In the module the user can specify the parameters, which are to be estimated. Within the automatic inversion procedure it is attempted to modify the selected parameters from their start values, in order to obtain a better fit with the remaining time-series in the input-data set. The objective function is sum of the squares of the deviations between measured and modelled values, what is usually known as least squares optimization. Parameters, not selected for the estimation procedure, remain on their starting value.

As input the MATLAB® inversion module requires time series, measured at least at two positions along the flow path. The first time series, given in the input data-set, is treated as a boundary condition; the other time series are used for the parameter estimation procedure. When several time-series are given there is the additional option to estimate parameters from various possible estimation intervals. For example, in case of three time series, the first can be treated as boundary condition, user either the second, or the second and the third for the estimation. Moreover, the second time series can be used as boundary condition, in

order to use the third for the estimation. In that way it is possible to obtain an impression of the variability of the parameters with the spatial intervals.

For each estimation run, MATLAB® finally produces a plot, visualizing the following:

- Measurements used as boundary conditions (one time series)
- Measurements used for parameter estimation
- Modelled concentration curve based on best-fit parameters

In the estimation runs for the enclosures, slow sand filters and column experiments, performed during the NASRI project, it turned out that the automatic inversion procedure did not deliver optimal results. The problem is well-known, as the algorithms find local minima of the objective function, which are not necessarily global minima. When the user suspects that the automatic solver has not found the global minimum yet, the algorithm is usually re-started again with a new starting set, which differs both from the obtained local minimum parameter set and from the previous starting values. Such 'fine-tuning' was required in almost all Reported simulations.

Moreover the comparison of parameter values, obtained for different spatial intervals (as described above) mostly revealed substantial differences. It can be concluded that parameters are obviously not constant, but change with space. A more detailed description, concerning phage transport in the enclosures, is presented by Holzbecher *et al*. (2005).

2.4.2 Results

2.4.2.1 Microcystin

The following figures show best fit results for enclosure experiments E2 and E3 for different parts of the flow path. Depicted are

- Measured concentrations at 1. position of concerned spatial interval, here denoted as 'inlet' (diamonds with scale on the right); used as boundary condition for inverse modelling
- Measured concentrations at 2. position of concerned spatial interval, here denoted as 'outlet' (crosses with scale on the left); used for objective function in inverse modelling
- Modelled concentrations at 2. position (line with scale on the left); simulated using best-fit parameter values.

Shown in the figure are also: velocities v and longitudinal dispersivities α_L, obtained form inverse modelling using VisualCXTFIT as well as retardation R and degradation rate λ, obtained form MATLAB® inverse modelling.

The intervals along the flowpath are denoted by 1->2, when the concentration in the input reservoir is taken as boundary condition, and the concentration at 20 cm depth for the

parameter estimation. In the analogous manner the other spatial intervals are denoted as: 2->3, 3->4, 4->5 and 5->6.

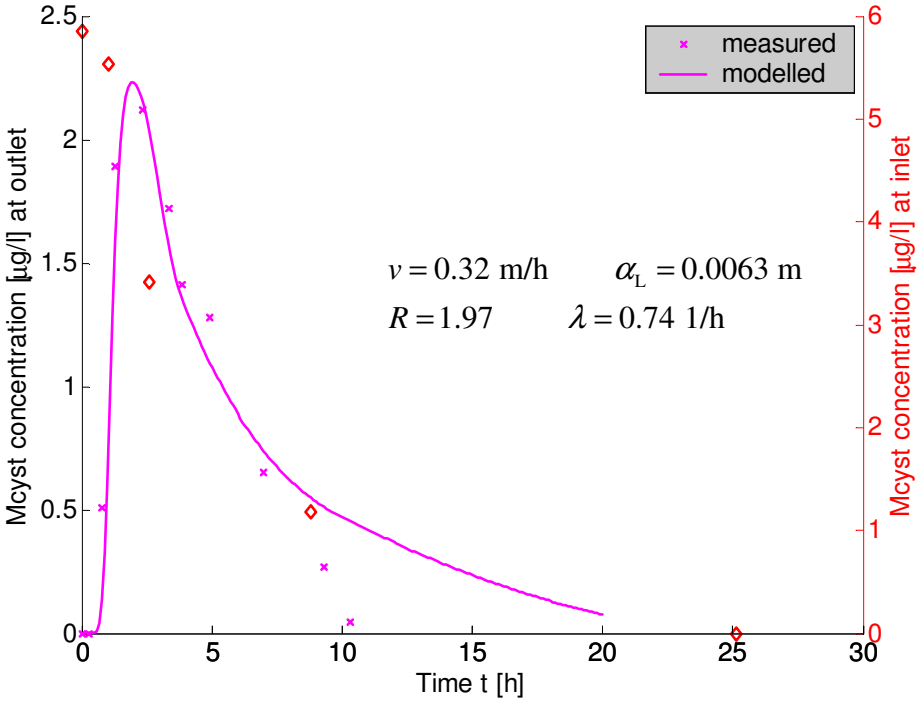

Figure 81 Inverse modelling result for EN2, 1->2

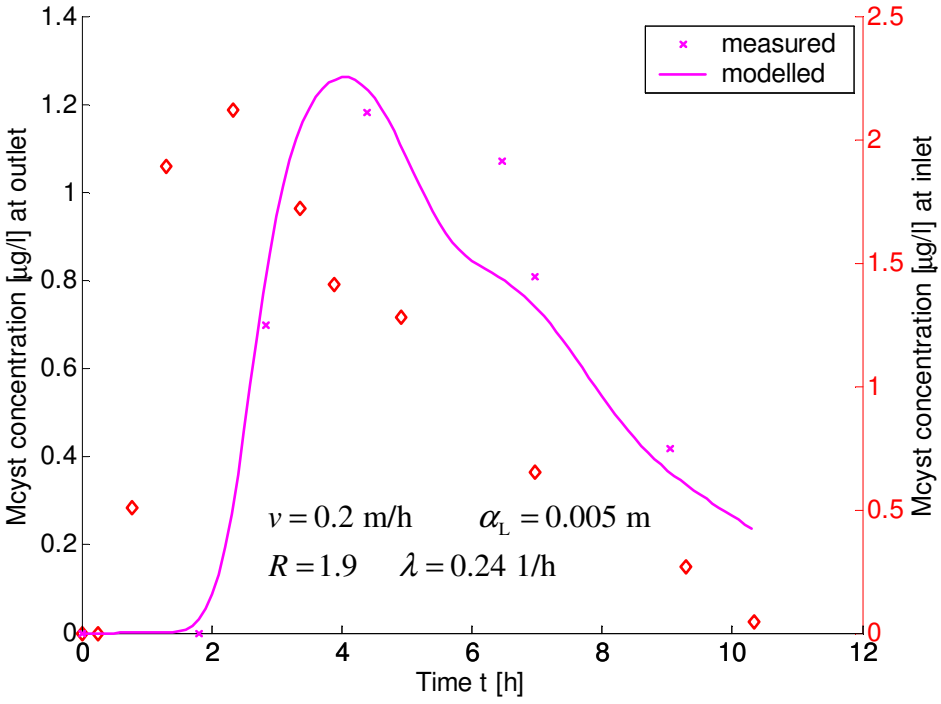

Figure 82 Inverse modelling result for EN2, 2->3

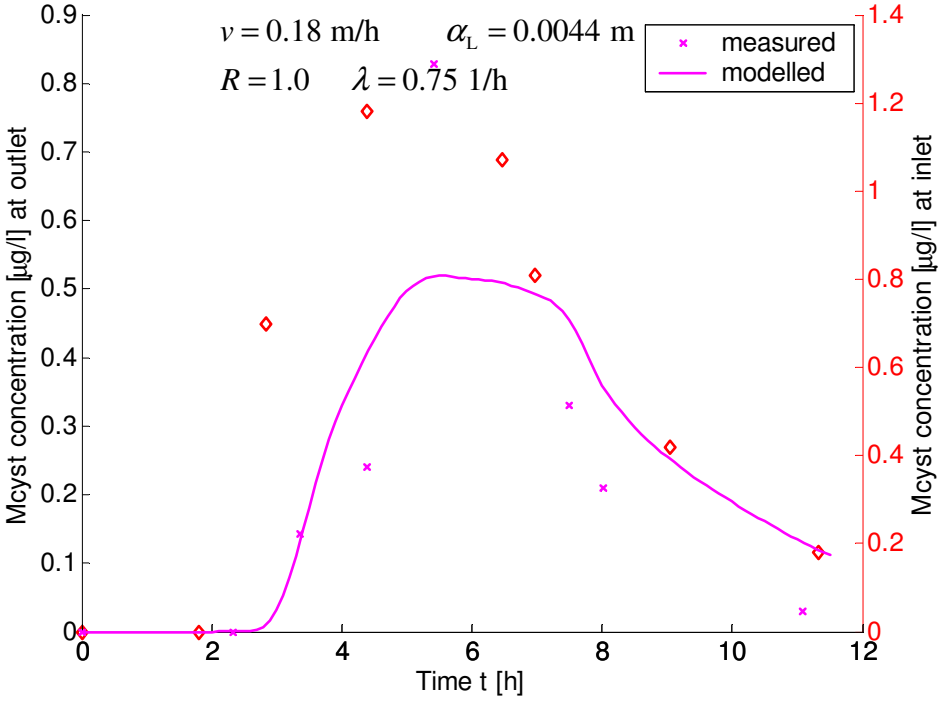

Figure 83: Inverse modelling result for EN2, 3->4

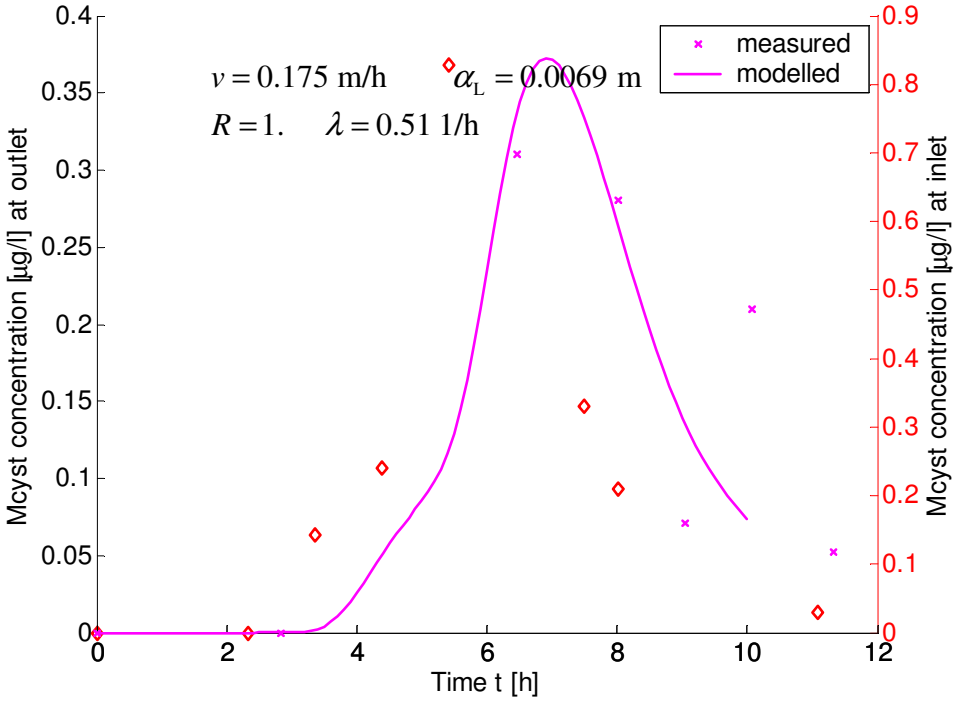

Figure 84 Inverse modelling result for EN2, 4->5

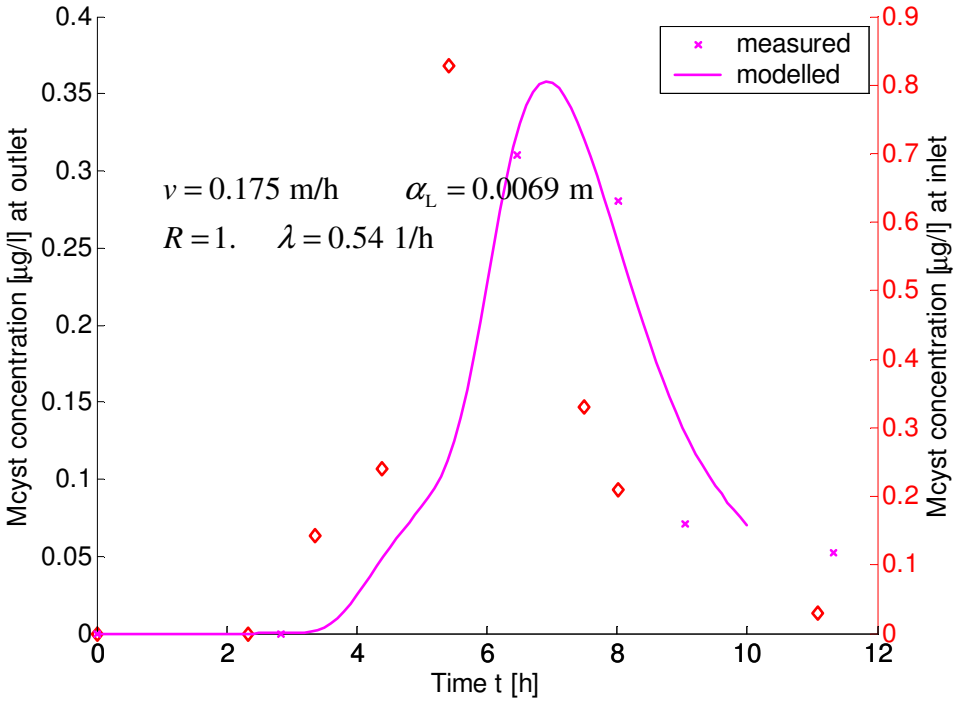

Figure 85 Inverse modelling result for EN2, 4->5; without outlier

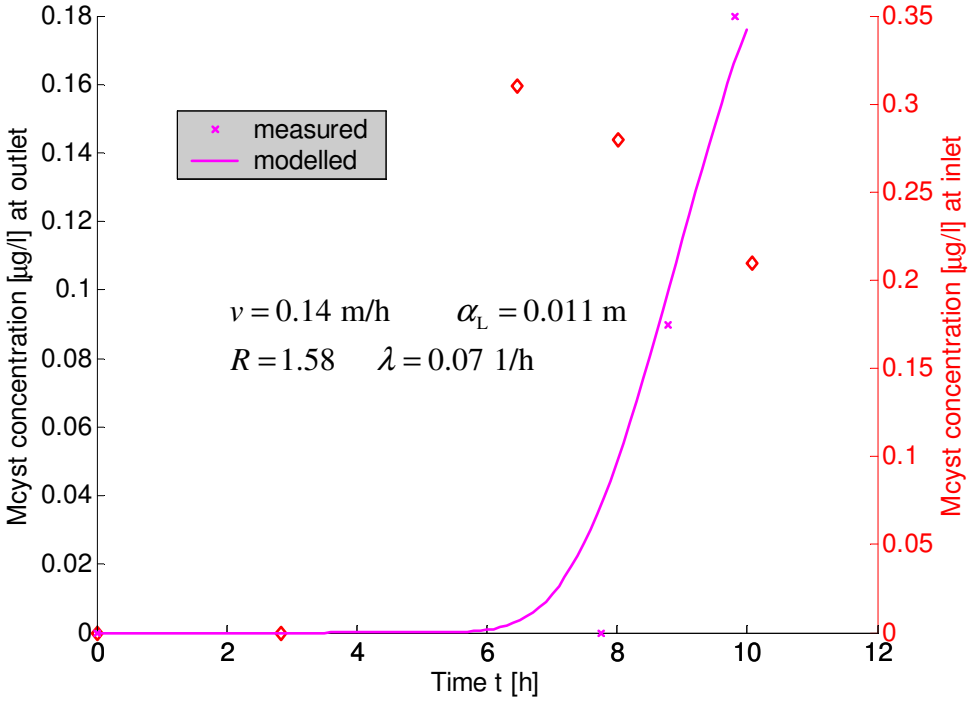

Figure 86 Inverse modelling result for EN2, 5->6

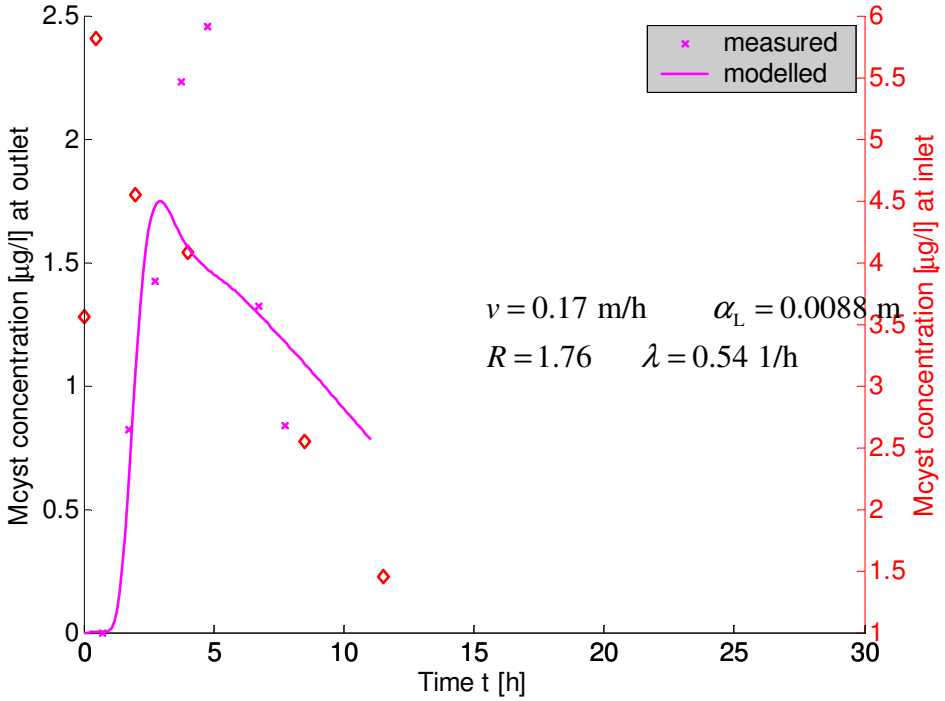

Figure 87: Inverse modelling result for EN3, 1->2

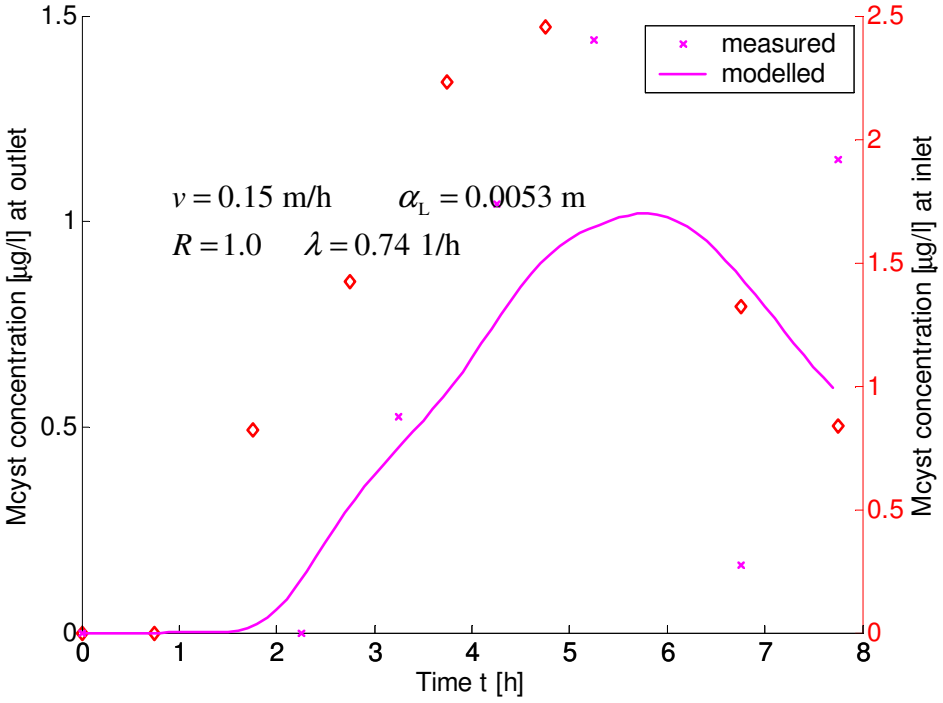

Figure 88 Inverse modelling result for EN3, 2->3

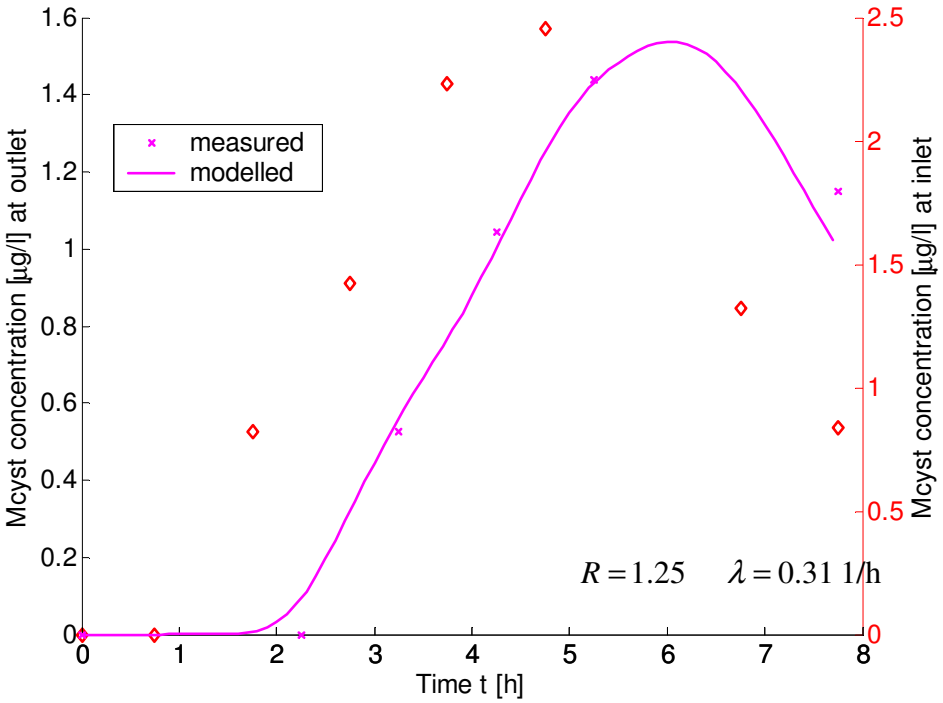

Figure 89 Inverse modelling result for EN3, 2->3, without outlier

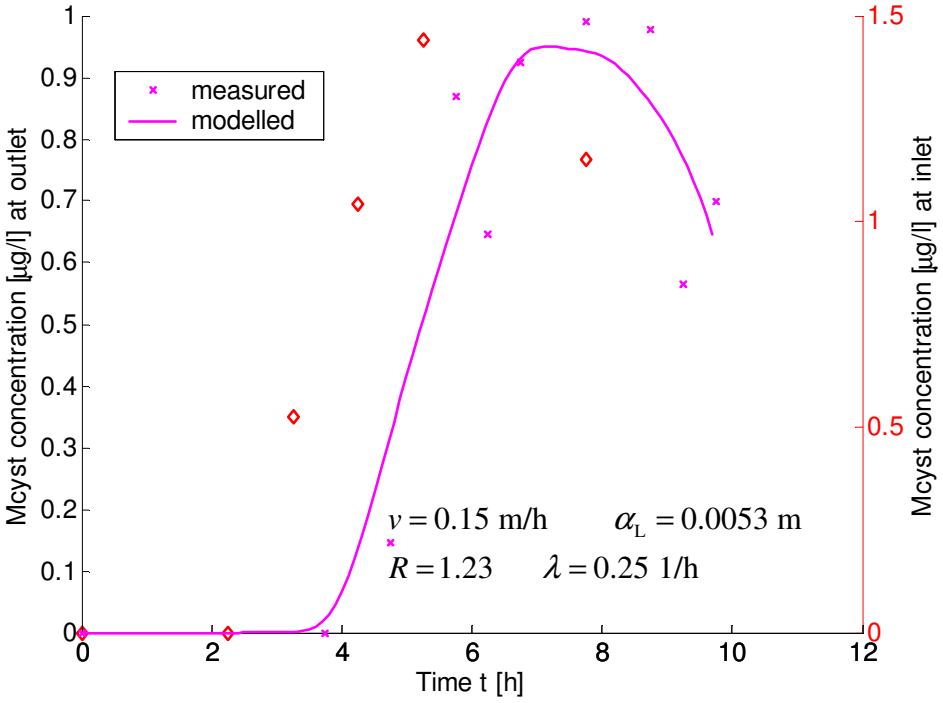

Figure 90 Inverse modelling result for EN3, 3->4

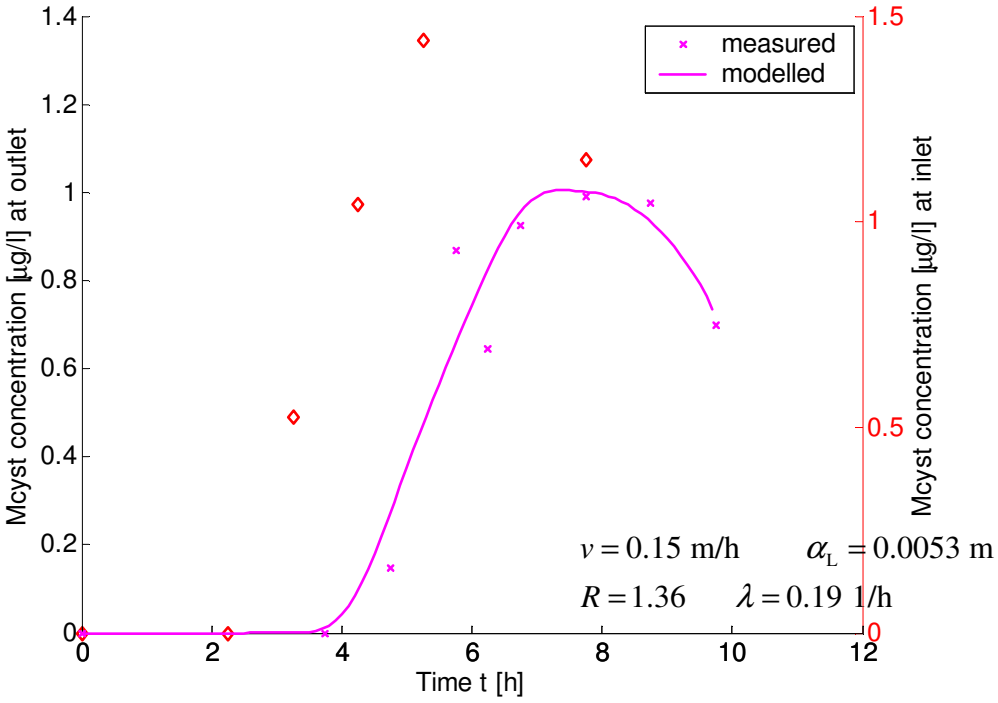

Figure 91 Inverse modelling result for EN3, 3->4, without outlier

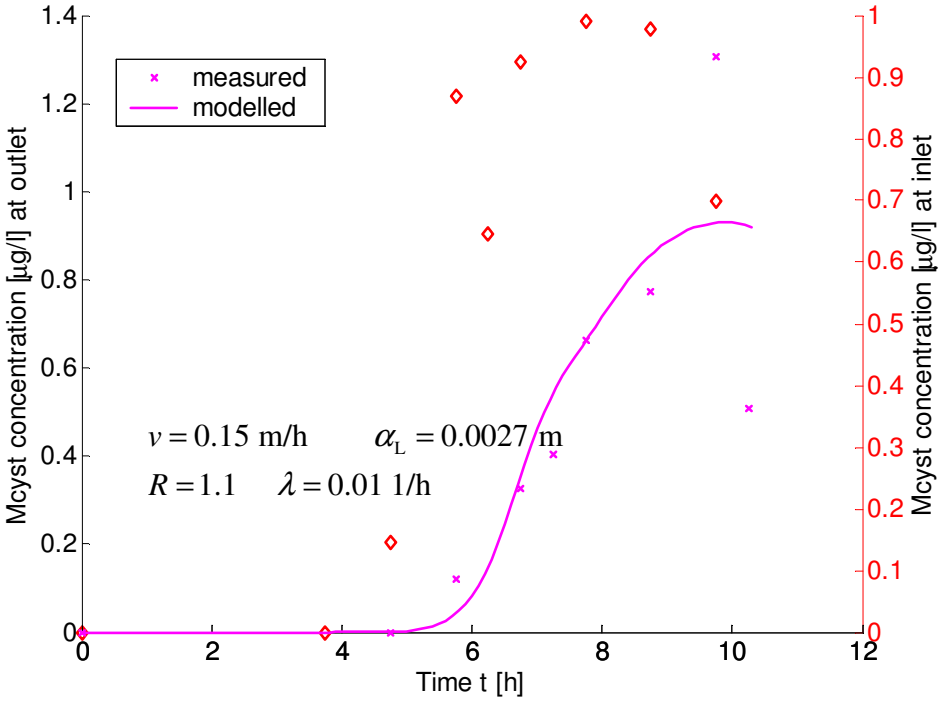

Figure 92 Inverse modelling result for EN3, 4->5

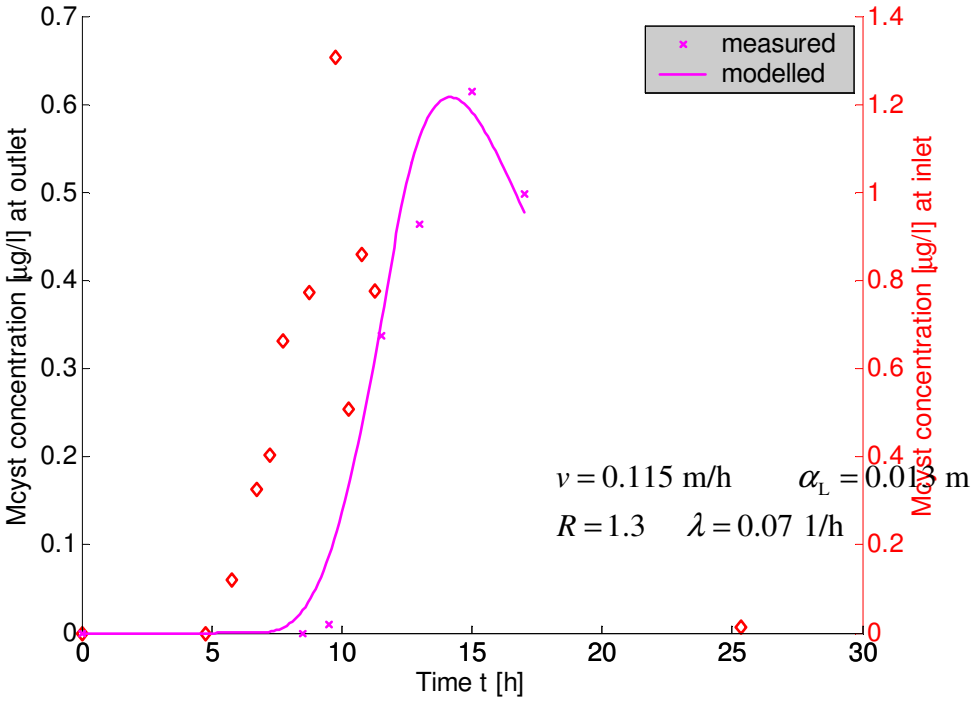

Figure 93 Inverse modelling result for EN3, 5->6, without outlier

The results of the inversion modelling procedure are depicted in Figures 1-13. For some simulations an additional start was performed, in which one or two outliers, observed in the measurements, were not considered in the parameter estimation procedure. In all cases the restart improved the fit substantially. Some parameter values changed significantly also by omission of outliers.

2.4.2.2 Bacteriophages

Enclosure experiments 2, 3, 9 and 10 were modelled. Modelling techniques were the same, as described in the section about microcystins. There were two steps:

- Velocity and dispersivity were obtained from inverse modelling based on tracer experiment measurements. Both the experiments as well as the inverse modelling were performed at the UBA. For inverse modelling VisualCXTFIT (Nützmann et al., 2005) was applied.
- Retardation and deactivation rate were obtained by inverse modelling, using MATLAB. The inversion module is described by Holzbecher (2005). Velocity and dispersivity values were taken from the first step.

The inversion was performed for different space intervals, as it turned out that 'global' values, valid for the entire column, are hardly to justify. All space intervals are related to the inlet of the enclosures, but have different lengths: 0.2, 0.4, 0.6, 0.8 and 1.2 m, if measurements are available.

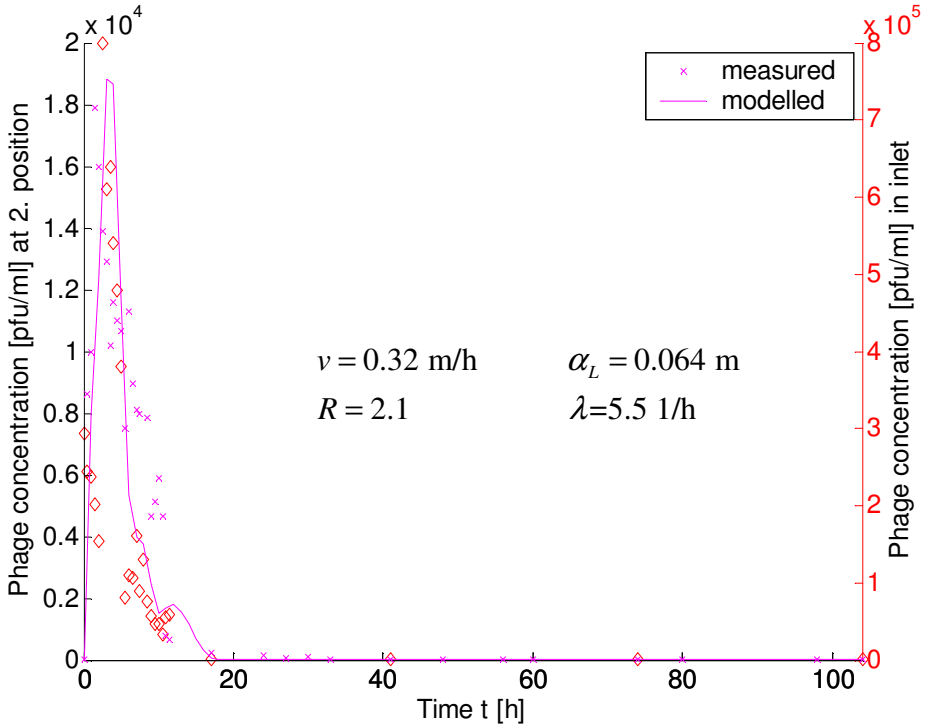

Figure 94 : *Phages 138, Encl 2, Flowpath: 20 cm*

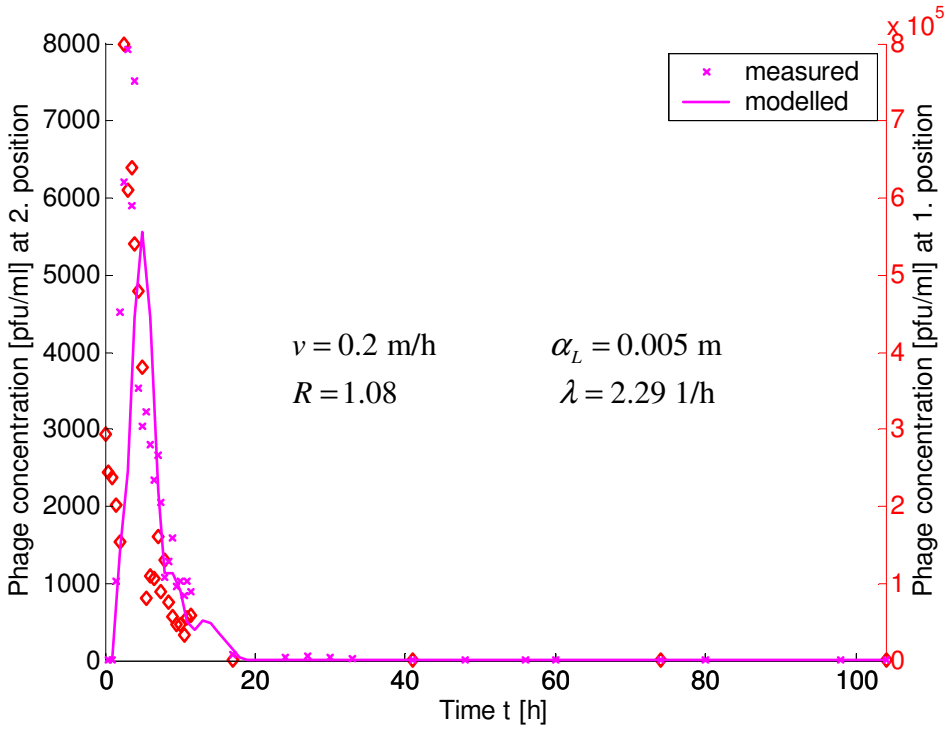

Figure 95 Phages 138, Encl 2, Flowpath: 40 cm

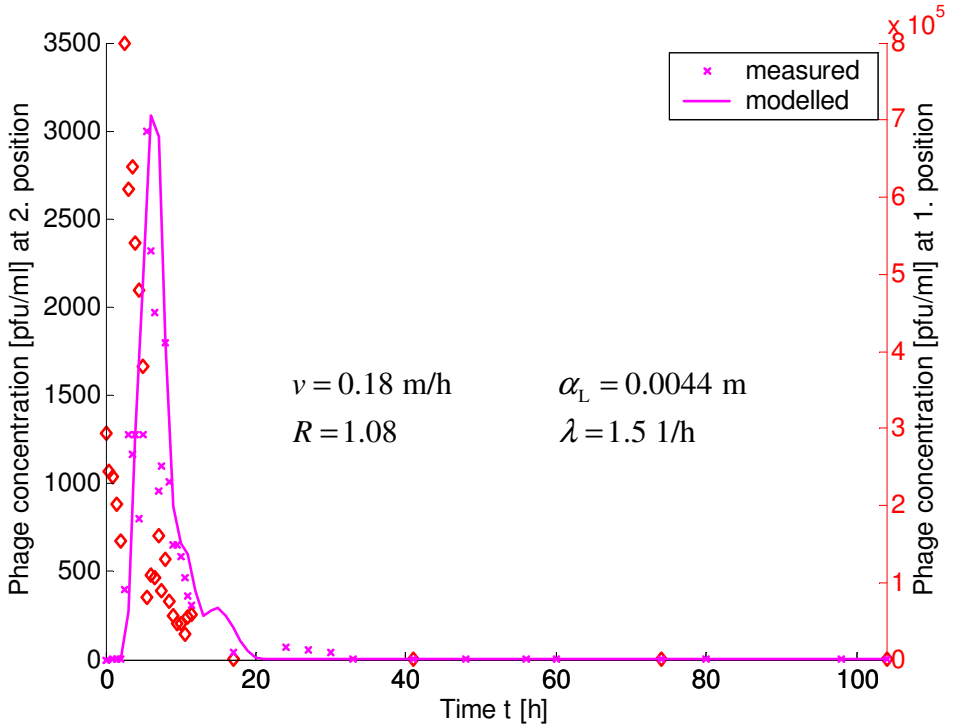

Figure 96 Phages 138, Encl 2, Flowpath: 60 cm

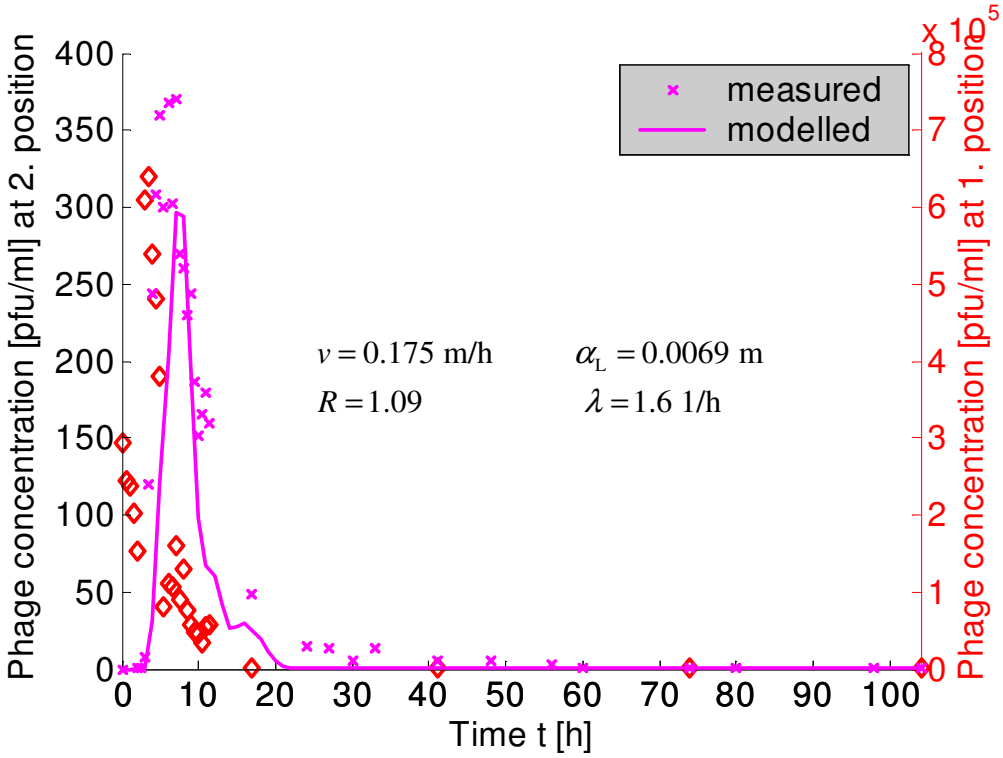

Figure 97 Phages 138, Encl 2, Flowpath: 80 cm

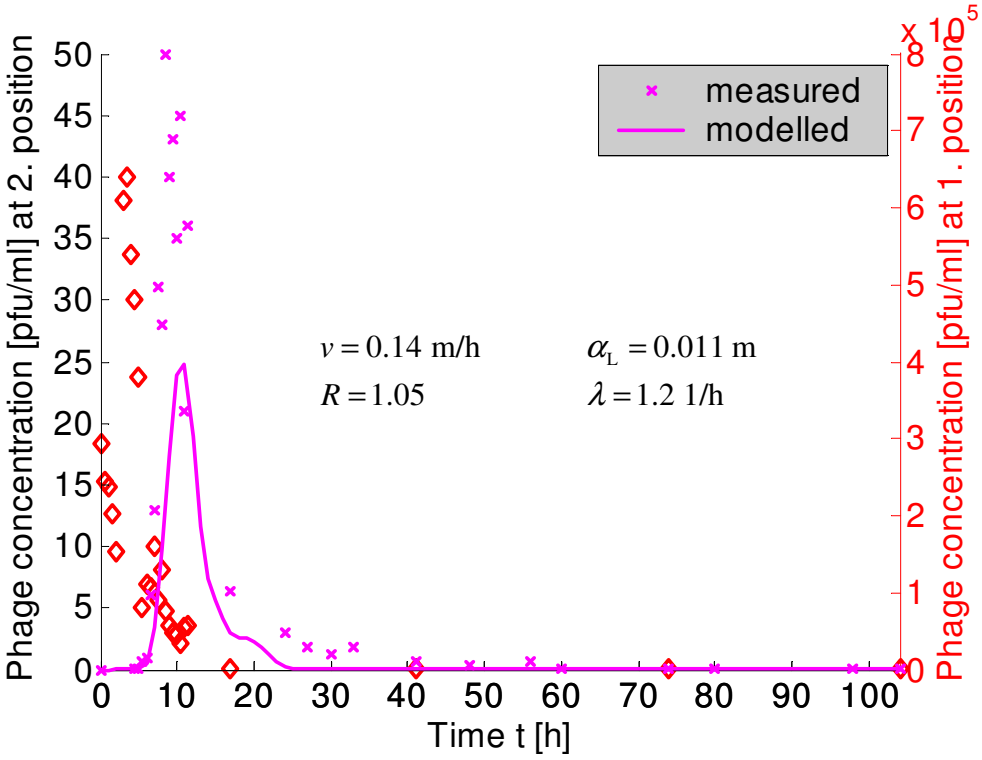

Figure 98 Phages 138, Encl 2, Flowpath: 120 cm

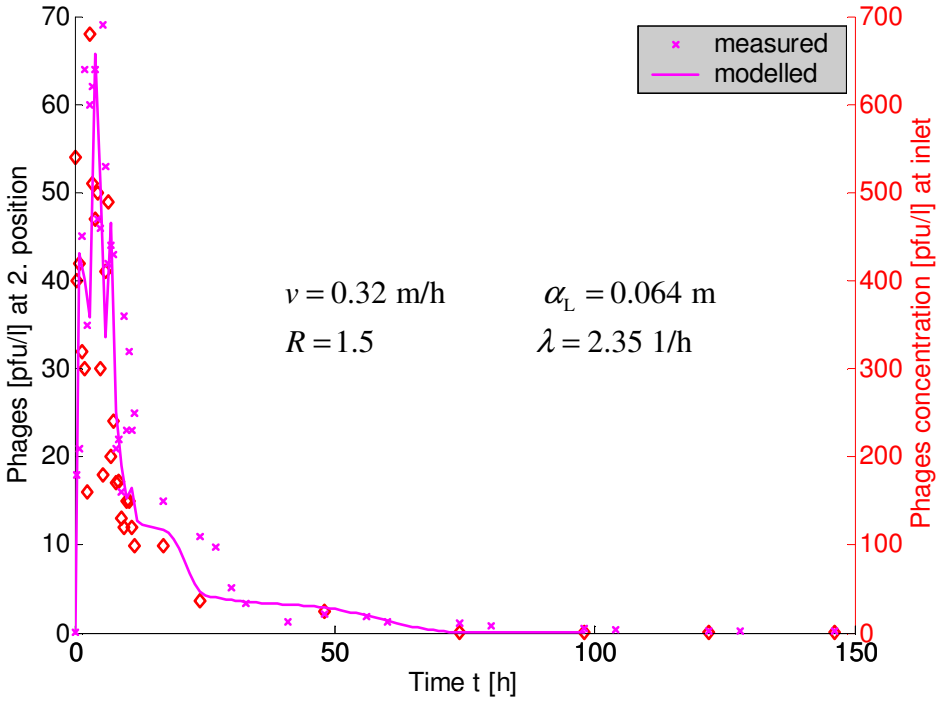

Figure 99 Phages 241, Encl 2, Flowpath: 20 cm

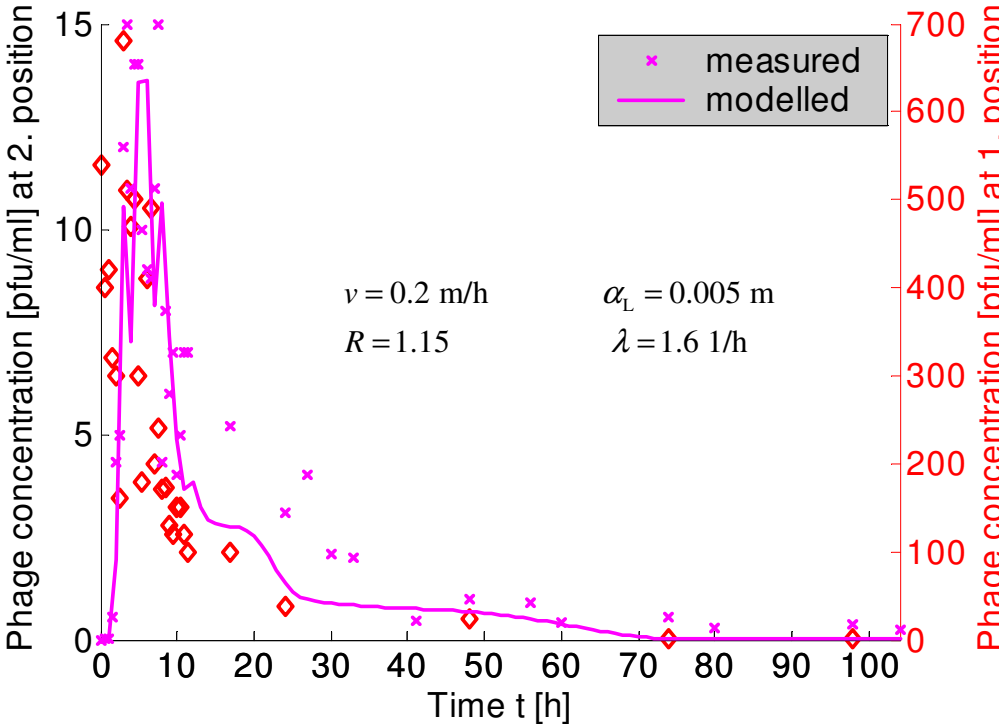

Figure 100 Phages 241, Encl 2, Flowpath: 40 cm

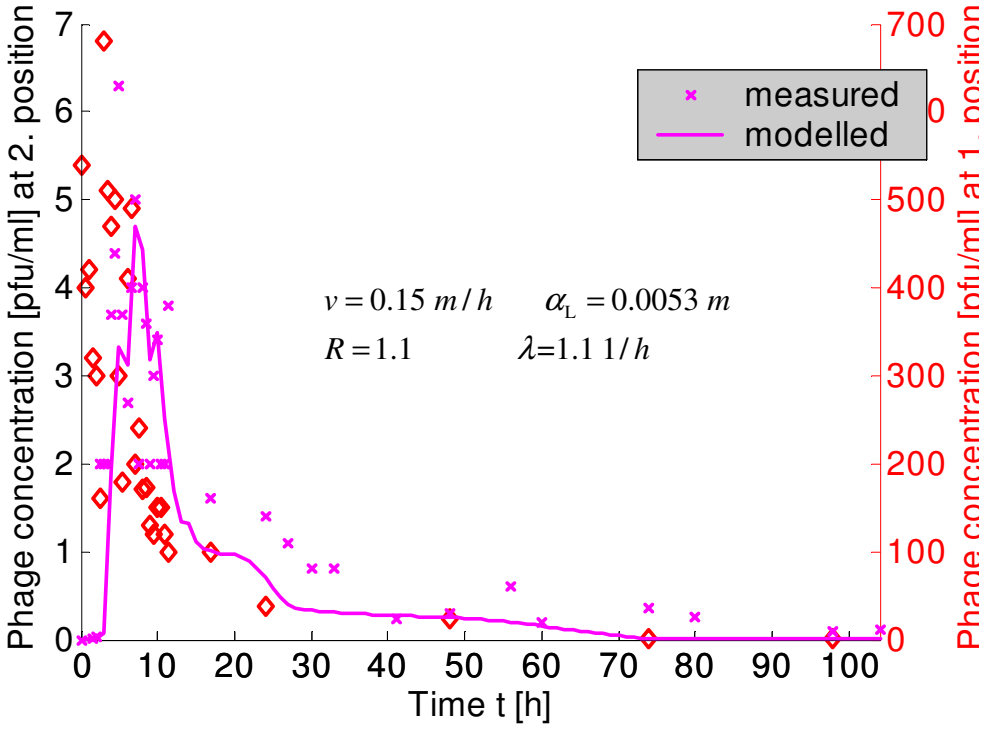

Figure 101 Phages 241, Encl 2, Flowpath: 60 cm

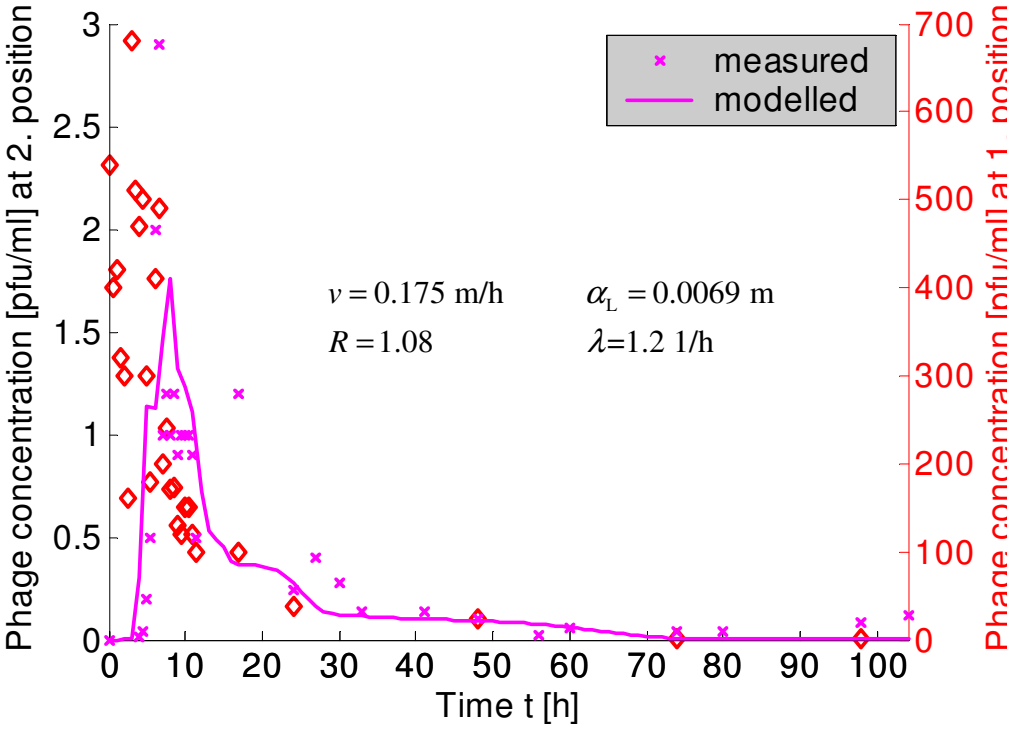

Figure 102 : Phages 241, Encl 2, Flowpath: 80 cm

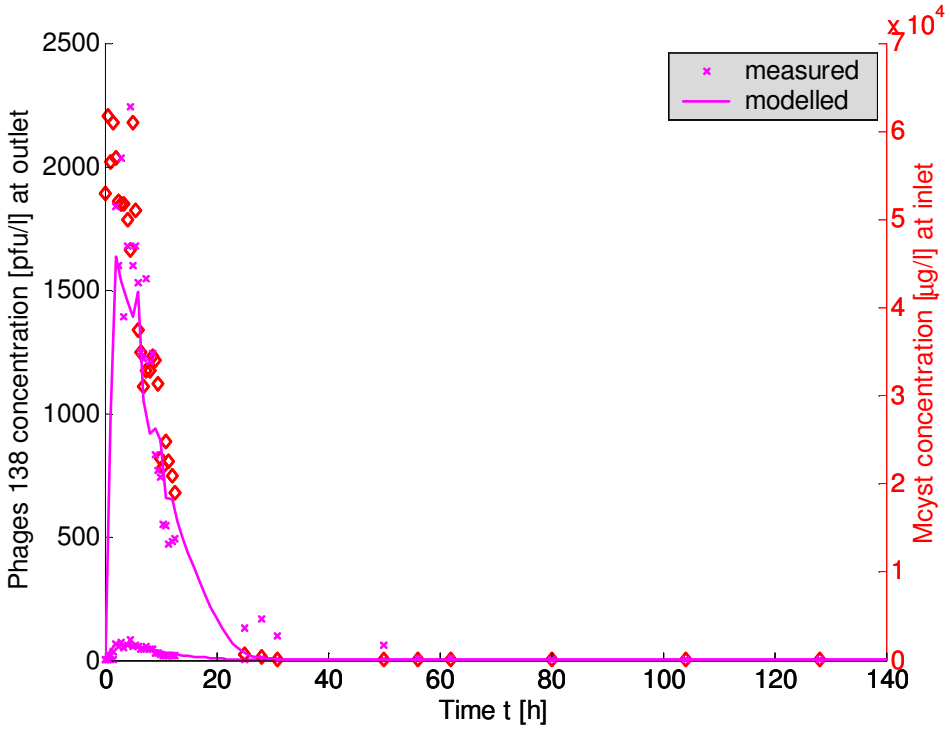

Figure 103 Phages 138, Encl 3, Flowpath: 20 cm

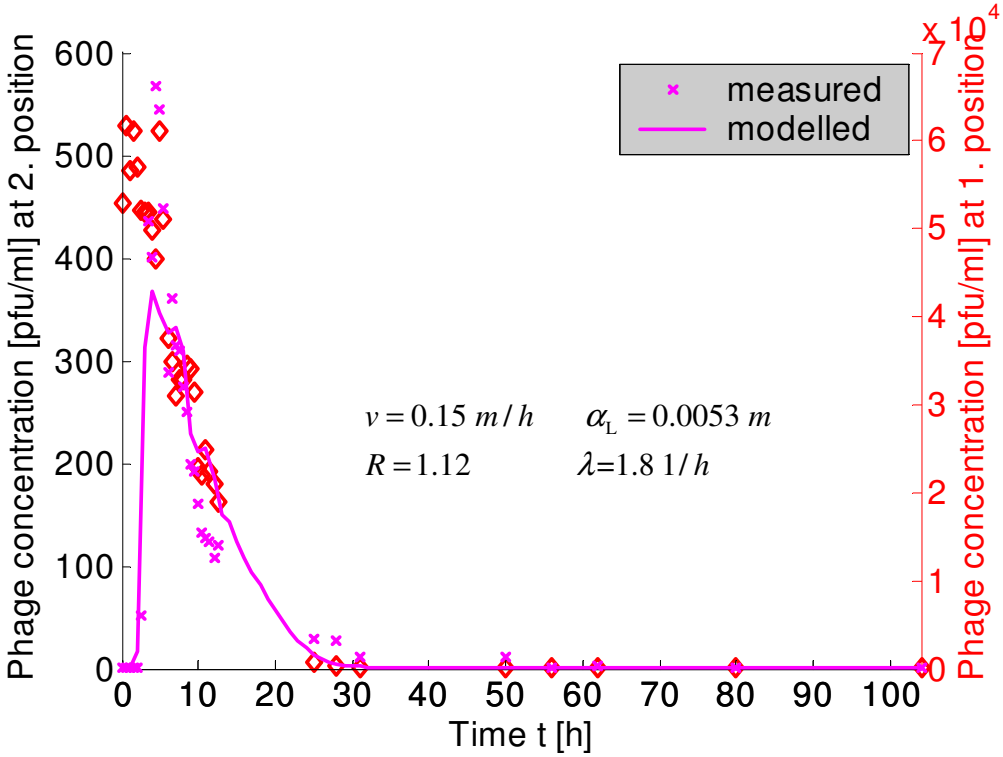

Figure 104 Phages 138, Encl 3, Flowpath: 40 cm

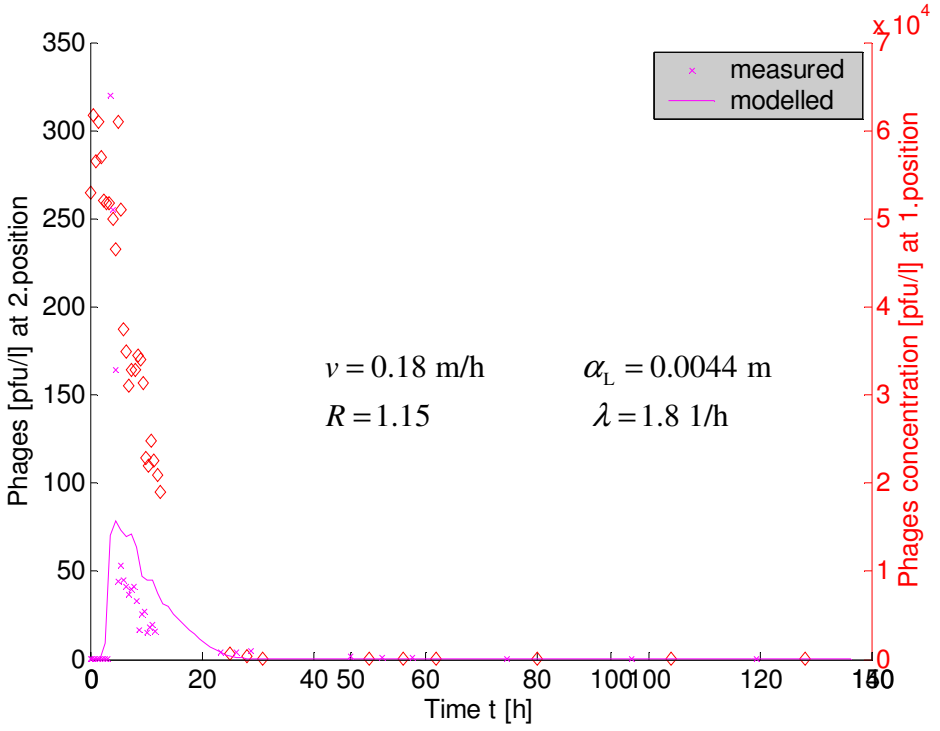

Figure 105 Phages 138, Encl 3, Flowpath: 60 cm

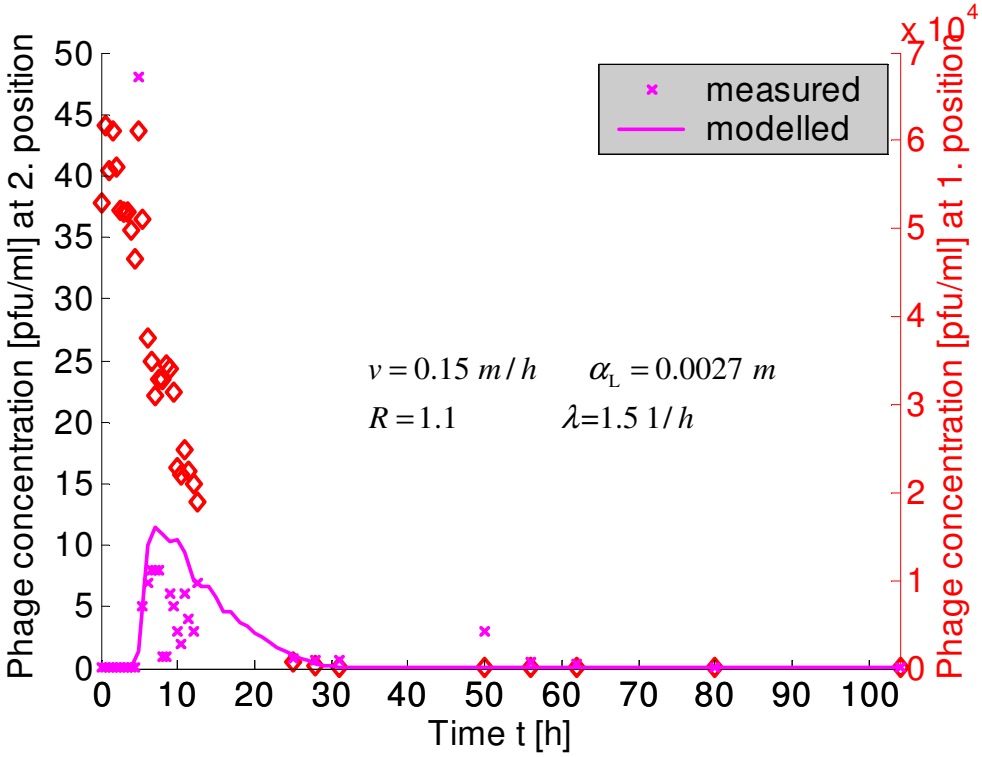

Figure 106 Phages 138, Encl 3, Flowpath: 80 cm

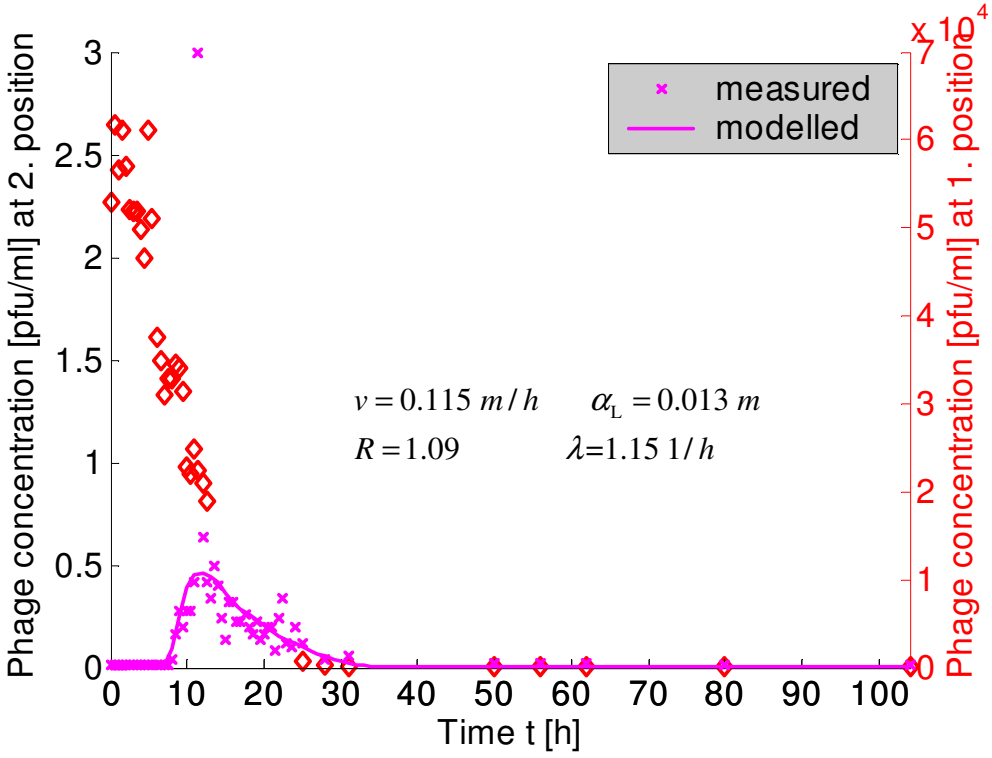

Figure 107 Phages 138, Encl 3, Flowpath: 120 cm

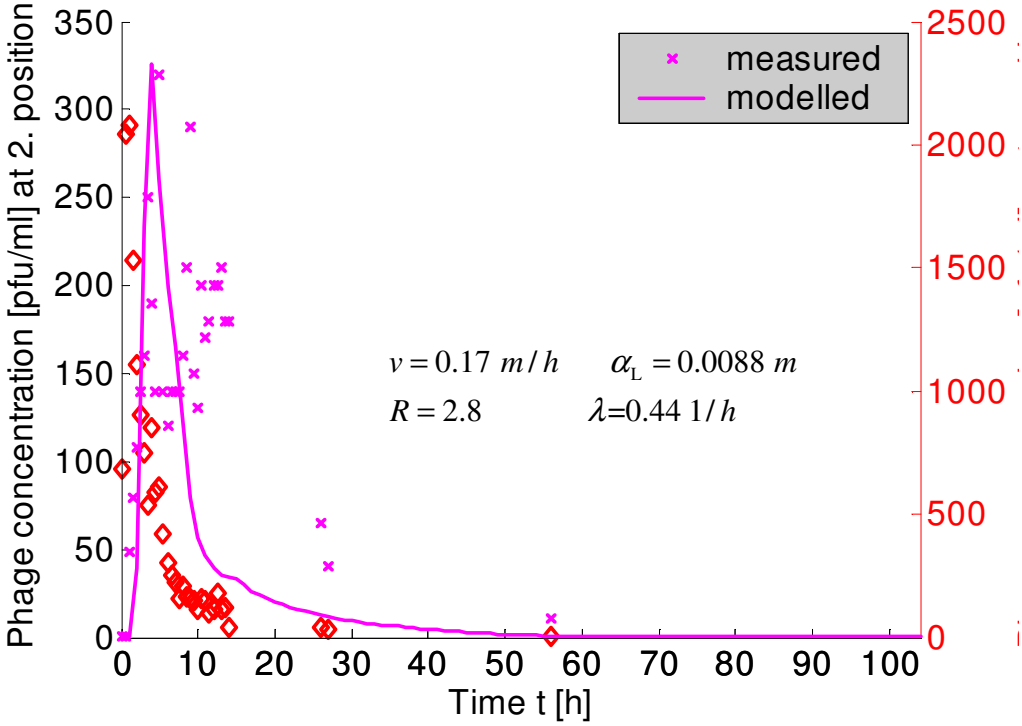

Figure 108 : Phages 241, Encl 3, Flowpath: 20 cm

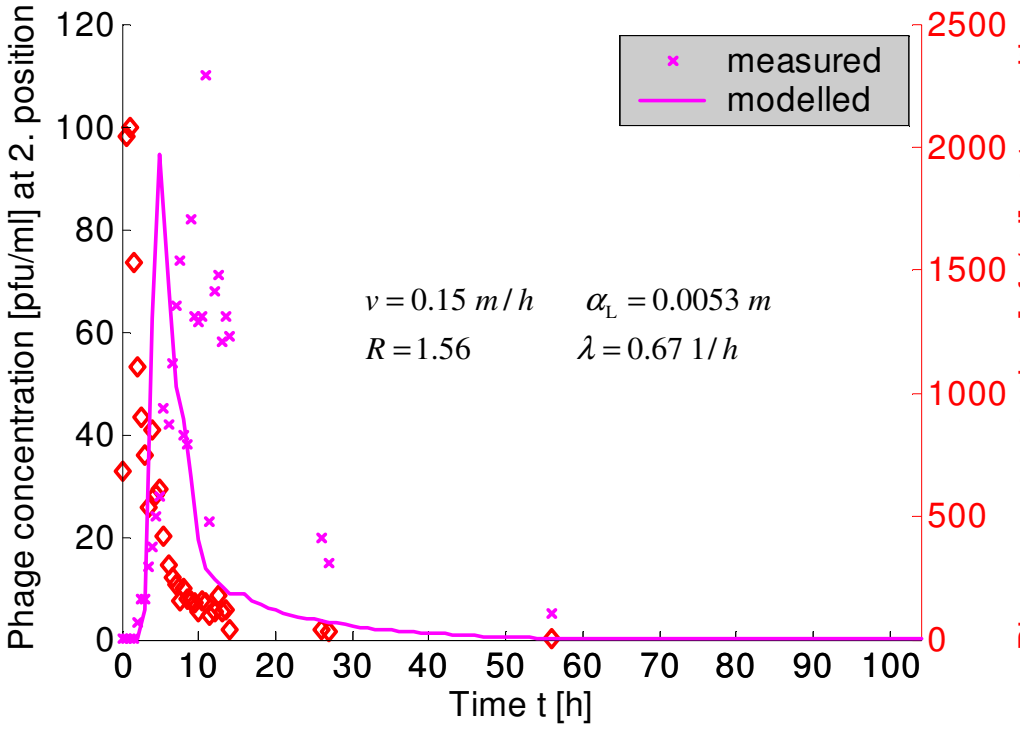

Figure 109 Phages 241, Encl 3, Flowpath: 40 cm

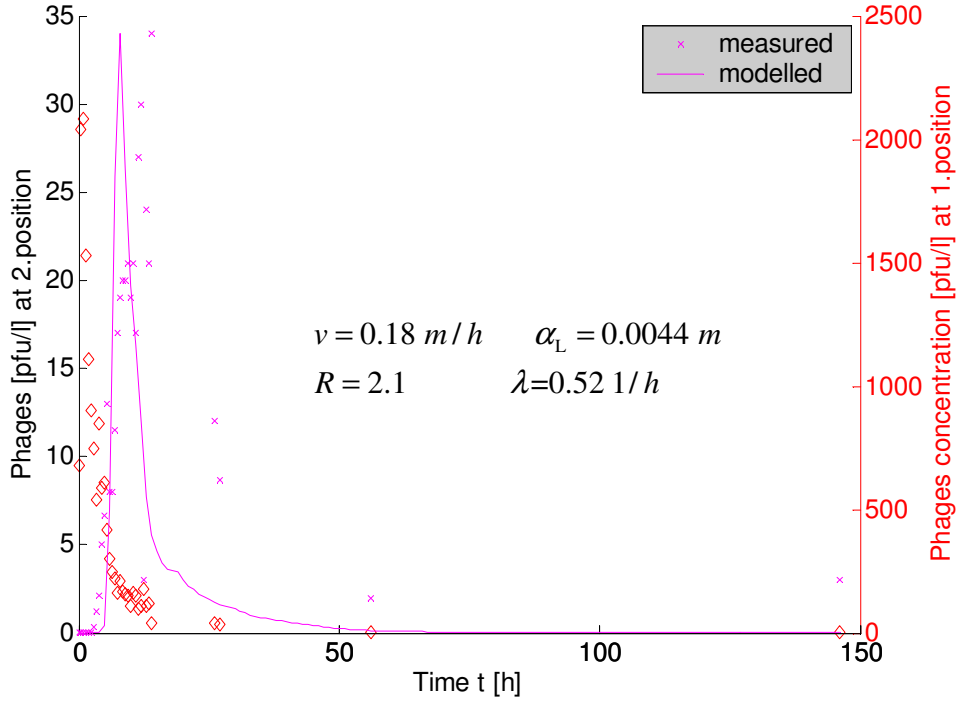

Figure 110 Phages 241, Encl 3, Flowpath: 60 cm

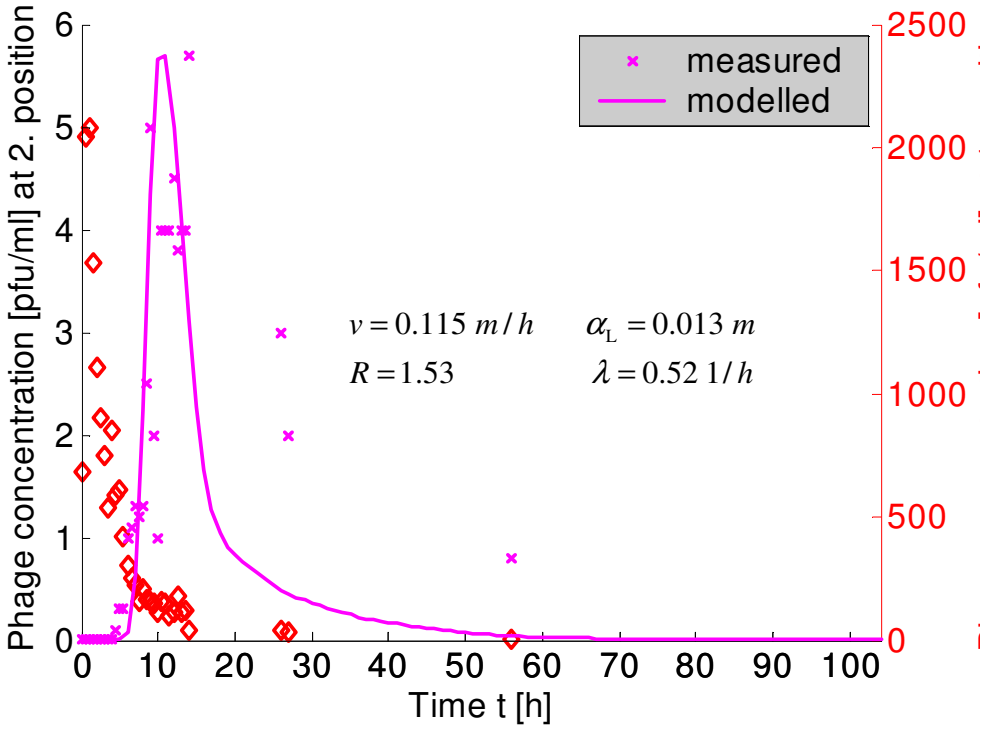

Figure 111 : Phages 241, Encl 3, Flowpath: 80 cm

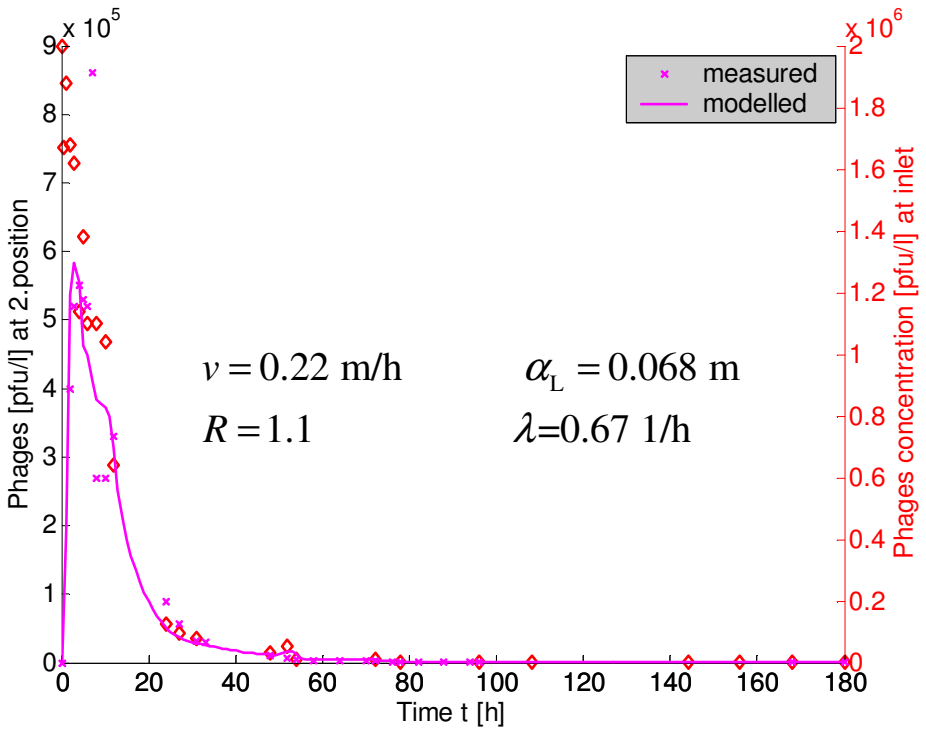

Figure 112 Phages 138, Encl 9, Flowpath: 40 cm

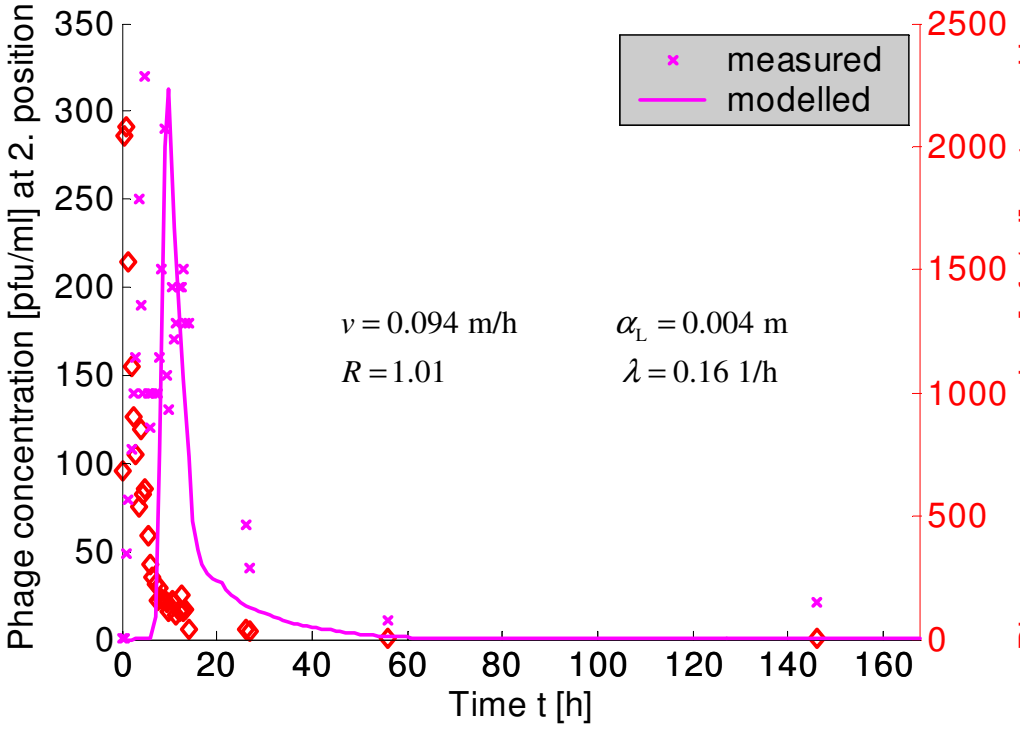

Figure 113 Phages 138, Encl 9, Flowpath: 80 cm

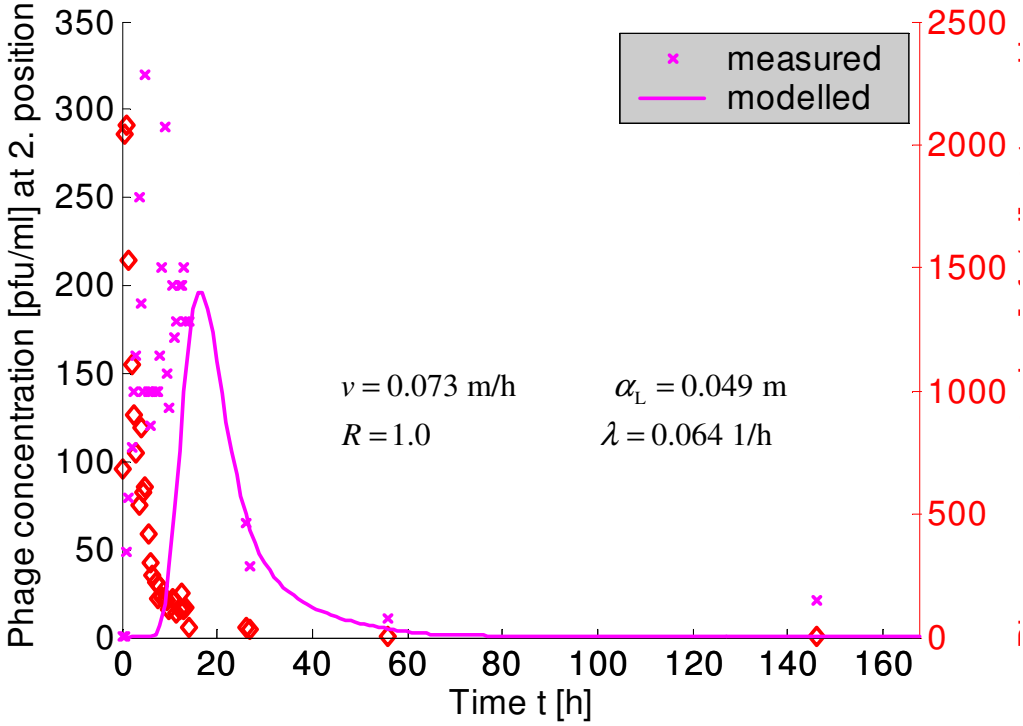

Figure 114 : Phages 138, Encl 9, Flowpath: 120 cm

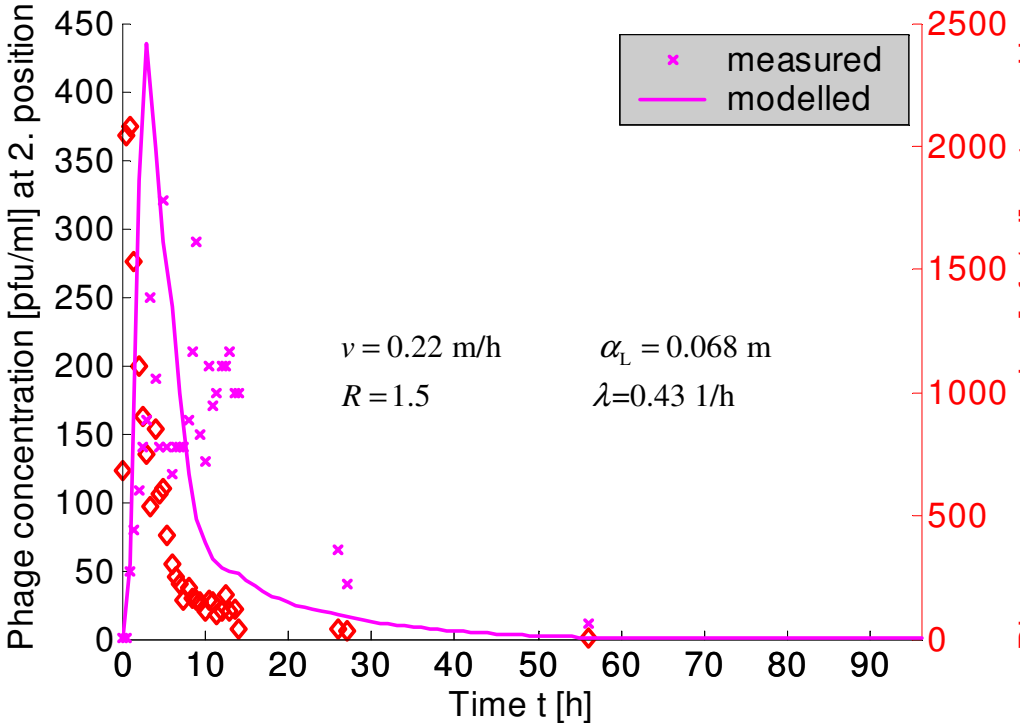

Figure 115 Phages 241, Encl 9, Flowpath: 40 cm

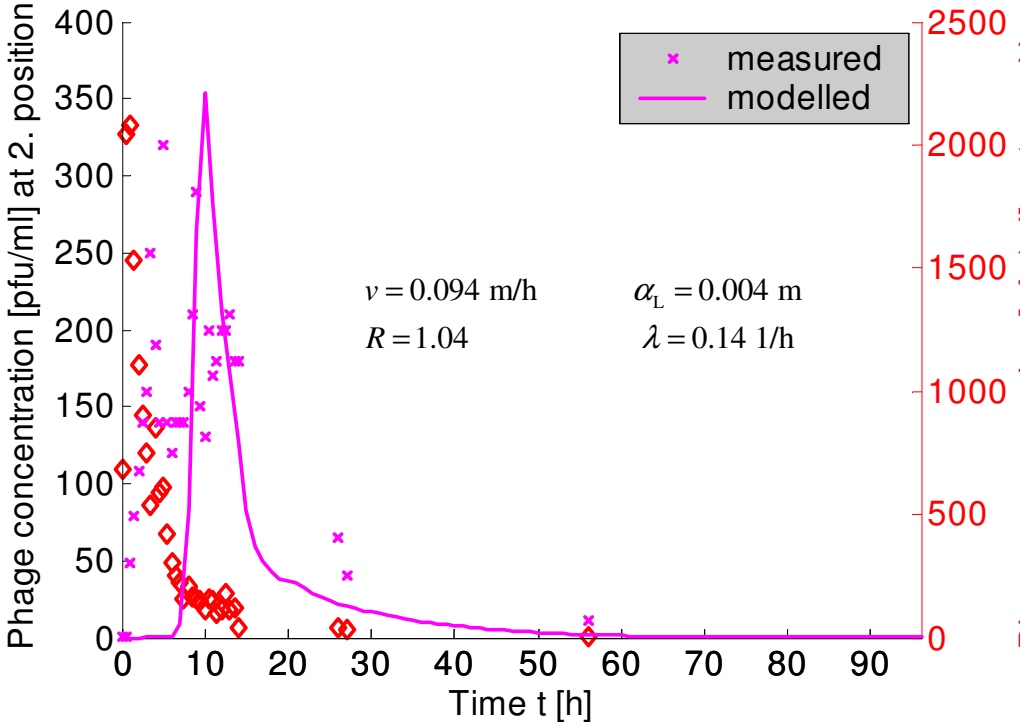

Figure 116 Phages 241, Encl 9, Flowpath: 80 cm

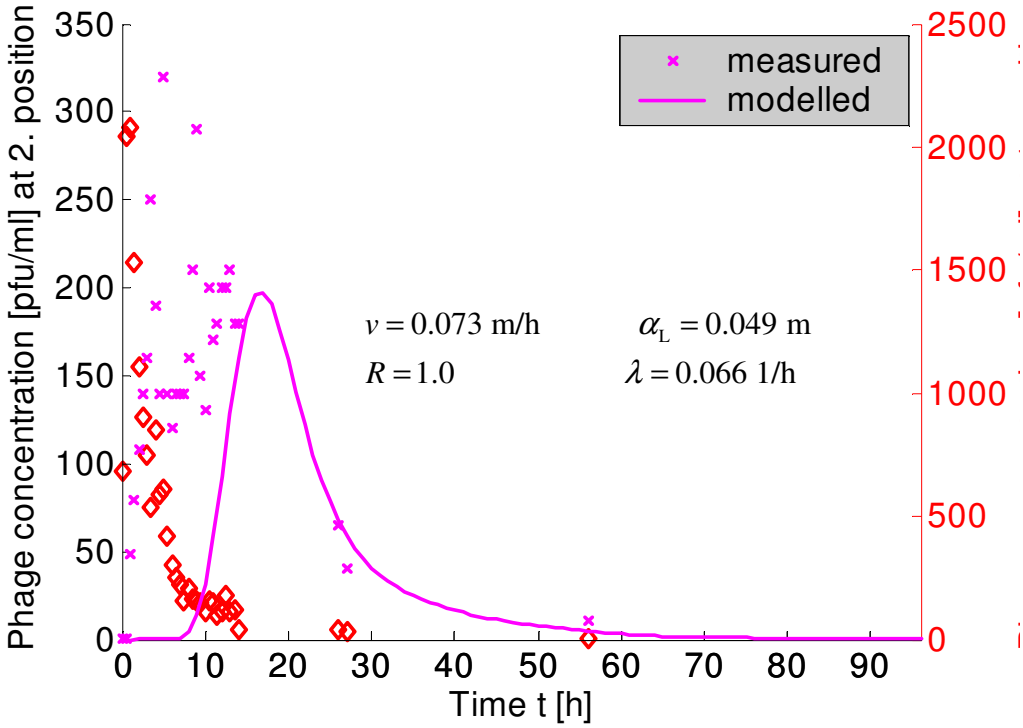

Figure 117 Phages 241, Encl 9, Flowpath: 120 cm

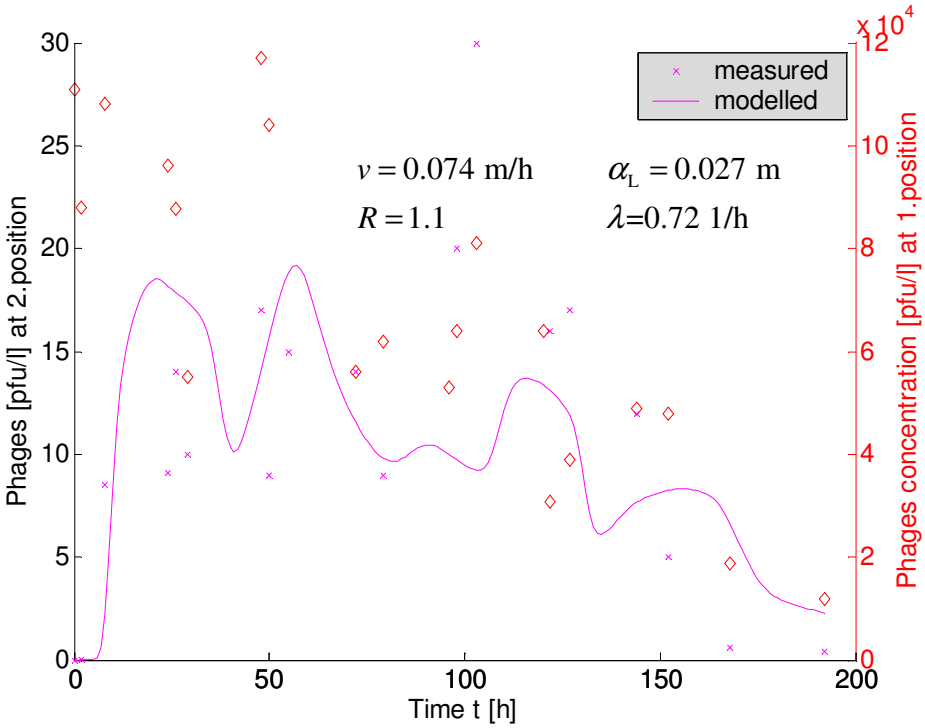

Figure 118 Phages 138, Encl 10, Flowpath: 120 cm

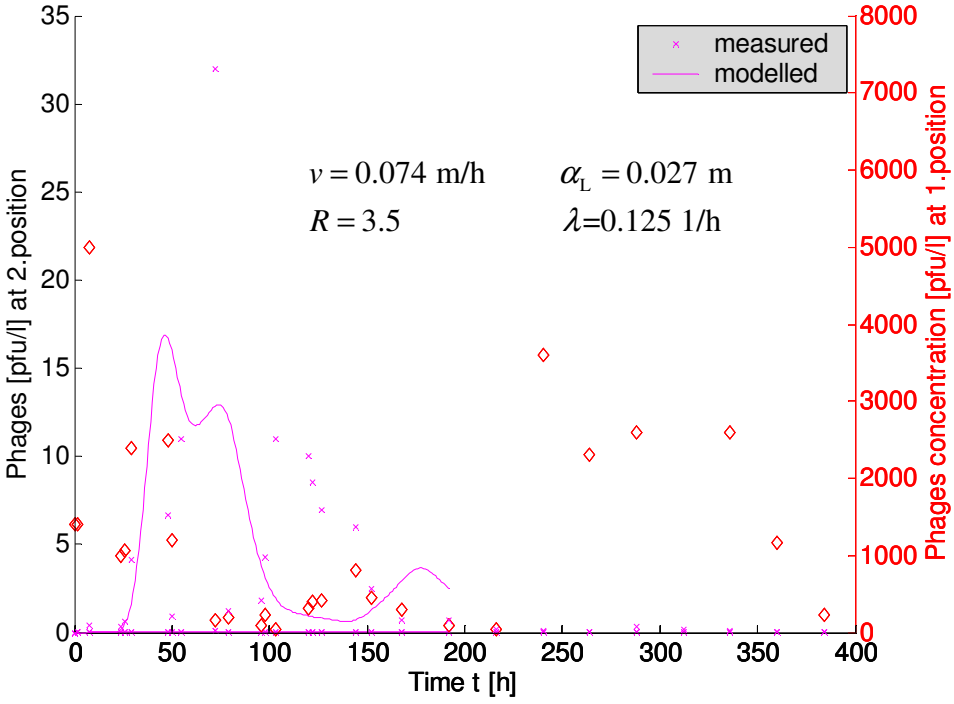

Figure 119 Phages 241, Encl 10, Flowpath: 120 cm

2.4.3 Summary of Results and Discussion

Results from the enclosure experiments with microcystin are summarized in Table 14. Retardations and degradation rates are listed for the experiments E2 and E3 and for the different spatial intervals along the flow path. Notation for intervals is adopted from the former sub-chapter .Also the last passage shows some peculiarities, maybe due to column-end-effects; note that the final part of the flow path is located in a gravel layer and the measurements were made in the outlet tube. For all experiments highest retardations and degradation rates are observed in the upper 20 cm.

Retardations and degradations show a tendency to decline along the flow paths. However outliers with respect to that rule are present in all columns.

Most peculiar is the flow path between 20 and 40 cm, with either a reduced degradation (E2), or reduced retardation (E3); a possible explanation is variable water saturation, which could be present in that horizon

Also the last passage shows some peculiarities, maybe due to column-end-effects; note that The final part of the flow path is located in a gravel layer and the measurements were made in the outlet tube.

Table 14 Estimated retardation and degradation rates from microcystin experiments

	Retardation		*Degradation [1/h]*	
Enclosure	E2	E3	E2	E3
$1 \rightarrow 2$	1.97	1.76	0.74	0.54
$2 \rightarrow 3$	1.9	1.25	0.24	0.31
$3 \rightarrow 4$	1.0	1.36	0.75	0.19
$4 \rightarrow 5$	1.0	1.14	0.54	0.01
$5 \rightarrow 6$	1.58	1.3	0.07	0.07

Results for both phages and all experiments (enclosures E2, E3, E9 and E10 with phages 138 and 241) are gathered in Table 15.

The following conclusions were drawn during the column meetings:

- Retardation and deactivation rates decrease with depth in the enclosure, i.e. along the flow path (there are few exceptions). In almost all cases the highest values for both parameters are in the uppermost 20 cm of the enclosures.
- Retardation and deactivation rates of phages 138 are smaller in enclosure E3 than in enclosure E2 (despite of beginning colmation, formation of clogging layer).
- In enclosure E3 there is almost no retardation of phages 138, whereas phages 241 are strongly retarded, in particular in the first part of the flow path.
- In anaerobic enclosure experiment E9 both retardation and deactivation are significantly reduced in comparison to experiments E2 and E3.
- Experiment E10 concerning phages 241 stands out due to high retardation and small deactivation, whereas there are no distinctive features concerning phages 138

The change of retardation and deactivation rates along the flow path can be explained by the presence of colloids (Holzbecher & Dizer, 2006). Depending on the conditions on the micro-scale effective parameter values, which are measured in experiments, may change along the flow path. The increased abundance of carriers in the initial part of the flow path may explain the observed behaviour in the enclosures.

Table 15 a: Estimated retardation and degradation rated for phages 138 experiments

Interval [cm]	Enclosure 2		Enclosure 3		Enclosure 9		Enclosure 10	
	R	**λ**	**R**	**λ**	**R**	**λ**	**R**	**λ**
0 - 20	2.1	5.5	1.08	3.25				
0 - 40	1.08	2.29	1.12	1.8	1.1	0.67		
0 - 60	1.08	1.5	1.15	1.8				
0 - 80	1.09	1.6	1.1	1.5	1.01	0.16		
0 - 120	1.05	1.2	1.09	1.15	1.0	0.064	1.1	0.72

b: Estimated retardation and degradation rated for phages 241 experiments

Interval [cm]	Enclosure 2		Enclosure 3		Enclosure 9		Enclosure 10	
	R	**λ**	**R**	**λ**	**R**	**λ**	**R**	**λ**
0 - 20	1.5	2.35	2.8	0.44				
0 - 40	1.15	1.6	1.56	0.67	1.5	0.43		
0 - 60	1.1	1.1	2.1	0.52				
0 - 80	1.08	1.2	1.53	0.52	1.04	0.14		
0 - 120					1.0	0.066	3.5	0.125

In Holzbecher *et al*. (2006) the following summary is given:

The parameter change within one experiment may reach a factor of 10 (for λ in E9). In most experiments, for most parameters a clear tendency is visible, but not always. Velocities decrease with increasing interval with a maximum factor of about 3 (E9). The dispersion parameter is decreasing also, if two measurements for the long intervals (from 0-80 cm for E2 and E9, and 0-120 cm for E2 and E3) are taken as outliers. Retardations mostly exceed 1 only marginally and maximum value is approximately 2 (E2). There is a slight tendency to decreasing sorption with longer spatial interval. Degradation rates are clearly decreasing with increasing interval where λ values are growing.

The results from the model with constant parameters clearly show that parameters are not constant. Otherwise the values, obtained for one experiment, should fluctuate around a mean value. Instead most parameters show a tendency within each experiment, as described. The parameters are surely not constant within the enclosures and the following conclusions are drawn:

An influence of the clogging layer could not be confirmed in the enclosure experiments. Temperature effects could be detected indirectly, as comparable experiments performed under different seasonal conditions showed different results: the deactivation of the phages increases with increasing temperature.

Redox conditions could be expected to play an important role as degradation / deactivation processes as well as sorption processes are often biologically mediated. The presented enclosure experiments show significantly different behaviour of the studied phages under aerobic and anaerobic conditions. It can not be excluded that some other conditions could be

responsible for the observed behaviour, but the redox state seems to be most pronounced difference (E9 in comparison to other experiments). The results confirm the message of Tufenkji et al. (2002) that redox processes are relevant for bank filtration systems. Similarly the migration of heavy metals or other problem substances may also be influenced by redox conditions, if the substance participates in microbial mediated reactions...

Redox dependencies, determined in controlled laboratory or enclosure experiments, can be used for modelling field situations with spatially or temporally changing redox conditions. A transport model, based on differential equations (1) and (2) with variable degradation and retardation factors, has to be complemented by a model of redox zones. Examples for redox zone modeling were presented by Hunter et al. (1998) or Holzbecher and Horner (2003). In that way degradation and sorption of harmful substances can be embedded in biogeochemical cycles, if necessary.

2.4.4 References

MATLAB® Version 6.5, Release 13 (2002). The MathWorks, Inc., 3 Apple Hill Drive, Natrick, MA 01760-2098, USA

Nützmann G., Holzbecher E., Strahl G., Wiese B., Licht E., Knappe A. (2006) Visual CXTFIT – a user-friendly simulation tool for modelling one-dimensional transport, sorption and degradation processes during bank filtration, Proceedings ISMAR 2005

Holzbecher E., (2005) Inversion of temperature time series from near-surface porous sediments, *Journal of Geophysics and Engineering*, Vol. 2, 343-348

Holzbecher E., Dizer H. (2006) Facilitated and retarded transport and degradation in porous media due to carriers, *Colloids and Surfaces A: Physicochemical and Engeering Aspects* (to appear)

Holzbecher E., Dizer H., Grützmacher G., Lopez-Pila J., Nützmann G., The influence of redox conditions on phage transport – enclosure experiments and modelling, *Environmental Engineering Science* (to appear)

Holzbecher E., Horner Ch. (2003). A reactive transport model for redox components. In: H.D. Schulz and Hadeler A., Eds., *Geochemical Processes in Soil and Groundwater*, Proceedings GeoProc2002, Wiley, Chichester, pp. 414-434.

Hunter K.S., Wang Y., van Cappellen P. (1998). Kinetic modeling of microbially-driven redox chemistry of subsurface environments: coupling transport, microbial metabolism and geochemistry. *J. of Hydrol*., Vol. 209, 53-80

Toride N., Leij F.J., van Genuchten M. Th., The CXTFIT code for estimating transport parameters from laboratory or field tracer experiments, U.S. Salinity Lab., Agric. Res. Service, US Dep. of Agric., Research Report No. 137, Riverside (CA), 1995

Tufenkji N., Ryan J.N., Elimemech M. (2002) Bank Filtration, Environm. Science & Techn., Vol. 36, 423A

2.5 ELEMENTS OF A MANAGEMENT MODEL

2.5.1 Overview

The following partial tasks were performed:

1. Implementation of a simulator for the evaluation of the hydraulics of generic bank-filtration situations
2. Partial implementation of a simulator for the evaluation of the hydraulics of specific bank filtration facilities
3. Set-up of a flow and transport model to identify increased concentrations in pumped water

The first two tasks were performed using MATLAB; the model in the third task was set up using FEMLAB. The product of the first task 'The NASRI Bank Filtration Simulator' was presented during the ISMAR 2005 conference, June 2005 in Berlin, Germany. The second task is an extension of the first task, which could not be completed within the NASRI project. The results of the third part were summarized in a manuscript, which is submitted for publication (Holzbecher, 2005).

2.5.2 The NASRI Bank Filtration Simulator

The product was developed in several steps using MATLAB, starting with version 1.1. The version 1.3 was presented at the ISMAR2005 conference; here the slightly extended version 1.3a is presented.

The purpose of the software is the evaluation of generic situations of bank filtration facilities. The user has to input basic characteristics of the aquifer (thickness, hydraulic conductivity, base flow and reference head value at the bank), of the bank (straight horizontal line or straight lines, meeting at an angle of 90°, clogging parameter), at of the well gallery (position and pumping rates of single wells). The user may also specify the spatial extension of the model region and the grid spacing, used for graphical output. Moreover several options concerning the graphical output can be specified: there are options to visualize head contours, streamlines, flowpaths and/or velocity arrow fields.

The graphical user interface of the NASRI Bank Filtration Simulator is depicted in Figure 120. After the specification of input data, computations are initiated by a click on the 'Plot' button. The variables of the flow field are calculated at the grid points and visualized at the graphic panel. Moreover the share of bank filtrate in pumped water is computed and shown in the corresponding output field. After the plot the user may alter input values in the graphical user

interface and perform new computations using the 'Plot' button again. The software is equipped with a help-system, which enables even novices to explore the program.

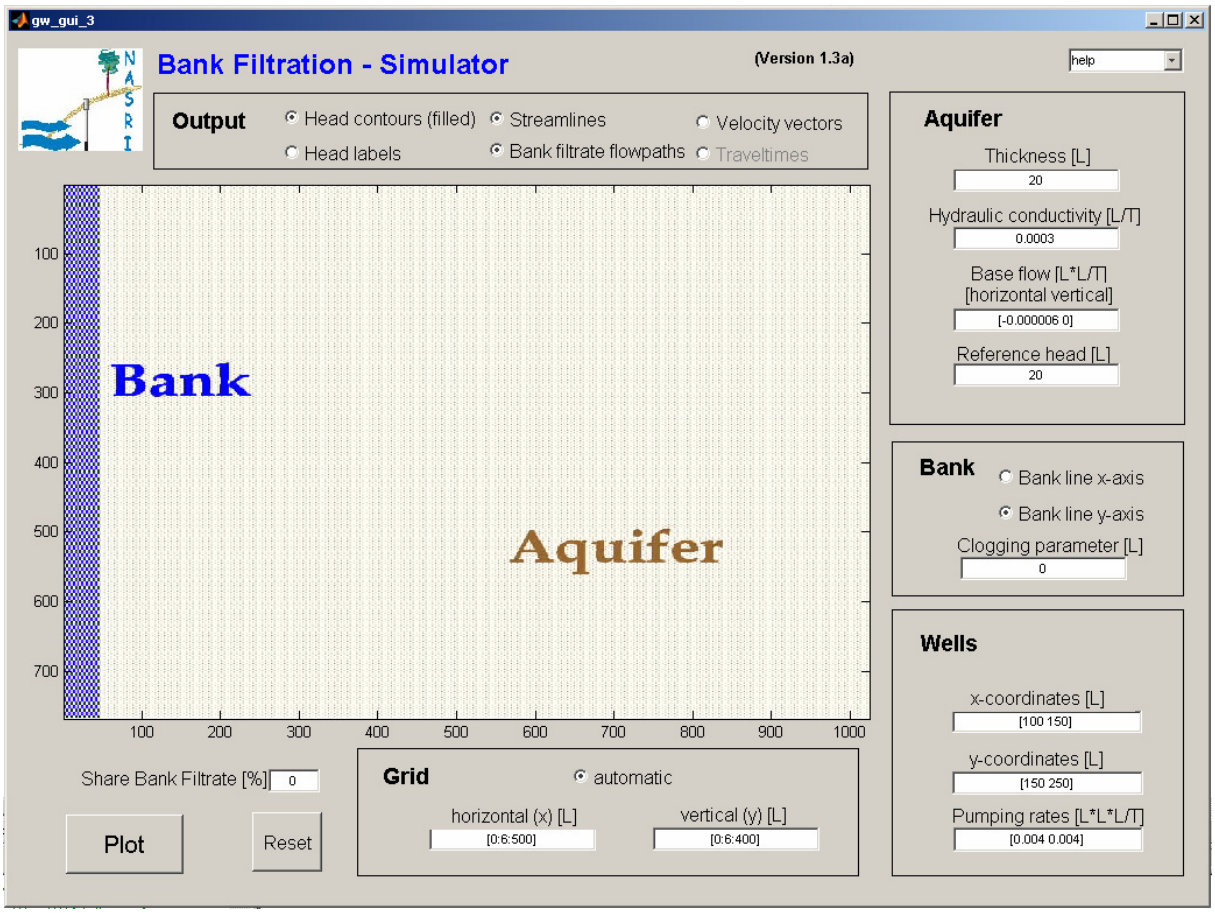

Figure 120 Graphical User Interface for the NASRI Bank Filtration Simulator, initial window

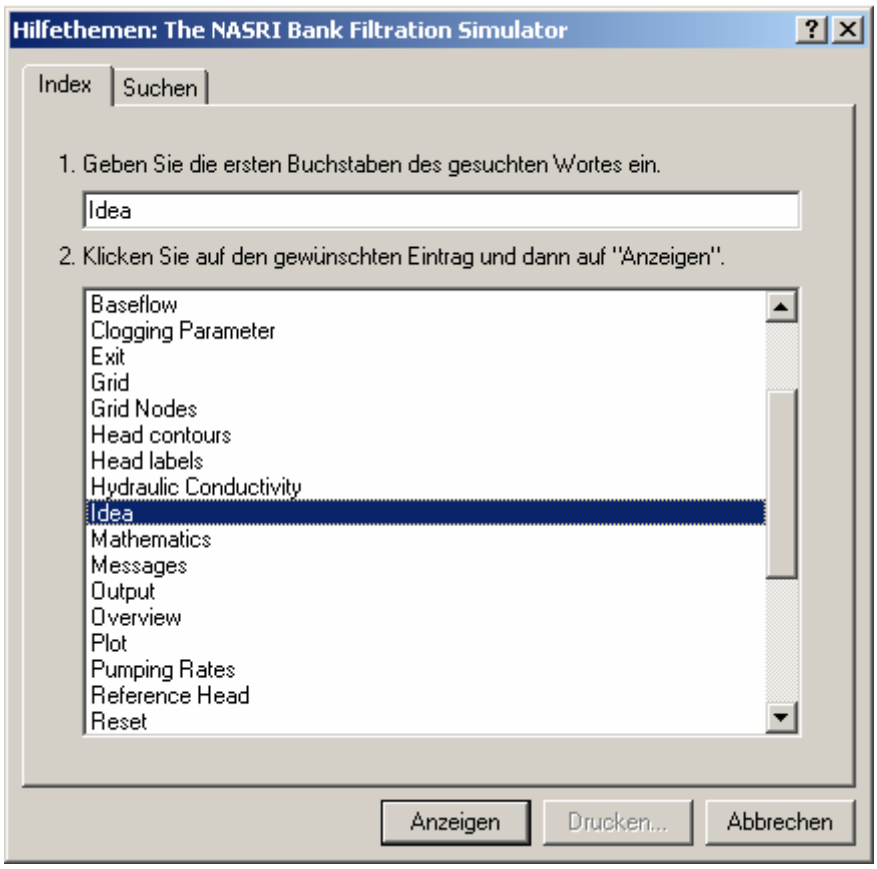

Figure 121 Keyword selection in the Help system of the simulator software

The user may choose from several keywords, for which information are given (Figure 121). In the following some excerpts from the 'Help'-system are given.

The idea of the NASRI Bank Filtration Simulator is described under the 'idea' keyword:

2.5.2.1 Idea

The idea for the Bank Filtration Simulator is derived from the following task.

Task: Assume you have to design a bank filtration facility at a location, where limited information is available only. Maybe one borehole has been drilled and there are some basic geological data. How to decide about:

- Positions of wells
- Distance between bank and wells
- Distance between wells
- Pumping rates
- ...

The program may hopefully provide some useful information in such a situation.

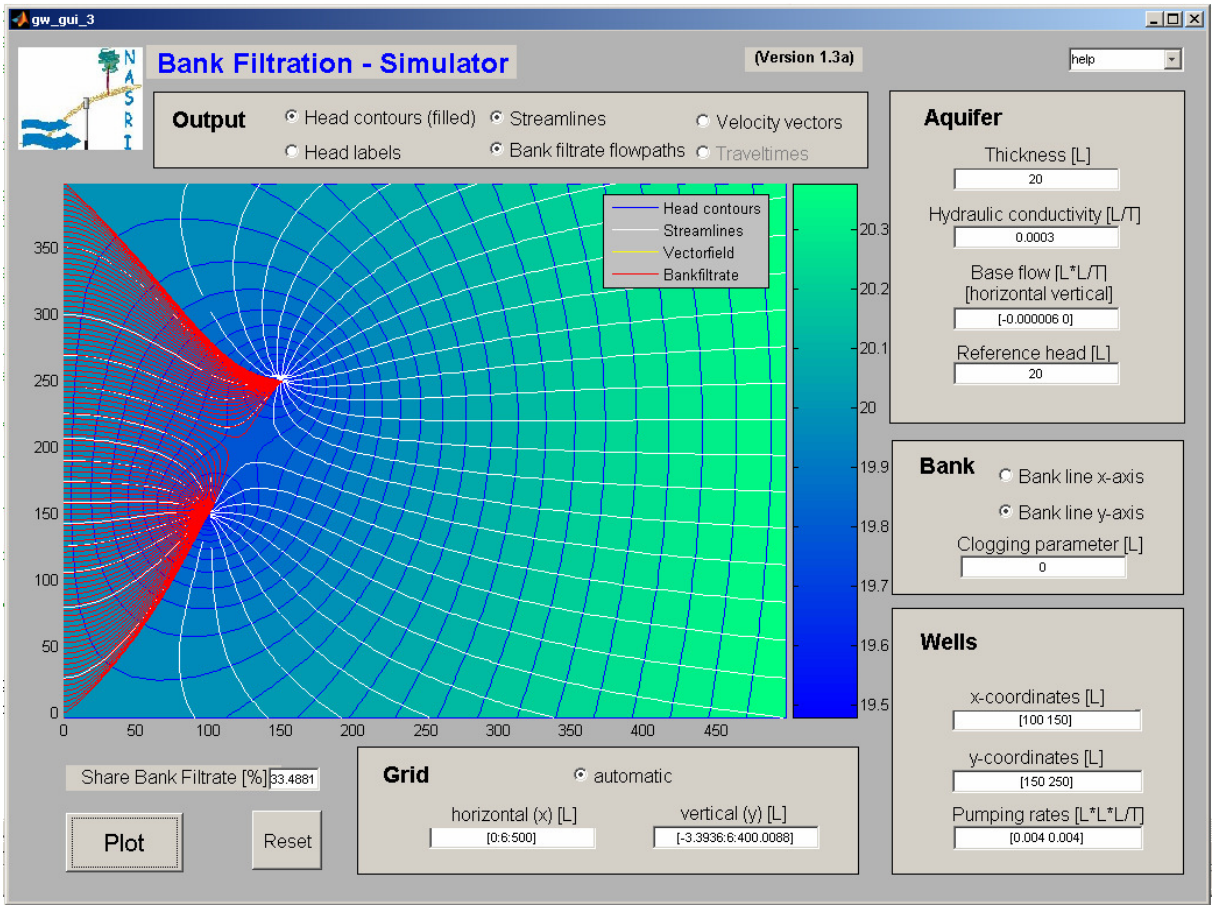

Figure 122 Graphical User Interface for the NASRI Bank Filtration Simulator with output for default settings

The output for the default settings of the program is shown in Figure 122. The distribution of piezometric head in the model region is shown by blue contours and a green-blue fill pattern. Bank filtrate flow paths, entering from the bank boundary on the left side of the panel are shown in red. A streamline pattern for the entire model region is depicted by white lines.

The vertical extension of the aquifer, represented in the graphic panel, is calculated automatically for the output, shown in Figure 122. The outer-most positions, where surface water enters the aquifer, are computed by the software, which is explained in more detail under the 'automatic gridding' keyword of the help system:

2.5.2.2 Automatic Gridding

Automatic gridding can be chosen by the user under the grid header. If automatic gridding is active, the grid spacing and extension of the grid along the bank is selected automatically. The region, represented in the graphical output window, is extended to capture the entire region of bank filtration.

Note: Automatic gridding is performed for the coordinate axes only, which are bank lines. The scales in vertical and horizontal direction may become quite different. If that is not

wished by the user, the coordinate scale can be adjusted manually after the automatic gridding run in the grid block of the graphical user interface.

Note: Automatic gridding is performed only, when there is a change between groundwater outflow and bank filtrate inflow on the bank. In situations, where there is bank filtrate only, either flowing to the wells or migrating further in the aquifer, the automatic gridding is not performed. Then the former limits of the graphics on the display remain unchanged.

The white lines illustrate the flow field not only by streamlines, but by streamtubes, as explained under the 'streamlines' keyword:

2.5.2.3 Streamlines

Streamlines provide a lot of information concerning the flow field. A pattern of streamlines for the situation, selected by the user, is given in the graphical output, after pressing the 'Plot' button. If the streamline option was selected, a pattern of white lines is shown on the display.

The flow of a water particle can be envisaged by following the streamlines. Moreover the strength of the flow at different parts of the figure, can be compared by the fact that between neighboured streamlines there is the same amount of flow everywhere. There are higher velocities, where streamlines are near to each other. Velocities are low, where there is a wide space between streamlines.

Spacing of streamfunction is chosen as the 20s part of the pumping rate of well number 1, if that is non-zero.

Method: Streamlines are calculated as contours of the streamfunction (see mathematics).

Note: The streamline figure depicts straight lines from the well positions to the left towards the y-axis. These are not streamlines, but by-effects of the analytical element method, as the complex logarithm is not a unique function in the complex plane. Details are found under mathematics.

In version 3.a the straight line plotting is circumvented!

Default: on

Aside from graphical output, after plotting one numerical value is presented on the display. This is the part of bank filtration in pumped water for the specified set-up. It is explained in the help system under the 'share of bank filtration' keyword.

2.5.2.4 Share of Bank Filtration

The share of bank filtration in pumped water is calculated by the Bank Filtration Simulator after pressing the plot button. The ratio of bank filtrate is valid for the pumping of the entire set-up, and does not distinguish between single wells.

Note: If there is no base flow across a bank line, either on the x-axis or on the y-axis, bank filtrate enters along the entire bank line (theoretically only of course). In that case the share of bank filtrate in pumped water is 100%.

Unit: -

For the default set-up bank filtration contributes to pumped water with a share of 1/3, as shown in Figure 122.

Using the NASRI Bank Filtration Simulator the user has the option to choose between three different options concerning the bank, as described in the help system:

2.5.2.5 Bank

The bank is assumed to be a straight line or the combination of straight lines. The optional cases are:

- The bank is identical with the x-axis
- The bank is identical with the y-axis
- The bank is located along x- and y-axis

Moreover the effect of a clogging layer can be taken into account, by choosing a clogging parameter.

The point is illustrated under the help topic 'bank line'.

2.5.2.6 Bank Line

In the NASRI Bank Filtration Simulator the bank line can be either along the x-axis, the y-axis or along both:

The user can choose between these alternatives, using two checkboxes under 'bank' header.

An example calculated with the third option, is given in Figure 123. Bank filtration in situations with general angles is described in detail by Holzbecher (1996).

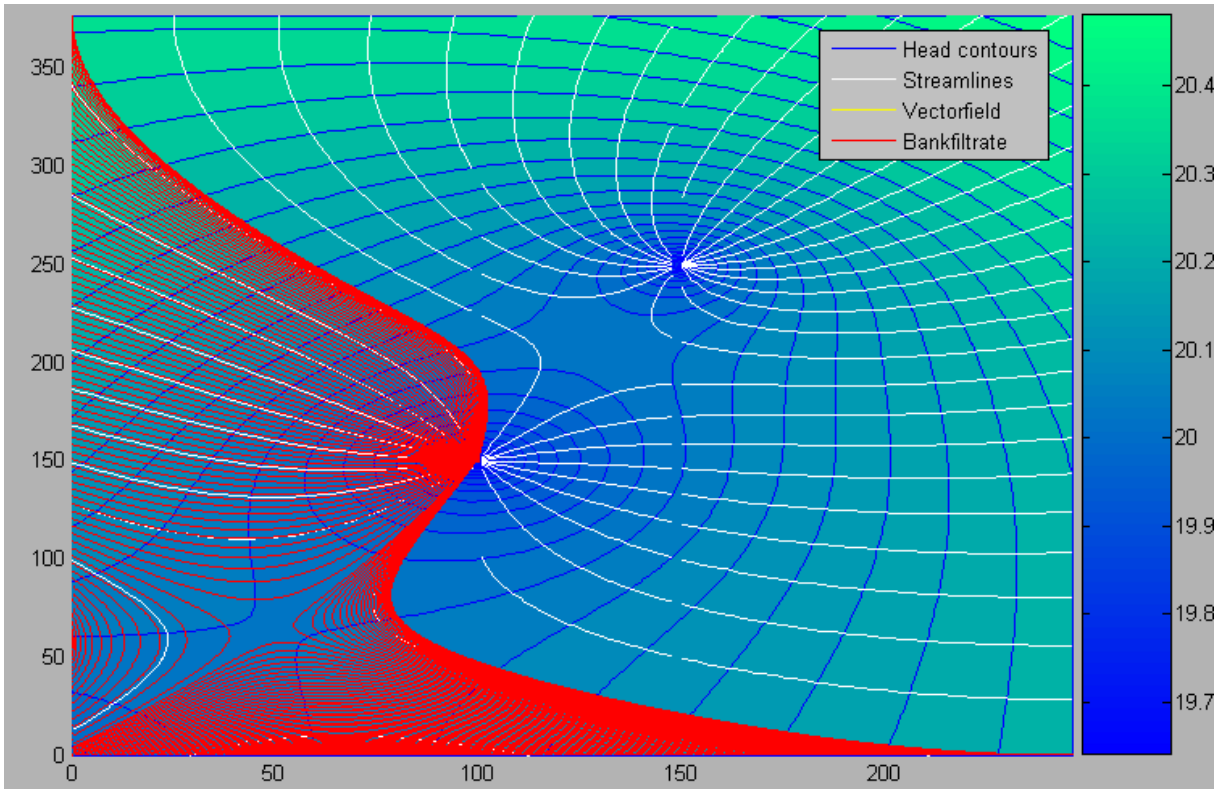

Figure 123 Example output for two wells and two banks, meeting by an angle of 90°

The user can influence bank filtration visualisation by changing the grid nodes manually, as explained in the help system under keywords 'grid nodes' and 'bank filtration flow paths':

2.5.2.7 Grid Nodes

A rectangular grid is specified by the two vectors for x- and y-coordinates of the grid nodes. These are input parameters for the user to be specified under the grid header. Concerning the choice of the units see remarks given in aquifer.

Both coordinates have to be given in two edit boxes in [ ]-brackets. It is convenient to use the double-dot option for equidistant grids, as shown by the following example.

Example: [0:6:400] gives 8 pumping wells, of which the two medium wells are pumping at the double rate than the outer wells.

Note 1: The user has to take care that the wells do not coincide with the grid nodes. Otherwise the program may calculate heads near to negative infinity, which may cause severe problems of the program. In any case the color bar scaling is effected and may show an unrealistic scale. Moreover the warning about the aquifer falling dry, may appear, which may no be true in reality – the program does not consider well diameters!

Note 2: Settings in the grid node edit vectors are ignored in case of automatic gridding.

Unit: L

Default: [0:6:500] for x-coordinates, [0:6:400] for y-coordinates

A revised figure for the same situation, depicted in Figure 123, is shown in Figure 124. The grid has been extended and refined.

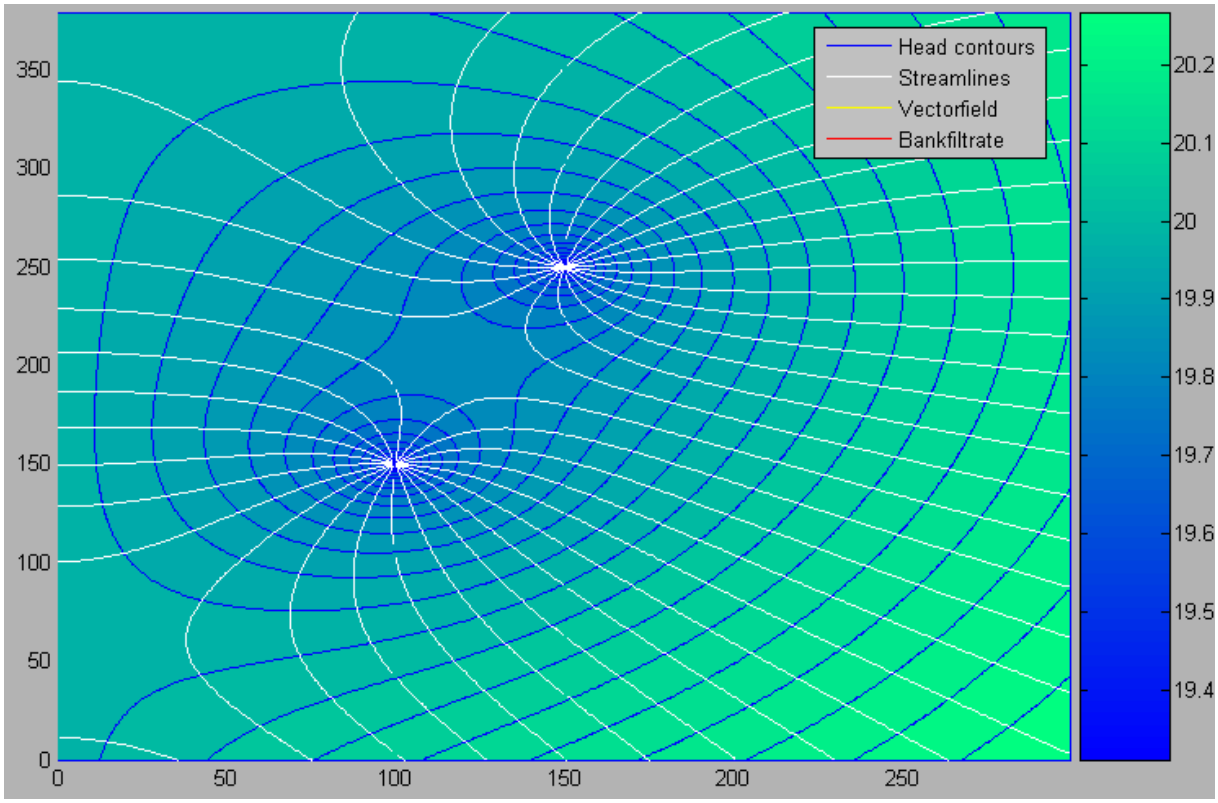

Figure 124Situation from Figure 4 with refined grid, without bank filtrate flowpaths

The bank filtrate flow paths the help system yields the following explanations:

2.5.2.8 Bank Filtrate Flow paths

Bank filtrate flow paths are calculated and drawn in the graphics window, if the corresponding option is set by the user. Bank filtrate flow paths are drawn in red. Starting positions for the bank filtrate are chosen automatically along the bank lines. The calculation is based on a flow path tracing algorithm, which works fine, if the grid spacing in x- and y-axis are identical. If spacing's in both directions do not coincide, a message box appears on the screen. The user may adjust the grid spacing manually (see Grid).

Note 1: Bank filtrate flow paths are calculated only for starting positions on the bank within the chosen spatial extension of the graphical output. Thus not the entire region of bank filtrate may be captured, if the minimum or maximum value of the grid is not appropriately selected. If the user selects automatic Gridding, the window is chosen wide enough automatically.

An exception is the situation, in which the bank filtrate infiltrates everywhere on the axes. Such a situation is given, when there is no base flow across a bank line. In that case the share of bank filtrate in pumped water is 100%.

Note 2: When bank filtrate flow paths are plotted, there is no distinction between bank filtrate flowing towards the wells or migrating further within the aquifer. Such a situation is given for base flow from the bank into the aquifer.

Note 3: Flow paths coincide with streamlines, if the flow path start position coincides with a streamline passing through the bank.

Default: on

Also the mathematical background of the computations is explained in the help system.

2.5.2.9 Mathematics

The mathematical calculations are based on the analytical element method. A elaborate description of the method is given by Strack (1989). The (x,y)-plane is identified with the complex z-plane by z = x + i*y. The following formulae are used for the calculation.

Formulae:

The complex potential for base flow:

$$\Phi(z) = -Q_0 \overline{z} \qquad \text{(I)}$$

The complex potential for a well:

$$\Phi(z) = \frac{Q_{well}}{2\pi} \ln(z - z_{well}) \qquad \text{(II)}$$

The complex potential for an image well across the x-axis:

$$\Phi(z) = -\frac{Q_{well}}{2\pi} \ln(z - \overline{z}_{well}) \qquad \text{(III)}$$

The complex potential for the clogging layer on the x-axis (van der Veer, 1993):

$$\Phi(z) = -\frac{Q_{well}}{\pi} \exp\left(\frac{i}{kc}(z + \overline{z}_{well})\right) E_1\left(\frac{i}{kc}(z + \overline{z}_{well})\right) \qquad \text{(IV)}$$

Real potential:

$$\varphi(z) = \mathrm{Re}(\Phi(z)) \qquad \text{(V)}$$

Streamfunction:

$$\Psi(z) = \mathrm{Im}(\Phi(z)) \qquad \text{(VI)}$$

Hydraulic head:

$$h(z) = \begin{cases} H/2 + \varphi(z)/KH & \text{if confined} \\ \sqrt{2\varphi(z)/K} & \text{if unconfined} \end{cases} \qquad \text{(VII)}$$

Velocities are calculated from the real potential using Darcy's Law.

Clogging can be considered using the approach of van der Veer (1994), where a clogging parameter with the unit of a length is introduced:

2.5.2.10 Clogging Parameter

The clogging parameter is an input parameter for the user to be specified under the "bank " header. Concerning the choice of the units see remarks given in "aquifer". For the NASRI Bank Filtration Simulator the clogging layer is assumed to be homogeneous and constant.

The clogging parameter is the product of clogging layer thickness and relative impermeability compared with the aquifer. If there is no clogging layer, the value of the clogging parameter is zero.

Example: If the clogging layer is 1 meter thick and 100 times less permeable than the aquifer, the clogging parameter is 100 in the MKS physical unit system.

Unit: L

Default: 0

The clogging layer is thus identified with the semi-permeable layer in the original publication. Another method, which was examined for implementation, was proposed by Anderson (2000). However, finally the approach of van der Veer was given the preference because of the isotropy of the less permeable layer: in Anderson's method the clogging layer has a higher conductivity tangential to the bank. When in the previous examples a clogging layer is considered, the following figure results:

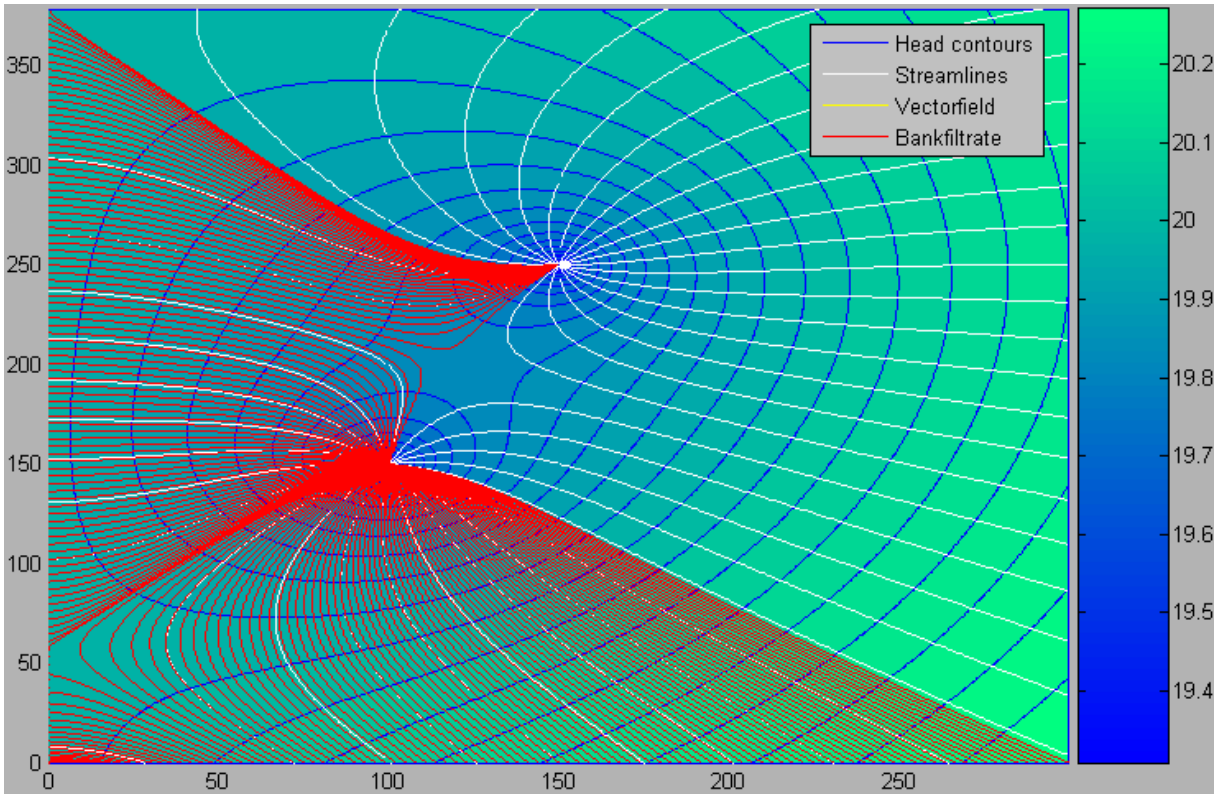

Figure 125 The two-well gallery from the previous figures under a consideration of a clogging layer with a clogging parameter of 10 m.

The menu entry 'travel times' is already present in the graphical user interface, but is not yet tested sufficiently, to become enabled.

2.5.3 Modified Version of the NASRI Bank Filtration Simulator

The development of a modified version of the NASRI Bank Filtration Simulator, which is designed for special set-ups, was started. In contrast to the former software specific settings of a given facility can be considered. An example, concerning Lake Wannsee gallery, is given in Figure 126.

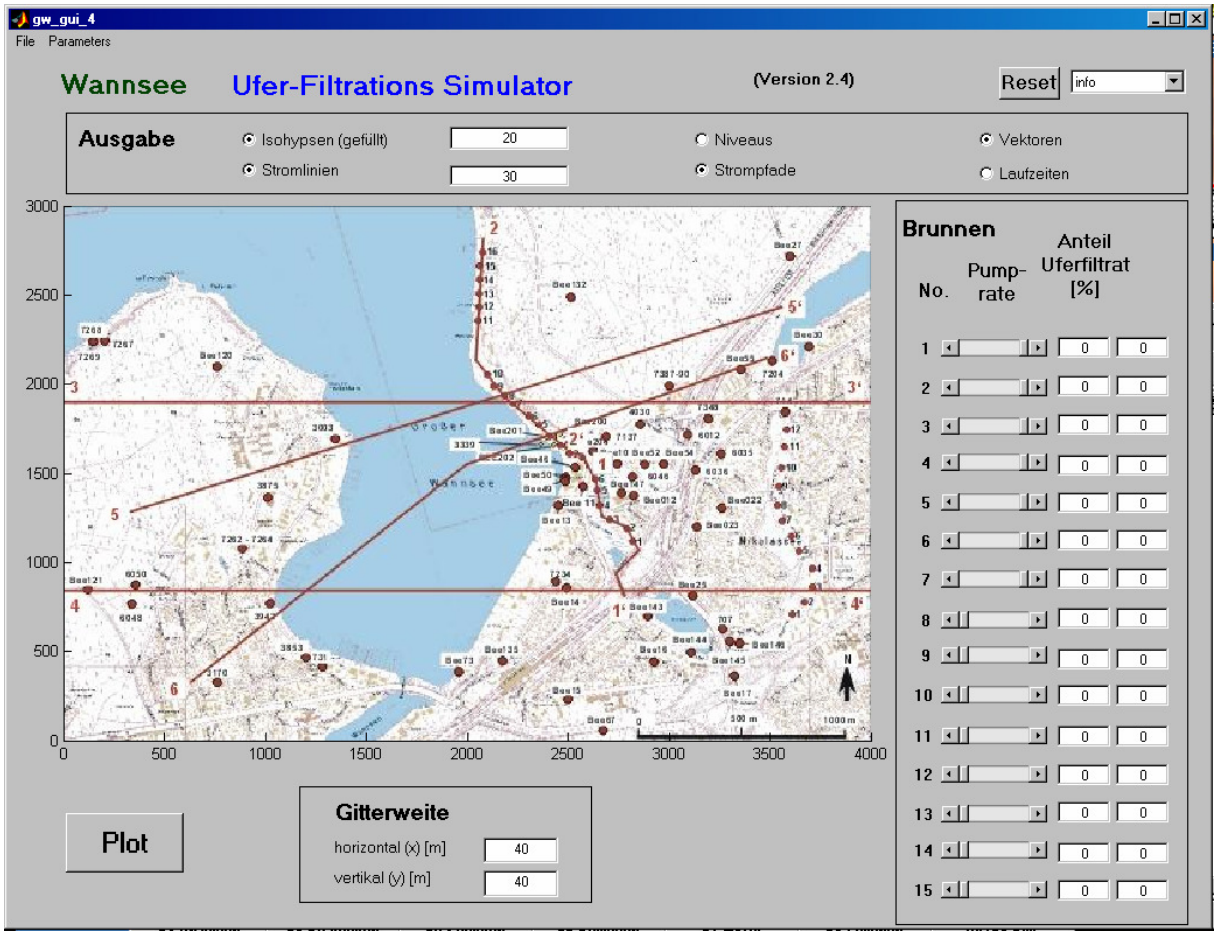

Figure 126 Modified version of the NASRIBank Filtration Simulator, as a blueprint for a management model for a specific facility, here the Lake Wannsee gallery in Berlin

The site-specific settings are specified in an initiation run. Based on a map in the background the user has to follow the bank-line by mouse clicks. In hat way a polygon is specified, which is an approximation of the bank-line and can be used for bank filtration calculations. Also wells are entered into the program by mouse clicks on the graphic panel.

In addition aquifer properties, bank characteristics, well locations and pumping rates are to be entered, as in the NASRI Bank Filtration Simulator. These values are site-specific, but can also be altered in a usual run of the management model by using the menu, as shown in Figure 127

The graphical user interface is designed to switch wells on and off and to explore the effects of various well operation schemes. The user may also change various output options as in the worked out bank filtration simulator, and to change the grid resolution. The corresponding input fields can be recognized in Figure 8. In the shown example, a maximum of 15 operating wells can be modelled.

An output field is added for each well, in which the share of bank filtrate in the well is to be shown. In addition the flow field is to be visualized in the graphic panel, as described in the previous chapter and as implemented already in the simulator software.

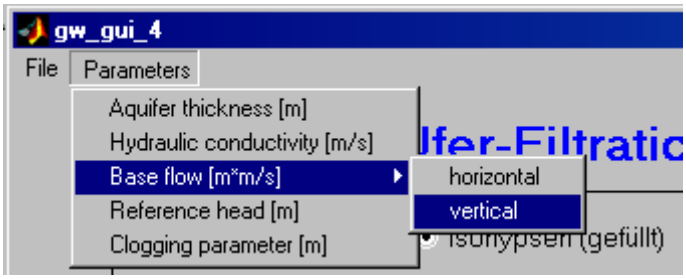

Figure 127 Menu for the site-specific version of the NASRI Bank Filtration Simulator.

The modified version of the simulator is not fully implemented, yet. Visualisation is to be improved, in order to restrict the output to regions land inward from the bank line. The calculation of the bank filtrate share on pumped water has to be implemented, too.
The site-specific version could be used for well gallery management, in order

- to visualize bank filtration flow towards wells
- to explore the effects of certain well operation decisions

The graphical output of the software shows the reach of a well gallery, i.e. the area and the part of the bank line, which is effected by bank filtrate for a specific pumping regime. Such information can be used to select between various pumping alternatives, if some regions are to be excluded from bank filtrate flow, for example.
The share of bank filtrate in each well is an appropriate indicator for optimal pumping regimes. It could be checked, for which operation regimes the share of bank filtrate is highest, in the entire gallery or for specific wells.

2.5.4 Flow and Transport Model

A flow and transport model was set up in order to identify increased concentrations in pumped water. The underlying problem for the model set-up is: what is the minimum degradation rate, for which a certain concentration margin in pumped water is exceeded? The idea is outlined in a submitted manuscript (Holzbecher, submitted), for which the following passages are taken. The figure numbers have been changed from the manuscript.

Along their path from the surface water body to the well, a biogeochemical substance may underlie several degradation processes. The relevant processes can be of biological, chemical, biochemical or physical nature and may depend on various conditions within the aquifer, as for example the redox state, the biogeochemistry within the pore space including the porous medium, the temperature, recharge conditions. Often the first few centimetres of the bank filtration path are crucial, where a clogging layer may have built up. Generally holds: the higher the degradation, the lower the concentration in the well, or vice versa: the lower the degradation, the higher the concentration in pumped water. There are problems with bank filtration, if the degradation of a potentially harmful substance is too low.

For both existing and projected facilities it is important to estimate the effect of natural attenuation on the concentration distribution along the flow path of bank filtrate and on the concentration of pumped water. Pumping rates should be kept below the threshold above which tolerable concentrations of problem substances in pumped water are exceeded. In the design of a projected well or well gallery the distance between bank and well should be chosen in accordance with requirements concerning the degradation of such possible problem substances.

Currently numerous studies are being undertaken to determine degradation characteristics on the microscale. Very often such studies result in a single value for the degradation parameter of a substance. The next question is, how relevant the obtained value is for a certain bank filtration facility. The aim of this paper is to present an inexpensive method for determining a range of degradation rates that are relevant for a given bank-well constellation in the field. Experimental work should be accompanied by such a method, as otherwise the meaning of determined degradation rates for a field situation remains uncertain.

The approach presented here does not aim at prediction in terms of forecasting but a mathematical-computational method. For that reason comparison with experimental results is not intended. The simplest possible approach for degradation was chosen, as it is intended to propose the method as a supplement within experimentally oriented research. It may prevent too much effort being invested in determining degradation rates that are above the relevant (or critical) range even under most unfavourable conditions for degradation-relevant species.

In this study the simplest degradation approach with a degradation rate in a first-order law is treated throughout. However, the outlined mathematical procedure can easily be applied to more complex degradation characteristics, such as Monod-type terms. This study is based on the fact that the validity of any mathematical degradation characteristics for the entire flow paths of bank filtrate can hardly be proved. Because of that uncertainty it is important to know which parameter range really counts. The question is about the minimum degradation rate, for which no significant breakthrough in the pumped water can be expected.

Numerical models are an appropriate and necessary tool not only for a quantitative evaluation of the effectiveness of natural attenuation processes. In the following a new approach is presented, which is easy to implement using mathematical tools for partial differential equations. Moreover the method is fast, as it solves for the steady state directly, and has small numerical errors, as it is combined with analytical solutions as far as possible.

2.5.4.1 The Modelling Concept

For many characteristic situations the flow of bank filtrate and groundwater towards wells can be computed by analytical methods. Using the analytical element method (Strack 1989, 1999) the solution for hydraulic potential φ and stream function Ψ is combined by superposition from basic solutions. For the following presentation the solutions for base flow are relevant

$$\varphi(x, y) = -Q_0 x \qquad \Psi(x, y) = Q_0 y \tag{1}$$

with base flow discharge Q_0 ([m^2/s] in MKS units) as product of Darcy velocity and aquifer depth; and for flow towards a well:

$$\varphi(x, y) = \frac{Q_{well}}{2\pi} \mathrm{Re}\left(\log\left(\mathbf{r} - \mathbf{r}_{well}\right)\right) \qquad \Psi(x, y) = \frac{Q_{well}}{2\pi} \mathrm{Im}\left(\log\left(\mathbf{r} - \mathbf{r}_{well}\right)\right) \tag{2}$$

with pumping rate Q_{well} ([m^3/s] in MKS units). The logarithm in formulae (2) is the complex logarithm, defined in the complex plane with $\mathbf{r} = x + i \cdot y$. $\mathbf{r}_{well}$ denotes the well location in the complex plane. Following the principle of superposition the distributions of base flow and wells to potential or stream function have to be added. The Darcy velocity **v** can be obtained from the stream function Ψ or from the potential φ, using the formulae:

$$v_x = -\frac{1}{h}\frac{\partial \Psi}{\partial y} \qquad v_y = \frac{1}{h}\frac{\partial \Psi}{\partial x} \qquad \text{or} \qquad \mathbf{v} = -\frac{1}{h}\nabla\varphi \tag{3}$$

In the vicinity of a straight isopotential boundary the method of images delivers the solution by introducing image wells. A detailed description of these methods is given by Strack (1989).

The presented method can be applied for the confined and for the unconfined aquifer, and also for situations in which the aquifer is partially confined and unconfined. The specific

situation, confined or unconfined, is taken into account when hydraulic head *h* is calculated from the potential φ to. Details are given in the next sub-section.

Transport, first-order degradation and equilibrium sorption are usually described by the transport equation (for example: Holzbecher, 1996):

$$\theta R \frac{\partial c}{\partial t} = \nabla \mathbf{D} \nabla c - \mathbf{v} \nabla c - \theta R \lambda c \tag{4}$$

with dispersion tensor **D**, velocity vector **v**, porosity θ, retardation coefficient *R* and decay constant λ. In two space dimensions the dispersion tensor is given by:

$$\mathbf{D} = \begin{pmatrix} D_m + (\alpha_L v_x^2 + \alpha_T v_y^2)/v & (\alpha_L - \alpha_T) v_x v_y / v \\ (\alpha_L - \alpha_T) v_x v_y / v & D_m + (\alpha_T v_x^2 + \alpha_L v_y^2)/v \end{pmatrix} \tag{5}$$

with diffusivity D_m, longitudinal dispersivity α_L, transversal dispersivity α_T, velocity components v_x and v_y, and $v = \sqrt{v_x^2 + v_y^2}$ (Bear, 1972). For the steady state the differential equation can be simplified to:

$$\nabla \mathbf{D} \nabla c - \mathbf{v} \nabla c - \mu c = 0 \tag{6}$$

with a modified degradation parameter $\mu = \theta R \lambda$, which depends both on the sorption and the degradation characteristic of the component. Equation (6) is a condition for the steady state concentration distribution, which can be obtained directly for a specified set of boundary conditions (see below).

Most modelling codes are implemented for the unsteady situation, as given in equation (4), and steady state solutions can be obtained by choosing long time periods in the simulation. As the time period necessary to come close to the steady state is not known beforehand, several runs of the transient simulation are usually necessary in order to obtain the steady-state concentration distribution. Moreover, at least one additional run is necessary in order to check whether the solution shows only marginal changes for an extended time period. These complications are avoided when the steady state is sought directly from equation (6). Mathematical tools allow such a direct approach. Here the FEMLAB® code was chosen for implementation.

2.5.4.2 FEMLAB® Implementation

FEMLAB® (2004) is a multi-purpose code for simulations of multi-physics situations. Various partial differential equations can be used and coupled for various sub domains. It is possible to combine various flow regimes with transport equations with general one-way or two-way couplings. Partial differential equations can be specified explicitly by the user in coefficient or general form, or can be chosen from a list of predefined alternatives. The transport equation (4) is included as a convection-diffusion equation and can be found under the 'diffusion' topic

or under 'classical PDEs'. In FEMLAB® there is an additional alternative between 'steady-state analysis' and 'transient analysis'; only the former is relevant for the aim of this paper.
For flow towards a well, the 'Poisson equation' from the 'classical PDEs' list could be chosen in combination with a weak term under 'point settings'. However, in order to be even more precise, the analytical solution, as described above, was explicitly implemented using the 'sub domain expressions':

$$
\begin{aligned}
r_1 &= (x + x_{well})^2 + y^2 \\
r_2 &= (x - x_{well})^2 + y^2 \\
q_x &= -Q_0 + \frac{Q_{well}}{2\pi}\left(\frac{x + x_{well}}{r_1} - \frac{x - x_{well}}{r_2}\right) \\
q_y &= \frac{Q_{well}}{2\pi}\left(\frac{y}{r_1} - \frac{y}{r_2}\right) \\
\varphi &= -Q_0 x + \frac{Q_{well}}{2\pi}\log\left(\sqrt{\frac{r_1}{r_2}}\right) \\
\Psi &= Q_0 y + \frac{Q_{well}}{2\pi}\left[\tan^{-1}\left(\frac{y}{x - x_{well}}\right) - \tan^{-1}\left(\frac{y}{x + x_{well}}\right)\right]
\end{aligned}
\tag{7}
$$

The vector $\mathbf{q}=(q_x,q_y)^T$ is the discharge vector (Strack 1989). Thus flow is explicitly given in the presented model and included in the specification of the transport model (convection-diffusion equation). Formulae for analytical solutions, as presented above, are difficult to introduce into the usual groundwater software. But they are easy to specify in general mathematical tools, such as FEMLAB®. However, for a site-specific model, including one extended well gallery or even several galleries in FEMLAB®, it is advisable to use the option for numerical flow solution.
The connection with transport is also implemented by 'subdomain expressions':

$$
\begin{aligned}
v_x &= q_x / h \\
v_y &= q_y / h \\
v &= \sqrt{v_x^2 + v_y^2} \\
D_{xx} &= D_m + (\alpha_l v_x^2 + \alpha_t v_y^2)/v \\
D_{yy} &= D_m + (\alpha_t v_x^2 + \alpha_l v_y^2)/v \\
D_{xy} &= (\alpha_l - \alpha_t) v_x v_y / v
\end{aligned}
\tag{8}
$$

with hydraulic head $h = \begin{cases} h_0 & \text{where the aquifer is confined} \\ \sqrt{h_0^2 + 2\varphi / K} & \text{where the aquifer is unconfined} \end{cases}$.

h_0 denotes the aquifer depth in the confined case, and hydraulic head along the bank for the unconfined case.

The first version of this model used the earlier 2.3 version of FEMLAB®, in which the implementation of a general dispersion tensor, as given in equation (5), was not possible. Thus the 'pde-general form' option was chosen (not the predefined 'convection-diffusion' mode), in which the differential equation has the general form:

$$\nabla \cdot \Gamma = F \tag{9}$$

For the bank filtration problem the subdomain settings in the general form are as follows:

$$\begin{aligned} \Gamma(c) &= \left(-D_{xx}c_x - D_{xy}c_y + v_x c, -D_{xy}c_x - D_{yy}c_y + v_y c\right) \\ F(c) &= -\mu c \end{aligned} \tag{10}$$

The FEMLAB® 3.0 and 3.1 versions allow the introduction of a full dispersion tensor. Thus the 'convection-diffusion' option could be chosen in these versions as alternative mode instead of the 'pde-general form'. If a more general degradation characteristic is to be taken into account, it can easily be specified in the source/sink term $F(c)$. The formulation, given in equation (10), represents first-order decay with degradation rate μ. Note that μ includes both sorption and degradation processes. For a linear sorption isotherm the formula $\mu = R \cdot \lambda$ is valid, with retardation factor R and degradation rate λ for a pure fluid environment.

The boundary conditions for the transport model were chosen as follows:

$$\begin{aligned} &\text{bank:} && g = 0,\ r(c) = c - c_0 && \text{(Dirichlet)} \\ &\text{aquifer:} && g(c) = (v_x n_x + v_y n_y)c && \text{(Neumann)} \\ &\text{well:} && g(c) = (v_x n_x + v_y n_y)c && \text{(Neumann)} \end{aligned} \tag{11}$$

where (n_x, n_y) denotes the vector normal to the boundary. There is a concentration c_0 specified at the bank. The problem substance is assumed to have a constant concentration c_0 in the surface water. For a field situation in which the concentration in surface water is not constant in time, a maximum value should be specified for a worst case simulation. All other boundaries have Neumann boundary conditions.

All mentioned parameters are introduced as constants in the related sub-menu of the FEMLAB® graphical user interface. Thus changes of the model are easy for non-expert users... .

As an example for the described concept an example for a single well near a straight boundary was set up as depicted schematically in the corresponding figure. The model region is a square of 200 by 200 m, extending from 0 to 200 m in x-direction and from -100 to 100 m in y-direction, with the well located at the central position $\mathbf{r}_{well}$=(100 m, 0 m) and the bank at the y-axis. The well diameter is 1 m. Parameters were chosen as:

$$
\begin{aligned}
\alpha_L &= 10 \text{ m} \\
\alpha_T &= 1 \text{ m} \\
Q_0 &= 6.25 \cdot 10^{-6} \text{ m}^3/\text{s} \\
Q_{well} &= 2.5 \cdot 10^{-3} \text{ m}^3/\text{s} \\
x_{well} &= 100 \text{ m} \\
h_0 &= 25 \text{ m} \\
\mu &= 5 \cdot 10^{-10} \text{ 1/s} \\
K &= 3 \cdot 10^{-4} \text{ m/s} \\
D_m &= 1 \cdot 10^{-9} \text{ m}^2/\text{s} \\
c_0 &= 1 \text{ g/m}^3
\end{aligned}
\tag{12}
$$

Some parameter values were adopted from a situation which is typical for bank filtration facilities in Germany, e.g. pumping rate Q_{well}, base flow Q_0, distance between bank and well x_{well}, and aquifer depth h_0. Similarly designed facilities are found at other locations in Europe (Jekel, 2003; Grischek et al., 2003), while in the United States wells are often placed nearer to the bank (Bouwer, 2003). Bank filtration facilities are mostly installed in sand or gravel aquifers: K is typical for gravel with relatively low hydraulic conductivity or coarse sand with relatively high conductivity. In many groundwater studies it has been observed that dispersion length values are correlated to the typical length of the observed phenomenon. They are one or two orders of magnitude smaller (Beims & Mansel, 1990; Luckner & Schestakow 1986). When the characteristic length scale for bank filtration is the distance between bank and well, the chosen value for α_L lies near the upper limit of the expected range. It is also common that the transversal dispersion length α_T lays one order of magnitude below the longitudinal dispersion length. For the given set-up the chosen values are thus in the expected range, but site-specific conditions may lead to substantially different parameters.

A finite element mesh is created by FEMLAB® for the square excluding the disk which represents the well. The initial coarse mesh was refined near the well and along the bank boundary and consists of 6285 nodes, 3055 elements and 175 boundary elements.

The problem for the steady-state solution of the two-dimensional concentration distribution $c(x,y)$ is solved directly following equation (6). The start solution is $c \equiv 0$ in the entire domain. Solutions for the linear equations are obtained by the UMFPACK direct method. For that method all default conditions were kept, a pivot threshold of 0.1 and automatic scaling for example.

2.5.5 Results and Discussion

Results for the confined case are depicted in Figure 9 as a contour plot and in Figure 10 as a surface plot. The unconfined case and the given parameters results differ only slightly from those presented for the confined situation. Streamlines can be obtained as contours of the streamfunction Ψ or using the FEMLAB® option to calculate streamlines from the velocity vector field. The latter approach has the advantage that cuts of the complex logarithm (see equation(2)) do not disturb the picture. On the other hand, contour plots to equidistant levels have the advantage of indicating flow velocities by contour distances (Holzbecher, 2002). For Figure 9 the FEMLAB® 'streamline' option (from the plot menu) was chosen. Along the bank (left boundary) the region with infiltrating surface water can clearly be recognized by streamlines (white lines) connecting bank and well. By contrast in the outer parts streamlines enter the bank from the aquifer, where flow has a negative *x*-component – these are regions with groundwater discharge into the river or lake.

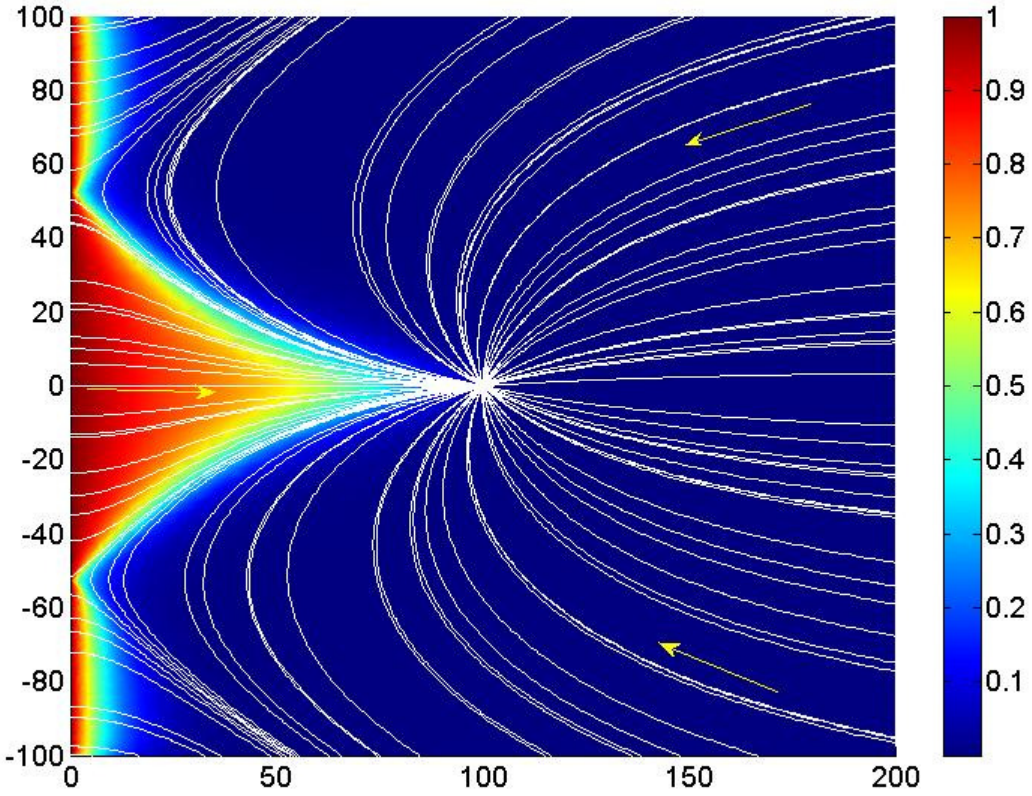

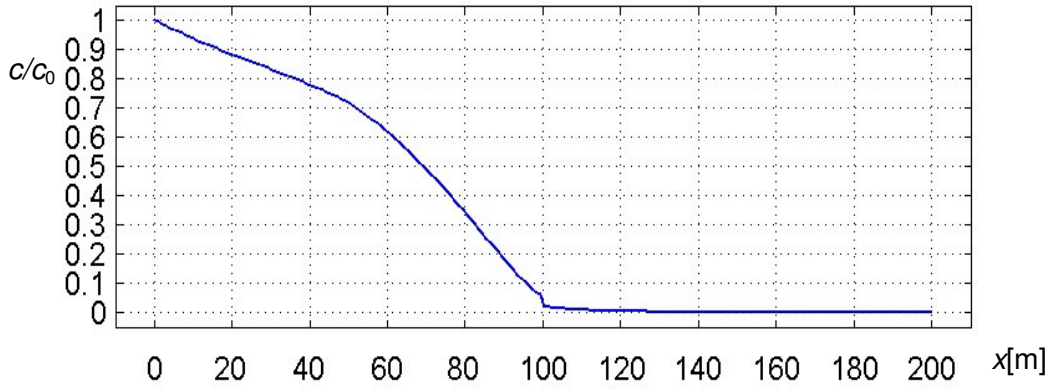

Figure 128 : Bank-filtration for a single well in the vicinity of a straight shoreline; depicted is a window of 200 m in both directions with a single well at the central position and bank line on the left; white lines are streamlines; the colour map depicts the steady state concentration distribution of a chemical component present in surface water, which is degraded during the bank filtration passage: red colour for high concentrations, blue colour for background concentrations; lower part of the figure provides normalized concentrations (c/c_0) along the central axis in horizontal direction through the well

Visualisation of the results shows increased concentrations within the bank filtrate flowing towards the well. The penetration is smallest at both stagnation points on the shore line, increasing again in the part with aquifer discharge. While the further penetration in the bank filtrate region is due to the flow regime, the difference between the stagnation points and the discharge region can be attributed to longitudinal dispersion. At the stagnation points both velocities and dispersion become almost negligible, which is not the case in the region of groundwater discharge.

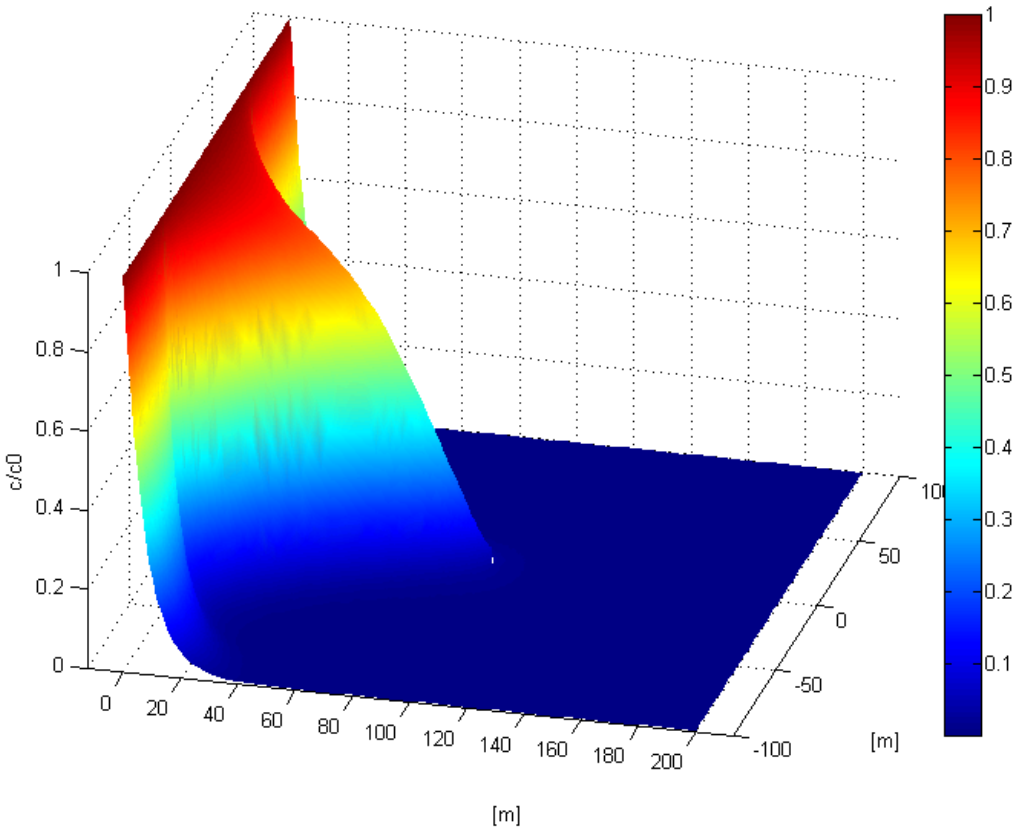

Figure 129 Concentration distribution due to the bank-filtration for the reference case, depicted in a surface plot

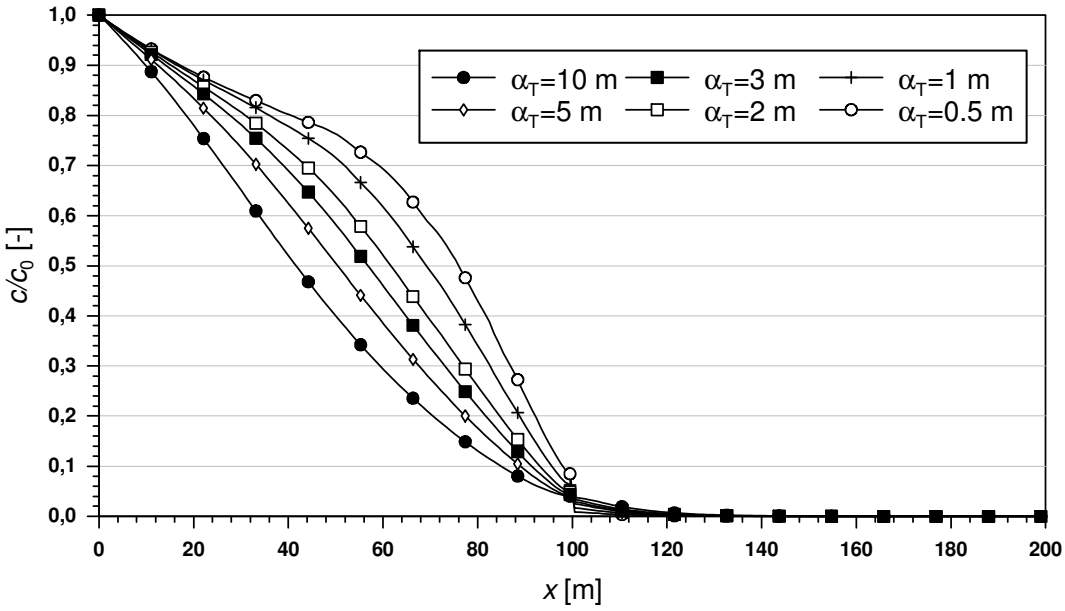

Figure 130 The effect of transversal dispersivity on the steady-state concentration profile along the shortest flowpath between bank and well

Another interesting observation can be made in the profile through the central axis (in x-direction) through the figure. The concentration profile obviously changes its gradient during the path towards the well: from a smoother to a steeper slope. The increase of velocity along the flowpath would lead us to expect the opposite: with higher velocities the effective degradation decreases and lowers the concentration gradients. However, the observed behaviour can be explained by another process:, transversal dispersion.

The sensitivity of the results to transversal dispersivity was examined for the unconfined aquifer, leaving all other parameters unchanged in comparison with the reference case, defined by list (12). The transversal dispersion coefficient α_T was varied between values of 0.5 and 10 m, representing factors between 1 and 20 for the α_L/α_T ratio. Higher values of α_T are unlikely, as transversal dispersivity almost never exceeds longitudinal dispersivity. Results are shown in Figure 130. For $\alpha_T = \alpha_L = 10\ \mathrm{m}$ the steady state concentration profile is smooth, whereas a bend becomes visible with decreasing α_T, showing the transition from a moderate to a steep gradient. It is clear that the effect of transversal dispersion increases when the bank filtration wedge becomes slender in the vicinity of the well (see Figure 128).

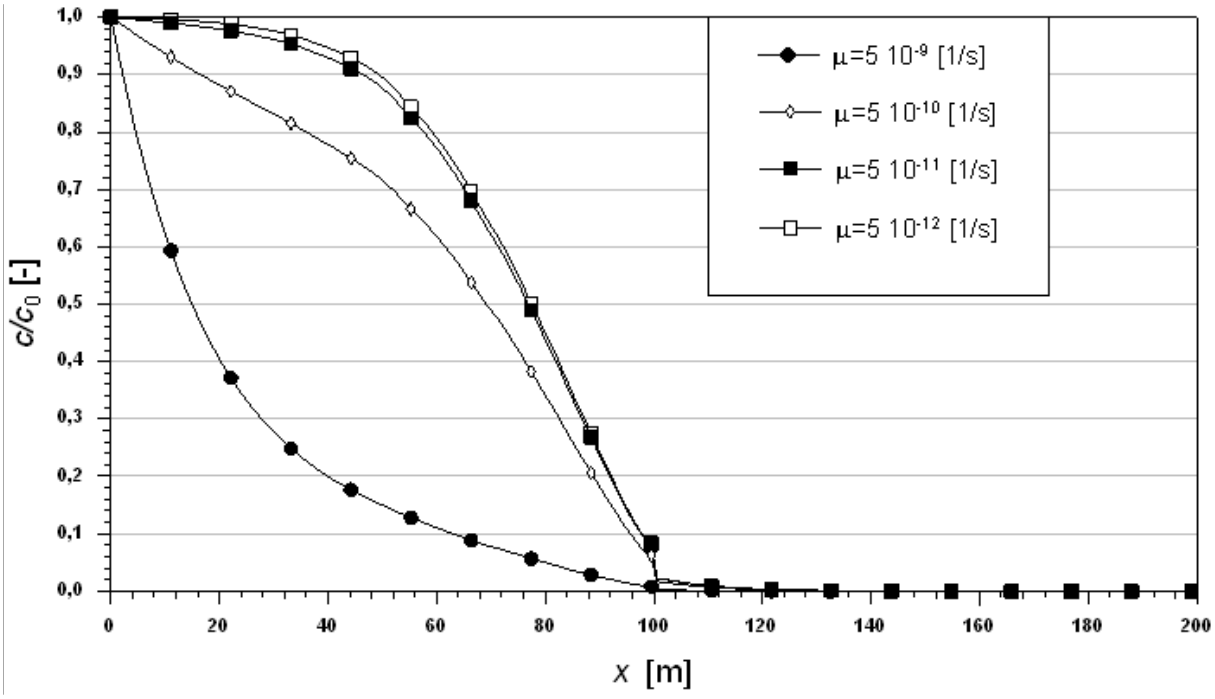

Figure 131 The effect of decay rate on the concentration distribution along the shortest flowpath between bank and well

The effect of the generalized decay rate μ is shown in Figure 131, demonstrating the transition from a concave to a convex shape. With four orders of magnitude between 10^{-9} and 10^{-12} [1/s] a wide parameter range is chosen. In fact degradation rates probably differ

even more, as they depend not only on the specie, but also on climatic, seasonal and redox conditions and on the biogeochemical environment in general. The variability of the parameter motivates the chosen range, as it represents the interval, where the value of the degradation rate becomes important. For values above 10^{-9} 1/s the substance reaches the well in very low concentrations. For values lower than 10^{-12} 1/s the concentration in the well is more likely to be relevant: concentrations in the direct vicinity of the well screen reach 1/10 of the concentration in the surface water, a level which under certain conditions may exceed the tolerable limit. A likely interpretation of Figure 130 is that for degradation rates below 10^{-10} 1/s the concentrations in pumped bank filtrate could reach levels comparable to input concentrations. These findings are valid for the chosen set-up and should not be transferred to other situations.

The total mass of substance per time unit, pumped with the water, can be obtained by the boundary integral:

$$q = \oint_{\text{well boundary}} h \cdot c \left(v_x n_x + v_y n_y \right) ds \tag{13}$$

FEMLAB® is able to perform such boundary integrals in the post processing mode. The integrant is specified exactly as given in formula (13). For the reference case the resulting value is $5 \cdot 10^{-7}$ g/s. The concentration in pumped water after mixing is therefore $c_{well} = q / Q_{well} = 2 \cdot 10^{-4}$ g/m^3.

2.5.6 Summary

The described method allows a direct and therefore fast computation of the steady-state solution for the bank filtration flow and transport problem. Concentrations of surface water substances can be expected to be higher in permanently pumping wells than in sporadically pumping wells. With appropriate parameters the steady state represents a worst case scenario and can be applied as such also for transient situations with changing pumping rates of the wells, and/or for changing concentrations of a problem substance in the surface water body. For the latter situation the highest measured concentration should be used in the boundary condition (c_0), see equation (11).

The margin at which degradation rates deliver values comparable to the inlet concentration was found to be around 10^{-10} 1/s: above that margin concentrations in pumped bank filtrate will be significantly lower than c_0. Experimental studies in enclosures under near field conditions, performed with phages within the NASRI project in Berlin (Germany), show values around 3 10^{-8} 1/s (Holzbecher *et al.*, to appear). Even under anaerobic conditions minimum degradation rates reach 2 10^{-9} 1/s, which according to the findings in this paper is a range for which problems with increased concentrations in pumped water cannot be

expected. In the same experiments for microcystins degradation rates above 10^{-7} 1/s were obtained, which is even more unproblematic.

The given estimation of a relevant parameter range is not valid for substances that are a potential hazard at concentrations several orders of magnitude below the concentration in surface water. Such a situation is conceivable in the case of a severe accident upstream in the surface water body. However, in such a case the steady-state assumption for the concentration distribution, as made above, would probably not be justified. However, multi-physics tools like FEMLAB® could handle emergency scenarios with unsteady transport as well.

The multi-physics approach presented here can easily be extended to account for more general degradation characteristics compared to the simple linear approach. However, in most cases it is unknown whether a more complex degradation regime is valid under field conditions for the entire flowpaths of bank filtrate towards a well. In such a situation one may consider adopting a conservative worst case study, as presented here, in which a more complex approach could also be implemented.

The presented approach with an analytical solution for flow calculation allows several extensions. Shorelines meeting at a certain angle can be represented by extending the method of mirror wells (Bear, 1972; Strack, 1989) or conformal mappings (Holzbecher, 2005). In case of a gradient on the bank an appropriate analytical solution is described by Wilson (1993). The approach proposed by van der Veer (1994) allows the consideration of a clogging layer at the bottom of the surface water body.

The presented concept can also be extended for more general situations. Multiple wells can be introduced. Such well galleries may also include recharge wells. As the notation for the explicit flow solution becomes lengthy in the case of multiple wells, it is recommended to let FEMLAB® calculate the flow solution using the 'Poisson' equation with point sink at the well location. Using the FEMLAB® flow solver it is also possible to take into account irregular boundaries, either at the bank or for the aquifer. Material properties are allowed to change, which allows the consideration of inhomogeneities in hydraulic conductivity, and of anisotropies. All such extensions can be performed using the multi-physics approach of FEMLAB®.

2.5.7 References

Anderson E.I., The method of images for leaky boundaries, *Adv. in Water Res.*, Vol. 23, No. 5, 461-474, 2000

Bear, J., 1972. Flow through Porous Media, Elsevier, New York, 764pp.

Beims, U., Mansel H., 1990. Assessment of groundwater by computer model design and pumping tests, in: Groundwater Monitoring and Management, IAHS Publ., No.173, pp11-22.

Bouwer, E.J., 2003. Riverbank filtration - the American experience. In: Melin, G. (Ed), Riverbank Filtration: the Future is Now, Proc. 2nd Riverbank Filtration Conf., National Water Research Institute, pp 105-110.

FEMLAB®, Version 3.1, 2004. COMSOL AB, Tegnérgatan 23, SE-111 40 Stockholm, Sweden.

Grischek, T., Schoenheinz, D., Worch, E., Hiscock, K., 2003. Bank filtration in Europe - an overview of aquifer conditions and hydraulic controls. In: Dillon P.J. (Ed), Management of Aquifer Recharge for Sustainability, Balkema, Lisse, pp485-488

Holzbecher, E., 1996. Modellierung dynamischer Prozesse in der Hydrologie: Grundwasser und ungesättigte Zone, Springer Publ., Heidelberg

Holzbecher, E., 2002. Groundwater Modelling - Simulation of Groundwater Flow and Pollution, Electronic Book on CD-ROM, FiatLux Publ., Fremont (USA)

Holzbecher E., Analytical solution for 2D groundwater flow in presence of two isopotential lines, *Water Resources Research*, Vol. 41, No. 12, W12502, 2005

Holzbecher E., Calculating the effect of natural attenuation during bankfiltration, to: *Computers & Geosciences,* submitted

Holzbecher, E., Dizer H., Grützmacher G., Lopez-Pila J., Nützmann G., The influence of redox conditions on phage transport – enclosure experiments and modelling, *Enviromental Engineering Science*, to appear

Jekel., M., 2003. Riverbank filtration: the European experience. In: Melin, G. (Ed), Riverbank Filtration: the Future is Now, Proc. 2nd Riverbank Filtration Conf., National Water Research Institute, pp105-110.

Luckner, L., Schestakow W.M., 1986. Migrationsprozesse im Boden- und Grundwasserbereich, Deutscher Verlag für Grundstoffindustrie, Leipzig.

Strack, O.D.L, 1989. Groundwater Mechanics, Prentice Hall, Englewood Cliffs, 732pp.

Strack, O.D.L., 1999. Principles of the analytic element method, *J. of Hydrol.* 226, 128-138.

van der Veer, P., 1994. Exact solutions for two-dimensional groundwater flow in a semiconfined aquifer, *J. of Hydrol*. 156, 91-99.

Wilson, J.L., 1993. Induced infiltration in aquifers with ambient flow, *Water Resources Research*. 29(10), 3503-3512.

Abbreviations:

GUI Graphical User Interface

SENSUT Senatsverwaltung für Stadtentwicklung und Umweltschutz, Environmental Authority of Berlin